12-2009

Mechanical Behavior and the Role of Deformation Twinning in Wrought Magnesium Alloys Investigated Using Neutron and Synchrotron X-ray Diffraction

Liang Wu
University of Tennessee - Knoxville

To the Graduate Council:

I am submitting herewith a dissertation written by Liang Wu entitled "Mechanical Behavior and the Role of Deformation Twinning in Wrought Magnesium Alloys Investigated Using Neutron and Synchrotron X-ray Diffraction." I have examined the final electronic copy of this dissertation for form and content and recommend that it be accepted in partial fulfillment of the requirements for the degree of Doctor of Philosophy, with a major in Materials Science and Engineering.

Peter K. Liaw, Major Professor

We have read this dissertation and recommend its acceptance:

Tai G. Nieh, Hahn Choo, John D. Landes

Accepted for the Council:

Carolyn R. Hodges

Vice Provost and Dean of the Graduate School

(Original signatures are on file with official student records.)

To the Graduate Council:

I am submitting herewith a dissertation written by Liang Wu entitled "Mechanical Behavior and the Role of Deformation Twinning in Wrought Magnesium Alloys Investigated Using Neutron and Synchrotron X-ray Diffraction." I have examined the final electronic copy of this dissertation for form and content, and recommend that it be accepted in partial fulfillment of the requirements for the degree of Doctor of Philosophy, with a major in Materials Science and Engineering.

Peter K. Liaw

Major Professor

We have read this dissertation and recommend its acceptance:

Tai G. Nieh

Hahn Choo

John D. Landes

Accepted for the Council:

Carolyn R. Hodges

Vice Provost and Dean of the Graduate School

(Original signatures are on file with official student records.)

Mechanical Behavior and the Role of Deformation Twinning in Wrought Magnesium Alloys Investigated Using Neutron and Synchrotron X-ray Diffraction

A Dissertation Presented for the

Doctor of Philosophy Degree

The University of Tennessee, Knoxville

Liang Wu

December, 2009

DEDICATION

This work is dedicated to them: my wife, *Fenglei (Christine) Cao*, and my daughter, *Juntao (Grace) Wu*, who have been giving me lasting loves, continuous supports and constant understandings. And also, to my parents, *Linru Wu* and *Ping Wang*, my brother, *Xiao Wu*, my sister, *Hongfen Wu*, my father- and mother-in-law, *Duaiting Cao* and *Lifang Zhang*, and the rest of my family and friends, for their believing in me, inspiring me, and encouraging me.

ACKNOWLEDGEMENTS

I would like to express my utmost gratitude to the committee members: *Prof. Peter K. Liaw, Prof. Tai G. Nieh, Prof. Hahn Choo, and Prof. John D. Landes,* for their great involvements in the present research efforts and giving all kinds of help to me, making it possible for me to finish my Ph.D. study. Special thanks are directed to my major advisor, *Prof. Peter K. Liaw*, who has been supporting me academically and financially through his continuous trust, inspiration, and encouragement. My sincere thanks go to *Prof. Sean R. Agnew* from the University of Virginia, as the courtesy committee member, for his constructive discussions and advices, which play significant contributions to complete the current research. I had learned a lot from *Dr. G. Migri Stoica* by closely working with her during the first three years. *Mr. Douglas E. Fielden*, and his team, *Mr. Larry D. Smith and Mr. Dan Hackworth*, at The University of Tennessee have always been great friends, making every effort possible to help me get the work done in a timely manner. I would like to thank *Dr. Don W. Brown and Dr. Bjorn Clausen* at the Los Alamos Neutron Science Center (LANSCE), and *Dr. Yang Ren and Dr. Jon Almer* at the Advanced Photon Source (APS) for providing the guidances and advices to conduct the nice measurements in the respective facilities. I would like to thank *Dr. Carlos N. Tome* of the Los Alamos National Laboratory, *Prof. H. Rudy Wenk* of the University of California at Berkley, *Prof. W. Reimers* of the Technical University Berlin, and *Dr. Andrew E. Payzant* of the Oak Ridge National laboratory for the helps in their respective areas of expertise.

I would like to express my gratitude to all my friends for their kindness throughout this work and also for providing the friendly environment in our group during the past five years of study. Many people helped me on many aspects that are indispensable. I'm thankful to *Dr. Gongyao Wang, Dr. Yandong Wang, Dr. Cang Fan, Dr. Guojiang Fan, Dr. Hongqi Li, Dr. Wenhui Jiang, Dr. Sheng Cheng, Dr. Lan Huang, Dr. Michael Benson, Dr. Dongchun Qiao, Dr. Jiawan Tian, Dr. Fengxiao Liu, Mr. Hao-Hsiang Liao, Mr. Feng Jiang, Mr. E-Wen Huang, Mr. Sooyeol Lee, Mr. Andrew Chuang, Mr. Wei Wu, Mr. Zhenke Ten, Mr. Matthew Freels, Ms. Li Li, Ms. Shenyan Huang, Ms. Lu Huang, Mrs. Carol Winn*, *Mrs. Roberta L. Campbell*, and other group members for their helps.

I am particularly grateful to the financial supports from the National Science Foundation (NSF): i) The Combined Research-Curriculum Development (CRCD) Program, under EEC-9527527 and EEC-0203415; ii) The Integrative Graduate Education and Research Training (IGERT) Program, under DGE-9987548; iii) The International Materials Institutes (IMI) Program, under DMR-0231320; and iv) the Major Research Instrumentation (MRI) Program, under DMR-0421219.

This work has benefited from the uses of LANSCE at the Los Alamos National Laboratory (LANL), and APS at the Argonne National Lab (ANL). The LANSCE is a national user facility funded by the United States Department of Energy, the Office of Basic Energy Science – Materials Sciences, under Contract W-7405-ENG-36 with the University of California. The use of APS was supported by the United States Department of Energy, the Office of Basic Energy Science – Materials Sciences, under Contract DE-AC02-06CH11357.

ABSTRACT

The mechanical behaviors and the associated deformation mechanisms with a focus on extension twinning under monotonic and cyclic loadings are investigated using neutron and synchrotron diffractions in the wrought magnesium alloys, ZK60A and AZ31B. It has been demonstrated that the extension twinning plays significant roles in the mechanical behaviors.

The significant tension-compression asymmetries and high anisotropies are observed. The tension-compression asymmetries are related to the twinning activation in one direction but not in the opposite direction. The high anisotropies are correlated with the initial texture distinction relative to the loading directions. The similar yielding stresses are noted irrespective of the strain direction and strain sign if the deformation is dominated by twinning, while they are usually different with respect to the loading conditions if the dislocation slip is dominant. The extension twinning under tension exhibits a similar behavior to that under compression, presumably due to the same Schmid stress introduced on the twinning plane along the twinning shear direction. However, the distribution of basal poles within the twins under tension is closely related to the initial texture, while they are always aligned with the compressive axis under compression.

The low-cycle fatigue resistances follow the empirical Basquin and Coffin-Manson relationships with the texture dependency observed, related to the different activation sequences of twinning and detwinning involved, respectively, under tension and

compression determined by the initial texture. Specifically, the post-detwinning deformation characteristics may be an important factor in understanding the texture dependency. The extension twinning is readily activated if an applied stress/strain supports c-axis extension of the hexagonal-close-packed (hcp) structure. The unique reorientation of the twins facilitates detwinning in the twinned areas during the subsequent strain/stress reversal. Therefore, the cyclic plastic deformation is dominated by the alternating twinning and detwinning, and the initial texture is recovered once detwinning capability is exhausted, concurrent with the disappearance of twin bands. In particular, detwinning occurs almost immediately in the twinned grains upon unloading, which is driven by the local tensile stress along their c-axes as a result of the stress redistribution between the soft- and hard-grain orientations due to the plastic anisotropy.

TABLE OF CONTENT

LIST OF TABLES

LIST OF FIGURES

CHAPTER 1 INTRODUCTION

Magnesium is the lightest structural metal available in the world with a density of 1.74 g/cm^3, 35.6% lower than that of aluminum and 61.3% lighter than titanium. Magnesium alloys are attractive due to the combined properties of the light weight, high strength-to-weight ratio and high specific stiffness at both ambient and elevated temperatures. However, its atomic structure, coupled with a low core potential and bi-valency arising from the *2s*-orbit electrons, restricts the physical properties of both the unalloyed magnesium and the family of magnesium-based alloys [1].

Nevertheless, the investigations on magnesium alloys are receiving continuing interests during the last two decades, due to the potential applications for lightweight structures in automobile, aircraft, 3C (computer, communication, and consumer) industries. As compared to the casting counterparts, wrought magnesium alloys exhibit improved mechanical properties, namely, higher tensile strength, yield stress, and fatigue resistance [2, 3]. However, the wide applications are restricted by the poor room-temperature formability and the associated high manufacturing cost [1], related to the complex plastic behavior due to their hexagonal-close-packed (hcp) crystal structures and, in particular, the presence of mechanical twinning [4]. The low formability of wrought magnesium alloys at room temperature, high cost involved in the high-temperature processing, and little experience and understanding of their unusual plastic behavior are responsible for the current limited utilization of wrought parts in the industries mentioned above [5].

1.1 Deformation Mechanisms in Magnesium

The low formability and unusual plastic behavior at room temperature in the hexagonal close packed (hcp) magnesium mainly arises from a limited number of slip and twinning systems available, and their asymmetrical distribution over the reference sphere [2, 6]. Owing to the low offer of possible slip systems within one slip system family, various primary and secondary slip and twinning systems are activated, which, in addition, can exhibit various critical resolved shear stresses (CRSS) [4]. In contrast to this, the relationship for face-centered cubic (fcc) metals are considerably simpler, where 12 possible slip systems belonging to the same primary slip system $\{111\} < 110 >$ are distributed symmetrically over the whole reference sphere [7]. Therefore, in fcc metals usually only slip systems of this one family become operative.

1.1.1 Potential dislocation-slip systems

In hexagonal structures, crystallographic Miller-Bravais indices are usually used on the basis of the three axes, $\mathbf{a}_1$, $\mathbf{a}_2$, and $\mathbf{a}_3$ within the basal plane and the axis, $\mathbf{c}$, orthogonal to them. Figure 1.1 illustrates the structure of an hcp crystal [8]. The crystal geometry, in particular, the ratio *c/a*, where *a* is the interatomic distance in the basal plane along any of the three $< 11\bar{2}0 >$ directions, and *c* is the distance between the first and the third layers, governs the deformation behavior of hcp materials. The ideal *c/a* ratio is 1.633, calculated based on a hard sphere packing. In real materials, it varies from 1.568 in beryllium to 1.886

for cadmium [6]. The increase in the *c/a* ratio means that the distance between the adjacent basal planes increases. Thus, they appear relatively more close-packed than the alternative planes, for example, prismatic or pyramidal planes. These planes are shown in Figure 1.2 [4, 8, 9]. For the above normal or ideal axial ratio, the basal plane (00.2) is the one most densely packed, including certain exceptions, such as, magnesium (Mg), cobalt (Co), and beryllium (Be). The axial ratio for magnesium is close to the ideal value, and at room temperature it is equal to 1.624.

The major slip and twin systems frequently quoted for magnesium at room temperature are shown in Table 1.1 and Figure 1.2 [5, 6, 9-11]. The movement of dislocations produces slip on particular planes, along a direction parallel to one of the close-packed rows of atoms. The dominant slip system of magnesium is the glide in the close-packed direction ($<1\bar{1}20>$ or <a>) on the close-packed plane [basal (0002) plane] (Fig. 1.2a) [2]. Other slip systems, such as the non-basal slips of <a> on the prismatic $\{10\bar{1}0\}$ planes (Fig. 1.2b), <a> on the pyramidal $\{10\bar{1}1\}$ planes (Fig. 1.2c), and <c+a> ($<\bar{1}\bar{1}23>$ direction) on the pyramidal $\{11\bar{2}2\}$ planes (Fig. 1.2d) were also observed in magnesium [4, 8, 12]. The combination of the basal and prismatic <a> slips provides total only four independent slip systems, which is exactly the same as those provided by the pyramidal <a> slip (Fig. 1.2c). These four independent slip systems are not enough for an arbitrary homogeneous deformation according to the Von Mises criterion [13]. The pyramidal <c+a> slip (Fig. 1.2d), which, in principle, provides the additional independent slip systems, and is the only slip system able to accommodate strains in the c-axis direction, is very hard at room temperature because of its high CRSS and easy dissociation into

sessile <c> dislocations to suppress the continuous slip [4, 9, 14-16]. However, the existence of the pyramidal <c+a> slip in magnesium is significant at elevated temperature, when twinning is suppressed.

1.1.2 Introduction to deformation twinning and detwinning

Deformation twins are formed by a homogeneous simple shear of a matrix lattice along a specific direction on a particular plane. A sphere is deformed into an ellipsoid by the shear and is schematically illustrated in Figure 1.3 [5, 6, 17], where a sphere is sheared along the direction, η_1, with a shear magnitude, γ. The shear associated with twinning leaves two lattice planes undistorted, that is, all distances and angles in these planes remain unchanged. These two planes, denoted as K_1 and K_2 by convention, are normal to the plane of shear, S, and inclined at an angle, θ, to each other. The plane K_1, also called as twinning plane, contains the shear direction and experiences no displacement during twinning. However, the plane, K_2, is rotated to K_2' by twinning. The plane, K_2, intersects the plane of shear in η_2 and η_2' before and after twinning, respectively. Thus, the shear magnitude, γ, can be represented as,

$$\gamma = 2\cot\theta \tag{1.1}$$

Therefore, the shear magnitude is determined by the crystallographic relationship between the two undistorted planes, and, thus, the twinning mode can be specified completely with the four twinning elements, K_1, K_2, η_1, and η_2, where only two of them, K_1 and η_2 or K_2 and η_1, are independent. Twin and matrix lattices are associated either by

a reflection in a certain plane like K_1 or by a rotation of 180 ^{o}C about a certain axis like η_1.

The most prominent twinning in hcp metals is $\{10\bar{1}2\}<10\bar{1}1>$. The twinning elements for the $\{10\bar{1}2\}<10\bar{1}1>$ twinning mode are displayed in Figure 1.4, where $K_1=\{10\bar{1}2\}$, $\eta_1=<10\bar{1}1>$, $K_2=\{10\bar{1}\bar{2}\}$, $\eta_2=<\bar{1}011>$, and $S=\{\bar{1}2\bar{1}0\}$. The conjugating twinning plane, K_2, and direction, η_2, are crystallographically equivalent to K_1 and η_1. Twinning shear of this mode changes sign at $c/a=\sqrt{3}$ at which the plane of shear becomes square such that $\gamma=0$, and no twin of this mode can be formed [9, 16, 18]. This is shown in Figure 1.5 for the twinning mode, $\{10\bar{1}2\}<10\bar{1}1>$. "Extension" twin, which extends c-axis, is activated if $c/a<\sqrt{3}$ like in Mg, while the "contraction" twin operates if $c/a>\sqrt{3}$ like in Zn. The shear magnitude of this mode is expressed as:

$$\gamma=\frac{3-(c/a)^2}{\sqrt{3}(c/a)} \tag{1.2}$$

For magnesium with $c/a=1.624$, a shear magnitude, $\gamma=0.1289$, is obtained. Therefore, the $\{10\bar{1}2\}<10\bar{1}1>$ twinning in magnesium results in an extension along the c-axis (Fig. 1.2d) [5, 9].

In magnesium, the two twin modes, extension twinning $\{10\bar{1}2\}<10\bar{1}1>$ (Fig. 1.2e) and contraction twinning $\{10\bar{1}1\}<10\bar{1}\bar{2}>$ (Fig. 1.2f), are commonly observed, with twinning $\{10\bar{1}2\}<10\bar{1}1>$ being the most common and easily-activated one. As mentioned above, the $\{10\bar{1}2\}<10\bar{1}1>$ twinning will lengthen the grain along the original basal

direction (extension twin) [9]. Therefore, this twining will operate efficiently associated with the extension parallel to the c-axis and, equivalently, with the contraction in a direction perpendicular to the c-axis (Fig. 1.6a). In contrast to that slip is geometrically reversible under tension or compression, twinning exhibits the polar nature due to the crystallographic relationship between the extended or compressed orientations. Therefore, the shear can occur only in one direction rather than in the opposite direction [4, 9, 16, 19, 20]. Consequently, a contraction along the c-axis cannot be accommodated by $\{10\bar{1}2\}<10\bar{1}1>$ extension twinning. In particular, the <a> dislocation slip cannot accommodate straining along the c-axis, and, thus, twinning is the only readily active mechanism at room temperature to accommodate plasticity in the c-axis direction [4]. Therefore, the ductility and formability of hcp metals and alloys are significantly influenced by the activity of operable twinning modes [9]. After extension twinning in magnesium, the c-axis will reorient to lie approximately (~ 86.3^{o}) in the original basal plane [2] (Fig. 1.6b). Another contributing effect of twinning to general plastic flow is that unfavorably orientated grains for slip and twinning are reoriented into a more favorable position upon twinning. Therefore, the total plastic strain can be increased considerably by the advent of second-order twinning, for example, $\{11\bar{2}1\}$ twinning inside the $\{10\bar{1}2\}$ twins in Zr [9] and $\{10\bar{1}1\}$ twinning followed by $\{10\bar{1}2\}$ twinning in Mg [21, 22]. Although twinning mechanisms offer more options for plastic accommodation, the contribution to the overall deformation is small compared to that of slip, and they generally require an accommodation mechanism of their own in order to avoid large internal-stresses leading to plastic instability and failure [4].

As illustrated in Figure 1.6b, the extension twinning $\{10\bar{1}2\}<10\bar{1}1>$ in Mg results in a nearly 90^{o} ($\sim 86.3^{o}$) reorientation of the basal pole. This unique orientation relationship between the parent and twin grains facilitates detwinning in the twinned areas during load reversals, with a tensile stress applied along the c-axes of the twinned materials [23-27]. Microscopically, detwinning can be characterized by the disappearance of existing twin bands. In other words, twins can disappear or become narrower under reversed loading. Therefore, a complete texture reversal is obtained, once the detwinning capability is exhausted. The crystallographic deformation process of detwinning is similar to twinning, except that nucleation is not required or occurs more readily. Thus, the stress required for detwinning is less than that for twinning nucleation, but greater than that for twinning growth [11]. Therefore, detwinning can also result in an inflected and concave-up strain-hardening flow curve [26].

Dislocation slip and twinning deformations, as two deformation mechanisms, are compared in Figure 1.7 for a single crystal that is subjected to a shear stress [7]. Dislocation slip ledges are shown in Figure 1.7a, and the shear deformation for twinning is homogeneous (Figure 1.7b). These two deformation mechanisms are different in several aspects. Firstly, the crystallographic orientation above and below the slip plane is the same both before and after the deformation for dislocation slip. For deformation twinning, there will be a reorientation across the twin plane. Secondly, dislocation slip occurs in distinct atomic spacing multiples, whereas the atomic displacement for twinning is less than the interatomic separation. Thirdly, deformation twinning occurs in metals that have body-centered cubic (bcc) and hcp crystal structures, at low temperatures, and at high rates

of loading (shock loading) conditions where the slip process is restricted; that is, there are few operable slip systems. Finally, the amount of bulk plastic deformation from twinning is normally small, relative to that resulting from dislocation slip. However, the significance of twinning lies in the accompanying crystallographic reorientations. As mentioned earlier twinning may place new slip systems in orientations that are favorable relative to the stress axis such that the slip process can now take place.

1.1.3 Factors influencing the activity of deformation mechanisms

The activation of deformation modes (e.g., slip or twinning) under certain conditions is dependent on the following factors [6]:

Schmid Factor: The Schmid factor is a purely geometrical relationship between the corresponding deformation mode and the direction of the applied force [7, 28]. The relationship between the resolved shear stress operative on the slip/twinning plane along the slip/twinning direction, the direction of the external applied force, and the specimen dimension is given in Figure 1.8:

$$\tau = \frac{F}{A}\cos\lambda\cos\chi \tag{1.3}$$

where:

- τ: resolved shear stress (RSS) on the slip/twinning plane in the shear direction;
- F: externally applied force in the direction of the rod axis;
- A: cross-section area of the rod sample;

- λ: angle between the normal to the slip/twinning plane and the direction of force of the external reference system; and
- χ: angle between the slip/twinning direction and net force of the external reference system.

In hcp metals, the resolved shear stresses of the various deformation modes are strongly dependent on the direction of the external applied force, especially with respect to the *c* axis. Figure 1.9 illustrates the variation of the ratio of resolved shear stress between prismatic and basal <a> slips with angle θ, after the analytical expression by Avery et al. [29]. It is observed that the larger θ results in a larger ratio. Therefore, due to the low number of slip systems and their asymmetrical distribution, the hcp metals with certain orientations show a pronounced tendency to geometrical hardening or softening.

Critical Resolved Shear Stress: For a given slip system, the acting resolved shear stress, τ_{rss}, must reach a certain critical value for it to become active [28]. This value is called the critical resolved shear stress (CRSS), τ_{crss}. It constitutes a materials property that may be influenced by deformation temperature, impurities and alloying elements, as well as by the mechanical and thermal history (rate of deformation and of recrystallization). However, it is generally accepted that the CRSS is essentially independent of the other stress components and of the hydrostatic pressure. Although the resolved shear stress in the twinning plane in the shear direction appears to be an important factor in the activation of twinning, the experimental evidence seems to indicate that the stress normal to the twinning plane can also play an important role. Nevertheless, a CRSS criterion is usually assumed for twinning, provided that the normal stress components are not much larger than

the CRSS. Gharghouri et al. [25] demonstrated the validity of this assumption for the $\{10\bar{1}2\}<10\bar{1}1>$ extension twinning in magnesium and reported a CRSS value of 65 – 75 MPa in the Mg-7.7at.%Al alloy. However, it must be emphasized that the twinning mechanism is dependent on the direction of deformation. In general, twinning is preferred to dislocation slip at low deformation temperatures, and high deformation rates; at higher temperatures and lower deformation rates, however, dislocation slip is more favorable.

Lattice Preferred Orientation: Texture is an important factor in determining the active deformation mechanisms in polycrystalline materials. If crystals were randomly oriented, the anisotropy of each grain would be largely averaged by the random distribution [28]. However, if the grains have a preferred lattice orientation, then the properties of the polycrystal approximate those of the single crystal. This behavior is more pronounced, the stronger and sharper the texture, and the coarser the grain, such as in magnesium and its alloys.

Again as shown in Figure 1.9, the ratio of the RSSes between the prismatic and basal <a> slips monotonically increases with θ. The large θ means less deviation from the basal texture, i.e., the c-axis distribution along the transverse direction (TD) in the annealed AZ31B sheet. Therefore, a strong basal texture activates a large fraction of prismatic slip, resulting in large r-values [4, 29], indicating high anisotropy.

Compatibility conditions: Assuming a constant volume, there must be, according to the von Mises criterion [13], at least five mutually independent deformation modes in a single grain embedded in a polycrystal in order to ensure a homogeneous deformation of

the grain on the macroscopic scale without cracking along the grain boundary. These compatibility conditions, that is, the accommodation of the deformation at the grain boundaries and at similar microstructure features, result in a superposition of inner stresses and externally applied stresses. This effect, which is more pronounced the smaller grain size and the higher the difference on orientation toward the next grain, makes it difficult to estimate the resulting stresses initiating the deformation system in a single grain. The interactions are even more complex if twinning is included in the accommodation process, as with hcp metals [6]. Therefore, the measurement of the internal-strains/stresses could help understand the grain-grain interaction and the stress relaxation and redistribution between different grain orientations.

1.2 Internal-strain/stress Development due to Mechanical Anisotropy

During deformation, polycrystalline materials develop internal-strains/stresses characteristic of three-length scales [30, 31]. *Type I*, or macro-, strains/stresses represent the average strains/stresses acting within all crystallites at a characteristic length scale similar to the entire sample or component, and are associated with inhomogeneous forming conditions. *Type II*, or intergranular, strains/stresses describe the mean deviation from the macroscopic strain/stress level of an individual crystallite, and arise from strain mismatch between grains with different orientations due to the elastic and plastic anisotropy at the grain level. Intergranular strains are of primary interest in the current research because their evolution is controlled by the active deformation mechanisms in the grains and by their

interactions. In cases where Type I internal or residual strains are of interest, the results of the current research provide a means to infer them even when the measured Type II strains/stresses exhibit strong variations depending on the reflection used [30]. *Type III*, or intragranular, strains/stresses represent the local deviation of the strains/stresses within an individual crystallite from its average strains/stresses (variations on the atomic scale), and are associated with dislocations and their structures. Figure 1.10 illustrates the phenomenological classification of the three internal-stresses described above. σ^{I}, σ^{II}, and σ^{III} are, respectively, macro-, intergranular, and intragranular stresses [31]. One could draw the same diagram with ε^{I}, ε^{II}, and ε^{III}, respectively, for macro-, intergranular, and intragranular strains.

For crystalline materials, diffraction-based techniques are perhaps best suited for measuring internal-stresses, and the high penetration of neutrons makes it possible to measure the distributions *in situ* during deformation of bulk samples for most engineering materials. The measurement of internal-stresses by diffraction methods is based on the peak shifts between the loaded and the load-free diffraction patterns. The method has been described in detail by Allen et al. [32] and by Hutchings et al. [33]. Each reflection originates from a different family of grains, oriented such that the given (*hk.l*) plane satisfies the Bragg's law. The average lattice strain for such grains is given by:

$$\varepsilon_{hk.l} = \frac{d_{hk.l} - d^{0}_{hk.l}}{d^{0}_{hk.l}} \tag{1.4}$$

where $d_{hk.l}$ and $d^{0}_{hk.l}$ are the plane d-spacings in the loaded and load-free conditions, respectively. Thus, a deviation of the lattice spacing in the loaded material for a given

reflection is associated with a lattice strain perpendicular to the reflecting planes. The lattice strain is measured parallel to the scattering vector, which is the bisector of the incident and diffracted beams. When the scattering vector does not move with respect to the specimen geometry, different (*hk.l*) planes correspond to different grain orientations.

The mechanical response of polycrystalline metals is an average of the response of individual crystals (grains). While the polycrystal may be isotropic on the macroscopic level, the individual crystallites on the grain level are always anisotropic. In general, crystals exhibit both elastic and plastic anisotropy. Therefore, it is the local mechanical anisotropy that gives rise to the observed differences in lattice strain within different grain orientations. The lattice strain for a given reflection is determined by the stress state in the corresponding grains. Load redistribution between the grains, therefore, leads to changes in the lattice strains. This redistribution of the load is obviously determined by a combination of the elastic and the plastic anisotropy of the material. It has been previously shown that a development of internal lattice strains during loading in different grain orientations can be used as a very sensitive indicator of microplasticity.

This is shown schematically in Figure 1.11 [34], where the development of internal lattice strains and the average stress-strain responses of three different grain families/orientations is depicted. This figure is also a schematic representation of the load redistribution and the evolution of internal lattice strains in elastically and plastically anisotropic single-phase material. The letters A-C denote 3 grain families/orientations oriented differently with respect to the load axis in the microplastic region, where majority of the load redistribution occurs (Fig. 1.11a), some grain families undergo plastic

deformation (Grains B) while some are still deformed elastically (Grains A and C). This inevitably leads to differences in the internal lattice strain accommodated between different grain families (Fig. 1.11b). Because the diffraction technique detects only changes in the elastic "lattice" strain, the measured internal lattice strain is necessarily proportional to the stress on that grain. In the elastic regime there is a linear relation between the macroscopic stress and the deviation in lattice spacing. However, due to the elastic anisotropy in most metals, this linear relation depends on the lattice plane, and large differences in the stress/strain levels between different families of grains with different lattice orientations are usually observed (leading to intergranular stresses or Type II stresses.) In the plastic regime, the orientation dependence is more complicated and the relation between the macroscopic stress and the deviation in the lattice spacing becomes highly non-linear. The deviation from the linearity between the macroscopic stress and lattice strain indicates stress redistribution among different grain orientations. When grains in a soft orientation micro-yield (e.g., Grains B), and, thus, share a smaller portion of the applied stress, a concomitant increase in the slope of the applied stress vs. lattice strain is observed. A vertical line in the plot indicates that the grains of this orientation have ceased to accept elastic strains, and are behaving in a perfectly-plastic fashion. At the same time, grains in hard orientation (e.g., Grains A and C) must accept a larger portion of applied stress, and this is manifested as a decrease in slope. Therefore, determining the internal-stress distributions within heterogeneous aggregates provides additional insight regarding the constitutive behavior of the individual constituents, above and beyond the insight provided by measurements of the individual behavior of the aggregate alone. Because of the nature of diffraction, the behavior of a particular diffraction peak represents an average of a

certain subset of grains within the polycrystal. For instance, the strain measured from the shift of the (10.0) diffraction peak represents the behavior of the subset of grains that have (10.0) planes oriented for diffraction.

Because of the near elastic isotropy in magnesium and its alloys, the intergranular strains primarily arise from plastic anisotropy, which is controlled by slip and twinning systems. Ultimately, a large build-up of internal-strains may lead to plasticity instability and failure. Therefore, a study of the internal-strain evolution during plastic deformation will give us more insights into the deformation mechanisms, particularly into the twinning mode in magnesium alloys. Understanding the underlying mechanisms may provide critical insights necessary to further develop usage of materials with formability problems such as magnesium. Several previous experiments [10, 27, 35-37] on the monotonic-compressive loadings of the magnesium alloy, AZ31B, have provided insights on stress/strain states of i) grains as they begin to twin, ii) twins as they appear, and iii) both the parent grain and twins as the deformation proceeds. These reports have shown the close relationship between the internal-strain evolution (more specifically, the internal-stress relaxation) and the twinning activity. In short, the diffraction-based technique can be used to probe the grain-level behavior of polycrystalline materials. Unfortunately, the technique does not directly probe the stress level within individual grains; rather an average of the stress levels within all grains that satisfy a given Bragg's condition is detected.

Nevertheless, the individual grain-level response can be inferred through a properly informed polycrystal plasticity model, which is beyond the scope of the current dissertation. Clausen, Agnew, and Tome [37-39] have been trying to expand the range of applicability of

the current visco-plastic self-consistent (VPSC) and elasto-plastic self-consistent (EPSC) models by incorporating the capabilities of the twinning and/or detwinning mechanisms. The polycrystal plasticity models and bulk diffraction techniques have successfully been used in combination to develop and validate constitutive models using diffraction measurements for simple deformation histories [40-42], and, then, to interpret the diffraction data for more complicated cases.

1.3 Motivation and Outline of the Research

Although the role of deformation twinning in wrought magnesium alloys has been well recognized, its role and the associated mechanical behaviors under monotonic and cyclic loadings are not yet well understood. This research has conducted the fundamental studies on the mechanical behavior and deformation mechanisms (with a focus on twinning) in the wrought magnesium alloys, which is essential to the future structural applications in the industries, since twinning play a significant role in such kind of issues in magnesium. The plastic deformation of polycrystalline materials with hexagonal structures exhibits special features, particularly, showing a significant change in the crystallographic texture even at small levels of strains. The studies of a close relationship between the crystallographic textures and plastic deformation mechanisms in wrought magnesium alloys, which reciprocally influence each other, provide the valuable information for the general understanding of the plastic deformation of polycrystalline materials with hexagonal structures, and to be beneficial for designing optimal alloying and forming

schemes to fabricate such wrought magnesium alloys.

The major objectives of the current research are to identify the role of deformation twinning (as one of the deformation mechanisms) on the plastic deformation behavior of wrought magnesium alloys, and its correlation with textures, based on a fundamental understanding of the mechanical properties under various loading conditions, using diffraction as the major characterization tool. The work constitutes a valuable benchmark for understanding the effects of the plastic deformation mechanisms, such as, dislocation slip, twinning, and detwinning on the mechanical behaviors in wrought magnesium alloys.

CHAPTER 2 LITERATURE REVIEW

The mechanical behavior is controlled by the relative strengths and hardening responses of a variety of dislocation slip and twinning modes. At room temperature, the initial texture, straining direction, and even straining sign play a significant role in determining the activity of the possible deformation modes in polycrystalline materials. The plastic behavior of wrought magnesium alloys is characterized by plastic yielding and hardening asymmetry between tension and compression tests in both the extruded and rolled conditions [1, 2], and high in-plane plastic anisotropy in the sheet form as well [1]. These unusual behaviors have been attributed to the variety and asymmetrical distribution of crystallographic deformation modes and, in particular, the deformation twinning on the $\{10\bar{1}2\}$ planes along the $<10\bar{1}1>$ directions and limited dominant slip systems [4]. Furthermore, the unique reorientation of the extension twinning between the parent and twin grains facilitates detwinning during unloading and reversed loading. Therefore, several features are very distinctive in magnesium alloys where twinning makes a substantial contribution to plastic deformation, including a very rapid texture development associated with twin reorientation; an unusual hardening response; and abrupt stress relaxation inside those grains undergoing twinning.

2.1 Tension-Compression Asymmetry

In wrought magnesium alloys, usually a significant fraction of grains are orientated with their c-axes nearly perpendicular to the prior working (rolling or extrusion) direction [43]. This initial texture combined with the polar nature of twinning leads to the easy activation of the extension twinning under some loading conditions but not in others [9]. This is the reason for the well-known tension-compression yield asymmetry of wrought magnesium alloys [1], where the yield strength in one direction is controlled by the stress required to activate twinning, while the yield strength in the other is controlled by the harder non-basal slip mechanisms [4, 23]. The stress-strain curve characteristic of twinning activation has an unusual concave-up shape: an abrupt transition from the elastic to plastic deformation is abrupt, a low yield stress and low hardening rate followed by a higher hardening evolution rate. In contrast, the stress-strain curve characteristic of dislocation-dominated deformation has a concave-down shape: a high yield stress with a smooth transition from the elastic to plastic deformation (Fig. 2.1).

Figure 2.2 illustrates the plane stress-yield loci for a magnesium sheet predicted using the proposed theory and experiments by Cazacu et al. [44] (where experimental points are represented by symbols). The 1% yield locus for the textured pure magnesium has a highly asymmetrical shape. The initial texture, with the strong basal-pole alignment along the through-thickness direction, favors $\{10\bar{1}2\}<10\bar{1}1>$ extension twinning under in-plane compression, but not under in-plane tension. This results in much lower in-plane compressive strengths, as compared to the in-plane tensile strengths. The yield locus at 5%

strain shows asymmetry similar to that of the locus at 1% strain. Since $\{10\bar{1}2\}<10\bar{1}1>$ twinning is not complete, the yield strength in compression is yet much lower than in tension. At 10% strain, the third quadrant strengths are comparable to the first quadrant strengths, owing to the exhaustion of $\{10\bar{1}2\}<10\bar{1}1>$ twinning at about 6.5% strain [11].

In general, at moderate temperature, plastic deformation occurs mainly by the glide of dislocations and possibly, depending on the material, by twinning. For both slip and twinning, the associated shear strains operate on given crystallographic planes along certain directions. If the material deforms by a reversible shear mechanism, yielding depends only on the magnitude of the resolved shear stress, and the yield stresses in tension and compression are identical [44]. On the other hand, twinning and martensitic shear are directional deformation mechanisms, and if they occur, yielding will depend on the sign of the stress [9, 45], resulting in the tension-compression asymmetry.

2.2 High Plastic Anisotropy

Figure 2.3 shows the variation of *r*-value as a function of sample orientation within the plane of the sheet [4]. While the RD samples of the H24 temper strain in a nearly isotropic fashion, $r \sim 1$, the TD samples exhibit high anisotropy, $r \sim 3$, at room temperature. Thus, the magnesium alloy, AZ31B, in the H24 condition exhibits large in-plane anisotropy at room temperature, including a higher flow stress along TD. In fact, the O tempered material exhibits even higher normal anisotropy, $r \sim 2$ and 4 for RD and TD, respectively.

The strength anisotropy is also evident in Figure 2.2, where the yield loci show pronounced deviations from the radial symmetry. Specifically, it is noted that the higher tensile strength in the transverse direction than in the rolling direction is observed. The greater spread of the texture about the transverse direction allows more widespread operation of basal slip by loading in the rolling direction. Hence the tensile strength is significantly lower in the rolling direction than in the transverse direction.

The strong anisotropy of magnesium alloys is mainly due to the initial texture, twinning, and the fact that the dominant slip mode, basal <a> slip, possesses only two independent slip systems, far from satisfying the five independent slip systems required by the von Mises criterion for an arbitrary homogeneous straining. In particular, the significant prismatic slip is responsible for the high anisotropy of magnesium alloy sheets [4, 46]. Non-basal prismatic <a> slip produces no strains along the ND direction. Thus, the ideal basal texture, where grains are oriented with their c-axes parallel to the sheet ND direction, will exhibit an infinite r-value [4].

2.3 Twinning and Detwinning

The effect of a compressive pre-strain on the stress-strain curve of longitudinal specimens (loaded along the extrusion direction) during tensile reloading is studied by Kleiner and illustrated in Figure 2.4 [26]. The pre-strain values of 1.0, 2.0, and 3.0% are the total strains, corresponding to the permanent compressive strains of 0.45, 1.40, and 2.35%, respectively. It is observed that a compressive pre-deformation results in a significant drop

in the tensile yield strength from about 200 MPa to roughly 125 MPa, irrespective of the amount of pre-strain. The reduced yield stress coincides with the initial compressive yield strength. Since $\{10\bar{1}2\}<10\bar{1}1>$ twinning leads to a reorientation of 86.3° of the crystal lattice, all basal planes in the twinned lattices lie nearly perpendicular to the extrusion direction after a compressive pre-strain. These twinned regions are capable of detwinning during reloading in tension. After the onset of detwinning at about 125 MPa, the curvature of the stress-strain curves becomes convex, which is characteristic of deformation by twinning. Furthermore, comparing the strain values of the pre-deformed specimens at the stress level of 200 MPa, it is observed that the differences in strain correlate quite well with the differences in the permanent compressive yield. This leads to the conclusion that all the strain imposed by twinning during compressive pre-deformation is recovered by detwinning during the tensile reloadings.

Figure 2.5 represents the microstructure evolution during in-plane tension following in-plane compression studied by Lou et al. [47]. The initial microstructure of the annealed AZ31B Mg alloy is free of twins. When the sample is compressively loaded, many twins in wider twin bands appear after yielding, as indicated by the texture evolution studied using synchrotron diffraction [48]. The area twin fraction increases from 26% ($\varepsilon = \sim 0.023$), to 58.4% ($\varepsilon = \sim 0.046$), and to 71.9% ($\varepsilon = \sim 0.072$), similar to the reported results obtained using neutron diffraction [10]. Upon subsequent reloading in tension to the 0.04 strain, the wide twin bands formed during the prior compression gradually disappear. Needle-shaped twins, similar to those observed in the monotonic uniaxial tension, appear in the sample. The area fraction of twins drops to about 6%. Therefore, detwinning is evidenced by the

microstructure and texture reversals [47]. It is noted that the shape of the stress-strain curve during tensile reloading is similar to those in Figure 2.3 due to the activation of detwinning.

2.4 Hardening Behaviors and the Associated Deformation Mechanisms

Besides the tension-compression yield asymmetry and high in-plane anisotropy discussed earlier, wrought magnesium alloys have unique hardening behaviors during plastic deformation. Usually, three distinctive plastic-flow characteristics, corresponding to the three dominant deformation modes, are usually observed in the stress-strain curves [49].

Firstly, *dislocation-slip dominated deformation (Slip Mode):* the dislocation slip is dominant throughout the plastic deformation under in-plane tension [30, 36, 41] or through-thickness compression [36, 50]; the flow curve is a normal concave-down shape with a high yield stress and a smooth transition from the elastic to plastic deformation [30, 36, 41, 48, 50-52] (please see "in-plane tension" in Fig. 2.1). The stress-strain response under this deformation mode in magnesium alloys is similar to the behavior of fcc or bcc metals having strong symmetry in slip activities and at least five independent slip systems [7]. The texture change or lattice reorientation is relatively small (Figs. 2.6b&c, and Fig. 2.7b). These texture modifications are consistent with the activity of the common slip systems in magnesium [36]. However, Jain and Agnew [40, 42] suggested that the presence of basal-pole intensity in the direction perpendicular to both the loading direction and the original normal direction (Figs. 2.6c & 2.7b) is a result of extension twinning, despite that

the initial texture places the majority of grains in an unfavorable orientation for such twinning.

Secondly, *twinning-dominated deformation (Twinning Mode):* an atypical concave-up shape of stress-strain curve, characterized by an abrupt elasto-plastic transition, a low yield stress and low hardening rate, followed by a rapidly increasing hardening, is usually observed (please see "in-plane compression" in Fig. 2.1). The extension twinning is dominating the strain accommodation initially, with massive twinning resulting in a low strain-hardening rate [10, 48, 50], and the rapidly rising flow stress is controlled by the harder dislocation slips once the twinning capability is exhausted [48]. The previous study has shown that as much as 80% of the volume fraction of favorably oriented grains is twinned during the first 8% strain [10]. Thus, the twin boundary is of great significance as barriers to dislocation motion, leading to more difficult post-twinning plastic deformation, where usually only limited post-twinning plastic strains can be accommodated before the final fracture [23, 53]. This kind of deformation behavior is commonly observed when a sample is loaded under in-plane compression or through-thickness tension. Due to the activation of extension twinning, this deformation mode results in a rapid texture change (Figs. 2.6d & 2.7c) [10, 36, 50], where the basal poles are oriented and tend to be aligned with the compressive loading axis after deformation. Conversely, this basal-pole alignment in the twin texture component can be used as a signature to characterize the activation of the extension twinning in magnesium alloys.

Finally, *detwinning-dominated deformation (Detwinning Mode):* during in-plane tension following in-plane compression or through-thickness compression following

through-thickness tension, detwinning is the initially dominated deformation mechanism. Thus, the initial concave-up shape of flow curve is expected, similar to that in the Twinning Mode (Compare Fig. 2.3 and Fig. 2.1). Nevertheless, as the detwinning capability is exhausted, dislocation-slip deformation takes over, resulting in a concave-down shape of the post-detwinning flow curve [23, 26, 39, 47, 49], similar to that under the Slip Mode (Compare Fig. 2.3 and Fig. 2.1). In contrast to twinning mode, the microstructure after detwinning is free of twins. Thus, dislocation motion is much easier, and the post-detwinning plastic flow is comparable to the Slip Mode. Consequently, the plastic flow behavior of Detwinning Mode can be roughly regarded as the combination of the Twinning Mode and the followed Slip Mode, resulting that the overall shape of the flow curve under the Detwinning Mode is an unusual S-shape [23, 26]. The plastic deformation under this mode results in a nearly complete texture reversal (Fig. 2.7d) [47, 54] and microstructure recovery (Fig. 2.5).

In addition, it is relatively uncommon that mechanisms become harder with an increase in temperature. However, metals with twinning-dominated deformation can exhibit such anomalous hardening. It is observed that there is a slight increase in the plateau stress with increasing temperature during in-plane compression of Mg alloy AZ31B sheets [42]. Furthermore, the exceptional high strain-hardening rates typically exhibited by hcp magnesium alloys undergoing extension twinning were highlighted recently at a MagNET (Magnesium NETwork) workshop [55], as compared to fcc metals. Kalidindi presented unusual strain-hardening trends observed in Mg alloys, and he attributed them to interfacial effects associated with twinning. Embury noted that the hardening rates were a large fraction of the shear modulus and, therefore, not attributed to

"normal" dislocation-based rules, suggesting possible "composite" effects. Barnett, Tome, and others noted that the texture evolution during twinning is a major contributor.

2.5 Fatigue Behavior

2.5.1 Strain-life fatigue approach [56-60]

The total strain amplitude, $\Delta\varepsilon_t/2$, which is controlled during the test, can be written as the sum of elastic strain amplitude, $\Delta\varepsilon_e/2$, and plastic strain amplitude, $\Delta\varepsilon_p/2$,

$$\frac{\Delta\varepsilon_t}{2} = \frac{\Delta\varepsilon_e}{2} + \frac{\Delta\varepsilon_p}{2} \tag{2.1}$$

The elastic strain is computed as the stress divided by the elastic modulus, the plastic strain amplitude is obtained by subtracting the elastic strain from the total strain (Fig. 2.8a).

The first term in the right hand side of Eq. (1) can further be expressed in terms of *Basquin equation*,

$$\frac{\Delta\varepsilon_e}{2} = \frac{\sigma_f^{'}}{E}(2N_f)^{-b} \tag{2.2}$$

where $\sigma_f^{'}$ is the fatigue strength coefficient, b is the fatigue strength exponent, E is the Young's modulus, and $2N_f$ is the number of reversals to failure.

Furthermore, the second term in the right hand side of Eq. (1) can be replaced by the *Coffin-Manson relationship*,

$$\frac{\Delta\varepsilon_p}{2} = \varepsilon_f^{'}(2N_f)^{-c} \tag{2.3}$$

where $\varepsilon_f^{'}$ is the fatigue ductility coefficient and c is the fatigue ductility exponent. Therefore, combining Eqs. (2.1), (2.2), and (2.3), we have,

$$\frac{\Delta\varepsilon_t}{2} = \frac{\sigma_f^{'}}{E}(2N_f)^{-b} + \varepsilon_f^{'}(2N_f)^{-c} \tag{2.4}$$

which provides a convenient engineering expression for characterizing the total fatigue life.

The cyclic-stress response is an important material property in designing an enhanced fatigue resistance. It relates the cyclic-stress amplitude to the plastic-strain amplitude in a strain-life fatigue, and it is useful for understanding the strain-controlled cyclic deformation. The cyclic stress-strain relationship can be represented by the *Holloman equation* in the form of

$$\frac{\Delta\sigma}{2} = K'(\Delta\varepsilon_p/2)^{n'} \tag{2.5}$$

where $\Delta\sigma/2$ is the cyclic stress amplitude, K' is the cyclic strength coefficient (at $\Delta\varepsilon_p/2 = 1$), and n' is the cyclic strain hardening exponent.

Eqs. (2.4) and (2.5) form the basis for the strain-life approach to fatigue design and have found widespread applications in industrial practice. The best straight line fits for the plastic- and elastic-strain amplitudes *vs.* reversals to failure curves, and for the cyclic stress *vs.* plastic strain amplitude curve can be obtained by linear regression analysis. The plastic strain amplitude *vs.* fatigue life curve is an indication of the resistance to crack initiation and stable crack propagation as well as fatigue failure. An extrapolation of the best fit on

the plastic strain amplitude *vs.* reversals to failure curve can give the value of the cyclic plastic-ductility coefficient, $\varepsilon_f^{'}$, which is related to the cyclic ductility of the material. The slope of the best fit line gives the fatigue-ductility exponent, *c*. On the other hand, the extrapolation of the elastic strain amplitude *vs.* reversals to failure curve to $2N_f = 1$ can be used to determine the value of the fatigue-strength coefficient, $\sigma_f^{'}$, while the slope of the elastic-strain amplitude *vs.* reversals to failure curve gives the value of the fatigue strength exponent, *b*. The parameters' definitions and their physical meanings described above are shown in Figure 2.8 [56].

2.5.2 Strain-life fatigue behavior in magnesium alloys

Magnesium alloys are usually classified into two categories: casting and wrought alloys. In casting magnesium alloys, defects such as casting porosity and inclusions, which commonly act as crack sources, are harmful for fatigue properties, and may facilitate fatigue crack initiation, reduce lifetimes, and decrease cyclic strength. On the contrary, wrought magnesium alloys are basically defect-free and, thus, exhibit better mechanical properties, particularly fatigue resistance than magnesium castings [42, 47, 61, 62]. Recently, a number of studies have been performed to understand the low-cycle fatigue performance of wrought magnesium alloys [57, 58, 63-71] and associated cyclic plastic deformation [34, 47, 72-74], including details characteristic of twinning and detwinning behavior [23, 26, 27, 75-77]. These reports document the fact that the cyclic-stress responses, including cyclic stress-strain curves and low-cycle fatigue lives, are affected by

various microstructure parameters.

It was usually observed that the magnesium alloy exhibits an asymmetric sigmoidal-shaped hysteresis loop due to twinning in compression and detwinning in loading reversal. As the total strain amplitude increases, the asymmetry of hysteresis loops, plastic strain amplitude, mean stress, and stress amplitude increase, while the ratcheting strain and pseudo-elastic modulus decrease. The relationship between elastic and plastic strain amplitudes with reversals to failure shows a monotonic linear behavior and can be well described by the Basquin and Coffin-Manson equations, respectively.

The role of twinning-detwinning on fatigue fracture morphology of AZ31 alloy has been investigated recently by Yin et al. [78]. It is shown that prolific lamella structure in the crack initiation and crack stable propagation zone mainly results from twinning, while dimple structure formed in the unstable crack propagation and final rupture zone is mainly due to slip. Twinning at the crack wake during compressive loading and detwinning at the crack tip during tensile loading play important roles in the formation of fthe racture morphology of this alloy. The formation mechanisms of corresponding morphologies were proposed, based on twinning and detwinning processes during compressive and tensile loading half cycles, respectively.

In a word, due to the roughly equal CRSS's between the twinning and the basal slip in magnesium alloy [47] and the initial basal or nearly basal texture, the deformation twinning and detwinning could be the dominant deformation modes and play significant roles in the mechanical behaviors of wrought magnesium alloys. However, limited research has been performed, especially for their unusual mechanical properties, in spite of

potential applications of magnesium alloys in various areas. Particularly, much more investigations need to be done to understand strain-life fatigue and their associated plastic-deformation behaviors for Mg alloys.

CHAPTER 3 EXPERIMENTAL MATERIALS AND CHARACTERIZATION TECHNIQUES

The advanced microstructural characterizations with a focus on diffraction have been employed to study the mechanical behavior and the role of extension twinning with two magnesium alloys, ZK60A and AZ31B, as the experimental materials, representing two typical rolling and extrusion textures. In the following, the description will cover the extensive thermo-mechanical tests, including monotonic and cyclic loadings, and (microstructural) characterization techniques using diffractions, such as Lab X-ray diffraction, neutron scattering, and synchrotron X-ray radiation.

3.1 Experimental Materials

The current research involves two wrought magnesium alloys, ZK60A and AZ31B, as the experimental materials. These two alloys are selected as model materials because they are the most common wrought magnesium alloys (i.e., practical interest and commercial availability), and because they exhibit two different initial crystallographic textures, respectively, typical for extrusion and rolling. The nominal chemical compositions of these two magnesium alloys are listed in Table 3.1. The commercial extruded plate, ZK60A, has a T5 temper (solution-treated at 535 ^{o}C for 2 hrs, quenched in hot water, and aged at 185 ^{o}C for 24 hrs). The commercial rolled plate, AZ31B, has a H24 temper (strain hardened and partially annealed). The as-received microstructure is free of twins with ZK60A, while there are some twins in the initial microstructure of AZ31B (Fig. 3.1).

The initial crystallographic textures (Fig. 3.2), measured by the conventional lab X-ray, are typical of wrought magnesium alloys. In Figure 3.2a, the initial texture of the as-extruded ZK60A alloy plate is a combination of typical rolling and extrusion textures. There are two major well-defined texture components, one with the basal poles parallel to the plate normal (ND), and the other with the basal poles parallel to the transverse direction (TD). There is a greater angular spread in the pole density from the ND toward TD than toward the extrusion direction (ED). In contrast, in Figure 3.2b, the initial texture of the as-rolled AZ31B alloy exhibits radial symmetry, namely, the basal poles are concentrated at the center of the (00.2) pole figure, and the intensity in the (10.0) pole figure is

essentially uniform around the perimeter. These two distinct crystallographic textures allow to study the effect of initial crystallographic texture on the mechanical behaviors and the associated roles of deformation twinning.

3.2 Mechanical Testing

The cylindrical specimens, with a gauge length of 6.35 mm and a gauge diameter of 2.92 mm (Fig. 3.3a), machined from the ZK60A and AZ31B magnesium-alloy plates, with their loading axes, respectively, parallel to the ND, TD, and ED or rolling direction (RD), were used for uniaxial tensile and cyclic testings.

The samples for monotonic compressions were cubes with a size of 15.24 × 15.24 × 15.24 mm^3. The cubic shape of the samples permits loadings along the three different strain directions with the same sample geometry. It also allows an easy preparation of flat specimens to quantify the texture using Lab X-ray at the end of each deformation history.

The monotonic tensile and compressive tests were performed at room temperature using a servohydraulic Material Test System (MTS) equipped with a TestStar IIs controller and data acquisition system at a constant crosshead speed resulting in an initial strain rate of $1 \times 10^{-3}\ s^{-1}$. A clip-on MTS miniature extensometer with a gauge length of 5 mm was used to monitor or control the axial strain.

The low-cycle fatigue tests were conducted under total strain control mode at room temperature on the same MTS machine, as described above. The total strains with a

triangular waveform and with fully reversed total strain amplitudes ranging from 0.4 to 3.0 % were imposed using a miniature MTS extensometer at a cyclic frequency of 0.5 Hz. The above total strain amplitudes were selected so that the samples were cycled giving lives of less than 10^4 cycles. All fatigue tests, where at least two specimens were used at each given strain amplitude, were run until a 50% drop in the maximal tensile stresses or actual separation of the specimens. The corresponding number of cycles was defined as the low-cycle fatigue life, i.e., the number of cycles to failure, N_f. During fatigue testings, the software displays and records the hysteresis loop (stress *vs.* strain) and the plot consisting of the peak (tensile) and valley (compressive) stresses *vs.* fatigue cycles. In addition, the elastic and plastic amplitudes with respect to the half-cycle fatigue lives can be obtained from the software for each total strain amplitude.

3.3 Metallography

For metallographic examination and texture measurements using the Lab X-ray, the samples were prepared, using standard metallographic techniques, finishing with 1 μm diamond paste in methanol. Acetic picral solution (5g picric acid, 10 ml water, 5 ml acetic acid, and 90 ml ethanol) was employed to etch the specimens for 10 – 45 s, which reveals the grains and/or twins.

3.4 Diffraction Techniques

3.4.1 Principles of diffraction

Diffraction using neutron or X-ray is a powerful tool to probe materials microstructures, based on the Laue equations or more simply on the Bragg's Law. This law establishes that a diffracted beam exists for a wavelength, λ, at an angle 2θ, relative to the incident beam, by the atoms lying in the $\{hkl\}$ lattice planes with a spacing, d_{hkl}, if the relation [79]:

$$2d_{hkl}\sin\theta = n\lambda \tag{3.1}$$

is satisfied, in which *n* is an integer defining the order of reflection.

Diffraction patterns of polycrystalline materials can be usually obtained using a diffractometer. Through the evaluation of the measured intensity distributions of the reflections (*hkl*), the primary data can be extracted from the diffraction pattern, including the peak positions, integral intensities, or other peak-shape parameters, such as full-width-at-half-maximum (FWHM) or integral breadths. These data deliver different basic information about the material state [31]:

- Based on the Bragg's equation, the interplanar lattice spacings, *d(hkl)*, can be obtained from the reflection positions, 2θ(*hkl*). The *hkl* values obtained are the fingerprint of the crystalline phases present in the material and the identification can be, subsequently, made by comparing with the standard data.

- The reflection position, 2θ(*hkl*), may be shifted due to the presence of

internal-stresses. Conversely, the internal-stress can be calculated based on the relative peak shift as discussed earlier and can be used as a sensitive indicator for studying the plastic-deformation mechanisms.

- The relative intensities of the reflection (*hkl*) of one crystalline phase are indicative of the orientation distribution within the reflecting crystallites. Thus, diffraction has been the most powerful technique to determine the crystallographic texture in polycrystalline materials.

- The relative intensities of the reflections (*hkl*) of the two or more crystalline phases can be used for the calculation of the crystalline phase volume fraction. This is one of the quantitative analysis using diffraction.

- The FWHM of the reflection profiles depends on the experimental conditions, especially the divergence of the beam, but also on the material state under study. Usually, small grain size and microstrain lead to a broadening of the reflection profiles. The effects of grain size and microstrain can be separated because they have different dependences on θ.

As a whole, the whole diffraction pattern can be analyzed through performing full profile fittings using various methods available, such as Rietveld refinement, for which a brief introduction will be given below. Due to the amount of data included in this way, additional information about microstructural defects like twin density, stacking fault, and dislocation densities can also be obtained.

3.4.2 Rietveld method for whole-profile refinement

The Rietveld method refines user-selected parameters to minimize the difference between a whole experimental pattern (observed data) and a model based on the hypothesized crystal structure and instrumental parameters (calculated pattern). It was originally developed for monochromatic neutron powder-diffraction analysis, and has been extended to monochromatic X-ray experiments and modified to allow time of flight neutron and X-ray energy dispersive data analysis. This method is numerically stable and has been initially proposed by Rietveld [80, 81]. It starts with roughly estimated integrated intensities, I_k^0, in order to calculate new intensities at the cycle, $n+1$, I_k^{n+1}, using the expression [82]:

$$I_k^{n+1} = \sum_i I_k^n \Omega_{ik} \frac{y_{io} - y_{ib}(n)}{y_{ic}(n) - y_{ib}(n)} \tag{3.2}$$

where y_{ib} is the background associated to the i^{th} measured intensity y_{io}. Then the Rietveld algorithm minimizes the following quantity:

$$M = \sum_i w_{io}(y_{io} - y_{ic})^2 \tag{3.3}$$

where $w_{io} = \frac{1}{\sigma_{io}^2}$ is the statistical weight associated with the observed intensity y_{io} at the i^{th} measured point (σ_{io} is the variance associated with the observed y_{io}) and $y_i = y_{io} - y_{ib}$. During the refinement, the used weights are $w_{io} = \frac{1}{y_{io}}$, while for a refinement using the maximum likelihood, they are $w_{ic} = \frac{1}{y_{ic}}$ [82]. Equation (3.3) implies that the measurements are independent and that variations of the observations obey a

normal frequency distribution. The second weighting scheme is then preferred for diagrams with low counting levels where normal distributions are not satisfied [82].

In the Rietveld refinement method, a mathematical model is developed that describes the measured intensities, y_{io}, from a powder or polycrystalline sample at every point in the pattern. The calculated intensities, y_{ic}, are determined by adding the contributions of all the peaks for all N_Φ phases in the sample, which are superimposed with the background contribution at each point *i*:

$$y_{ic} = y_{ib} + \sum_{\Phi=1}^{N_\Phi} S_\Phi \sum_{k=K_1}^{K} j_{\Phi k} Lp_{\Phi k} P_{\Phi k} \left|F_{\Phi k}\right|^2 \Omega_{i\Phi k} \tag{3.4}$$

in which:

- S_Φ : A scale factor, proportional to the volume fraction for each refined phase, Φ;
- $j_{\Phi k}$: The multiplicity factor of the peak for phase Φ;
- $Lp_{\Phi k}$: The Lorentz-polarisation factor;
- $P_{\Phi k}$: A correction factor describing preferred orientations of phase, Φ;
- $\left|F_{\Phi k}\right|$: The modulus of the structure factor (including thermal agitation) of phase, Φ;
- $\Omega_{i\Phi k}$: The profile function of the peaks of phase, Φ, which represents instrumental and potential sample broadenings.

The first sum runs for all phases in the sample and the second for all the reflections, k, which contribute to the i^{th} measured point. As the feet of the function, $\Omega_{i\Phi k}$, are often rapidly decreasing, the calculation of the contribution of a given reflection, k, at the angle, $2\theta_i$, is necessary only in a limited range on each side of the peak barycenter. For a Gaussian shape, this range is typically 1.5 times of the FWHM of the peak. However, this value may be increased (sometimes up to 20 FWHMs) for profiles comprising Lorentzian contributions).

As described above, the Rietveld method uses all information of the experimental spectral range, including the information outside the diffraction peaks. The used variables include:

- The instrumental characteristics (resolution curve of the diffractometer, displacement parameters concerning goniometer misadjustments, experimental geometry, detector characteristics …);
- The structural parameters (unit cell parameters, atomic positions, atomic occupations, thermal vibrations …);
- The microstructural parameters (mean crystallite sizes and microstrains, defects …);
- The sample parameters (preferred orientations, residual stresses, eccentricity, thickness, transparency, absorptions, phase fractions …).

The structure refinement using the whole-pattern or Rietveld method is a powerful

technique for extracting structural details from powder diffraction data. With the present methods, structures with up to 200 structural parameters can be refined successfully, if care is taken, and the data are of sufficiently high quality [83]. The Rietveld method is actually the most intensively used technique because of its efficiency in powder diffraction when the crystal structure of the sample is known. It has been incorporated into a large number of programs. Most of these programs allow visual interfacing and easy handling of most functions. One of the programs, MAUD (Materials Analysis Using Diffraction) program by Lutterotti et al. [84, 85], allows the combination of many different approaches (texture, stress, structure …) and experimental configurations. The MAUD program allows the full pattern analysis by combining Rietveld and other codes, including the quantitative texture analysis (QTA) (will be discussed below), and works for X-ray, and neutron data, both at monochromatic or energy-dispersive and time of flight experiments. The program is written in Java and benefits from an object-oriented implementation for easy modification and extensibility. The core of the package is a Rietveld fitting routine (least squares) of multiple spectra extended to analyze texture, phase quantities, crystallite size and microstrain, residual stresses and reflectivity [86]. The program is driven by a graphical interface, and it has an automatic mode, mainly for routine structure refinements from powders, and a manual mode. The automatic procedure requires the user to input only the spectra, the instrument employed, the phase present in the sample and the choice of which models to use for texture, microstructure, etc. For simple materials, such as magnesium alloys, it works out good results using the texture wizard for texture analysis, which refines the most important parameters in four cycles.

3.4.3 Quantitative texture analysis and refinement method

The properties of polycrystalline materials depend on the properties of the crystallites of which they consist and on the arrangement of the crystallites in the polycrystalline aggregates. Since most of the crystal properties are anisotropic, the orientation distribution (texture) of the crystallites is one of the most important aggregate parameters and, hence, one of the most important parameters, affecting both the physical properties of polycrystalline materials and possible failure modes [87]. Texture measurement is therefore necessary in order to understand the properties of polycrystalline materials of any kind, and can be also used to characterize the microstructural evolution. Particularly, in the case of magnesium with a hcp structure, the $\{10\bar{1}2\}<10\bar{1}1>$ twinning results in the reorientation of grains by almost ~ 90°, which results in rapid texture change as deformation proceeds, and this represents a signature that has been utilized to characterize the amount of twinning as a function of deformation [10, 37]. The studies of a close relationship between the crystallographic textures and deformation mechanisms in magnesium alloys, which reciprocally influence each other, are expected to provide the valuable information for a fundamental understanding of the plastic deformation.

The variation of the integral intensity of the diffraction peaks is mainly related with the preferential orientation of the grains, namely the crystallographic texture. Hence, the texture measurements are designed to determine the intensity variation of a certain diffraction peak, indexed $\boldsymbol{h} = (hkl)$, as a function of the measurement direction ($\boldsymbol{y}$) relative to the sample-reference frame. After corrections and normalizations, the probability maps,

$P(\boldsymbol{h},\boldsymbol{y})$, or *pole figures* can be constructed to describe the distribution of different crystal directions in the sample space. Under many simple circumstances, pole figures (PFs) and inverse-pole figures (IPFs) are useful tools for describing texture. While the PFs are obtained by keeping the crystal direction constant, the IPFs can display the texture by keeping the sample orientation constant, and the crystal direction is varied, thus, mapping a particular sample direction in the crystal space. Both methods contain some partial data about the orientation-distribution function (ODF), which is a mapping of the probability of each of the possible grain orientation with respect to the macroscopic or sample coordinates. Two circumstances contribute to this behavior [88]: Firstly, the ODF is defined in 3-D, and the PFs and IPFs in 2-D will result from the integration of all crystal orientations with a particular direction fixed; Secondly, because of the crystal symmetry, each measured *hkl* corresponds to many equivalent directions in the crystal frame.

The quantitative determination of the texture is based on the concept of Orientation Distribution Function, *f(g)*, which represents the statistical distribution of the orientations of the constitutive crystals (crystallites) in a polycrystallite aggregate [82]:

$$\frac{dV(g)}{V} = \frac{1}{8\pi^2} f(g)dg \tag{3.5}$$

where $dg = \sin\beta d\beta d\alpha d\gamma$ is the orientation element, defined by three Euler angles $g = \{\alpha, \beta, \gamma\}$ in the orientation space.

Traditionally, an ODF is determined from pole figures for a relatively small number of reflections. These pole figures are most commonly measured with X-rays or neutrons, using a fixed detector position at the center of an individual diffraction peak for a large

number of different sample orientations. Experimental measurements are the so-called direct pole figures, $I_h(y)$, with $h =< hkl >$ and $y = (\vartheta_y, \varphi_y)$. They are always incomplete in some way. They determine the distribution of the normals $h =< hkl >$ to the crystallographic planes $\{hkl\}$ which are diffracting for the $y = (\vartheta_y, \varphi_y)$ orientation of the sample in pole figure space. For the direct pole figure, *y* is varied in order to cover the maximum range of orientations. The diffracted intensities, $I_h(y)$, depend on the porosity, crystalline state …, of the sample. To compare samples from each other a quantity only depending on the orientation has to be calculated. This quantity is the normalized pole figure, $P_h(y)$, representing the distribution densities of ***h*** direction on the pole sphere, comprised inside $dy = \sin\vartheta_y d\vartheta_y d\varphi_y$:

$$\frac{dV(\varphi_y, \vartheta_y)}{V} = \frac{1}{4\pi} P_h(\varphi_y, \vartheta_y) \sin\vartheta_y d\vartheta_y d\varphi_y \tag{3.6}$$

and similarly to *f(g)*, every pole figure of a random sample will have the same density $P_h(y) = 1$ m.r.d. (multiples of random distribution). The $P_h(y)$ are in fact the factors $P_{\Phi k}$ of Equation (3.4). The normalization of the pole figures is operated though:

$$\int_{\varphi_y=0}^{2\pi} \int_{\vartheta_y=0}^{\pi/2} P_h(\varphi_y, \vartheta_y) \sin\vartheta_y d\vartheta_y d\varphi = 2\pi \tag{3.7}$$

Following Equations (3.5) and (3.6), we can obtain the fundamental equation of texture analysis:

$$P_h(y) = \frac{1}{2\pi} \int_{h // y} f(g) d\tilde{\varphi} \tag{3.8}$$

This equation represents the fact that each pole figure (a 2D object) is a projection

along a certain path, $\tilde{\varphi}$, of the ODF (a 3D object), which of course depends on the crystal symmetry. Several approaches have been developed to solve the Equation (3.8) to find the ODF from at least three PFs. The algorithm of obtaining the ODF from a set of PFs consists of finding the vectors, which connect each cell from the orientation space to the cells of the various PFs. The following will discuss the Williams-Imhof-Matthies-Vinel (WIMV) method.

The WIMV approach [89-91] for the refinement of the OD is an iterative way, which based on the numerical refinement of *f(g)* at step *n+1*:

$$f^{n+1}(g) = N_n \frac{f^n(g) f^0(g)}{\left(\prod_{h=1}^{I} \prod_{m=1}^{M_h} P_h^n(y) \right)^{\frac{1}{IM_h}}} \tag{3.9}$$

where the product extends over I experimentally measured pole figures and for all the poles multiplicity M_h, $f^n(g)$ and $P_h^n(y)$ represent the refined values of $f(g)$ and $P_h(y)$ at the n^{th} step respectively. The number N_n is a normalized factor. The $P_h^n(y)$ values are calculated at each cycle with Equation (3.8). The first step in this procedure is to evaluate $f^0(g)$:

$$f^0(g) = N_0 \left(\prod_{h=1}^{I} \prod_{m=1}^{M_h} P_h^{\exp}(y) \right)^{\frac{1}{IM_h}} \tag{3.10}$$

in which $P_h^{\exp}(y)$ stands for the measured pole figures.

The regular WIMV method necessitates an OD discretised in a finite number of regular cells. Inside each cell, a discrete value of the OD is associated. When the WIMV calculation is inserted inside the Rietveld refinement procedure, it requires two additional

steps: i) the extraction of the pole figures or texture weights, and ii) the interpolation of these weights to fit the regular grid. This renders non-optimized values of the OD, particularly for sharp texture and coarse irregular coverage of the OD [82].

The E-WIME (Extended WIMV) approach can be used with irregular coverage of the OD space and includes smoothing. The extension of the method provides with an iterative scheme of the OD refinement, which is very close to the maximization of entropy. The E-WIMV method is, then, often called the Entropy-modified WIMV. The OD-cell values are computed through an entropy iteration algorithm that includes the reflection weights:

$$f^{n+1}(g) = f^{n}(g) \prod_{m=1}^{M_h} \left(\frac{P_h(y)}{P_h^n(y)} \right)^{r_n \frac{w_h}{M_h}} \tag{3.11}$$

in which r_n is a relaxation parameter such that $0 < r_n < 1$, M_h is the number of division points for the discretisation of the integral of all orientations around the scattering vector of the pole figure, $\boldsymbol{h}$. The reflection weights, w_h, is introduced to take into account the different accuracy of the more intense and less overlapped reflections with respect to the smaller ones, and is calculated analogously to the weight factors of the Rietveld analysis.

The commercial codes, such as the Preferred-Orientation Package Los Alamos (PopLA) [92], Beartex [28, 93], and MAUD [84, 85] are available for the quantitative texture analysis from the measured PFs data. In particular, the MAUD is also capable to conduct the quantitative texture analysis (combining the Rietveld and E-WIMV procedures) directly from the 2D diffraction images or diffraction patterns, respectively, measured using synchrotron X-ray or neutron diffraction.

3.4.4 Low-energy X-ray diffraction (LE-XRD)

Today, diffraction techniques are most widely used to measure crystallographic texture. X-ray diffraction with a PF goniometer is a routine method, although synchrotron X-ray and neutron diffractions provide unique advantages for some applications. Here, Bragg's Law for monochromatic radiation is applied. The principle for LE-XRD texture measurement is simple [28]: in order to determine the orientation of a given lattice plane, *(hkl)*, of a single crystallite, the detector is first set to the proper Bragg angle, 2θ, of the diffraction peak of interest, then the sample is rotated in a goniometer until the lattice plane, *(hkl)*, is in the reflection condition (i.e., the normal to the lattice plane or the diffraction vector is the bisector between incident and diffracted beam). The goniometer rotations are related to the angular coordinates which define a sample orientation. In the case of a polycrystalline sample, the intensity recorded at a certain sample orientation is proportional to the volume of crystallites with their lattice planes in reflection geometry. With the X-ray laboratory instruments, the incomplete PFs can be recorded, because the low-energy X-rays (8KeV for CuK_{α}) show a small penetration into the material, and the measurement becomes difficult at a small incidence angle. This impediment can be overcome using the neutron diffraction or synchrotron radiation with high-energy X-rays (80 – 100 keV). The texture measurements using synchrotron radiation will be discussed in the next section.

The diffractometer used to obtain the PFs is a Scintag XDS2000 at the High Temperature Materials Lab (HTML) of the Oak Ridge National Lab (ORNL). The

schematic of the measurements is illustrated in Figure 3.4a [94]. The PFs of the {10.0}, {00.2}, and {10.1} reflections on the normal planes were recorded with Cu-Kα radiations at 45 kV and 40 mA, a point source with a 2 mm diameter incident beam collimator, and a four-axis PTS (power-texture-stress) goniometer (Fig. 3.4c). The PFs were collected for the sample tilts ranging from $\chi = 0^o$ to 75^o, with a step of 5^o, and for the sample rotations ranging from $\varphi = 0^o$ to 355^o, at the rate of 100^o/min (Fig. 3.4b) [28, 94]. The LE-XRD PFs were analyzed using popLA software [92], including the PFs extrapolation for the tilting angle, $\chi > 75^o$.

3.4.5 High-energy synchrotron X-ray diffraction

The most important advantage of synchrotron texture analysis is that it provides a high penetration depth for most materials combined with excellent brilliance and high spatial resolution. Hence, texture measurements can be carried out on bulk samples from the statistical average of the microscopic behavior in transmission geometry [31]. This, thus, eliminates spurious surface effects often present in texture measurements with conventional laboratory X-ray source or electron backscattering (EBSD) [88]. In addition, the divergence of synchrotron X-rays is extremely small so that high orientation resolution can also be achieved ($< 0.01^o$). By employing an area detector in transmission, full Debye-Scherrer rings are recorded simultaneously such that significant reduction of measuring time and high angular resolution are achieved. Therefore, synchrotron X-rays offer the possibility for *in situ* measurements under various environments, due to the fast

measuring time together with high penetration power and small wavelength [31].

The principle of pole figure measurement using synchrotron X-rays is similar to that of laboratory X-ray measurement. Figure 3.5a illustrates the basic diffraction geometry for texture measurement, including the incoming synchrotron X-ray beam, sample, orientation sphere, Debye cone (the left shaded cone with an opening angle of 4θ, where diffracted X-rays lie), and area detector [86]. If the sample is stationary, only lattice planes (*hkl*) that are inclined by an angle of $90^o - \theta$ to the incoming beam satisfy the Bragg's condition, where the corresponding reciprocal lattice vectors lie on a cone with an opening angle of $180^o - 2\theta$ (the right shaded cone). This cone intersects the orientation sphere of the sample resulting in a small circle (with a radius or 'pole distance' $90^o - \theta$), which corresponds to a Debye ring (with opening angle 4θ). The intensity variations along the Debye ring are directly proportional to the pole-density variations on the small circle on the orientation sphere. The angle η on the Debye ring corresponds to the pole sphere azimuth, when viewed along the incident X-ray. Because of centrosymmetry, there is an equivalent small circle on the opposite hemisphere. The pole figure as a pair of lines separated by a distance 2θ (Fig. 3.5b) is a direct projection of the small circles along the rotation axis Y. For a sample at normal incidence ($\omega = 0^o$), the pair of lines are horizontal in the pole figure. Tilting the sample by ω around the Y axis rotates the lines on the pole figure by the same angle. Images with more different sample rotations are combined to increase pole figure coverage.

As mentioned earlier, twinning results in a sudden reorientation of the volume fraction of the crystals that is being twinned rather than the gradual reorientation of

dislocation slip. Therefore, twinning can induce a significant change in texture even for small levels of straining. Furthermore, twinning takes place throughout the volume of the sample, the high penetration into the samples by synchrotron hard X-rays (or neutrons) is necessary to provide the reliable volumetric information. It is, thus, well suited to detect twinning/detwinning via texture evolution using synchrotron diffraction technique. The texture measurements using synchrotron diffraction are more complete than other data obtained. For example, the current *in situ* neutron diffraction experiments (will be discussed in the next section) simultaneously monitor only two directions in the sample space. The uniqueness of the current synchrotron measurement comes from the ability to assess the complete orientation space within each grain orientation family.

The *in situ* and *ex situ* texture measurements were conducted at APS, ANL, on the high energy beamline 11-ID-C (Fig. 3.6b) with a wavelength of 0.10748 Å, a beam size of 0.5×0.5 mm^2, and a simple goniometer. The threaded-end cylindrical sample (Fig. 3.3a), having a gage length of 6.35 mm with a diameter of 2.921 mm, was mounted on a screw-driven load frame with the loading axis aligned vertically (Fig. 3.6a). The sample is placed in the beam with the loading axis perpendicular to the beam line, and macroscopic strains were recorded using an extensometer or macroscopic crosshead displacements were monitored for calculating the macroscopic strain during *in situ* measurements. The texture measuring points during *in situ* monotonic loadings were selected along the stress-strain curve corresponding to characteristic points: a) initial undeformed, b) after yielding, c) lower hardening-rate region or quasi-steady-state plastic deformation, d) higher hardening rate region, and e) maximal strain, total 5 ~ 8 measuring points for each loading condition.

At each of the measuring points, loading was interrupted but not released; as shown in Figure 3.6a, the 2-D images were registered by a 3,450 × 3,450 image-plate detector at 10 different tilt angles, rotating the sample around the vertical loading axis (perpendicular to the beam) through 90^{o} in 10^{o} interval to increase the pole-figure coverage. The exposure time for each image was 30 seconds. This setup produces the pole figure coverage as shown in Figure 3.7. The coverage can be further improved by more rotations of the sample, but 10 rotations are enough to provide good pole figure coverage for the calculation of the full ODF in the current measurements. A typical example of the two-dimensional synchrotron images is shown in Figure 3.8, which is recorded for the as-rolled AZ31B alloy with the RD aligned vertically and the ND parallel to the beam line (Please refer to Fig. 3.6a). In Figure 3.7a, the first three rings from the center are indexed, respectively, as (10.0), (00.2), and (10.1) planes. The texture is intuitively visible by the intensity variation along the Debye rings, yielding information about the orientation of the specific lattice planes. The same procedure was used for the texture measurements of the cyclic-loading conditions, except they were performed *ex situ* because the current load frame available is not able to conduct cyclic loading. The six samples, corresponding to the six feature points (e.g., the maximal strain, zero strain, or zero stress) along the hysteresis loop in the first cycle deformation, were prepared beforehand for each cyclic loading condition using interrupted method.

The MAUD software package has been used to perform texture analysis *via* Rietveld method. First of all, the CeO_2 standard sample spectra were used to calibrate the sample-to-detector distance (1.5289 m) and refine instrumental parameters in MAUD

including a bulk scaling intensity, a peak width function, and a zero offset. Once the calibration was done, the instrument-related parameters were fixed for all other analyses. The sample images were first processed in FIT2D [95, 96], and the beam center was determined. The full 360^{o} coverage of each image was integrated over 5^{o} increments of the azimuthal angle into 72 slices (spectra). Figure 3.7 shows the integrated area over 5^{o} azimuthal angle as an example from the as-rolled AZ31B diffraction image (Fig. 3.8a). The corresponding integrated spectrum and the final fitted profile during the texture analysis *via* Rietveld refinement are also shown (Fig. 3.8b). Total 720 slices (corresponding to the ten images for each texture measurement) were then input for simultaneous refinement using texture-analysis wizard in the MAUD program, where the tomography based E-WIMV algorithm is used for texture refinement. The program runs four cycles during the Rietveld refinement of texture [97]:

Cycle 1: Refining the scale, background parameters and phase fractions for multiphase systems. Backgrounds are fitted to a seventh-order polynomial.

Cycle 2: In addition to the previous parameters peak positions are adjusted during this cycle by refining cell parameters and instrument errors based on observed d-spacings. The waviness is corrected.

Cycle 3: The microstructural parameters (crystallite size and microstrains) are added to the refinement to adjust peak shapes. Only one overall temperature factor, B, is used for all atoms of a phase to avoid correlations and minimize possible errors. Other structural parameters such as atomic coordinates are not refined with the Texture Wizard.

Cycle 4: The orientation distribution is refined. Intensities of individual peaks start to match. Finally, pole figures such as (00.2), (11.0) and (10.1) poles can be calculated from the ODF (Orientation Distribution Function). Pole densities are expressed in m.r.d..

The wizard refinement is often sufficient to capture the main texture features. But we may wish to continue to refine additional parameters from all the many possibilities offered by MAUD. They include lattice parameters for accessory phases, atomic coordinates, temperature factors, anisotropic grain size, and residual stresses. The details regarding the data reduction and texture analysis, please refer to the papers by Lonardelli et al. [86] and Miyagi et al. [98]. Once the satisfactory pole figures are obtained, the pole figures or ODFs can be exported to be further analyzed using the Beartex software [93]. In Beartex, a number of options are available: smoothing, plotting, rotating, and etc. In particular, the twin volume fraction can also be determined from the ODFs by calculating the integral intensity of the OD inside a given sphere in the orientation space (intensity of a spherical component).

3.4.6 *In situ* neutron scattering

Neutrons have many properties that make neutron diffraction an important tool for characterizing materials behavior. For the purposes of this work, neutrons penetrate deeply into most engineering materials, such that the entire volume of a specimen can be probed by neutron beam regardless of the specimen orientation during the measurements, thus, the information obtained is averaged over a bulk sampling volume. As mentioned earlier,

twinning takes place throughout the volume of the sample; the full penetration of the samples by neutrons provides the reliable volumetric information [24, 25]. It is, thus, quite easy to detect twinning by neutron diffraction, which results in a change in the peak intensity.

The Spectrometer for MAterials Research at Temperature and Stress (SMARTS), at the Manuel Lujan Jr. Neutron Scattering Center, Los Alamos Neutron Science Center (LANSCE) at the Los Alamos Nation Laboratory (LANL), is a third-generation neutron diffractometer, optimized for the study of engineering materials. SMARTS provides an exciting range of capabilities for studying polycrystalline materials focusing on two areas: the measurement of deformation under stress and extreme temperature, and the measurement of spatially resolved strain fields. The threaded-end sample (Fig. 3.3b) is mounted in the horizontal load frame. The loading axis is oriented at 45^{o} relative to the incident beam (Fig. 3.9a), and the two detector-banks situated at $\pm\ 90^{o}$ simultaneously record two complete diffraction patterns, with the diffraction vectors, respectively, parallel ($Q_{\parallel}$) and perpendicular ($Q_{\perp}$) to the applied load.

The *in situ* neutron diffraction spectra can reveal a number of different aspects related to the evolutions of the microstructure and stress state in the sample. For instance, the appearance or disappearance of peaks can signify a phase transformation, or, in the present case, mechanical twinning, as mentioned above. Due to the ~ 90^{o} reorientation of the basal poles which occurs with $\{10\bar{1}2\}<10\bar{1}1>$ extension twinning and the initial strong basal texture in the magnesium alloys, the intensity transfer of the basal (00.2) peak between the parallel and transverse detector banks can be directly related to the degree of

twinning that has occurred. In particular, this experimental configuration on the SMARTS enables the separation of the daughter (twin) grain orientations from the parent (matrix) grain orientations. This fact was exploited to advantage in previous *in situ* studies of twinning in Mg [10, 24, 27, 37]. *In situ* neutron diffraction can be also used to measure the internal-stresses that develop in differently oriented grains as a function of deformation. The internal-strains can be calculated based on the peak shift of (*hk.l*) planes between the loaded and load-free patterns, as presented in Section 1.2.

Because a large sample (total 4" of length, see the geometry in Fig.3.3b) is required for the loading frame of the SMARTS, the samples can be cut only along the ED/RD or TD directions of the plates. For the AZ31B alloy, due to the near in-plane symmetry of the initial texture, the RD and TD samples are expected to exhibit the similar behavior, thus, only a RD sample was cut for the measurements. For the cyclic deformations at a strain amplitude of ± 3%, diffraction patterns were recorded at a 0.5 % strain interval for the first cycle, at a 1.0 % strain interval for the second cycle, and thereafter at the six feature points (e.g., at the maximal strain, zero strain, or zero stress) respectively, for the selected cycles of 5, 10, 15, 20, 30, and etc. along the stress-strain hysteresis loops. For the sample tested at a strain amplitude of ± 1.2%, diffraction patterns were collected at a 0.2% strain interval for the first two cycles, and thereafter at the six feature points for the selected cycles of 5, 10, 20, 50, 100, 200, 300, and etc. The monotonic or cyclic tests were performed using the Instron-customized loading frame under strain control mode. The sample orientations were carefully aligned in the horizontal for different purposes (Fig. 3.9). The macroscopic strains were measured using an extensometer attached to the sample, and the imposed

cyclic frequency is 0.5 Hz. The initial loading can be compressive or tensile, which resulted in the different sequences of twinning activation during the first cycle.

The neutron scattering patterns were processed using single-peak fitting integrated in the code of SmartsSPF [99], and the peak position, peak intensities, FWHM, and their errors can be obtained. The lattice strain can then be calculated based on the Eq. 1.4. However, due to the strong initial texture, some diffraction peaks may be initially not strong enough for obtaining a precise d-spacing. In this case, we used the technique successfully developed for interpreting such data by Brown et al. [10] to obtain the d-spacing data for the strain-free condition. For a strain-free material that is elastically isotropic, the ratios between the given (*hk.l*) peak positions in banks 1 and 2 should be the same. These ratios were employed to obtain the lattice parameters for peaks initially weak in one of the banks. The Rietveld refinement of the whole profiles can be conducted in the software packages of MAUD or GSAS (general structure analysis system), written by Larson and Von Dreele of Los Alamos National Laboratory [100]. Figure 3.10 shows the examples of the experimental and fitted patterns using GSAS, which are collected from the as-extruded ZK60A alloy. The crosses are the measured data, the overlapped lines through them are the Rietveld fits, and the lower curves are the differences between the measured data and the calculated lines. The fitted backgrounds have been subtracted from both the observed and calculated intensities for clarity.

CHAPTER 4 MONOTONIC MECHANICAL BEHAVIOR AND THE ASSOCIATED TEXTURE EVOLUTION

In this chapter, the monotonic mechanical responses and the concomitant texture evolutions were extensively studied in the two wrought Mg alloys, ZK60A and AZ31B, with different initial textures loaded along the three orthogonal directions. The *in situ* neutron and synchrotron diffraction was employed to study the microstructural evolutions and the stress states during monotonic loadings.

4.1 Monotonic Mechanical Behavior

4.1.1 ZK60A extruded magnesium alloy

Figures 4.1 shows the monotonic true stress *vs.* true strain curves for the extruded ZK60A Mg alloy, respectively, loaded along the three orthogonal directions under tension and compression. The tension-compression yielding asymmetry in the ED samples is significant, while the asymmetries in the TD and ND samples are pronouncedly reduced. The high anisotropy between the three loading directions is observed.

The flow curve under the ED tension (labeled as "ED-T" in Fig. 4.1) shows the normal, concave-down shape with a high yielding stress, a low hardening evolution upon yielding, and a smooth transition from the elastic to plastic deformation. It is well accepted that the dislocation slips are the major deformation mechanism in the ED/RD tensile loadings [30, 49] of wrought magnesium alloys. In contrast, if the alloy is compressed along the ED direction, the stress-strain curve (labeled as "ED-C" in Fig. 4.1) exhibits a concave-up shape. It displays an abrupt yielding, with about a half yielding stress compared to that in the ED tensile loading, a low hardening rate plateau followed by a rapidly increasing hardening. Usually an inflection (typically at 6 – 8% strains) is observed when the twinning ability is exhausted. This type of strain hardening plateau is typical of materials which deform by twinning, including hexagonal close packed Mg alloys [10, 14, 26] and Zr alloys [38, 101], as well as low symmetry martensite shape-memory alloys such as NiTi [102]. The observed exceptional hardening phenomenon is under analysis using EPSC modeling trying to understand the intrinsic mechanisms. After 8% strain

compression along the ED direction, a large volume fraction of grains are oriented with their basal poles aligned with the ED direction (e.g., the compressive loading axis) (Fig. 4.3b). This type of texture development is a signature of the extension twinning in magnesium alloys. Using *in situ* neutron diffraction measurements focused on the monotonic compressive deformation of an extruded AZ31B alloy along the prior ED direction, Brown et al. [10] has reported that as much as 80% of the volume fraction of favorably oriented grains can undergo such twinning during the first 8% strain.

If, on the other hand, the samples are loaded along the TD and ND directions, the compressive and tensile flow curves show low yielding stresses, reduced asymmetries between tension and compression, and moderate strain hardening evolutions upon yielding. They are distinct from both the ED tensile and ED compressive flow curves. Nevertheless, all yielding stresses are comparable to the one under the ED compression, suggesting that the yieldings under these loading conditions are possibly controlled by the same deformation mechanism as that in the ED compression. As will be shown later, the plastic deformation in the TD tensile loading is initially dominated also by extension twinning. However, the flow curve of the TD tensile sample is also distinct from that under the compression loaded along the ED direction, which is typical due to the activation of extension twinning in Mg alloys. The TD compressive sample (labeled as "TD-C") results in a significant texture change (Fig. 4.3c) with a large volume of grains aligned with their c-axes along the compressive axis (e.g., TD direction), signaling the activation of extension twinning. The similarity of the deformation behaviors between the TD and ND loadings is a result of the initial fiber texture along the ED axis, while the subtle difference is due to the subtle deviation of the initial texture from the ideal fiber.

4.1.2 AZ31B rolled magnesium alloy

Figure 4.2 represents the tension-compression asymmetries and high anisotropy in the AZ31B Mg alloy with the loading axis, respectively, parallel to the RD, TD, and ND directions. Compared to the mechanical responses shown in Figure 4.1 of the extruded ZK60A alloy, the rolled AZ31B alloy shows both the differences and similarities in terms of the plastic deformation behavior. The tension and compression asymmetries in all three directions are significant, and the high anisotropy is evident.

If the samples are loaded along the RD and TD directions, the compressive flow curves (respectively, labeled as “RD-C” and “TD-C” in Fig. 4.2) exhibit the same features resulting from the in-plane texture symmetry. And their overall characteristics are also the same as that under the ED compression in the ZK60A alloy shown in Figure 4.1. A low yielding stress, an initial low hardening rate followed by a rapidly increasing hardening, and the limited post-twinning deformation are observed. This is characteristic of the twinning-dominated plastic deformation in magnesium alloys. The texture evolutions (Figs. 4.4b&c) corroborate the twinning activations because the new texture components parallel to the loading axis are observed after compression. In parallel, the tensile flow curves (respectively, labeled as “RD-T” and “TD-T”) have the same nature as the one under the ED tension, where the dislocation slips dominate the plastic deformation.

However, if the sample is extended along the ND direction, the stress-strain curve (labeled as “ND-T”) has a concave-up shape, similar to the ED compression in ZK60A alloy and the in-plane compressions in AZ31B alloy. In this loading condition, the applied

tensile stress stretches the c-axes of the hcp matrix lattices in most grains and leads to the activation of extension twinning. The basal poles of the resulting texture is uniformly distributed along the perimeter in the (002) pole figure as will be shown later, and they are reoriented by ~ 90^{o} relative to the original orientation concentrated at the center (Fig. 4.4a). Under compression, the ND sample is very brittle with a much higher flow stress and very little ductility (~ 5%), since both basal or prismatic <a> slip are unable to accommodate inelastic shape change along the c-axis due to a small Schmid factor, and the <c+a> pyramidal slip and contraction twinning seem to result in shear instability at room temperature [9, 15, 16]. The texture after the ND compression is intensified due to the dislocation slips (Fig. 4.4d).

In summary, in the ZK60A alloy, except the ED tension which is dominated by dislocation slips, the alloy exhibits the similar yielding stresses (~ 160 MPa) for the other loading conditions with the extension twinning dominating the initial plastic deformation. Similarly, if the plastic deformation in the AZ31B alloy is initially accommodated by extension twinning, the similar yielding stresses (~ 100 MPa) are also observed. This suggests that the yielding stresses are not related to the strain direction and strain sign if the twinning is the dominating plastic deformation mechanism. In contrast, the yielding stresses are usually different with respect to the loading directions due to the difference of Schmid factor, if the dislocation slips are dominant throughout the plastic deformation.

4.2 Lattice Reorientation Detected by *in situ* Neutron Scattering

Figure 4.5 shows the evolution of the diffraction patterns collected from the TD and ED directions during the *in situ* tensile deformation of the as-extruded magnesium alloys, ZK60A, along the TD direction at various strain states: a) as-extruded, b) 1.0%, c) 3.0 %, d) 5.0%, e) 7.0%, f) 9.0%, g) 11.0%, and 13.0%. In the neutron measurements, the TD direction was parallel to the loading axis (corresponding to the parallel bank 2), and the ED direction was aligned transverse to the loading axis in the diffraction plane (corresponding to the transverse bank 1). The complete spectra with more than ten peaks were recorded in both directions (see the examples in Fig. 3.10), but only three peaks are shown here, respectively, for the (10.0), (00.2), and (10.1) reflections. Consistent with the strong initial preferred lattice orientation, the (00.2) diffraction peak is strong in the TD direction, while it is very weak in the ED direction, in the strain-free diffraction patterns (please refer to the patterns labeled as 'a' at the bottom in Fig. 4.5). Correspondingly, the (10.0) diffraction peak is relatively strong in the ED direction, while it is weak in the TD direction. It is observed that the peak-intensity change and peak shift are significant in these patterns with tension undergoing from the bottom to the top in Figure 4.5. As the tensile strains increase, the intensity of the basal poles in the TD direction is gradually decreasing to the background intensity. Concurrently the one in the ED direction is keeping increasing. On the other hand, the peaks gradually shift to the right in the TD direction due to the tensile stress along the loading axis, while the peaks shift to the left in the ED direction due to the subjected compression along the transverse direction by the Poisson's strains. Therefore, these patterns reveal a number of different aspects related to the evolutions of the

microstructure and stress state in the sample.

In the present experimental setup, the microstructure development of the parent and twin grains can be obtained from the (00.2) and (10.0) peaks. The intensity transfer of the diffraction peaks between the TD and ED directions is shown as a function of imposed engineering strains in Figure 4.6. As discussed above, the initial high basal (00.2) peak intensity in the TD direction is indicative of the large volume of "parent" grains, which are oriented in a favorable orientation for the extension twinning under tensile loading, and can be correlated with the high intensity in the basal (00.2) pole figure parallel to the TD direction of the initial texture (Fig. 3.2a). The initial low intensity in the ED direction corresponds to the original low intensity in the (00.2) basal pole figure along the ED direction. An increase in the (00.2) peak intensity within the ED direction indicates an increase in the volume fraction of twins, and is correlated with a concurrent decrease in the corresponding intensity in the TD direction diffracted from the parent grains. The (00.2) diffraction intensity in the TD begins to decrease at a strain of ~ 0.8% with a concomitant increase in the ED. This point agrees well with the plastic-yielding point observed in the macroscopic stress-strain curve (labeled as "TD-T" in Fig. 4.1), indicating that as soon as the sample yields, twinning occurs almost immediately. The (00.2) intensity diffracted to the TD direction is continuously decreasing at a gradually reduced rate until the background level at a strain of ~ 13 %, where the twinning capability appears to be nearly exhausted (Fig. 4.6). The fact that all parent grains favorably oriented have twinned is evidenced as the disappearance of the (00.2) peak in the TD (labeled as "h" in Fig. 4.5a). The disappearance of the (00.2) poles at the center of the (00.2) pole figure measured by *in situ* synchrotron diffraction (will be discussed in detail later) further corroborates the

observation (Fig. 4.7g). The aforementioned behavior is very similar to that under compression reported by Brown et al. [10] for the extruded AZ31 alloy. In addition, the gradually reduced rates in the intensity change of the (00.2) basal poles in the TD direction suggest that the relative activity of the twinning is diminishing with the applied strains. Consequently, more basal or prismatic slips must be activated to accommodate the imposed strain.

In the current study, the twin grains under tension are expected to be oriented with their c-axes at an angle of nearly 90^{o} to the loading axis. This subset of twin grains is in a hard orientation in terms of basal dislocation slip. Thus, they cannot accommodate more plastic deformation unless the harder non-basal slips or contraction twinning can be activated in these twinned grains. However, the initial texture indicates that there are some grains possibly favorable for basal and/or prismatic slips, relative to the current loading axis. Therefore, as the relative activity of extension twinning is gradually diminishing locally in the TD texture component, and, concurrently, as the tensile stress increases, more and more basal and/or prismatic slips within the grains, having basal poles oriented outside the TD and ND texture components, shown in the (00.2) pole figure (Fig. 4.3a), may be activated. Consequently, more plastic strains can be accommodated progressively by the dislocation slips, and, correspondingly, fewer strains are accommodated by twinning. Therfore, an inflection in the flow curve is not observed, presumably due to the smooth transition from the twinning-dominated to the dislocation-slip dominated flows.

4.3 Texture Evolutions Measured by *in situ* Synchrotron Diffraction

4.3.1 ZK60A alloy under tensile loading along the TD direction

Based on the *in situ* neutron measurements discussed above, the extension twinning behavior under tension shows the same behavior as that under compression. However, how the basal poles in the twin grains distribute around the loading axis is not yet experimentally clarified, because the current experimental configuration for the neutron measurements recorded the scattering patterns only along the two directions, e.g., the TD and ED directions. Nevertheless, as expected that the twinned grains reorient away from the loading axis at a nearly 90^{o} is evident from the neutron results. The texture measurements using *in situ* synchrotron diffraction provide the complete orientation information, supplemental to the neutron data. Figure 4.7 shows the crystallographic texture evolution for the as-extruded and the strained conditions, respectively, a) as-extruded, b) 1.0 % strain, c) 3.0 % strain, d) 5.0% strain, e) 7.0 % strain, f) 9.0 % strain, and g) 13.0% strain.

As mentioned earlier, the initial basal poles in the as-extruded condition are dominantly perpendicular to the ED direction of the plate, and the prismatic poles are mostly aligned with the ED (Fig. 4.7a). It is worthwhile to emphasize that the parent grains in the TD texture component are favorably oriented for extension twinning under the TD tension. When the sample is strained to 1.0 %, the change in the pole figures is not obvious due to the elastic deformation initially (Fig. 4.7b). At the strain of 3.0 %, a decrease of the basal-pole intensity at the center of (00.2) pole figure is observed, and, concurrently, the

basal poles appear at the ED direction and the other four locations around the perimeter with a 60^{o} tilt angle relative to the ED direction (Fig. 4.7c), besides the preservation of the ND component. With the deformation going on, the basal-pole intensity at the center is continuing to decrease, while the basal-pole intensities corresponding to the six twin locations along the perimeter of the (00.2) pole figure progressively increase (Figs. 4.7d – g). At the strain of 13.0 %, the basal poles completely disappear at the center of the (00.2) pole figure (Fig. 4.7g), indicating that those grains with their c-axes parallel to the loading axis completely twinned under tensile loading along the TD direction. This trend agrees well with the decrease of the basal pole intensity in the TD direction, and the increase in the ED direction measured by *in situ* neutron scattering (Fig. 4.6). Nevertheless, the overall texture evolution is significantly different from that under compression, where the basal poles show the pronounced tendency to be aligned with the compressive loading axis [10, 47].

The observed texture evolution can be explained to be associated with the extension twinning using the overlapped schematic in Figure 4.7g. In Figure 4.7g, a hexagon is included at the center, indicating the initial lattice orientation of the most grains within the TD texture component, and the arrows are denoting the six orientations of the possible twin variants. In magnesium alloy, extension twinning occurs along the $<10\bar{1}1>$ directions on the $\{10\bar{1}2\}$ planes. Because of the crystal symmetry with a hexagonal lattice structure, there are six possible $\{10\bar{1}2\}$ planes with a specific $<10\bar{1}1>$ shear direction on each plane. Several reports have demonstrated that the extension twinning in magnesium can be understood in terms of the Schmid Law [25, 26, 103-105]. When a tensile load is applied

along the TD direction, the TD texture component is favorably oriented for extension twinning on the six equivalent extension twinning systems with the same Schmid Factors of 0.498 [105]. Therefore, the basal poles are reoriented to the six locations, corresponding to six twin variants, around the perimeter of the (00.2) pole figure. In contrast, a contraction along their c-axes is induced in the grains of the ND component, and, thus, they are not expected to undergo extension twinning as manifested in the negative values of the Schmid factors. Consequently, the ND component is preserved in the (00.2) pole figure (Fig. 4.7g). Figure 4.8 shows the texture comparison at a tensile strain of 13%, respectively, measured by neutron and synchrotron X-ray diffractions. The figure exhibits the similar texture components, except that the intensity difference between the two is observed.

4.3.2 AZ31B alloy under tensile loading along the ND direction

The texture evolution measured *in situ* during the tensile loading of the rolled AZ31B Mg alloy along the ND direction is presented in Figure 4.9. In the initial grain orientation (Fig. 4.9a), most grains are aligned with their basal poles parallel to the ND direction (e.g., the loading axis), and, thus, extension twinning will be active under tension. When the sample is loaded to a strain of 1.0%, it is noted that some basal intensity is observed in the TD direction (Fig. 4.9b), indicating a small volume fraction of grains are already reoriented by ~ 90^{o} and aligned with their c-axes along the TD direction. When the sample is, further, strained to 3.0% strain, more parent grains are rotated and, concurrently, the central intensity is significantly reduced, but twin grain orientations are not evenly distributed at a ~ 90^{o} around the loading direction but with a higher intensity along the TD

direction (Fig. 4.9c). With the straining continues, more and more grains are distributed along the perimeter, and less and less grains are concentrated at the center, manifested as an intensity reduction at the center (Figs. 4.9d – g). Finally, when the sample is loaded to 13.0% strain, the basal texture component at the center is completely disappeared due to twinning (Fig. 4.9g). Compared to the texture evolution of the ZK60A Mg alloy under the TD tension (Fig. 4.7), the final distribution of the basal poles along the perimeter of the (00.2) pole figure in the AZ31B Mg alloy under the ND tension is essentially uniform (Fig. 4.9g). This is due to the significant difference between the initial textures in the two alloys. The initial texture in the as-rolled AZ31B alloy shows the radial symmetry with the prismatic poles distributed uniformly in the plane, while the prismatic poles are aligned with the ED direction in the as-extruded ZK60A alloy.

In a word, the extension twinning in magnesium alloys results in the rapid and complete texture change within the texture component that is favorably oriented. The texture change is reasonably correlated with the reorientation by the extension twinning. The lattice reorientations associated with dislocation slips are negligible, compared to that produced by the extension twinning.

4.4 Internal-strain Evolution Measured by *in situ* Neutron Scattering

The internal-stresses can be obtained *via* Hooke's law from the internal-strains based on the peak shift of (*hk.l*) planes between the strained and strain-free patterns using Equation 1.4. The internal-strain evolutions for the (10.0), (00.2), (10.1) and (11.0)

reflecting planes as a function of applied stress are shown in Figure 4.10. The sample initially undergoes tensile elastic deformation. Thus, the internal-strains (tensile or compressive sign) increase linearly with the macroscopic applied stress at a nearly same slope for all grain orientations, owing to the near-elastic isotropy in Mg. It is noted that the slopes in the transverse direction (e.g., the ED direction) are steeper than those in the parallel direction (e.g., the TD direction) as a result of the Poisson's effect and the lack of external boundary constraint. The basal plane of the (10.1) grain orientation in the parallel direction is inclined at a degree of 28^{o} to the loading axis, yielding a Schmid factor of ~ 0.305 for basal slip. Thus, this subset of grains is favorably oriented for basal <a> slip (or in a soft orientation) relative to the other neighboring grains. They yield first, and smaller elastic strains are observed in the yielded grains. Thus, the corresponding curve diverges from the linear response with an increasing slope. A similar transition is observed for the (10.1) grain orientation in the transverse direction. It can be inferred that the other subsets of grains in hard orientations must share a larger portion of load and their associated slopes decrease. This phenomenon can be well understood largely in terms of the elastic load transfer between soft- and hard- grain orientations behaving like a composite material [32]. This trend agrees well with the reports by Agnew, Brown, and Clausen for the extruded magnesium alloy, AZ31B, under monotonic compression [10, 30, 37, 41].

When the sample starts to plastically deform by twinning at the stress of – 141 MPa (~ 0.8% strain), the (00.2) parent grains (please see the TD direction in Fig. 4.10) are relaxed, relative to the stress field in the surrounding grains. The stress relaxation is so significant that a significant drop step is observed in the curve of applied stress vs.

internal-strain for the (00.2) grain orientations, that is, the internal-stresses are significantly redistributed among the various grain orientations as twinning begins, and the applied load is repartitioned according to the grain orientations. The newly-formed twin grains (please refer to the (00.2) reflection in the ED direction in Fig. 4.10) have a much smaller stress than the other grain orientations, indicating that they are initially relaxed relative to the neighbors. This exactly same phenomenon is also reported by Clausen et al. [37] for the extruded AZ31B alloy under compression. However, the twins are in a plastically hard orientation with respect to basal slip. Thus, the internal-stress within the twins accumulates quite quickly, and they absorb a larger fraction of the applied load.

4.5 Summary

The two magnesium alloys, the extruded ZK60A and the rolled AZ31B, have been investigated under tension and compression, respectively, loaded along the three orthogonal directions. The significant tension-compression asymmetries and high anisotropies are observed. The tension-compression asymmetries are related to the activation of extension twinning in one direction but not in the opposite direction. The high anisotropies are correlated with the initial texture distinction with respect to the loading axis and direction, resulting in the different deformation mechanisms activated. The similar yielding stresses for each alloy are observed irrespective of the strain direction and strain sign if the deformation is dominated by extension twinning, while they are usually different relative to the loading conditions if the plastic deformation is dominated by

dislocation slips. The monotonic mechanical properties serve as a basis for further performing the cyclic deformation and low-cycle fatigue studies.

In situ neutron and synchrotron diffraction was used to study the behavior of the extension twinning and its role on the texture evolution and internal-strain/stress evolution under the monotonic loadings of the two wrought magnesium alloys. The initial crystallographic texture of the as-extruded magnesium plate contains grains with their c-axes parallel to the TD direction, which allows us to study the behavior of the extension twinning under monotonic tension using SMARTS, usually restricted by the limited dimension along the aligned basal-pole direction. The obtained results show that the extension twinning under monotonic tension exhibits a similar behavior as that under monotonic compression, presumably due to the fact that these two different loading conditions introduce the same Schmid stress on the twinning plane and in the twinning shear direction within strongly textured wrought magnesium alloys. However, the basal poles within the twin grains under tension in the ZK60A alloy are distributed at the six locations corresponding to the six twin variants at a near 90^{o} inclined to the tensile loading axis, while they are always closely aligned with the compressive axis under compression. The texture evolution under the TD tensile loading of ZK60A alloy can be well understood by the six equivalent twinning systems due to the crystal symmetry of the hexagonal lattice structure using the Schmid Law. Due to the radial symmetry in the initial texture in the AZ31B alloy, the resulting texture after the ND tension, though dominated by the same extension twinning, exhibits the significant difference, with the basal poles distributed essentially uniformly along the perimeter in the basal pole figure.

CHAPTER 5 LOW-CYCLE FATIGUE BEHAVIOR AND THE ASSOCIATED PLASTIC DEFORMATION

The objectives of the current chapter are to investigate the low-cycle fatigue behavior and the associated cyclic plastic deformation characteristics with a focus on the extruded magnesium alloys, ZK60A. The analogous study was also conducted on the rolled magnesium alloy AZ31B, but only the differences observed are presented in detail. It has shown that the Coffin-Manson's and Basquin's relationships can be used to describe the fatigue resistance of the alloys quite well. The low-cycle fatigue properties are discussed in terms of plastic strain amplitude, cyclic stress response, and hysteresis loop.

The cyclic twinning and detwinning behavior and the concurrent internal-stress relaxation and load redistribution are presented and discussed. The activation sequence of twinning and detwinning during cyclic loadings, characterized by *in situ* neutron diffraction and *ex situ* synchrotron texture measurements, is responsible for the various shapes of the hysteresis loops.

5.1 Low-Cycle Fatigue Property

5.1.1 Low-cycle fatigue in the extruded ZK60A Mg alloy

Low-cycle fatigue behavior under the ED loading: The fatigue-life data of the as-extruded magnesium alloy, ZK60A, loaded along the ED direction, i.e., various strain amplitudes (elastic strain and plastic strain) *vs.* numbers of reversals to failure, are shown in Figure 5.1a. All symbols represent the experimental data taken from the half-life hysteresis loops, and the solid lines are the best linear fits obtained using linear regression analysis. In general, the relationships of the elastic strain amplitude and the plastic strain amplitude *vs.* the reversals to failure are linear, and the Basquin (Eq. 2.2) and Coffin-Manson (Eq. 2.3) laws can be, respectively, used to describe the relationships appropriately. The cyclic stress-strain curve is shown in Figure 5.1b. It is observed that the experimental cyclic stress-strain characteristics of the alloy when loaded along the ED direction can be basically depicted by a linear relationship on a log-log scale, following the Holloman relation (Eq. 2.5). Using the linear regression method, the coefficients and exponents in the Basquin, Coffin-Manson, and Holloman equations can be determined as listed in Table 5.1, while the fitted equations are also included in Figures 5.1a and 5.1b. Based on the Basquin and Coffin-Manson equations, the calculated curve relating the total strain amplitude to the fatigue resistance under the ED loading at room temperature is given by the dashed line in Figure 5.1a, which indicates that the low-cycle fatigue resistance can be predicted by the combined Basquin and Coffin-Manson equation (Eq. 2.4), and compare well with the experimental data.

The analysis of the stress-strain hysteresis loops can give us more insights into the cyclic deformation behavior. Figure 5.1c illustrates the stress-strain hysteresis loops at different strain amplitudes under the ED loading, which are also obtained at the half-life cycles. The pronounced asymmetric deformation behavior under tension and compression is observed at the moderate strain amplitudes. At the lowest strain amplitude of 0.4%, the asymmetry of the hysteresis loop is not so obvious, where it can be readily understood that the strain is accommodated mostly by the elastic deformation. As the total strain amplitude increases (from 0.6% to 2.0%), the asymmetry between tension and compression becomes more and more significant. The tensile peak stress is significantly higher than the compressive one, resulting in a tensile mean stress for these strain-controlled tests. This tension-compression asymmetry is attributed to the fundamental difference of deformation modes, where twinning dominates compressions, while detwinning is active under subsequent unloadings and tensile reloadings, followed by the harder dislocation slips. These mechanisms will be discussed in details below in Section 5.2.4, based on the lattice reorientation of the (00.2) basal planes from the *in situ* neutron scattering and the *ex situ* synchrotron texture evolution. If the total strain amplitude is imposed with a 3.0% total strain, the asymmetry of the hysteresis loop is, again, reduced with a less difference observed between the peak and valley stresses. At such a high strain amplitude (corresponding to a total compression of ~ 6.0% strain), most grains initially preferentially oriented are already twinned during the compression [44], i.e., the capability of twinning is almost exhausted before the maximal compression. The additional compressive strain accommodation demands the activation of harder deformation modes, such as non-basal slip or contraction twinning, leading to a great stress increase in compression.

The variation of the stress response with fatigue cycles (N_f) is an important feature of the low-cycle fatigue process. The cyclic stress response, which was determined by monitoring the stress response with increasing the cycle numbers, provides useful information pertaining to the cyclic stability of the material. The cyclic stress response at various strain amplitudes under the ED loading are shown in Figure 5.1d. It is noted that the cyclic stress response of the alloy is closely dependent on the imposed strain amplitudes. Generally, the alloy exhibits higher cyclic tensile and compressive stresses with increasing the total strain amplitude. At all tested strain amplitudes, the alloy shows a continuous cyclic compressive hardening behavior. This might be related to the gradually increased maximal twins in the material during cyclic deformation suggested by the *in situ* neutron scattering below. Nevertheless, the cyclic tensile stress response is more complicated. At the low total strain amplitudes of 0.4 % and 0.6 %, the alloy exhibits a continuous cyclic tensile strain hardening until a sharp stress drop before the final failure. For the moderate and high applied total strain amplitudes above 1.0 %, the tensile peak stress initially shows cyclic hardening, then cyclic softening until the final abrupt stress drop. This cyclic stress response will be further discussed in Section 5.2.5, based on the hysteresis-loop variation and the *in situ* neutron results.

Low-cycle fatigue behavior under the TD loading: Figure 5.2 represents the low-cycle fatigue behavior of the as-extruded magnesium alloy, ZK60A, loaded along the TD direction: a) ε–N fatigue-life curves, b) cyclic stress-strain curve, c) hysteresis loops at the half life for various total strain amplitudes, and d) cyclic tensile and compressive stress responses. Similarly, the relationships between the plastic amplitude, elastic amplitude and

reversals to failure in Figure 5.2a can be also well described by the best linear fits, and the best fitted lines are overlapped on the experimental data, respectively, indicated by different symbols. The calculated curve using Eq. 2.4, depicting the relationship between the total strain amplitude and the fatigue life, is given by the dashed line in Figure 5.2a. The result shows that the low-cycle fatigue lives under the TD loading can be predicted by the combined Basquin and Coffin-Manson equation, and agree well with the experimental data. The cyclic stress amplitude with respect to the plastic strain amplitude exhibits the linearity in Figure 5.2b, closely following the Holloman relation.

Figure 5.2c shows the hysteresis loops at the half-life cycle for various total strain amplitudes. The shapes of the hysteresis loops at all strain amplitudes are nearly symmetric and distinct from those in Figures 5.1c. Therefore, the different plastic deformation mechanisms must be involved in the cyclic deformation. This will be further discussed based on the *in situ* neutron diffraction and *ex situ* texture evolution below in Section 5.3.

Figure 5.2d represents the cyclic tensile and compressive peak stress responses at various total strain amplitudes. It is obvious that both the tensile stress and compressive stress increase continuously with cycling, regardless of the total strain amplitude. The hardening mainly results from the considerable increase in the twin volume fractions with cycling, as shown later. Certainly, the increased densities of dislocations also enhance the resistance to slip and twinning [73].

Low-cycle fatigue behavior under the ND loading: Figure 5.3 shows the low-cycle fatigue behavior under the ND loading analogous to that under the TD loading, suggesting that the overall behavior under the ND loading is similar to that under the TD loading,

although there are subtle distinctions. The overall similarity is expected and attributed to the symmetry of the near-fiber texture along the ED direction (Fig. 3.2a).

Comparison between the three loading directions: The discussions above have shown that the low-cycle fatigue properties can be well described and predicted by the Basquin, Coffin-Manson, and Holloman equations for all loading directions. Table 5.1 lists the fitted low-cycle fatigue parameters together with the uncertainties, respectively, for the three loading conditions, following the three mentioned relationships. Based on those data, the strain-fatigue properties can be explored related to the loading direction. It is noted that the fitted parameters under the ED loading are distinct from those under the TD and ND loadings, while only a subtle difference is observed with the those numbers between the TD and ND loadings. The ED loading shows the higher fatigue ductility coefficient ($\varepsilon_f^{'}$) and fatigue ductility exponent (*c*), and the fatigue strength coefficient ($\sigma_f^{'}$) is also higher. Therefore, the alloy loaded along the ED direction has a higher fatigue resistance compared to the others. This advantageous feature is visually manifested in Figure 5.4, where the ED loading condition has the best fatigue resistance at almost every total strain amplitude, while the TD and ND loadings show the similar fatigue lives. Furthermore, the significant deviations and low numbers in *goodness of fit* (e.g., low R^2) of the "all" fitted parameters from those respective fitted data of the three loading conditions corroborate that the low-cycle fatigue properties are different with respect to the loading direction. (Please note that the "all" parameters are fitted by linear regression analysis from the combined data with all loading directions.)

5.1.2 Low-cycle fatigue in the rolled AZ31B Mg alloy

In parallel, the strain-fatigue behavior for the rolled AZ31B Mg alloy was also studied. Figures 5.5 – 5.7 show the low-cycle fatigue behaviors loaded, respectively, along the RD, TD, and ND directions. The plastic strain amplitudes and elastic strain amplitudes *vs.* the numbers of reversals to failure follow, respectively, the Coffin-Manson and Basquin relationships. The calculated curves using Eq. 2.4, depicting the relationships between the total strain amplitude and the fatigue resistance are given by the dashed lines accordingly in the figures, and compare well with the experimental data. This again indicates that the low-cycle fatigue resistances in the rolled AZ31B Mg alloy can be also predicted by the combined Basquin and Coffin-Manson equation (e.g., Eq. 2.4). The relationships of the cyclic stress amplitude *vs.* the plastic strain amplitude obey the Holloman law (e.g., Eq. 2.5). Due to the in-plane texture symmetry, the RD and TD loadings exhibit the similar behaviors, which are comparable to the ED loading in the extruded ZK60A Mg alloy. However, the ND loading with the inverted hysteresis-loops exhibits a different behavior from both the RD loading and TD loadings, indicating different plastic deformation mechanisms, respectively, involved in the compression and tension. Compared to the Figure 5.1c, Figure 5.5c and Figure 5.6c, it is reasonably assumed that under the tensile cycles the alloy undergoes twinning, while detwinning dominates the subsequent unloadings and compressive reloadings. This assumption will be corroborated by the *ex situ* texture evolution measured using synchrotron diffraction below. In contrast to the tensile mean stress in the RD and TD loadings (see Figs. 5.5d and 5.6d), a compressive mean stress is obtained under the ND loading (see Fig. 5.7d). Figure 5.7d represents the

cyclic hardening behaviors under both tensile and compressive cycles. It is obvious that both the tensile and compressive stresses increase continuously with cycling, regardless of the total strain amplitude.

Table 5.2 lists the fitted low-cycle fatigue parameters together with the uncertainties, respectively, for the three loading conditions, following the three mentioned relationships. As manifested in Figure 5.8, the alloy under the RD loading exhibits the best low-cycle fatigue resistance, yet comparable to that under the TD loading. It is also noted that the fitted parameters under the ND loading are distinct from those under the RD and TD loadings. The ND loading has a much smaller fatigue ductility coefficient ($\varepsilon_f^{'}$) and fatigue ductility exponent (*c*), compared to both RD and TD loadings, while the fatigue strength coefficient ($\sigma_f^{'}$) and the fatigue strength exponent (*b*) are, respectively, almost twice those of the RD and TD loadings. Therefore, the alloy loaded along the ND direction has the lowest low-cycle fatigue resistance compared to the others, although, according to the common sense, a compressive mean stress under the ND loading would be beneficial to the fatigue performance. Furthermore, the alloy under the ND loading exhibits a higher cyclic stress hardening, compared to those under the RD and TD loadings, indicated by the fact that the fitted cyclic strength coefficient ($K^{'}$) and cyclic strain hardening exponent ($n^{'}$) are, respectively, nearly twice the numbers under the RD and TD loadings. This demonstrates that the current wrought Mg alloy exhibits the texture-dependent low-cycle fatigue properties, that is, the low-cycle fatigue behaviors are different in terms of the loading directions (i.e., with different initial crystallographic texture). As will be discussed later after the cyclic plastic deformation behavior, this seems due to the different cyclic plastic

deformation as a result of the grain preferential orientation, relative to the cyclic loading direction.

5.1.3 Comparison between the two Mg alloys and with other alloys

As discussed above, the low-cycle fatigue property under the ED loading is different from those under the TD and ND loadings in the ZK60A Mg alloy, while in the AZ31B Mg alloy, the low-cycle fatigue property under the ND loading is distinct from those under the RD and TD loadings. This demonstrates that the low-cycle fatigue behavior in the current two wrought Mg alloys is texture dependent. The discussions below with the neutron and synchrotron diffraction suggest that this is correlated to the distinctions in the associated plastic deformation behavior, respectively, under tension and compression, which is largely controlled by the initial texture.

Figure 5.9 shows the comparison of the fatigue resistances between the extruded ZK60A and the rolled AZ31B Mg alloys, respectively, loaded along the three directions. It is noted that these two wrought Mg alloys exhibit the comparable strain-controlled low-cycle fatigue properties, although the differences are noticed in terms of the strain direction in each alloy. Figure 5.10 represents the comparison of the low-cycle fatigue resistances in the current studied magnesium alloys with those reported by several researchers [57, 58, 66, 67, 72, 106], who independently worked on various wrought or cast magnesium alloys. All magnesium alloys included in the Figure 5.10 have shown the validity of the Coffin-Manson relationship. The current fatigue lives agree well with those

fatigue resistances in the wrought magnesium alloys obtained from the literature, and fall in the same band as indicated. It is observed that the extruded magnesium alloys show the better low-cycle fatigue resistances than the magnesium casts at high strain amplitudes, possibly due to the limited ductility in the magnesium casts because the fatigue lives at high strain amplitudes are mainly controlled by the plasticity.

The comparison is also extended to the aluminum alloys as shown in Figure 5.11, where the low-cycle fatigue resistances of the Mg alloys are compared with those of traditionally used structural Al alloys. The structural Al alloys considered include AA7XXX-type alloy, AA7175 and AA7150 alloys [107-110]. The data in Figure 5.11 emphasize that the Mg alloys generally possess the better low-cycle fatigue resistances at high strain amplitudes, the low-cycle fatigue resistances of the two categories of alloys are comparable at the intermediate strain amplitudes, and furthermore, the Al alloys show a tendency with a superior low-cycle fatigue resistance at the lower strain amplitudes.

5.1.4 Fractography

Figure 5.12 shows the typical fractography of the fatigued ZK60A alloy sample loaded along the ED direction with the total constant strain amplitude of 1.2% at room temperature. There exist a great number of parallel traces, and secondary cracks propagate in a transgranular mode along specific directions, which are presumably related to twin boundaries. The connection between fatigue cracking and deformation twinning is beyond the major focus of the current research. However, it might be further investigated by

sectioning through the fracture surface and performing electron backscattered diffraction, in conjunction with fractographic stereology, as has recently been applied to aluminum alloys [111]. During the cyclic deformation, there are presumably strong interactions between the slip and twinning [9, 38, 112]. This is particularly important because the newly-formed twins are in a plastically hard orientation with their basal poles parallel to the compressive straining direction [27]. Furthermore, the increasing volume fraction of residual twins with cycles may serve as barriers to the dislocation motion and *vice versa* [14, 56]. Such complicated deformation interactions may be important damage accumulation mechanisms that ultimately lead to the massive shear-band formation and crack initiation, once slip and twinning cannot accommodate the further plastic straining [9, 23].

5.2 Cyclic Plastic Deformation under the ED Loading

5.2.1 Strangely-shaped hysteresis loops

Figure 5.13a clearly shows that the hysteresis loops loaded along the extrusion direction are distinct from those loaded along the transverse direction (Fig. 5.13b) with a 1.2% total strain amplitude. In Figure 5.13b, the normal-shape loops are symmetric between the compression and tension cycles, which will be discussed in Section 5.3. In contrast, the hysteresis loops in Figure 5.13a are asymmetric with a sigmoidal shape characteristic of mechanical twinning [27].

Upon the initial compressive yielding at ~ 150 MPa, the sample shows little

hardening and the maximal compressive stress at – 1.2 % is ~ 170 MPa, characteristic of twinning in magnesium alloys. Upon reversal, a significant Bauschinger effect is observed, such that the material yields even before the stress becomes positive. The reverse yielding is much more gradual than the abrupt elasto-plastic transition observed during the initial compression. During the reversal, at ~ 0 % strain the loop shows an inflection, and beyond this point, the hardening rate rapidly increases. It will be shown below that this increase in the hardening rate correlates with the exhaustion of the detwinning mechanism. Once the grains are completely detwinned, the resulting orientation is hard with respect to tensile deformation by basal slip. This demands activation of the harder non-basal dislocation slip [4] or $\{10\bar{1}1\}<10\bar{1}\bar{2}>$ compression twinning mechanisms [14, 41]. Thus, a high maximal tensile stress of ~ 310 MPa is reached.

On the unloading from + 1.2 % strain, the deviation from linear elastic unloading occurs roughly at a stress of – 100 MPa and a strain of + 0.2 %. Because the yielding during the second compression cycle starts early, more compressive plastic strain is induced prior to reversing a second time. Interestingly, the maximal compressive stress during the second compressive cycle is similar to the first, and this is an additional testimony to the very low hardening rate which accompanies twinning dominated deformation in Mg alloys. Furthermore, it suggests that more twinning occurs during the second cycle than the first, and the *in situ* neutron diffraction data discussed below corroborates this conclusion.

The maximal tensile stress during the second cycle is comparable to that of the first as well; however, the inflection of the tensile curve appears later, at a strain of ~ 0.5 %. Again, if it is understood that more twinning takes place during the second compressive

cycle, and more strain is required to detwin the material during the second tensile cycle than during the first. The *in situ* diffraction data enable us to make firm conclusions regarding these points. The subsequent hysteresis loops closely follow the shape of the second cycle. Nevertheless, in the compressive quarter cycles, the material showed an ever increasing hardening during the later cycles (For example, see the hysteresis loop of the cycle 200 in Fig. 5.13a), in addition, the maximal compressive and tensile stresses developed distinctly with increasing cycles (Fig. 5.1), which will be discussed in Subsection 5.2.5.

5.2.2 Pseudo-elasticity due to detwinning

In the most general sense, any non-linearity in the unloading curve can be referred to as pseudo-elasticity. Upon reloading, the non-linearity leads to a hysteresis loop. Such a pseudo-elastic response is an important mechanical feature of some engineering materials such as magnesium alloys. For example, engineering design of components made of such materials using a constant value of elastic modulus may lead to problems. The materials show enhanced damping due to the inherent hysteresis in elasticity. The fatigue property, as well as the energy absorption characteristics, might also be affected. If the pseudo-elastic effect is large, conventional formulae relating stress and strain may become invalid, and the use of finite element method may be required.

Pseudo-elasticity has been related to various mechanisms: i) reversible movement of dislocations generated in the forward deformation [113-115], ii) detwinning within the

twinned materials [75, 76, 116], and iii) stress induced thermo-elastic martensitic transformations [117-120]. Detwinning induced pseudo-elasticity is caused by the reversible movement of twin boundaries [116, 121]. The position of the twins in the deformed state is not stable, a driving force causes them to return back upon unloading, and concomitantly, the plastic deformation is partially recovered. Caceres et al. [75] and Mann et al. [76] attributed this phenomenon in magnesium alloys to the partial reversal of $\{10\bar{1}2\}<10\bar{1}1>$ extension twins upon unloading. They drew the conclusion from *in situ* optical observation of moving twins during cyclic loading-unloading of the AZ91 magnesium cast. Zhou et al. explained the hysteresis effect in hcp metals at small plastic strains based on their theory of formation of fully reversible dislocation-based "incipient kink bands" [122]. Recently, Muransky et al. demonstrated that the observed pseudoelastic-like behavior of AZ31 in compression is due to the activation of twinning-detwinning processes in the polycrystal during loading-unloading cycle. Furthermore, they proposed that the detwinning event upon unloading is driven by the peculiar internal redistribution of stresses [123].

As mentioned earlier, the fact that the material deviates from the linear stress-strain curve almost immediately upon unloading (i.e., no tensile reloading is required) results in a Bauschinger-type non-linear unloading curve (Fig. 5.13c). The *in situ* neutron diffraction below suggests that this is due to the detwinning in the twinned grains, leading to some plastic dissipation. In this way, the extension twinning in magnesium is demonstrated to be a pseudo-elastic phenomenon [75, 124], not unlike the stress-induced martensite formation observed in some shape-memory alloys [118, 125, 126]. However, the recoverable (or

pseudoelastic) strain, ~ 0.13%, is quite small in the current case (indicated in Fig. 5.13c). In contrast, the linear unloading curve from tension is due to the elastic deformation. This asymmetry between the compressive unloading and the tensile unloading in the hysteresis loop does not appear to be related to the fact that the total macroscopic strain imposed during tensile loading is more than the one imposed during the initial compression.

5.2.3 *In situ* neutron diffraction patterns

Figure 5.14 represents the diffraction patterns collected from the ED and ND directions at various points indicated in Figure 5.13c, along the hysteresis loop during the first deformation cycle, when the sample is loaded along the ED direction at a total strain amplitude of 1.2%. From the bottom to the top, the diffraction patterns correspond to a) 0% (initial state), b) – 0.8% strain, c) – 1.2% strain, d) 0 MPa stress, e) – 0.4% strain, f) 0% strain, g) + 1.2% strain, and h) 0 MPa stress.

Due to the strong texture, the initial diffraction peak reflected from the (00.2) basal planes is absent in the ED, while it is strong in the ND. The diffraction peak of the (10.0) prismatic planes is very weak in the ND, while it is quite strong in the ED, in the initial load-free diffraction patterns (please refer to the patterns ‘a’ at the bottom in Figure 5.14). The pyramidal (10.1) peaks are present in both directions. The initial diffraction spectra are consistent with the pole figures shown previously (Please see Fig. 3.2a), which were measured by conventional X-ray diffraction. It is observed that as deformation proceeds, the peak intensity changes and peak shifts are significant. For example, the intensity of the

(00.2) peak in the ED direction is increasing gradually with compression undergoing, and it continues to decrease until the background intensity during the reversed loading. The peak position of the same (00.2) peak is shifting to the left during the initial compression, and then it is shifting back to the right gradually during the reversal.

It is worthwhile to emphasize that the *in situ* neutron diffraction patterns reveal a number of different aspects related to the evolutions of the microstructure and stress state in the sample. In the subsection 5.2.4 below, the cyclic twinning-detwinning behavior is presented and discussed with relation to the intensity changes of the diffraction peaks and the corresponding strangely-shaped hysteresis loops. The cyclic stress variation is explained based on the cyclic twinning and detwinning behavior in the subsection 5.2.5. In the subsection 5.2.6, the internal-strain (stress) evolutions derived from the peak shifts are examined in details. Thereafter, in the subsection 5.2.7, the activation stresses for twinning and detwinning events are approximated, based on the relaxation of the internal-stresses in the matrix and twin grains, respectively. Finally, the peak broadening is discussed in terms of intergranular and intragranular stresses (in the subsection 5.2.8).

5.2.4 Cyclic twinning and detwinning

As stated in the experimental chapter of this dissertation, complete diffraction spectra were collected using the time-of-flight technique in detector banks located at + 90º and – 90º from the incident beam. Due to the 45º orientation of the sample stress axis, these detector banks collect information from grains with their diffracting plane normal vectors oriented *parallel* and *transverse* to the stress axis, respectively. In the current loading

condition, the sample was carefully aligned with the loading axis parallel to the ED, while the ND is transverse to the same loading axis in the diffraction plane. As mentioned, the diffraction data reveal a number of different aspects related to structure and stress state of the material. For example, the lattice spacings derived from Braggs law can be used to determine the state of internal lattice strain (and stress *via* Hooke's law) [10]. The appearance or disappearance of peaks can signify a phase transformation or, in the present case, mechanical twinning. Due to the ~ 90º reorientation of the basal poles which occurs with $\{10\bar{1}2\}<10\bar{1}1>$ twinning and the initial texture, the changes in the basal (00.2) peak intensities in the parallel (i.e., the ED direction) and transverse detector banks (i.e., the ND direction) can be directly related to the degree of twinning that has occurred. This fact was exploited to advantage in the previous *in situ* studies of twinning in Mg alloys [25, 27].

Figure 5.15 shows the normalized diffraction intensity evolutions of the basal (00.2) peak during the cyclic deformation along the ED direction, corresponding to the hysteresis loops presented in Figure 5.13a. The intensity data is plotted as a function of the 'run number' (which was used for the experimental bookkeeping to identify the diffraction data), and the actual cycle number is also indicated in the plot. The initially high basal (00.2) peak intensity in the ND direction is indicative of the large volume fraction of 'parent' grains, which are favorably oriented for twinning during the compression cycle, and can be correlated with the high intensity in the basal (00.2) pole figure parallel to the ND of the initial texture (Fig. 3.2a). The initially low intensity in the ED direction correlates with the initially low intensity in the (00.2) basal pole figure along the ED (Fig. 3.2a). An increase in the (00.2) peak intensity within the ED direction indicates an increase

in the volume fraction of twins and may be correlated with a concurrent decrease in the corresponding intensity diffracting from the parent grains in the ND direction. An intensity decrease in the ED direction is, in the present set of experiments, correlated with detwinning events (or the shrinking of twins and reversion to the parent orientation).

A detailed view of the intensity evolution is provided for the first few cycles in Figure 5.16. At the initial compression, the intensity of the basal (00.2) poles keeps unchanged because the deformation is elastic, and the initial microstructure of ZK60A with T5 temper is free of twins (Fig. 5.17a). Upon yielding, at a strain of ~ – 0.2% (Fig. 5.13a), the intensity begins to gradually increase, which indicates that twinning is activated, and lots of twin bands are observed in some favorably oriented grains at the strain of – 1.2 % (Fig. 5.17b). As mentioned, the previous *in situ* diffraction experiments focused on the monotonic deformation have shown that as much as 80 % of the volume fraction of favorably oriented grains can undergo twinning during the first 8 % strain [10, 37]. There is a direct relationship between the volume fraction of twins, f^t, the characteristic twinning shear, γ^t (for extension twins in Mg alloys, $\gamma^t = 0.130$ [11]), the Schmid factor of the twin variant and grain orientation, $m^{g,t}$, and the macroscopic strain, ε^t, accommodated by twinning:

$$\varepsilon^t = f^t m^{g,t} \gamma^t \quad . \tag{5.1}$$

In the present case, the Schmid factor for twinning in the parent grains with basal poles parallel to ND or TD can be approximated as ~ 0.5. Determining the volume fraction of twins from the increase in the (00.2) intensity within the ED direction confirms that the plastic deformation during the compression stroke is dominated by twinning. Because

twinning is dominating the strain accommodation, and the overall strain hardening rate is low, it can be inferred that massive twinning leads to a low strain-hardening rate (Fig. 5.13a) [23].

The stress-strain response departs from linear elastic compressive unloading almost immediately (Fig. 5.13a), indicating the activity of some plastic dissipation. Correspondingly, as soon as the straining is reversed, the (00.2) intensity begins decreasing. This indicates that detwinning requires much lower absolute stresses to occur in the ZK60A alloy relative to the stress required to activate the twins themselves. This places the present results in agreement with previous twinning-detwinning observations of alloy AZ31B [27, 47]. In fact, the detwinning begins so quickly that it is suggested that the twins and parents must contain significant internal-stresses that drive the detwinning event. This hypothesis has been confirmed by the collected *in situ* lattice strain data, and will be discussed in details in the subsection 5.2.6.

The (00.2) intensity in the ED direction, indicative of the twin volume fraction, continued to decrease all the way back to the background intensity until the plastic compressive strain is recovered at 0 %. As suggested in the discussion of the hysteresis loops above, this result confirms that the twin grains formed during the compressive deformation are almost entirely removed by detwinning, which is corroborated by the observed disappearance of twins at the maximal tensile strain of + 1.2% in Figure 5.17c. Again, this trend explains why the stress-strain curve becomes concave up at 0% (Fig. 5.13a), and beyond this point, the deformation is accommodated by the harder deformation mechanisms within the parent grains, such as prismatic <a> and pyramidal <c+a>

dislocation slips [30] along with possible $\{10\bar{1}1\}<10\bar{1}\bar{2}>$ compression twinning [14, 41]. These mechanisms result in a higher strain hardening rate up to the maximal tensile stress (Fig. 5.13a), but they do not result in a rapid texture evolution. Thus, the (00.2) peak intensities remain unchanged during this portion of the hysteresis loop (compare Figs. 5.13a and 5.16).

During the unloading from the maximal tensile strain, the (00.2) pole intensity is equal to the background intensity through the zero stress until the plastic deformation begins again during the second compression stroke at a strain of + 0.5%, at which point the intensity curve increases once again (Fig. 5.16). Actually, the plastic straining begins at + 0.2% (Fig. 5.13a), however, we did not collect *in situ* diffraction data at this point. Because the second compressive straining induces more plastic strains than that introduced in the first cycle (Fig. 5.13a), a large volume fraction of twins are formed and, consequently, the maximal intensity is higher at the end of the second compressive cycle than that of the first cycle.

During the second tensile reversal, the inflection point in the hysteresis loop appears at ~ + 0.5%, which is considerably larger than the strain required to reach the inflection point during the first tensile reversal, but is comparable to the starting point of the second compression (Fig. 5.13a). Because a larger volume fraction of twins are available to be detwinned, and concurrently, more tensile strain can be accommodated by detwinning. Notably, the strain accommodated by detwinning is the same as that of twinning, only opposite in sign (see Equation 5.1). This hypothesis is confirmed by the fact that the (00.2) peak intensity in the ED direction does not return close to the background level at 0% strain

as in the first cycle. Unfortunately, diffraction data was not collected at levels intermediate to + 0% and + 1.2% to confirm the exact strain level at which the detwinning mechanism is exhausted, however, it can be inferred to be ~ 0.5%, based on the hysteresis-loop shapes of the first and second cycles (Fig. 5.13a).

Figure 5.18 represents the measured crystallographic texture evolution along the hysteresis loop during the first cycle deformation of the ZK60A alloy with the loading axis parallel to the ED direction using *ex situ* synchrotron diffraction: a) strain-free, b) – 3.0 % strain, c) 0 MPa stress, d) 0 % strain, e) + 3.0 % strain, and f) 0 % strain. The strain-free texture (Fig. 5.18a) shows that most grains are initially oriented with their c-axes aligned perpendicular to the ED direction. Therefore, most grains are favorably oriented for extension twinning if the sample is compressed along the ED direction. When the sample is compressed to a strain of – 3.0%, a large volume fraction of grains are observed to be reoriented by ~ 90^{o}, and a new texture component is observed with the basal poles aligned with the ED direction as shown in Figure 5.18b. The compressive unloading doesn't result in a significant texture change (Fig. 5.18c). Once the sample is reloaded to the point 'd' (Fig. 5.18d), the texture is almost completely reversed, which is a signature of detwinning event. Beyond this point, the texture at the point 'e' is intensified due to the dislocation slips (Fig. 5.18e). When the sample is compressed for the second time, the resulting texture (Fig. 5.18f) is again characteristic of twinning reorientation with the appearance of the ED texture component. The overall trend in the texture evolution agrees well with the intensity evolution of the basal pole (Fig. 5.16) obtained using *in situ* neutron diffraction.

In summary, the intensity evolutions of (00.2) basal poles observed *via in situ*

neutron diffraction (see Figs. 5.15 and 5.16) and the crystallographic texture evolution (see Fig. 5.18) measured using *ex situ* synchrotron diffraction can be correlated with the cyclic activation of the $\{10\bar{1}2\}<10\bar{1}1>$ twinning under compression and detwinning mechanism during unloading and tensile reloading, and the post-detwinning activation of the harder dislocation slips in this material. These data may be used to explain the strangely-shaped hysteresis loops (Fig. 5.13a), as a result of the different deformation mechanisms under tension and compression when the sample is loaded along the ED direction.

5.2.5 Cyclic-stress variation

Figure 5.19 is the cyclic stress response curves of the ZK60A alloy loaded along the ED direction at the total strain amplitude of 1.2%, showing the variation of tensile and compressive stresses with the fatigue cycles. The variation of the stress response with the number of fatigue cycles is an important behavior of the low-cycle fatigue process. Such cyclic-stress response mainly depends on the mechanical and/or cyclic stability of the intrinsic microstructural features, particularly as a result of the competitive processes between the hardening from the multiplication of dislocations [57] and the twin boundaries as barriers to dislocation slip [112], and the softening due to the annihilation and rearrangement of dislocations [57, 127, 128]. The peak compressive stress exhibits continuous cyclic hardening until the final fracture. The neutron diffraction data suggest that this is due to an increasing volume fraction of twins which form during the cycling (Fig. 5.15). On the other hand, the material exhibits a tensile hardening during the initial 10

cycles, and then, the cyclic tensile softening dominates till a final abrupt stress drops. The overall shape of the hysteresis loops and the neutron diffraction data again provide an explanation for this more complicated observation.

The cyclic hardening and softening behavior can also be explained by the variations in the loop shapes, when considered in light of the corresponding *in situ* neutron diffraction data. The continuously increasing basal (00.2) peak intensity in the ED direction and the corresponding decreasing of the (00.2) peak intensity in the ND direction, at the point of maximal compressive strain, indicate the presence of an ever increasing volume fraction of twins (Fig. 5.15). This coincides with the compressive hardening of the material with increasing the number of cycles (Fig. 5.19). Similarly, the inflection point on the tensile side of the hysteresis loops is delayed to an increasing strain level (Fig. 5.13a), and thus the exhaustion of detwinning keeps being delayed to higher strain levels. The strain at which the hysteresis loop inflects is important because it is only beyond this point that the strain hardening rapidly increases and the cyclic softening observed on the tensile side of the hysteresis loops at the later cycles (Fig 5.19) is most probably related to the decreasing amount of the post-detwinning dislocation-based flow in the parent grains. From approximately 25 cycles onwards, the basal (00.2) peak intensity in the ED direction never returns to the background level (Fig. 5.15) and this suggests that there is a residual twin content that remains throughout the entire cycle. With increasing the number of cycles, the volume fraction of residual twins increases (Fig. 5.15), resulting in an ever increasing hardening rate observed in the compressive quarter cycles of the hysteresis loops (Fig. 5.13a). It is suggested that an increasing amount of dislocation debris within the material makes twinning-detwinning more difficult with cycling, which could simultaneously

explain both the cyclic hardening on the compression side and cyclic softening on the tensile side of the hysteresis loops.

5.2.6 Internal-strain/stress development

It is worth emphasizing that each line in the plot of applied stress vs. lattice strain represents the response of a family of grains oriented such that the plane normal to the given (*hk.l*) lattice plane is parallel to the scattering vector. Figure 5.20 shows the hysteresis loops (applied stress vs. internal-strain) for the four reflecting planes in the longitudinal direction during the first cycle of deformation of ZK60A alloy loaded along the ED direction. Different loop areas are observed for the various grain orientations, indicating different Bauschinger-type effects. The (10.0) grain orientation in the parallel direction (e.g., the ED direction) has a much smaller Bauschinger effect as compared to the (10.1) grain orientation. This difference may be explained in terms of the grain orientation and Schmid factor for the basal slip, e.g., a soft grain orientation has a larger Bauschinger effect, while the effect is smaller for hard orientations.

The following detailed discussion is based on Figure 5.21 which shows internal-strain evolutions during the first deformation cycle in the ZK60A sample loaded along the ED direction with the strain amplitude of 1.2%, respectively, for a) initial compressive loading, b) compressive unloading and tensile reloading, and c) tensile unloading (please also see Fig. 5.13c). Also included are the intensity evolutions of the basal poles in the ED direction, related to the degree of twinning and detwinning. The

sample initially undergoes compressive elastic deformation and the internal-strains (with a compressive sign) increase linearly with the macroscopic applied stress at nearly same slopes for all grain orientations (Fig. 5.21a), owing to the near elastic isotropy of Mg. The slopes in the ND direction are much steeper than those in the ED direction as a result of Poisson effect and the lack of external boundary constraint [129]. The basal planes of the (10.1) grain orientations in the ED direction are inclined at a degree of 28^{o} to the loading axis yielding a Schmid factor of ~ 0.305 for basal slip. Thus, this subset of grains is favorably oriented for basal <a> slip (e.g., in a soft orientation) relative to their neighbors. They yield first, and smaller elastic strains are observed in the yielded grains, so that the corresponding curve diverges from the linear response with an increasing slope. A similar transition occurs for the (10.1) grain orientation in the ND direction. It can be deduced that the other subset of grains, in hard orientations, must share a larger portion of load and their associated slopes decrease. This behavior can be understood largely in terms of the elastic load transfer between soft and hard grain orientations behaving like a composite material [32]. However, the volume fraction of (10.1) grains is small in this strongly textured material. Thus, their effect on the overall behavior is small. This trend agrees well with the reports by Agnew, Brown and Clausen [10, 30, 37, 41] for the extruded magnesium alloy, AZ31B, under the monotonic compressive loading. When the sample starts to macroscopically plastically deform by twinning at the stress of ~ – 150 MPa, the (00.2) peak in the ED appears (Fig. 5.21a), and thereafter the lattice strain in the twins can be calculated accordingly.

Once the twinning is activated, the (00.2) parent grains (please refer to the ND

direction in Fig. 5.21a) are relaxed relative to the stress field in the surrounding grains. Therefore, the (10.0) and (11.0) parent grains (Fig. 5.21a, in the ED direction) share more stress, and their slopes of the internal-strain curves decrease. The newly-formed daughter grains (please refer to the (00.2) reflection in the ED in Fig. 5.21a) have a much smaller stress than other grains. However, the twins are in a plastically hard orientation with respect to basal slip. Therefore, the stress within the twins accumulates very quickly.

During the unloading from the maximal compressive stress, the lattice strains in all observed grain orientations (hk.l) change at the same pace (another expression of elastic isotropy and evidence that little plastic unloading occurs.) However, the internal-stress state in the daughter grains along the parallel direction (please refer to the (00.2) reflection in the ED direction in Fig. 5.21b) changes its sign at ~ – 80 MPa. Beyond this point, the (00.2) daughter grains are, thus, placed in a tensile stress field along their c-axis, which is effective in driving the detwinning event, as manifested by the initiation of the basal intensity drop in the right plot of Figure 5.21b. At zero applied stress, the (00.2) daughter grains are in a much greater tensile stress field along their c-axes, compared to the other grain orientations (Fig. 5.21b, in the ED direction). In fact, it is a sufficient level of stress to initiate detwinning. Detwinning is a mechanism of plastic deformation, so this is an example of a classical Bauschinger effect in that plastic deformation occurs at a lower absolute stress during reloading than it did during the initial monotonic loading. In this case, intergranular stresses that arise due to plastic anisotropy appear to assist the Bauschinger effect. It was suggested earlier that the twins and parents must contain significant internal-stresses that drive the detwinning event to occur immediately upon *unloading* (i.e.,

it does not require reverse *loading*). The measured internal-strains (stresses) in Figure 5.21 have confirmed this hypothesis.

When the sample is reloading in tension, the detwinning dominates the plastic deformation until the twins appear to be completely removed at an applied stress of ~ 100 MPa (Fig. 5.13a). Once the sample is completely detwinned, the resulting orientation is again hard with respect to tensile deformation by the basal slip. This demands the activation of the harder non-basal dislocation slip [4] or $\{10\bar{1}1\} < 10\bar{1}\bar{2} >$ compressive twinning mechanisms [14, 25, 41]. However, the grains in a soft orientation, such as (10.1) grains in the parallel direction again micro-yield, and their corresponding curve departs from linearity (Fig. 5.21b), and these grains stop to accept more internal-stresses, while other subsets of grains are continuing to take more internal-stresses.

Although we already have a detailed discussion of the internal-strain evolution above based on Figure 5.21, the correlation between the internal-strains and the twinning-detwinning behaviors can be more clearly observed in Figure 5.22, which shows the internal-strain evolution in both ED and ND directions as a function of the macroscopic strain for the first few cycles. Also included is a curve of the (00.2) pole intensity evolution, which provides a measure of the volume fraction of twinning and detwinning . Once twinning is activated and twin grains appear, the internal-stresses both in the ED (longitudinal) and ND (transverse) directions are relaxed, and, subsequently, increase more slowly with the macroscopic strain. The internal-strain accumulation in the (00.2) parent grains (please refer to the ND direction) especially decrease due to the significant stress relaxation. When the twinned grains are exhausted at the strain of ~ 0%, the plastic

deformation continues through the activation of the harder prismatic or pyramidal dislocation slips, the internal-stresses in both directions accumulate more quickly. However, as discussed above, because the (10.1) grains are oriented favorably for the basal slip, the internal-strain in those grains rise more slowly compared to the other grain orientations. The twinning and detwinning behavior clearly play a significant role in the cyclic deformation of this material, and these mechanisms are, in turn, significantly affected by the generation and relaxation of internal-strains (stresses). The cyclic evolution of the internal lattice strains is shown in Figure 5.23, which is an extension of Figure 5.22 to include more cycles. The lattice strains for the four grain orientations are plotted as a function of the 'run number', which is used for experimental bookkeeping to identify the diffraction data. We can conclude that the internal-strain development in the following cycles closely follows the evolution during the first cycle deformation. Nevertheless, the amplitude of the internal-strains (stresses) are gradually escalating with increasing the cycle number (Fig. 5.23). The rise in internal-strain with cycles is a form of cyclic hardening due to exhaustion of the twinning-detwinning mechanism.

As mentioned, the detwinning event almost immediately occurs when the sample is unloaded from the maximal compressive stress. Upon unloading, the sample is still in a compressive stress field, and the stress axis is parallel to the c-axis of the twinned grains. Considering the orientation of the twinned grains, it looks that they cannot be detwinned. Nevertheless, the observed local tensile stress (Fig. 5. 21b) is hypothesized to provide the necessary driving force for the detwinning event. Very recently, Muransky et al. [123] use the schematic illustrated in Figure 5.24 to explain the load redistribution and the local

tensile stress development. It shows three neighboring grains deforming elastically (A → B) and plastically (B→ C) in compression. The plastic deformation is accommodated by slip and twinning, though the twinning occurs only in the middle of the parent grain (PG2). The stress in the parent (PG2) and twinned (TG) lattice (twin grain) is equally by definition and relaxed with respect to the neighboring grains when the twinning event occurs at the peak stress at point C. Upon unloading (C → D), the elastic strain is recovered but the twinning strain in the middle grain is not. As a result, the middle grain may temporarily sustain the opposite tensile stress, even if the macroscopic stress is still compressive. Considering the orientation of the twinned grain, it becomes clear that the local tensile stress must stretch the crystallographic c-axis of the twinned grain. This could provide the necessary driving forces for the re-activation of the extension twinning in the already twinned grains.

In summary, the internal-strain (stress) evolutions in the different grain orientations observed *via in situ* neutron diffraction measurements can be understood in terms of load transfer among those grain orientations, where the twinning and detwinning behaviors play an important role. Due to the stress redistribution between different grain orientations, a local tensile stress is developed in the twinned grains and provides the apparent absent driving forces for the detwinning event.

5.2.7 Approximation of the activation stresses

As mentioned in Chapter 1, deformation twinning, like dislocation slip, is primarily controlled by the resolved shear stress on the twin plane and in the twinning direction [130], thus, a Schmid law is assumed and given by:

$$\tau_{CRSS} = \sigma_c \cos\lambda \cos\chi \tag{5.2}$$

where λ and χ are the angles between the loading axis and the twin plane normal and twin direction, respectively, σ_c and τ_{CRSS} are the critical applied stress and the critical resolved shear stress (CRSS). The uniaxial form of the Schmid law listed above schematically represents the full tensorial relationship, where the tensorial stress applied at the grain-level is resolved in a similar way using the Schmid tensor (the dyadic cross product of the twin plane normal and twin shear direction.) For simplicity of presentation, we have assumed that the stress state at the grain-level is uniaxial. However, it is recognized that the local stresses depart from those applied to the aggregate.

As stated above, the internal-stress in the (00.2) parent grains in the ND direction (Fig. 5.21a) linearly increases during the initial compression until the extension twinning is activated, at which point the internal-stress in the (00.2) parent grains is relaxed (please also see Fig. 5.22, in the ED direction). Thus, a maximal internal-stress observed within the (00.2) parent grains (please see Fig. 5.21a, in the ND direction) can be reasonably employed for the calculation of the activation stress for extension twinning. In the current measurement, the maximal internal-strain of the parent (00.2) grains is 770 με, which suggests a stress of 37 MPa *via* the uniaxial Hooke's Law, given the (00.2) specific elastic

modulus of 48 GPa [10] for magnesium. The activation stress is, thus, the resolved shear stress, 15 MPa, along the twinning direction $<10\bar{1}1>$ in the twinning plane $\{10\bar{1}2\}$ with a Schmid factor of ~ 0.40. This activation stress agrees well with the number of 15 MPa employed by Agnew [14] for the visco-plastic self-consistent (VPSC) simulation of an AZ31B magnesium alloy, while in the elasto-plastic self-consistent (EPSC) model, initial values of 30 MPa and 54 MPa are assumed, respectively, by Agnew et al. [30] and Clausen et al. [37] for the same alloy with different models to account for the effects of twinning.

The stress-strain response departs from the linear elasticity almost immediately, indicating the onset of detwinning even at a strain of – 1.0% (please see the Fig. 5.16). However, when the sample is further unloaded to a strain of – 0.8 %, the rate of detwinning increases. This point is further evidenced in Figure 5.22, the internal-strain curve for the (00.2) twin grain orientation between – 1.0 and – 0.8 % strains (please refer to the ED direction) has a lower slope than that between – 1.2 % and – 1.0 % strains. This indicates that the (00.2) twin grains are relaxing more quickly due to a higher detwinning rate. Consequently, the internal-stress in the twin grains at a strain of – 0.9 %, 15 MPa (e.g., an internal-strain of 310 με) can be again resolved to a shear stress, 6 MPa, along the twinning direction $<10\bar{1}1>$ in the twinning plane $\{10\bar{1}2\}$, roughly as the activation stress for detwinning event, which is lower than that of twinning. This result agrees qualitatively with the observations in the alloy, AZ31B [27, 47]. The difference between the activation stresses of twinning and detwinning events is 9 MPa, which places the present directly measured result in quantitative agreement with the number derived theoretically by Lou et al. [47].

5.2.8 Peak broadening

In addition to changes in peak intensity and peak position, the neutron diffraction data also manifest that there are changes in peak width. Figure 5.25 shows the broadening of the (00.2), (10.1), and (11.0) reflections, respectively, for the ED and ND direction, as a function of run number. In the both directions, the (00.2) grain orientation has the largest overall peak broadening, while the (11.0) grain orientation has the smallest overall peak broadening. In the present study, the most significant contributing factors to the peak broadening are i) grain-to-grain variations in the intergranular stresses (the focus of this paper) and ii) intragranular stresses due to dislocations [10, 131]. Because of the dominated twinning deformation, many dislocations are present in the (00.2) grain orientation due to accommodation requirements during twinning, and this lead to the largest peak broadening. This statement is further corroborated by the fact that the (00.2) peak broadening is cyclically developing with the twinning and detwinning alternately active (Fig. 5.25). The (10.1) grains in both detector banks are in a soft orientation with respect to the activation of basal slip system. Hence, there are more basal dislocations in these grains than other grains in a hard orientation, such as the (11.0) grain orientation, which has a smallest peak broadening. Finally, the overall peak broadening is gradually increasing with the cycling continues, which indicates an accumulation of residual twins and/or dislocations. Actually, a small volume fraction of residual twins (twins which fail to detwin completely) was detected, and gradually increases with increasing cycles (please refer to Fig. 5.15). Furthermore, it is that the mutual interactions between the twin boundaries and dislocation slips are related to the applied cyclic stress reported previously (please see Fig. 5.19), and,

correspondingly, the amplitude of the internal-strains (stresses) (Fig. 5.23).

5.3 Cyclic Plastic Deformation under the TD Loadings

5.3.1 Cyclic twinning and detwinning behaviors

Figures 5.26 and 5.27 show the hysteresis loops in the ZK60A alloy loaded along the TD direction at the total strain amplitude of 3.0%, respectively, with the compression and tension as the first deformation stroke. The hysteresis loops are nearly symmetric between compression and tension cycles, distinct from those under the ED loading with a sigmoidal asymmetric shape. The stress-strain curves deviate from the linearity almost immediately upon unloading from the maximal compressive or tensile stresses, indicating the dissipation of some plasticity during the unloadings. Both loading conditions result in the similar fatigue lives, 48 and 50 cycles, respectively, for the compression and tension first.

As shown in Figure 3.2a (Lab x-ray texture) or Figure 5.30a (Synchrotron texture), two texture components can be defined in the initial (00.2) pole figure of the as-extruded ZK60A alloy: i) the first one with the basal poles parallel to the plate normal (ND component), and ii) the second one with the c-axes aligned with the transverse direction (TD component). Based on the knowledge we have learned above from the cyclic deformation along the ED direction, combined with the initial texture, we may propose the following plastic deformation behaviors, when the alloy is loaded along the TD direction. A tensile loading results in the c-axis extension of the grains within the TD texture component, and, thus, they will twin under tension, while the ND texture component is

readily oriented for twinning under compression. If the first deformation stroke is compression, the grains within the ND component with their c-axes perpendicular to the compressive loading axis will undergo extension twinning, resulting that their basal poles rotate towards to the TD component. The parent grains within the TD component, initially unfavorably oriented for twinning, will have to deform only by dislocation slips. The new TD component, which has accumulated within the initial TD component, is now unfavorable for extension twinning in compression, but favorable for twinning activation in tension. Therefore, during the subsequent compressive unloading and/or tensile reloading, the newly formed twins (from the prior compression) will detwin and return back to the original orientation. The parent grains within the TD component that have not yet undergone twinning will twin, because their original orientation supports extension along the c-axes. In the other hand, if the first deformation stroke is tension, those grains corresponding to the TD component are favorable for extension twinning because their c-axes are parallel to the load axis, and will be reoriented according to the six equivalent twin variants and the new texture components appear as discussed in Chapter 4. However, only very little twins grains could be reoriented towards to the ND direction. During the subsequent unloading and/or compressive reloading, the twinned grains formed from the prior tension are expected to be detwinned and return to the original TD component. The parent grains within the ND component is ready to undergo twinning, thus, their c-axes will be aligned with the TD direction. With the cyclic loading continuing, the deformation in the later cycles will follow the first cycle deformation, similarly as we have observed from the ED cyclic loading.

The proposed behaviors above have actually been detected by the *in situ* neutron

data below. Figures 5.28 shows the normalized-intensity evolutions of the basal poles in the TD and ND directions, for the ZK60A alloy loaded along the TD direction at the total strain amplitude of 3.0% with compression as the first deformation stroke. It is noted that in the current experimental configuration, the detector bank 1 (transverse detector) recorded the diffraction patterns from the ND direction, and the detector bank 2 (parallel detector) collected those diffracted from the TD direction. As the sample is firstly compressed along the TD direction, the basal intensity in the TD direction continues to increase as expected due to the activation of extension twinning, with the complementary decreasing in the ND direction. When the sample is unloaded to a strain of – 2.5%, the measured basal intensity is decreased, though the corresponding macroscopic is still in a compressive stress field. Nevertheless, it is observed the decreasing rate of the basal intensity is at a low rate before the macroscopic stress becomes positive. When the sample is reloaded in tension, the basal intensity in the TD direction continues to decrease until the maximal strain at + 3.0%, indicating detwinning and/or twinning activations. At 0% strain, the basal intensity in the ND direction with a relative intensity of ~ 0.91 is lower than the original one (the relative intensity is 1), suggesting that the detwinning is not complete. This is not consistent with the observed phenomena in the ED loading, where the detwinning is almost exhausted at the point of 0% strain in the first cycle. At the same point of 0% strain, the basal intensity in the TD direction is also lower than the original one, which suggests that twinning is already active before the strain is reversed to positive. At this point, the newly formed twins, as barriers, could potentially slow the detwinning event and, thus, delay the exhaustion of the detwinning event, compared to the ED loading condition.

As discussed, under the initial compression, the new TD texture component involves the newly formed twins from the compression and the parent grains initially existing in the TD texture component. Both the newly formed twins and the parent grains are oriented with the c-axes parallel to the loading axis, therefore, they are expected to be detwinned or twinned upon unloading and/or tensile reloading. This significantly complicates the situation, and the current experimental configuration is NOT able to clearly discriminate both events by diffraction. However, as we have observed in the ED loading that detwinning readily begins during compressive unloading, and does not need to wait till tensile reloading. Furthermore, detwinning of the new twins within the TD component will reorient the grains to the original orientation, which can be entirely monitored by the intensity increase in the ND direction. However, the basal poles are rotated to the six equivalent orientations as a result of the twinning activation in the TD component under tension, and only very little twinned grains are aligned with their c-axes parallel to the ND direction which can be captured by the corresponding detector bank 1. Carefully examining the intensity evolution in Figure 5.28 upon unloading from the maximal compressive strains, it is observed that only beyond the 0.5% strain, the intensity increasing rate in the ND direction is markedly reduced, indicating the deformation is more controlled by twinning, and detwinning may be already exhausted or significantly slow down. However, the exact strain points for the detwinning exhaustion and the twinning activation is not yet able to be determined by the current measurements.

Upon unloading from the maximal tensile strain, the basal intensities in the TD and ND direction, respectively, increase and decrease again. At the point of 1.5% strain, the basal intensity in the ND direction starts to decrease in a much higher rate. This is an

indication that beyond this point the parent grains in the ND component are twinned, because the basal intensity increase in the ND direction due to the detwinning of the twins formed from the TD component is very limited. The subsequent basal intensity evolutions with cyclic loading closely follow the evolutions in the first cycle. Nevertheless, the maximal twins under compression cycles (corresponding to the maximal basal intensity in the TD direction) is significantly increasing with cycling, while the maximal twins under tension cycles is increasing initially and then decreasing after initial 10 cycles (corresponding to the initial decrease and then increase in the minimal basal intensity of the TD direction).

Figure 5.29 shows the basal intensity evolutions when the sample is loaded with tension as the first deformation stroke along the TD direction at the total strain amplitude of 3.0%. The overall evolutions are comparable to those shown in Figure 5.28, so the detailed description is omitted here for brevity.

The overall cyclic twinning and detwinning is also manifested by the texture evolution measured by *ex situ* synchrotron diffraction (Fig. 5.30). The texture change from the point ‘a’ to ‘b’ is pronounced due to the twinning (Fig. 5.30a&b). When the sample is unloaded from ‘b’ to ’c’, the texture is partially recovered, indicating the occurrence of detwinning (Fig. 5.30c). The texture at the point ‘d’ is more reversed to the initial texture, a new texture component along the ED direction is observed, and the basal intensity in the TD direction is a little bit reduced (Fig. 5.30d), suggesting some activity of the twinning besides the detwinning. When the sample is reloaded in tensile strain to + 3.0% strain, the resulting texture is with a great volume of grains initially aligned with the loading axis

reoriented by ~ 90^{o} and, concomitantly, the new texture components are noted similar to that observed under monotonic tension, characteristics of the significant occurrence of extension twinning within the TD component. Upon the straining is reversed, the (00.2) basal pole at the point 'f' is partially recovered (Fig. 5.30f), again due to detwinning. At the strain point 'g', the original texture is reversed at a larger degree with the appearance of the ED texture components (Fig. 5.30g), obviously as a result of the simultaneous activities of detwinning and twinning events, and suggesting that the detwinning is not complete.

Figure 5.31 shows the cyclic stress evolutions for both compression and tension as the first deformation stroke along the TD direction with the total strain amplitude of 3.0%. It is noted that the cyclic tensile stress curves are almost overlapped, and the pronounced difference is observed with the cyclic compressive stress curves between the two loading conditions. The cyclic tensile stress evolutions initially exhibit hardening, and then softening. This can be understood with the basal intensity evolutions at the maximal strain points in Figures 5.28 and 5.29, where the minimal intensity in the TD direction is reduced during the initial 10 cycles, and after the initial 10 cycles, the minimal intensity is visibly increased. This is an indication that during the initial 10 cycles, more and more parent grains are twinned with cycling (that is, more twins are formed with initial cycling), while during the subsequent cycles, less and less twins are formed. This trend is coincident well with the cyclic tensile stress evolutions. The cyclic compressive stress evolutions show the continuous hardening during the whole fatigue life span. This is coincident with the escalating trend of the maximal intensity of the basal poles in the TD direction in both cases. The maximal compressive stresses with tension first are always higher than those with compression first.

In a word, the intensity evolutions of (00.2) basal poles observed *via in situ* neutron diffraction (see Figs. 5.28 and 5.29) and the crystallographic texture evolution (see Fig. 5.30) measured using *ex situ* synchrotron diffraction can be correlated with the cyclic activation of the $\{10\bar{1}2\}<10\bar{1}1>$ twinning and detwinning mechanisms in this alloy. The nearly symmetric hysteresis loops are a result of the symmetric deformation mechanisms under tension and compression, when the alloy is loaded along the TD direction.

5.3.2 Internal-strain/stress evolutions

Figures 5.32 and 5.33 represent the internal-strain evolutions during the cyclic loadings of the Mg alloy, ZK60A, along the TD direction, respectively with compression or tension as the first deformation stroke, corresponding to Figures 5.26 and 5.27). As we learned from the internal-strain/stress evolution under the ED loading, the twinning/detwinning activation leads to stress relaxation in the parent grains, and the internal-stresses are accumulated very quickly in the newly formed twins. In Figure 5.32a, upon yielding, the internal-strains in the (00.2) parent grains along the ND direction is relaxed, and concurrently, the (00.2) grain orientation in the TD direction (please be emphasized that the new twins stacked within the initial TD texture component) takes more portion of the applied load. During compressive unloading and tensile reloading (Fig. 5.32b), the internal-strain curve of the (00.2) grain orientation in the TD direction exhibits two inflection features, the first one with a decreasing slope and the second with an increasing slope. As we know, the lattice strain/stress evolution is a very sensitive indicator

of deformation mechanisms. Comparing the intensity evolution in the TD direction in the right plot, it is derived that the first inflection corresponds to the enhanced detwinning activity when the macroscopic stress becomes positive. The second one corresponds to the twinning activation within the TD texture component, considering the *in situ* neutron results shown in Figure 5.28. The second inflection point appears roughly at the applied stress around 80 ~ 90 MPa, corresponding to an approximate strain of ~ – 1.5%. This provides the additional evidence that the twinning occurs before the applied strain is reversed to positive. However, the exact point in terms of twinning activation is not yet able to be determined since large strain intervals were used during the data acquisition. Similarly, as shown in Figure 5.32c, during tensile unloading and compressive reloading, the internal-strain evolution in the (00.2) grain orientation along the TD direction suggests the transition of the detwinning-dominated to the twinning-dominated plastic deformation.

In parallel, when the sample is loaded along the TD direction with tension as the first deformation stroke, the analogous internal-strain evolution involved with the twinning and detwinning mechanisms is evident as shown in Figure 5.30. For brevity, the detailed description is not presented.

Different from the development of the local tensile stress in the twinned grains under the ED loading, the similar phenomenon is not observed. Because the newly formed twins accumulated with the existing parent grains along the same orientation, the current diffraction CANNOT separate the two sets of grains, the measured internal-strains are the averaged numbers of the twins and the parent grains. Therefore, a study on the grain-level twinning and detwinning within individual grains in polycrystals using microdiffraction or

3 dimentional XRD microscopy is needed in order to clarify the problems above.

5.4 The Effect of Texture on the Twinning and Detwinning Behavior in the AZ31B Alloy

Figures 5.34 – 5.39 represent the initial texture effect on the cyclic deformation of the rolled AZ31B magnesium alloy, and the associated texture evolution during the first cycle of deformation at the strain amplitudes of 3.0 %, respectively, loaded along the RD (Figs. 5.34 & 5.35), TD (Figs. 5.36 & 5.37), and ND (Figs. 5.38 &5.39) directions.

It is worthwhile to emphasize that most grains are initially oriented with their c-axes parallel to the ND direction, and the prismatic poles are essentially randomly distributed in the rolling plane (Fig. 5.34a), and only few twins are visible in the initial microstructure (Fig. 5.35a). Therefore, the initial grains are preferable for the activation of extension twinning, if the alloy is compressed within the plane of the plate. After the alloy compressively yields, the hardening rate is so low that the flow stress keeps almost constant until the maximal compressive strain at – 3.0%. At this strain point, a large volume fraction of grains are reoriented due to extension twinning, resulting in the development of a new texture component with the basal (00.2) poles aligned with the RD direction (e.g., the loading axis) (Fig. 5.34b). Concurrently, a great number of twin bands are observed in most grains (Fig. 5.35b). When the alloy is unloaded to the zero stress at the point “c” on the hysteresis loop in Figure 5.34, no significant difference in the pole figures (Fig. 34c) is observed, compared to Figure 5.34b, although the *in situ* neutron study of

ZK60A alloy discussed earlier indicates that the detwinning is almost immediately active upon unloading. This is possibly because of the high resolution and sensitivity with *in situ* neutron diffraction and the low resolution in texture evolution. However, at the strain of 0%, the texture is almost completely reversed (Fig. 5.34d), concurrent with the disappearance of twins bands (Fig. 5.35d). This provides the strong evidence that the twins return to the original orientation by detwinning, rather than retwinning, where the twins are replaced by new twin variants, which would result in a deviation from the initial texture and the existence of new twin bands. Because the resulting grain orientation is hard related to the basal slip and extension twinning, once the detwinning capability is exhausted, the further deformation is supposed to be accommodated by the elastic deformation [73] or the harder pyramidal dislocation slips [132]. Therefore, the alloy exhibits a higher hardening rate beyond the "d" point. At the maximal tensile strain of + 3.0%, the basal texture is further enhanced due to the dislocation slips (Fig. 5.34e). When the alloy is compressed to point "f" starting another cycle, some grains are again reoriented and aligned with the loading direction (Fig. 5.34f). Thus, it is derived that the overall texture evolution for the subsequent cycles closely follows the first cycle based on the assumed cyclic twinning and detwinning behavior. This assumption is corroborated by the cyclic lattice reorientation of basal (00.2) planes obtained from *in situ* neutron scattering (not shown here for brevity), analogous to Figure 5.15.

In Figures 5.36 and 5.37, the texture and microstructural evolutions when the alloy is loaded along the TD direction are, respectively, represented. An analogous texture and microstructural evolutions are observed compared to those under the RD loading (Figs. 5.34 &5.35); the only difference is that the texture component related to the twin grains is

aligned with the TD direction, e.g., the current loading axis. This is the case due to the unique reorientation of twin grains (~ 90^{o}) in magnesium, resulting that the twin grains with the basal poles after compression are always parallel to the loading axis, as discussed in Chapter 4. In other words, the basal planes are always perpendicular to the loading axis.

It seems that the hysteresis loop in Figure 5.38 is inverted, with respect to the in-plane loading cases in Figures 5.34 and 5.36. As mentioned, most grains are initially aligned with the c-axes parallel to the ND direction. The alloy is very hard under the ND compression, usually with the restricted activation of basal, prismatic, and extension twinning, resulting in a high compressive stress and limited ductility (Fig. 4.1b). This leads to the lack of significant texture change (Fig. 5.38a), comparable to the initial texture (Fig. 5.34a). Nevertheless, most grains are preferentially oriented for extension twinning, if the alloy is extended along the ND direction as indicated by the fact that the basal poles of the twin grains are reoriented nearly 90^{o} and distributed perpendicular to the ND direction (e.g., the loading axis) (Fig. 5.38b), when the alloy is strained to the point "b". As the alloy is further strained to the maximal tensile strain at + 3.0%, more grains are reoriented to the twin orientations. Consequently, the intensity of basal (00.2) poles is highly reduced at the center, while the corresponding intensity along the perimeter in the (00.2) pole figure is greatly increased (Fig. 5.38c). The observation of optical microstructures confirm the existence of twin bands at the strain of + 3.0% (Fig. 5.39c). As the strain direction is reversed and unloaded to the point "d", where the texture (Fig. 5.38d) is comparable to the corresponding texture in Figure 5.38c. The texture is partially reversed (Fig. 5.38e), as the alloy is loaded to the point "e", a signature of the activation of detwinning. When the alloy

is further strained to the maximal compressive strain at – 3.0%, the resulted texture is a complete recovery of the initial texture (Fig. 5.38f), concurrent with the microstructure reverse exhibited as the absence of twins (Fig. 5.39f).

In a word, the texture evolution shows that the cyclic plastic deformations are very similar for the RD and TD loading conditions, due to the initial in-plane texture symmetry. Although the macroscopic hysteresis under the ND loading is distinct from in-plane cases, all of them are dominated in nature by twinning and detwinning mechanisms. The different activation sequence of twinning and twinning mechanisms under compression and tension are determined by the initial crystallographic texture, such that the inverted hysteresis loops between the in-plane and through-thickness loadings are observed.

5.5 Correlation between the Low-cycle Fatigue Behavior and the Cyclic Plastic Deformation

As mentioned, the two wrought magnesium alloys studied exhibit the texture-dependent low-cycle fatigue properties, that is, the low-cycle fatigue behaviors in each alloy are different in terms of the loading directions. This is presumably correlated with the significant differences in the cyclic plastic deformations as a result of grain preferential orientation when loaded along the various directions, where, correspondingly, these two alloys exhibit the three types of hysteresis loops as follows:

Type I, asymmetric S-shape (e.g., in-plane loadings in AZ31B and ED loadings in ZK60A) (Fig. 5.40a), where the compressive strains are accommodated mainly by

extension twinning, detwinning is dominating the compressive unloadings and initial tensile reloadings, and the non-basal <a> dislocation slips are readily active for the post-detwinning deformation. Because the non-basal <a> dislocation slips typically demand a higher stress, a tensile mean stress is usually obtained.

Type II, inverted asymmetric S-shape (e.g., through-thickness or ND loading in AZ31B) (Fig. 5.40b), where tensile strains are mainly introduced by extension twinning, while the initial compressive reloadings are accommodated by detwinning. Under the through-thickness loading, most grains are oriented with the c-axes along the loading direction (Fig. 3.2b), and this is a brittle orientation with a lowest ductility than others as shown in Figure 4.2b, because the plastic deformation along the c-axis requires non-basal <c+a> slip [4], which is very hard to enforce in single-crystal Mg. Particularly, during the first compression and post-detwinning compression under the through-thickness loading, extension twinning is not active or detwinning is exhausted, and, furthermore, the <c+a> pyramidal slip and contraction twinning [14, 41] are difficult to be activated at room temperature. This results in plastic shear instability because no primary deformation modes are readily active to accommodate, especially, the inelastic contraction along the c-axes once detwinning is exhausted. Typically, a compressive mean stress is observed.

Type III, nearly symmetric shape (e.g., TD loading in ZK60A) (Fig. 5.40c) , where under tensile unloadings and compressive reloadings the twins formed during the prior tension from the TD texture component detwin and the ND texture component twins, while under compressive unloadings and tensile reloadings, the new TD texture component accumulated with the original TD component during the prior compression detwin and

twin. Obviously, under this type of cyclic plastic deformation, the post-detwinning deformation is accommodated by extension twinning of parent grains within a different texture component. Because of the nearly symmetric deformation, the mean stress is close to zero.

Therefore, these different shapes of hysteresis loops are determined by the different activation sequences of twinning and detwinning mechanisms under tension and compression, due to the variance of the initial crystallographic texture with respect to the loading directions. Specifically, the deformation mechanisms during the first compression and the post-detwinning deformation have a significant influence in dictating the low-cycle fatigue behavior. Because there are no primary plastic deformation modes available for the post-detwinning deformation under the through-thickness loading of AZ31B alloy, this loading condition exhibits the worst low-cycle fatigue resistance compared to the in-plane cases. Under the ND and TD loadings of ZK60A alloy, the extension twinning within the different texture components is active for the post-detwinning deformation, their low-cycle fatigue resistances show a much less difference from the ED loading.

5.6 Summary

In this chapter, the low-cycle fatigue behavior and the associated cyclic plastic deformation characteristics in the two wrought Mg alloys are presented and discussed in terms of loading direction. Due to the different crystallographic textures, the three types of cyclic plastic deformation behaviors and the respective post-detwinning deformations are

summarized. The texture-dependent low-cycle fatigue behaviors are correlated with the various cyclic plastic deformations, and, particularly, the post-detwinning deformation features.

CHAPTER 6 SUMMARY AND CONCLUSIONS

Based on the studies of the mechanical behaviors and the associated plastic deformation mechanisms under monotonic and cyclic loadings of the extruded ZK60A and rolled AZ31B magnesium alloys, the following conclusions can be drawn:

1) The significant tension-compression asymmetries and high anisotropies are observed in the two Mg alloys. The tension-compression asymmetries are related to the activation of extension twinning in one direction but not in the opposite direction. The high anisotropies are correlated with the initial texture distinction with respect to the loading axis and direction, resulting in the different activities of various deformation modes.

2) The similar yielding stresses are observed irrespective of the strain direction and strain sign if the deformation is dominated by extension twinning, while they are usually different with respect to the loading conditions if the dislocation slips are dominant throughout the plastic deformation.

3) The results show that the extension twinning under monotonic tension exhibits a similar behavior as that under monotonic compression, presumably due to the fact that these two different loading conditions introduce the same Schmid stress on the twinning plane along the twinning shear direction within strongly textured wrought magnesium alloys.

4) The basal poles within the twin grains under tension in the ZK60A alloy are distributed at the six locations corresponding to the six twin variants at a near 90^{o} inclined to the tensile loading axis, while they are always closely aligned with the compressive axis under compression. Due to the radial symmetry in the initial texture of the AZ31B alloy, the resulting texture after the ND tension, though dominated by the same extension twinning, exhibits the significant difference, with the basal poles distributed essentially uniformly along the perimeter in the basal pole figure.

5) The relationships between the elastic and plastic strain amplitudes with the numbers of reversals to failure can be well described, respectively, by the empirical Basquin and Coffin-Manson equations. Conversely, the low-cycle fatigue resistances with respect to the total strain amplitude can be predicted by the combined Basquin and Coffin-Manson equations.

6) The different activation sequences of twinning and detwinning mechanisms under compression and tension are determined by the initial crystallographic texture relative to the loading axis, such that three types of hysteresis-loop shapes, corresponding to three types of cyclic plastic deformation behaviors, can be predicted. The differences in the cyclic-stress responses and hysteresis-loop shapes are related to the respective cyclic twinning-detwinning behaviors.

7) The different low-cycle fatigue properties in each alloy are observed with respect to three orthogonal loading directions, resulting from the different

plastic deformation behaviors with respect to the loading directions. Specifically, the deformation mechanisms during the first compression and the post-detwinning deformation have a significant influence in dictating the low-cycle fatigue behavior.

8) The unique orientation relationship between the parent and the twin grains in the magnesium alloys facilitates the investigation of the twinning-detwinning behavior using the two-detector *in situ* neutron diffraction system of the SMARTS spectrometer, which is advantageous to study the internal-strains (stresses) in the parent grains and twin grains separately.

9) The intensity transfer of the (00.2) basal poles in the two detector banks can be reasonably related to the activation of $\{10\bar{1}2\}<10\bar{1}1>$ extension twinning and detwinning in the magnesium alloys, which are characterized by the strangely shaped hysteresis loops with a pronounced asymmetry.

10) The fact that twinning and detwinning alternates with the cyclic loading was confirmed using *in situ* neutron scattering, and the plastic deformation in the studied materials under cyclic loading is dominated by cyclic twinning and detwinning, i.e., most twins formed during compression are removed via detwinning when the load is reversed.

11) A small volume fraction of residual twins was detected, which gradually increases with increasing cycles, and may be an important factor in understanding the low-cycle fatigue behavior of the magnesium alloys.

12) While extension twinning is active, the load-induced internal-stresses in the (00.2) parent and twin grains are relaxed, and they are significantly smaller compared to the internal-stresses in the other grains orientations.

13) The (00.2) twin grains sustain a tensile stress along the c-axes (resulting from the significant twinning), which is hypothesized to be effective for driving the detwinning event under a macroscopic compressive stress field. In this way, extension twinning takes place almost immediately upon unloading (e.g., no tensile reloading is required), and extension twinning, thus, is a pseudo-elastic phenomenon, not unlike the stress-induced martensite formation observed in some shape memory alloys.

14) The load redistribution between the soft- and hard-grain orientations is attributed to the plastic anisotropy, and responsible for the development of the mentioned local tensile stress in twins.

15) The activation stresses of the extension twinning and detwinning were calculated from the internal-strains at which twinning or detwinning begins to be active for plastic deformation, based on a simplified uniaxial Schmid law.

CHAPTER 7 DIRECTIONS FOR FUTURE WORK

Magnesium alloys are ideal model materials for studying twinning, because of near elastic isotropy and near isotropic coefficients of thermal expansion, which results in negligible residual stress after hot deformation. Furthermore, wrought magnesium alloys usually have a very strong basal texture. Therefore, by tailoring the initial texture and applied loading relative to the texture, it is possible to introduce a stress state, where extension twinning is the major deformation mechanism. The following investigations could contribute to an in-depth mechanistic understanding of the unusual plastic deformation behaviors in wrought magnesium alloys during monotonic and/or cyclic loadings:

1) Polycrystal plasticity modeling, such as the EPSC simulation combined TEM observation is helpful to understand the exceptional hardening behavior in magnesium alloys.

2) More investigations need to be conducted to understand strain-life fatigue, including fatigue crack growth behavior, fatigue damaging mechanisms, and life prediction for Mg alloys.

3) The determination of the full strain (or stress) state in grains will give us important evidences necessary for the deformation modeling, and give us insights into the twinning and detwinning mechanisms in the materials.

4) Grain-level twinning and detwinning behavior in wrought magnesium alloys

using *in situ* synchrotron microdiffraction is supplemental to the current studies. The previous studies CANNOT provide the information within single grains, since those diffraction represents an average state of all grains which contribute to a given diffraction peak, based upon a satisfaction of the Bragg condition. In contrast, the novel 3-dimensional XRD (3DXRD) microdiffraction could be used to study the grain reorientation and the development of internal-strain within individual grains, such that the orientation and full strain tensor can be determined within a single grain as a function of strain, which is untwined, partially twinned and completely twinned. The proposed research will give us more insights into the twinning and detwinning mechanisms at a grain level, and the experimental data are invaluable to improve the existing crystal-plasticity models.

5) Grain-grain interaction and detwinning mechanisms using 3DXRD and/or tomography could provide the necessary clues to better understand the detwinning mechanisms in magnesium alloys.

REFERENCES

REFERENCES

[1] M. M. Avedesian, H. Baker, *Magnesium and magnesium alloys (ASM Specialty Handbook)*, ASM International, Materials Park, OH, 1999.

[2] C. S. Roberts, *Magnesium and its Alloys*, John Wiley & Sons, Inc., New York, 1960.

[3] C. J. Bettles, M. A. Gibson, *Current wrought magnesium alloys: Strengths and weaknesses*, JOM 57 (2005) 46-49.

[4] S. R. Agnew, O. Duygulu, *Plastic anisotropy and the role of non-basal slip in magnesium alloy AZ31B*, International Journal of Plasticity 21 (2005) 1161-1193.

[5] M. Li, *Consitutive modeling of slip, twinning and untwinning in AZ31B magnesium*, In: Materials Science and Engineering, Ph.D Thesis, Ohio State University, Columbus, OH (2006).

[6] E. Tenckhoff, *Deformation mechanisms, texture, and anistropy in zirconium and Zircaloy*, American Society for Testing and Materials, Philadelphia, PA, 1988.

[7] W. D. Callister, Jr., *Materials science and engineering: An introduction, 7th edition*, John Wiley & Sons, Inc., York, PA, 2007.

[8] A. V. Staroselsky, *Crystal plasticity due to slip and twinning*, in: Mechanical Engineering, Ph.D Thesis, Massachusetts Institute of Technology, Cambridge, MA (1998).

[9] M. H. Yoo, *Slip, twinning, and fracture in hexagonal close-packed metals*, Metallurgical Transactions A 12 (1981) 409-418.

[10] D. W. Brown, S. R. Agnew, M. A. M. Bourke, T. M. Holden, S. C. Vogel, C. N. Tome, *Internal strain and texture evolution during deformation twinning in magnesium*, Materials Science and Engineering A 399 (2005) 1-12.

[11] P. G. Partridge, *The crystallography and deformation modes of HCP metals*, Metallurgical Reviews 12 (1967) 169-194.

[12] A. Staroselsky, L. Anand, *A constitutive model for hcp materials deforming by slip and twinning: application to magnesium alloy AZ31B*, International Journal of Plasticity 19 (2003) 1843-1864.

[13] U. F. Kocks, D. G. Westlake, *The importance of twinning for the ductility of CPH polycrystals*, Transactions of the Metallurgical Society of AIME 239 (1967) 1107-1109.

[14] S. R. Agnew, M. H. Yoo, C. N. Tome, *Application of texture simulation to understanding mechanical behavior of Mg and solid solution alloys containing Li or Y*, Acta Materialia 49 (2001) 4277-4289.

[15] M. H. Yoo, J. R. Morris, K. M. Ho, S. R. Agnew, *Nonbasal deformation modes of HCP metals and alloys: Role of dislocation source and mobility*, Metallurgical and Materials Transactions A 33 (2002) 813-822.

[16] M. H. Yoo, J. K. Lee, *Deformation twinning in hcp metals and alloys*, Philosophical Magazine A 63 (1991) 987-1000.

[17] J. W. Christian, S. Mahajan, *Deformation twinning*, Progress in Materials Science 39 (1995) 1-157.

[18] W. F. Hosford, *The mechanics of crystals and textured polycrystals*, Oxford University Press, New York, 1993.

[19] M. R. Barnett, Z. Keshavarz, A. G. Beer, D. Atwell, *Influence of grain size on the compressive deformation of wrought Mg-3Al-1Zn*, Acta Materialia 52 (2004) 5093-5103.

[20] L. Jiang, J. J. Jonas, R. K. Mishra, A. A. Luo, A. K. Sachdev, S. Godet, *Twinning and texture development in two Mg alloys subjected to loading along three different strain paths*, Acta Materialia 55 (2007) 3899-3910.

[21] M. R. Barnett, *Twinning and the ductility of magnesium alloys Part II. "Contraction" twins*, Materials Science and Engineering A 464 (2007) 8-16.

[22] M. R. Barnett, *Twinning and the ductility of magnesium alloys Part I: "Tension" twins*, Materials Science and Engineering A 464 (2007) 1-7.

[23] Y. N. Wang, J. C. Huang, *The role of twinning and untwinning in yielding behavior in hot-extruded Mg-Al-Zn alloy*, Acta Materialia 55 (2007) 897-905.

[24] E. C. Oliver, M. R. Daymond, P. J. Withers, *Neutron diffraction study of extruded magnesium during cyclic and elevated temperature loading*, Materials Science Forum 490-491 (2005) 257-262.

[25] M. A. Gharghouri, G. C. Weatherly, J. D. Embury, J. Root, *Study of the mechanical properties of Mg-7.7at.% Al by in-situ neutron diffraction*, Philosophical Magazine A 79 (1999) 1671-1695.

[26] S. Kleiner, P. J. Uggowitzer, *Mechanical anisotropy of extruded Mg-6% Al-1% Zn alloy*, Materials Science and Engineering A 379 (2004) 258-263.

[27] D. W. Brown, A. Jain, S. R. Agnew, B. Clausen, *Twinning and detwinning during cyclic deformation of Mg alloy AZ31B*, Materials Science Forum 539-543 (2007) 3407-3413.

[28] U. F. Kocks, C. N. Tome, H. R. Wenk, *Texture and Anisotropy: preferred orientations in polycrystals and their effect on materials properties*, Cambridge University Press, Cambridge, UK, 1998.

[29] D. H. Avery, W. F. Hosford, W. A. Backofen, *Plastic anisotropy in magnesium alloy sheets*, Transactions of the Metallurgical Society of AIME 233 (1965) 71-78.

[30] S. R. Agnew, C. N. Tome, D. W. Brown, T. M. Holden, S. C. Vogel, *Study of slip mechanisms in a magnesium alloy by neutron diffraction and modeling*, Scripta Materialia 48 (2003) 1003-1008.

[31] W. Reimers, A. R. Pyzalla, A. Schreyer, H. Clemens, *Neutrons and synchrotron radiation in engineering materials science: From fundamentals to mateiral and component characterization*, Wiley-VCH Verlag GmgH & Co., KGaA, Weinheim, 2008.

[32] A. J. Allen, M. A. M. Bourke, S. Dawes, M. T. Hutchings, P. J. Withers, *The*

analysis of internal strains measured by neutron-diffraction in Al-Sic metal matrix composites, Acta Metallurgica Et Materialia 40 (1992) 2361-2373.

[33] M. T. Hutchings, P. J. Withers, T. M. Holden, T. Lorentzen, *Introduction to the characterization of residual stress by neutron diffraction*, Taylor & Francis Group, LLC, Boca raton, Florida, 2004.

[34] O. Muransky, D. G. Carr, M. R. Barnett, E. C. Oliver, P. Sittner, *Investigation of deformation mechanisms involved in the plasticity of AZ31 Mg alloy: In situ neutron diffraction and EPSC modelling*, Materials Science and Engineering A 496 (2008) 14-24.

[35] T. L. Brown, S. Swaminathan, S. Chandrasekar, W. D. Compton, A. H. King, K. P. Trumble, *Low-cost manufacturing process for nanostructured metals and alloys*, Journal of Materials Research 17 (2002) 2484-2488.

[36] S. R. Agnew, D. W. Brown, S. C. Vogel, T. M. Holden, *In-situ measurement of internal strain evolution during deformation dominated by mechanical twinning*, Ecrs 6: Proceedings of the 6Th European Conference on Residual Stresses 404-4 (2002) 747-752.

[37] B. Clausen, C. N. Tome, D. W. Brown, S. R. Agnew, *Reorientation and stress relaxation due to twinning: Modeling and experimental characterization for Mg*, Acta Materialia 56 (2008) 2456-2468.

[38] G. Proust, C. N. Tome, G. C. Kaschner, *Modeling texture, twinning and hardening evolution during deformation of hexagonal materials*, Acta Materialia 55 (2007) 2137-2148.

[39] G. Proust, C. N. Tome, A. Jain, S. R. Agnew, *Modeling the effect of twinning and detwinning during strain-path changes of magnesium alloy AZ31*, International Journal of Plasticity 25 (2009) 861-880.

[40] A. Jain, O. Duygulu, D. W. Brown, C. N. Tome, S. R. Agnew, *Grain size effects on the tensile properties and deformation mechanisms of a magnesium alloy, AZ31B, sheet*, Materials Science and Engineering A 486 (2008) 545-555.

[41] S. R. Agnew, D. W. Brown, C. N. Tome, *Validating a polycrystal model for the elastoplastic response of magnesium alloy AZ31 using in situ neutron diffraction*, Acta Materialia 54 (2006) 4841-4852.

[42] A. Jain, S. R. Agnew, *Modeling the temperature dependent effect of twinning on the behavior of magnesium alloy AZ31B sheet*, Materials Science and Engineering A 462 (2007) 29-36.

[43] E. W. Kelly, W. F. Hosford Jr., *The deformation characteristics of textured magnesium*, Transactions of Metallurgical Society of AIME 242 (1968) 654-661.

[44] O. Cazacu, F. Barlat, *A criterion for description of anisotropy and yield differential effects in pressure-insensitive metals*, International Journal of Plasticity 20 (2004) 2027-2045.

[45] R. Vaidyanathan, M. A. M. Bourke, D. C. Dunand, *Stress-induced martensitic transformations in NiTi and NiTi-TiC composites investigated by neutron diffraction*, Materials Science and Engineering A 273 (1999) 404-409.

[46] S. R. Agnew, *Plastic anisotropy of magnesium alloy AZ31B sheet*, in: TMS Annual Meeting, vol Magnesium Technology 2002, TMS, Seattle, Washington, USA, 2002, pp. 169-172.

[47] X. Y. Lou, M. Li, R. K. Boger, S. R. Agnew, R. H. Wagoner, *Hardening evolution of AZ31B Mg sheet*, International Journal of Plasticity 23 (2007) 44-86.

[48] S. B. Yi, C. H. J. Davies, H. G. Brokmeier, R. E. Bolmaro, K. U. Kainer, J. Homeyer, *Deformation and texture evolution in AZ31 magnesium alloy during uniaxial loading*, Acta Materialia 54 (2006) 549-562.

[49] M. G. Lee, R. H. Wagoner, J. K. Lee, K. Chung, H. Y. Kim, *Constitutive modeling for anisotropic/asymmetric hardening behavior of magnesium alloy sheets*, International Journal of Plasticity 24 (2008) 545-582.

[50] D. W. Brown, S. R. Agnew, S. P. Abeln, W. R. Blumenthal, M. A. M. Bourke, M. C. Mataya, C. N. Tome, S. C. Vogel, *The role of texture, temperature, and strain rate in the activity of deformation twinning*, Icotom 14: Textures of Materials, Pts 1and

2 495-497 (2005) 1037-1042.

[51] S. B. Yi, H. G. Brokmeier, R. Bolmaro, K. U. Kainer, J. Homeyer, *The texture evolutions of Mg alloy, AZ31, under uni-axial loading*, Icotom 14: Textures of Materials, Pts 1and 2 495-497 (2005) 1585-1590.

[52] S. B. Yi, H. G. Brokmeier, R. E. Bolmaro, K. U. Kainer, T. Lippmann, *In situ measurements of texture variations during a tensile loading of Mg-alloy AM20 using synchrotron X-ray radiation*, Scripta Materialia 51 (2004) 455-460.

[53] Y. Chino, K. Kimura, M. Hakamada, M. Mabuchi, *Mechanical anisotropy due to twinning in an extruded AZ31 Mg alloy*, Materials Science and Engineering A 485 (2008) 311-317.

[54] R. H. Wagoner, X. Y. Lou, M. Li, S. R. Agnew, *Forming behavior of magnesium sheet*, Journal of Materials Processing Technology 177 (2006) 483-485.

[55] S. R. Kalidindi, J. D. Embury, M. Barnett, C. N. Tome, *MagNET Workshop on deformation mechanisms in magnesium alloys*, The Unvniversity of British Columbia, Vancouver, November 6-7, 2008.

[56] S. Suresh, *Fatigue of materials*, Cambridge University Press, Cambridge England ; New York, 1998.

[57] L. J. Chen, C. Y. Wang, W. Wu, Z. Liu, G. M. Stoica, L. Wu, P. K. Liaw, *Low-cycle fatigue behavior of an as-extruded AM50 magnesium alloy*, Metallurgical and Materials Transactions A 38 (2007) 2235-2241.

[58] S. Begum, D. L. Chen, S. Xu, A. A. Luo, *Strain-Controlled Low-Cycle Fatigue Properties of a Newly Developed Extruded Magnesium Alloy*, Metallurgical and Materials Transactions A 39A (2008) 3014-3026.

[59] Y. H. He, L. J. Chen, P. K. Liaw, R. L. McDaniels, C. R. Brooks, R. R. Seeley, D. L. Klarstrom, *Low-cycle fatigue behavior of HAYNES (R) HR-120 (R) alloy*, International Journal of Fatigue 24 (2002) 931-942.

[60] T. S. Srivatsan, L. Wei, C. F. Chang, *The cyclic strain resistance, fatigue life and final fracture behavior of magnesium alloys*, Engineering Fracture Mechanics 56

(1997) 735-740.

[61] S. R. Agnew, J. W. Senn, J. A. Horton, *Mg sheet metal forming: Lessons learned from deep drawing Li and Y solid-solution alloys*, JOM 58 (2006) 62-69.

[62] S. R. Agnew, *Wrought magnesium: A 21st century outlook*, JOM 56 (2004) 20-21.

[63] L. Wu, G. M. Stoica, H.-H. Liao, S. R. Agnew, E. A. Payzant, G. Wang, D. E. Fielden, L. Chen, P. K. Liaw, *Fatigue-property enhancements of magnesium alloy, AZ31B, through equal-channel-angular pressing (ECAP)*, Metallurgical and Materials Transactions A 38 (2007) 2283-2289.

[64] C. Potzies, K. U. Kainer, *Fatigue of magnesium alloys*, Advanced Engineering Materials 6 (2004) 281-289.

[65] K. Tokaji, M. Kamakura, Y. Ishiizumi, N. Hasegawa, *Fatigue behaviour and fracture mechanism of a rolled AZ31 magnesium alloy*, International Journal of Fatigue 26 (2004) 1217-1224.

[66] S. Hasegawa, Y. Tsuchida, H. Yano, M. Matsui, *Evaluation of low cycle fatigue life in AZ31 magnesium alloy*, International Journal of Fatigue 29 (2007) 1839-1845.

[67] X. Z. Lin, D. L. Chen, *Strain controlled cyclic deformation behavior of an extruded magnesium alloy*, Materials Science and Engineering A 496 (2008) 106-113.

[68] S. M. Yin, F. Yang, X. M. Yang, S. D. Wu, S. X. Li, G. Y. Li, *The role of twinning-detwinning on fatigue fracture morphology of Mg-3%Al-1%Zn alloy*, Materials Science and Engineering A 494 (2008) 397-400.

[69] L. Bian, F. Taheri, *Fatigue fracture criteria and microstructures of magnesium alloy plates*, Materials Science and Engineering A 487 (2008) 74-85.

[70] S. Ishihara, Z. Nan, T. Goshirna, *Effect of microstructure on fatigue behavior of AZ31 magnesium alloy*, Materials Science and Engineering A 468 (2007) 214-222.

[71] P. K. Liaw, T. L. Ho, J. K. Donald, *Near-threshold fatigue crack-growth behavior in a magnesium alloy*, Scripta Metallurgica 18 (1984) 821-824.

[72] G. Eisenmeier, B. Holzwarth, H. W. Hoppel, H. Mughrabi, *Cyclic deformation and fatigue behaviour of the magnesium alloy AZ91*, Materials Science and Engineering A 319 (2001) 578-582.

[73] S. M. Yin, H. J. Yang, S. X. Li, S. D. Wu, F. Yang, *Cyclic deformation behavior of as-extruded Mg-3%Al-1%Zn*, Scripta Materialia 58 (2008) 751-754.

[74] M. Gotting, B. Scholtes, *Influence of tension-compression loading history on plastic deformation of Mg wrought alloy AZ31*, International Journal of Materials Research 97 (2006) 1378-1383.

[75] C. H. Caceres, T. Sumitomo, M. Veidt, *Pseudoelastic behaviour of cast magnesium AZ91 alloy under cyclic loading-unloading*, Acta Materialia 51 (2003) 6211-6218.

[76] G. E. Mann, T. Sumitomo, C. H. Caceres, J. R. Griffiths, *Reversible plastic strain during cyclic loading-unloading of Mg and Mg-Zn alloys*, Materials Science and Engineering A 456 (2007) 138-146.

[77] J. B. Hess, R. L. Dietrich, *X-ray studies of twinning and untwinning in magnesium alloys*, Transactions of the American Institute of Mining and Metallurgical Engineers 175 (1948) 564-569.

[78] S. M. Yin, F. Yang, X. M. Yang, S. D. Wu, S. X. Li, G. Y. Li, *The role of twinning-detwinning on fatigue fracture morphology of Mg-3%Al-1%Zn alloy*, Materials Science and Engineering A 494 (2008) 397-400.

[79] A. Guinier, *X-ray diffraction in crystals, imperfect crystals, and amorphous bodies*, Dover Publications, Inc., 1994.

[80] H. M. Rietveld, *Line profiles of neutron powder-diffraction peaks for structure refinement*, Acta Crystallographica 22 (1967) 151-157.

[81] H. M. Rietveld, *A profile refinement method for nuclear and magnetic structures*, Journal of Applied Crystallography 2 (1969) 65-71.

[82] D. Chateigner, *Combined analysis: structure-texture-microstructure-phase-stresses -reflectivity determination by x-ray and neutron scattering*, http://www.ecole.ensicaen.fr /~chateign/texture/combined.pdf (2007).

[83] L. B. McCusker, R. B. Von Dreele, D. E. Cox, D. Louer, P. Scardi, *Rietveld refinement guidelines*, Journal of Applied Crystallography 32 (1999) 36-50.

[84] L. Lutterotti, M. S., H.-R. Wenk, *MAUD (Material Analysis Using Diffraction): a user friendly Java program for Rietveld Texture Analysis and more*, Proceeding of the Twelfth International Conference on Textures of Materials (ICOTOM-12) 1 (1999) 1599.

[85] H. R. Wenk, L. Cont, Y. Xie, L. Lutterotti, L. Ratschbacher, J. Richardson, *Rietveld texture analysis of Dabie Shan eclogite from TOF neutron diffraction spectra*, Journal of Applied Crystallography 34 (2001) 442-453.

[86] I. Lonardelli, H. R. Wenk, L. Lutterotti, M. Goodwin, *Texture analysis from synchrotron diffraction images with the Rietveld method: dinosaur tendon and salmon scale*, Journal of Synchrotron Radiation 12 (2005) 354-360.

[87] R. B. VonDreele, *Quantitative texture analysis by Rietveld refinement*, Journal of Applied Crystallography 30 (1997) 517-525.

[88] G. M. Stoica, *Equal-channel-angular processing (ECAP) of materials: Experiment and theory*, in: Materials Science and Engineering, Ph.D Thesis, The University of Tennessee, Knoxville, TN (2007).

[89] R. O. Williams, *Analytical methods for representing complex textures by biaxial pole figures*, Journal of Applied Physics 39 (1968) 4329-4334.

[90] J. Imhof, *Textures and microstructures*, 4 (1982) 189-200.

[91] S. Matthies, G. W. Vinel, *On the reproduction of the orientation distribution function of texturized samples from reduced pole figures using the conception of a conditional Ghost correction*, Physica Status Solidi B-Basic Research 112 (1982) K111-K114.

[92] J. S. Kallend, U. F. Kocks, A. D. Rollett, H. R. Wenk, *Operational texture analysis*, Materials Science and Engineering A 132 (1991) 1-11.

[93] H. R. Wenk, S. Matthies, J. Donovan, D. Chateigner, *BEARTEX: a Windows-based program system for quantitative texture analysis*, Journal of Applied

Crystallography 31 (1998) 262-269.

[94] V. Randle, O. Engler, *Introduction to texture analysis: Macrotexture, microtexture & orientation mapping*, CRC Press, Boca Raton, Florida, 2000.

[95] A. P. Hammersley, *FIT2D: An introduction and overview*, ESRF Internal Report, ESRF97HA02T (1997).

[96] A. P. Hammersley, *FIT2D V9.129 reference manual V3.1*, ESRF Internal Report, ESRF98HA01T (1998).

[97] H. R. Wenk, L. Lutterotti, *LANSCE RESEARCH HIGHLIGHTS: Neutron texture analysis with HIPPO at your fingertips*, (2007).

[98] L. Miyagi, S. Merkel, T. Yagi, N. Sata, Y. Ohishi, H. R. Wenk, *Quantitative Rietveld texture analysis of CaSiO3 perovskite deformed in a diamond anvil cell*, Journal of Physics 18 (2006) S995-S1005.

[99] B. Clausen, *SMARTSware Manual*, Los Alamos National Laboratory, 1998.

[100] A. C. Larson, R. B. Von Dreele, *General Structure Analysis System (GSAS)*, Report No. LAUR 86-748, Los Amamos National Laboraroty (2004).

[101] C. N. Tome, P. J. Maudlin, R. A. Lebensohn, G. C. Kaschner, *Mechanical response of zirconium - I. Derivation of a polycrystal constitutive law and finite element analysis*, Acta Materialia 49 (2001) 3085-3096.

[102] Y. Liu, Y. L. Li, K. T. Ramesh, *Rate dependence of deformation mechanisms in a shape memory alloy*, Philosophical Magazine A 82 (2002) 2461-2473.

[103] L. Wu, S. R. Agnew, D. W. Brown, G. M. Stoica, A. Jain, B. Clausen, D. E. Fielden, P. K. Liaw, *Internal-stress relaxation and load redistribution during the twinning-detwinning-dominated cyclic deformation of a wrought magnesium alloy, ZK60A*, Acta Mater 56 (2008) 3699-3707.

[104] J. Jiang, A. Godfrey, W. Liu, Q. Liu, *Identification and analysis of twinning variants during compression of a Mg-Al-Zn alloy*, Scripta Materialia 58 (2008) 122-125.

[105] S. Godet, L. Jiang, A. A. Luo, J. J. Jonas, *Use of Schmid factors to select extension twin variants in extruded magnesium alloy tubes*, Scripta Materialia 55 (2006) 1055-1058.

[106] F. Li, Y. Wang, L. J. Chen, Z. Liu, J. Y. Zhou, *Low-cycle fatigue behavior of two magnesium alloys*, Journal of Materials Science 40 (2005) 1529-1531.

[107] T. S. Srivatsan, D. Lanning, *Cyclic Strain Resistance and Fracture-Behavior of 7150-Aluminum Alloy*, Engineering Fracture Mechanics 42 (1992) 877-892.

[108] T. S. Srivatsan, *The Low-Cycle Fatigue and Cyclic Fracture-Behavior of 7150-Aluminum Alloy*, International Journal of Fatigue 13 (1991) 313-321.

[109] G. Salerno, R. Magnabosco, C. de Moura, *Mean strain influence in low cycle fatigue behavior of AA7175-T1 aluminum alloy*, International Journal of Fatigue 29 (2007) 829-835.

[110] H. C. Heikkenen, F. S. Lin, E. A. Starke, *The Low-Cycle Fatigue Behavior of High-Strength 7Xxx-Type Aluminum-Alloys in the T7351 Condition*, Materials Science and Engineering 51 (1981) 17-23.

[111] Y. J. Ro, S. R. Agnew, R. P. Gangloff, *Uncertainty in the determination of fatigue crack facet crystallography*, Scripta Materialia 52 (2005) 531-536.

[112] A. Serra, D. J. Bacon, R. C. Pond, *Twins as barriers to basal slip in hexagonal-close-packed metals*, Metallurgical and Materials Transactions A 33 (2002) 809-812.

[113] H. Y. Yasuda, M. Aoki, Y. Umakoshi, *Effect of the ordering process on pseudoelasticity in Fe3Ga single crystals*, Acta Materialia 55 (2007) 2407-2415.

[114] A. Brinck, H. Neuhauser, *Yield stress and dislocation mechanisms in the D0(3) ordered intermetallic phase Fe3Al in the temperature range 240-500 K*, Materials Science and Engineering A 387-89 (2004) 969-972.

[115] E. Langmaack, E. Nembach, *Pseudoelasticity in Fe3Al single crystals*, Philosophical Magazine A 79 (1999) 2359-2377.

[116] H. Numakura, K. Hasegawa, M. Koiwa, *Pseudoelastic and anelastic effects due to the motion of twin boundaries in copper-based alloys*, Acta Metallurgica Et Materialia 40 (1992) 1365-1375.

[117] C. P. Frick, S. Orso, E. Arzt, *Loss of pseudoelasticity in nickel-titanium sub-micron compression pillars*, Acta Materialia 55 (2007) 3845-3855.

[118] R. F. Hamilton, H. Sehitoglu, C. Efstathiou, H. J. Maier, Y. Chumlyakov, *Pseudoelasticity in Co-Ni-Al single and polycrystals*, Acta Materialia 54 (2006) 587-599.

[119] Y. Sutou, T. Omori, K. Yamauchi, N. Ono, R. Kainuma, K. Ishida, *Effect of grain size and texture on pseudoelasticity in Cu-Al-Mn-based shape memory wire*, Acta Materialia 53 (2005) 4121-4133.

[120] C. Lexcellent, B. C. Goo, Q. P. Sun, J. Bernardini, *Characterization, thermomechanical behaviour and micromechanical-based constitutive model of shape-memory Cu-Zn-Al single crystals*, Acta Materialia 44 (1996) 3773-3780.

[121] M. Wuttig, C. H. Lin, *Twinning pseudoelasticity in in-Tl*, Acta Metallurgica 31 (1983) 1117-1122.

[122] A. G. Zhou, S. Basu, M. W. Barsoum, *Kinking nonlinear elasticity, damping and microyielding of hexagonal close-packed metals*, Acta Materialia 56 (2008) 60-67.

[123] O. Muransky, D. G. Carr, P. Sittner, E. C. Oliver, *In situ neutron diffraction investigation of deformation twinning and pseudoelastic-like behaviour of extruded AZ31 magnesium alloy*, International Journal of Plasticity 25 (2009) 1107-1127.

[124] X. X. Wang, C. Y. Zhang, *Pseudoelastic behavior in an Fe-Mn-Si-Ni-Co shape memory alloy*, Journal of Materials Science Letters 17 (1998) 1795-1796.

[125] S. Daly, G. Ravichandran, K. Bhattacharya, *Stress-induced martensitic phase transformation in thin sheets of Nitinol*, Acta Materialia 55 (2007) 3593-3600.

[126] L. Orgeas, D. Favier, *Stress-induced martensitic transformation of a NiTi alloy in isothermal shear, tension and compression*, Acta Materialia 46 (1998) 5579-5591.

[127] H. F. Chai, C. Laird, *Mechanisms of cyclic softening and cyclic creep in low-carbon steel*, Materials Science and Engineering 93 (1987) 159-174.

[128] C. Laird, *Fatigue hardening mechanisms*, Journal of Metals 36 (1984) 39-39.

[129] T. Lorentzen, M. R. Daymond, B. Clausen, C. N. Tome, *Lattice strain evolution during cyclic loading of stainless steel*, Acta Materialia 50 (2002) 1627-1638.

[130] R. E. Reed-Hill, R. Abbaschian, *Physical metallurgy principles*, 3rd edition, in: PWS Publishing Company, Boston, MA, 1994, pp. 4143-4153.

[131] T. Ungar, *Micro structural parameters from X-ray diffraction peak broadening*, Scripta Materialia 51 (2004) 777-781.

[132] L. Wu, A. Jain, D. W. Brown, G. M. Stoica, S. R. Agnew, B. Clausen, D. E. Fielden, P. K. Liaw, *Twinning-detwinning behavior during the strain-controlled low-cycle fatigue testing of a wrought magnesium alloy, ZK60A*, Acta Materialia 56 (2008) 688-695.

APPENDIX: Tables and Figures

Table 1.1. Possible slip and twin systems in magnesium at room temperature.

Type of system	**System**	**Number of slip modes**	
		Total	**Independent**
basal <a> slip	$(0001)<1\bar{1}\bar{2}0>$	3	2
prismatic <a> slip	$\{10\bar{1}0\}<1\bar{1}\bar{2}0>$	3	2
pyramidal <a> slip	$\{10\bar{1}1\}<1\bar{1}\bar{2}0>$	6	4
pyramidal <c+a> slip	$\{1\bar{1}\bar{2}2\}<\bar{1}\bar{1}23>$	6	5
extension twinning	$\{10\bar{1}2\}<10\bar{1}1>$	N/A	N/A
contraction twinning	$\{10\bar{1}1\}<10\bar{1}2>$	N/A	N/A

Table 3.1. Nominal chemical compositions for the two magnesium alloys (Weight percentage).

Material	**Al**	**Zn**	**Zr**	**Mg**	**Temper**
AZ31B	3.0%	1.0%	n/a	balance	H24
ZK60A	n/a	6.0%	0.5%	balance	T5

Table 5.1. Fitted low-cycle fatigue parameters for the as-extruded ZK60A loaded, respectively, along the ED, TD, and ND directions, based on the Basquin, Coffin-Manson, and Holloman Equations. The "all" column lists the parameters fitted from the combined data from all directions.

Parameters		**Loading directions**			
		ED	**TD**	**ND**	**All**
Coffin-Manson	$\varepsilon_f^{'}$	**2.91 ± 1.18**	**0.45 ± 0.08**	**0.36 ± 0.06**	**0.93 ± 0.37**
	c	**1.04 ± 0.06**	**0.68 ± 0.03**	**0.64 ± 0.02**	**0.82 ± 0.06**
	R^2	0.9700	0.9947	0.9957	0.9221
Basquin	$\sigma_f^{'}$, MPa	**877.39 ± 119.95**	**693.16 ± 60.08**	**661.99 ± 62.16**	**794.03 ± 109.83**
	b	**0.17 ± 0.02**	**0.18 ± 0.01**	**0.17 ± 0.01**	**0.18 ± 0.02**
	R^2	0.9278	0.9843	0.9804	0.8345
Holloman	K', MPa	**463.21 ± 43.83**	**458.47 ± 48.43**	**454.25 ± 48.30**	**347.61 ± 69.58**
	n'	**0.1093 ± 0.02**	**0.18 ± 0.02**	**0.17 ± 0.02**	**0.10 ± 0.03**
	R^2	0.8609	0.9641	0.9635	0.5011

Table 5.2. Fitted low-cycle fatigue parameters for the as-rolled AZ31B alloy loaded, respectively, along the RD, TD, and ND directions, based on the Basquin, Coffin-Manson, and Holloman Equations. The "all" column lists the parameters fitted from the combined data from all directions.

Parameters		**Loading directions**			
		RD	**TD**	**ND**	**All**
Coffin-Manson	$\varepsilon_f^{'}$	**1.54 ± 0.53**	**0.59 ± 0.25**	**0.36 ± 0.07**	**0.75 ± 0.03**
	c	**0.90 ± 0.05**	**0.78 ± 0.07**	**0.70 ± 0.03**	**0.78 ± 0.03**
	R^2	0.9874	0.9675	0.9888	0.9755
Basquin	$\sigma_f^{'}$, MPa	**693.04 ± 126.84**	**686.12 ± 87.63**	**1361.29 ± 208.73**	**921.26 ± 99.86**
	b	**0.15 ± 0.03**	**0.16 ± 0.02**	**0.26 ± 0.02**	**0.21 ± 0.02**
	R^2	0.8999	0.9443	0.8662	0.9071
Holloman	K', MPa	**375.20 ± 32.18**	**393.04 ± 13.70**	**731.48 ± 75.64**	**471.32 ± 43.31**
	n'	**0.11 ± 0.01**	**0.13 ± 0.01**	**0.25 ± 0.02**	**0.16 ± 0.02**
	R^2	0.9365	0.9910	0.9638	0.8666

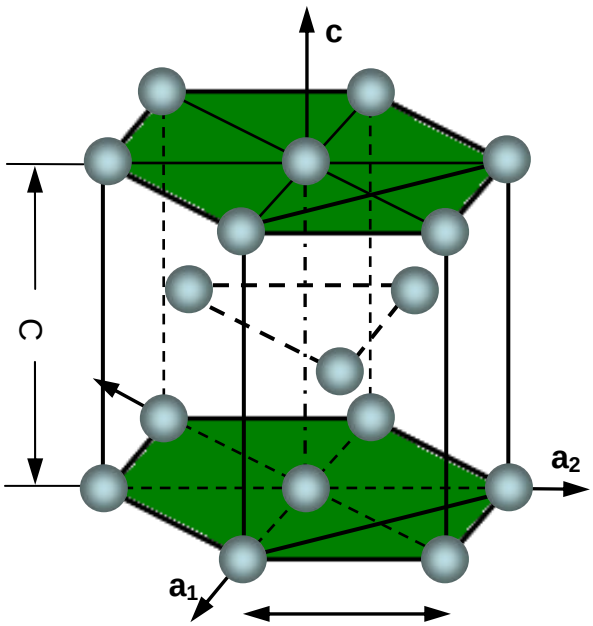

Cd	=	1.886	
Zn	=	1.856	Above normal
		1.633	Hard – sphere model
Co	=	1.628	Below normal
Mg	=	1.624	
Re	=	1.615	
Tl	=	1.598	
Zr	=	1.593	
Ti	=	1.587	
Hf	=	1.581	
Y	=	1.571	
Be	=	1.568	

(a)

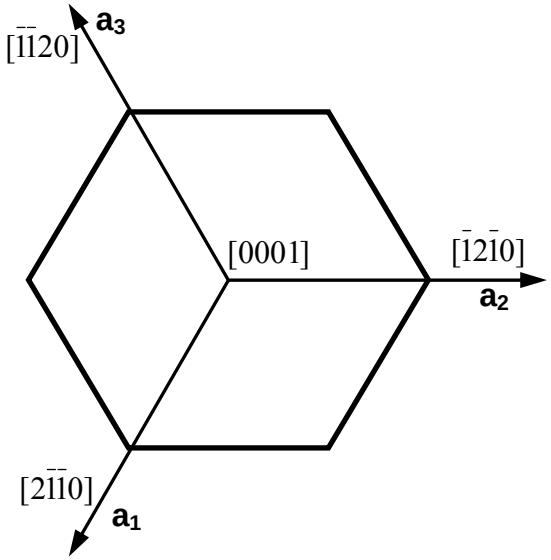

(b)

Figure 1.1. Structure of a hcp crystal [6, 8].

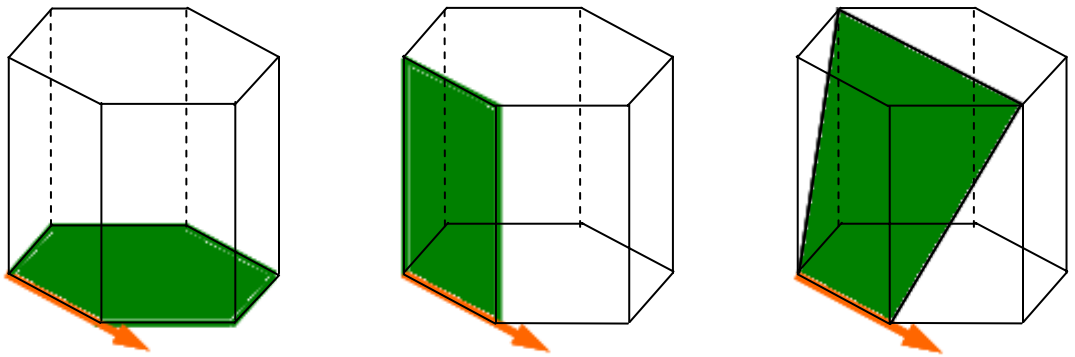

(a)

$(0002)\langle 1\bar{1}20\rangle$

basal <a> slip

(b)

$\{1\bar{1}10\}\langle 1\bar{1}20\rangle$

prismatic <a>slip

(c)

$\{10\bar{1}1\}\langle 1\bar{1}20\rangle$

pyramidal <a> slip

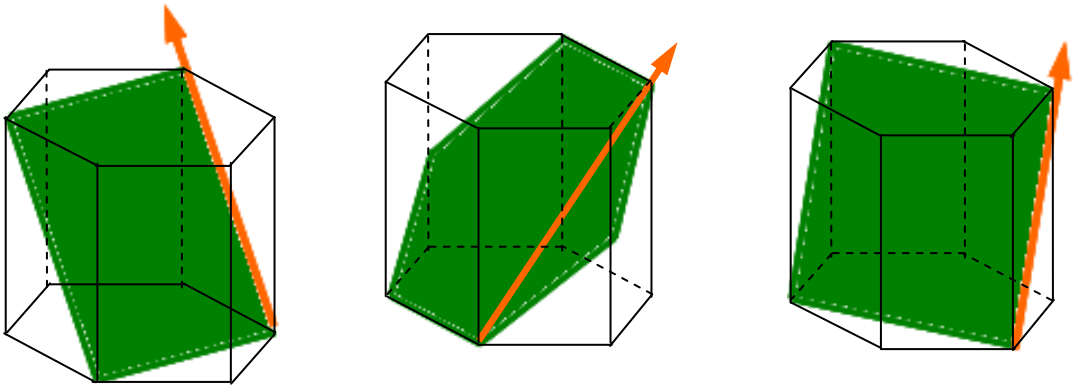

(d)

$\{1\bar{1}22\}\langle 1\bar{1}23\rangle$

pyramidal <c+a> slip

(e)

$\{10\bar{1}2\}\langle 10\bar{1}1\rangle$

extension twin

(f)

$\{10\bar{1}1\}\langle 10\bar{1}2\rangle$

contraction twin

Figure 1.2. Potential deformation systems in magnesium [8, 9, 11].

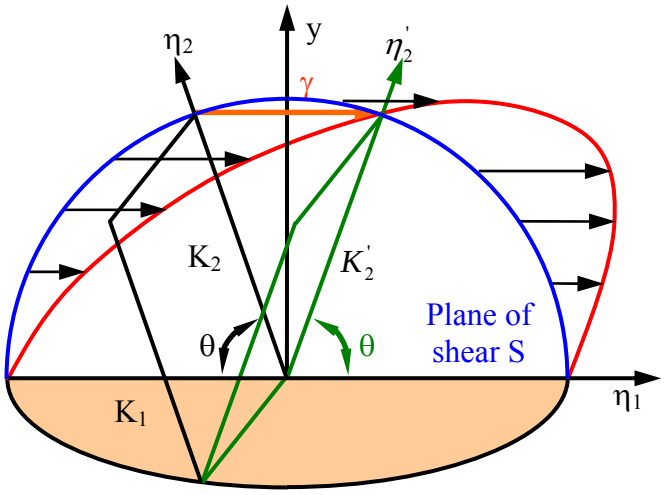

Figure 1.3. Crystallographic elements of twinning [5, 6]

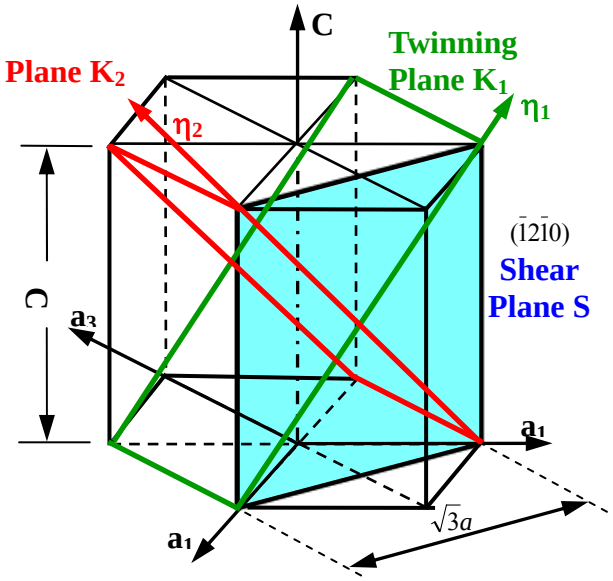

Figure 1.4. Twinning elements of twinning mode $\{10\bar{1}2\}<10\bar{1}1>$ [5].

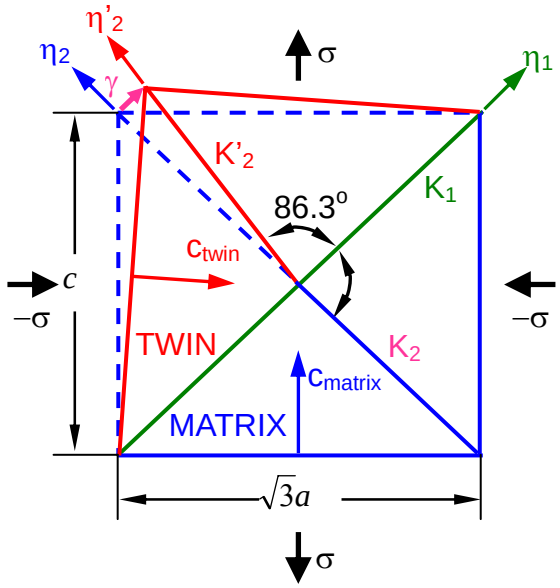

(a) $c/a < \sqrt{3}$, e.g., Mg

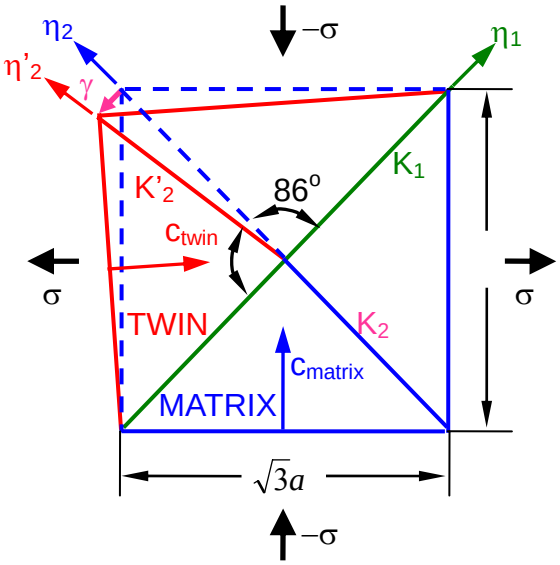

(b) $c/a > \sqrt{3}$, e.g., Zn

Figure 1.5. Dependence of deformation direction on c/a ratio in the example of $\{10\bar{1}2\}<10\bar{1}1>$ twinning for $c/a < \sqrt{3}$ (a) and for $c/a > \sqrt{3}$ (b) [6, 18].

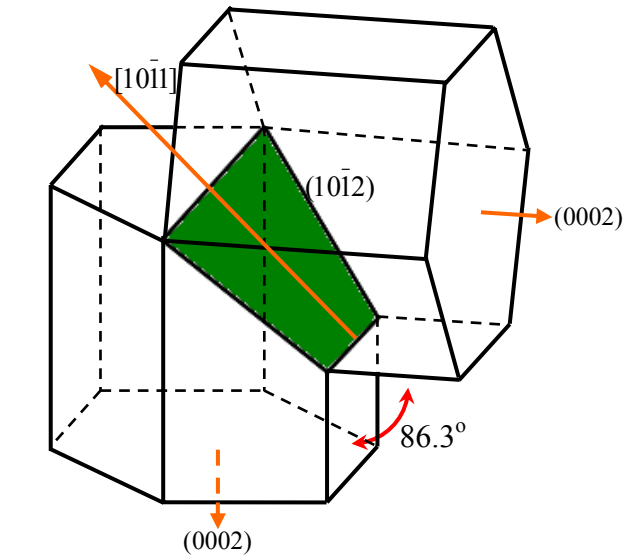

(a)

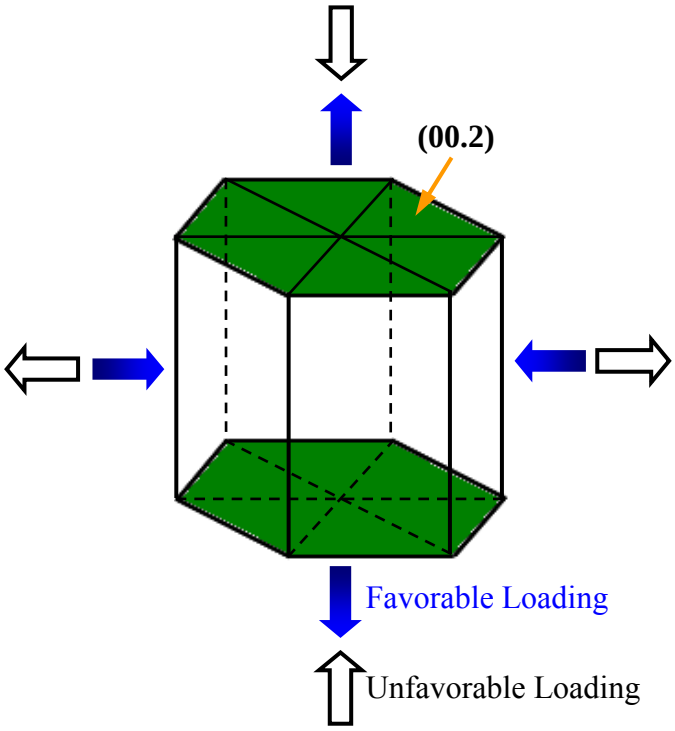

(b)

Figure 1.6. Schematic of the $\{10\bar{1}2\}<10\bar{1}1>$ extension twin system in magnesium: (a) 86.3° reorientation of the twin grain relative to the parent grain [23]; (b) applied loading directions with respect to the c-axis. The solid arrows indicate the favorable loading directions, and the open arrows indicate the unfavorable loadings [2].

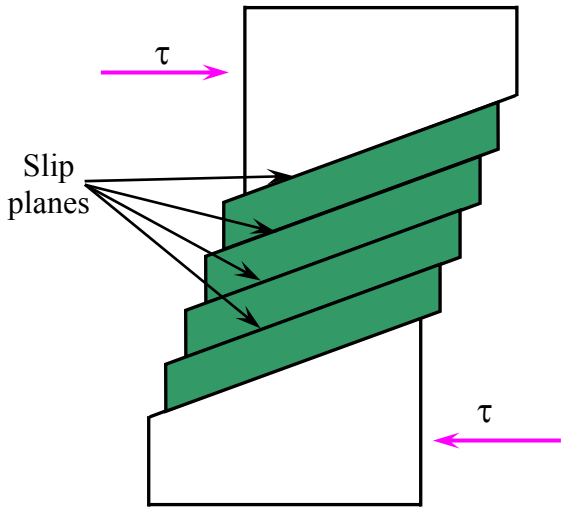

(a) Deformation by dislocation slip

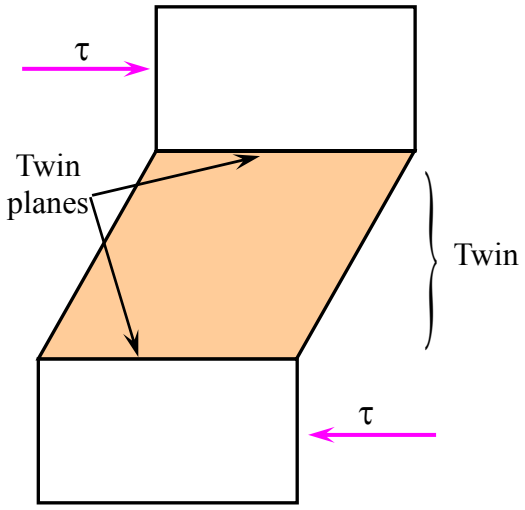

(b) Deformation by twinning

Figure 1.7. For a single crystal subjected to a shear stress τ, a) deformation by dislocation slip; and b) deformation fby twinning [7].

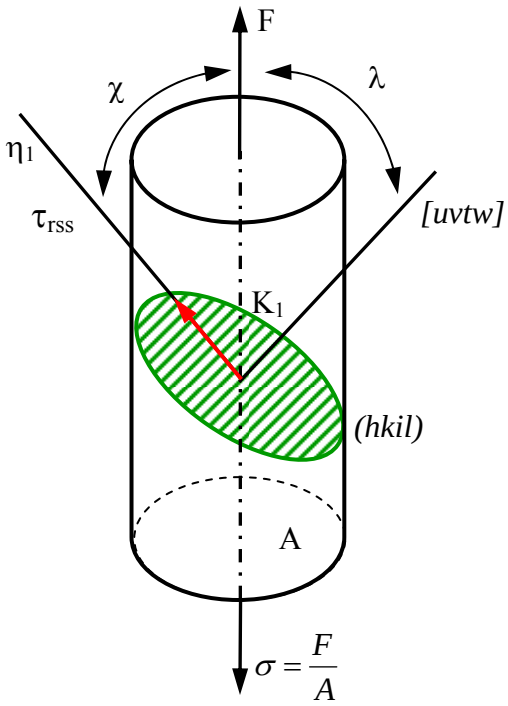

Figure 1.8. Relationship between the resolved shear stress acting on the deformation system and the force applied externally on the single-crystal rod. [6, 7].

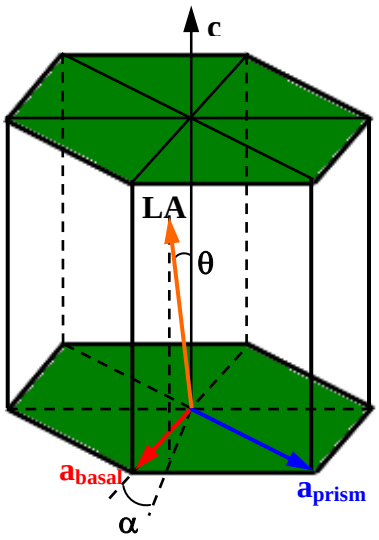

(a)

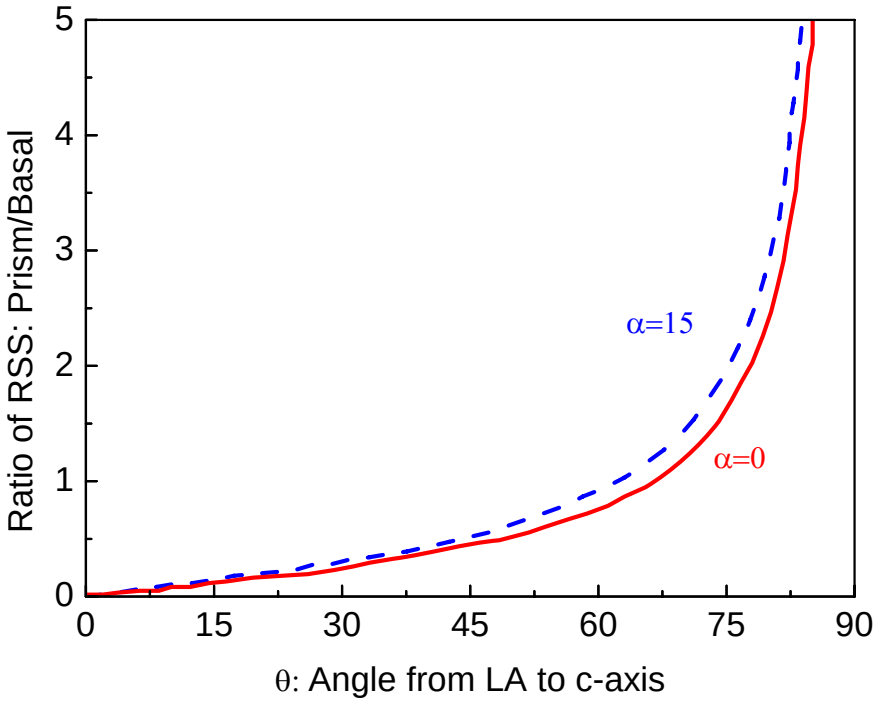

(b)

Figure 1.9. a) Schematic of single crystal under uniaxial loading; (b) Variation of the ratio of resolved shear stress (RSS) between prismatic and basal <a> slips with an angle between the loading axis (LA) and c-axis [29].

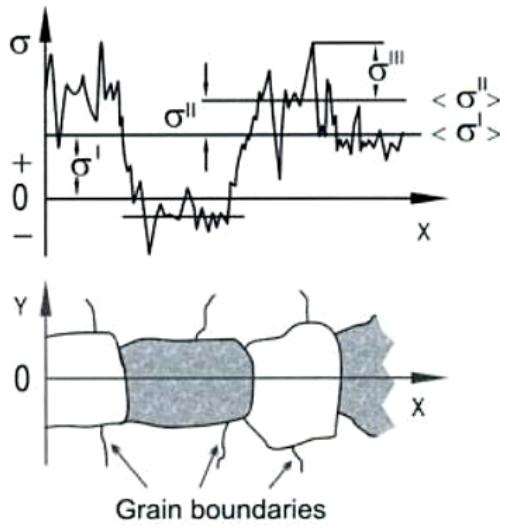

Figure 1.10. Definition of type I (σ^{I}), type II (σ^{II}), and type III (σ^{III}) internal-stresses. The same diagram could be drawn with strain types ε^{I}, ε^{II}, and ε^{III}, respectively [31].

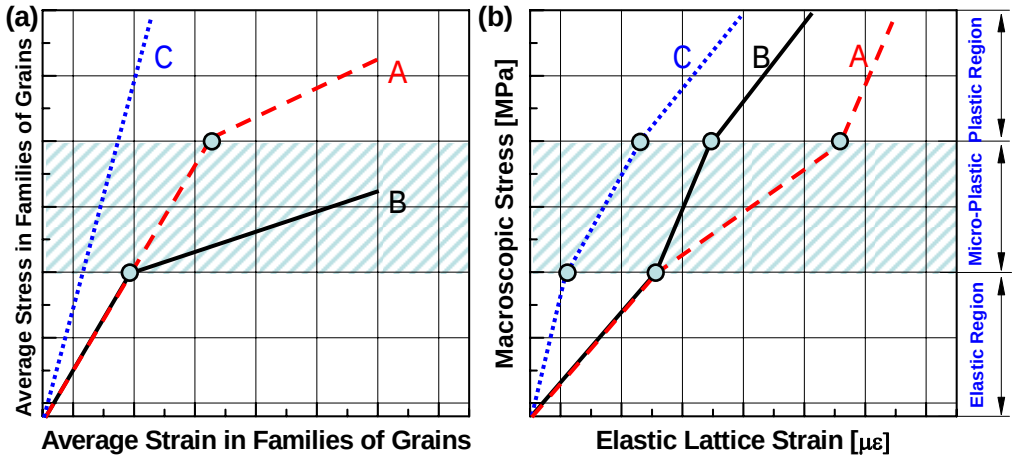

Elastic Region:
Elastic response for the A, B grain families is different from that of C grain family due to the elastic anisotropy.

Micro-Plastic Region:
The external load is redistributed from plastically softer grain family (B) towards plastically harder grain family (A, C).

Plastic Region:
Plastic deformation proceeds cooperatively in most of the polycrystal grain families (A, B).

Figure 1.11. Schematic representation of the load redistribution (a); together with the evolution of elastic lattice strains (b) in elastically and plastically anisotropic single phase material. The letters A–C denote 3 different families/orientations of equally oriented grains with respect to the load axis [34].

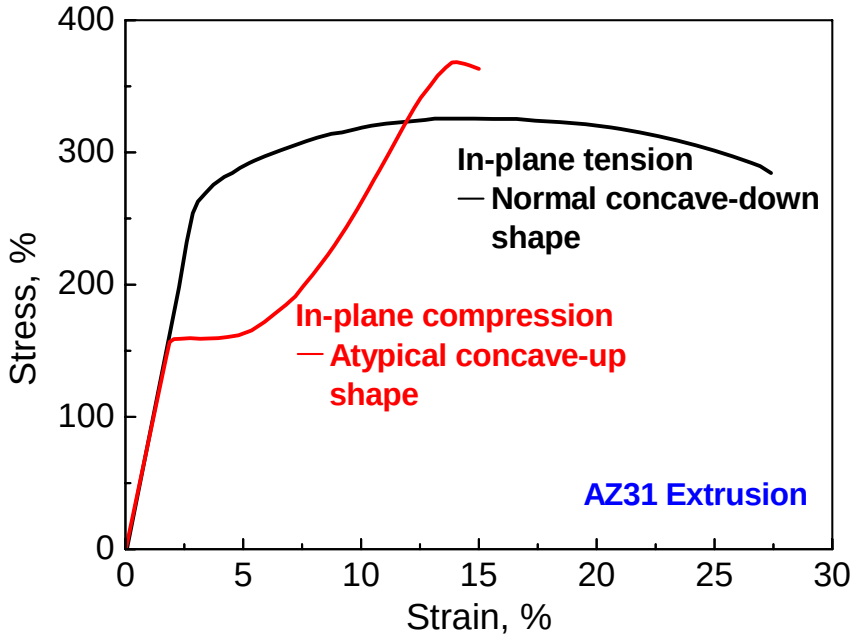

Figure 2.1. Typical engineering compressive and tensile stress-strain curves of the as-extruded AZ31 samples loaded parallel to the extrusion direction showing the well-known tension-compression asymmetry [23].

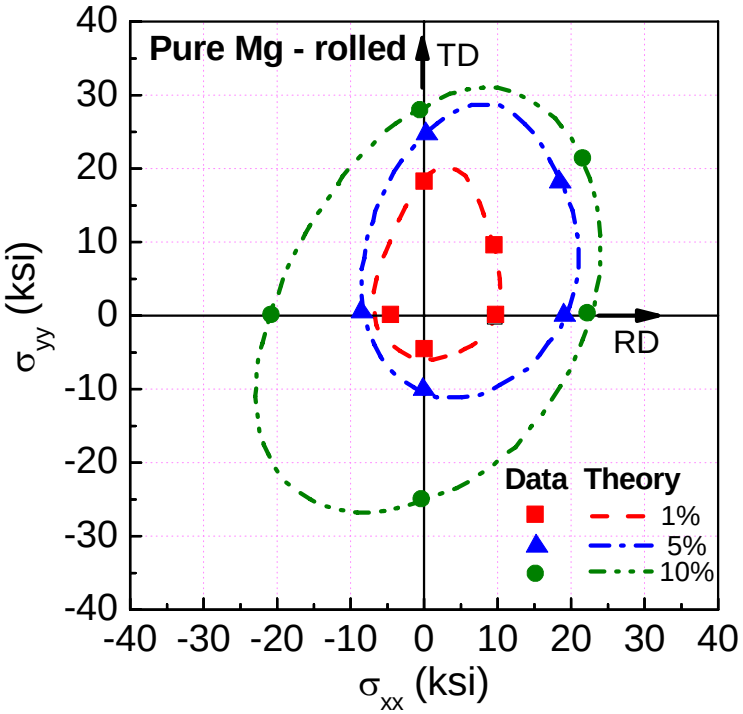

Figure 2.2. Comparison between the plane stress yield loci for a magnesium sheet predicted by the proposed theory and experiments [44].

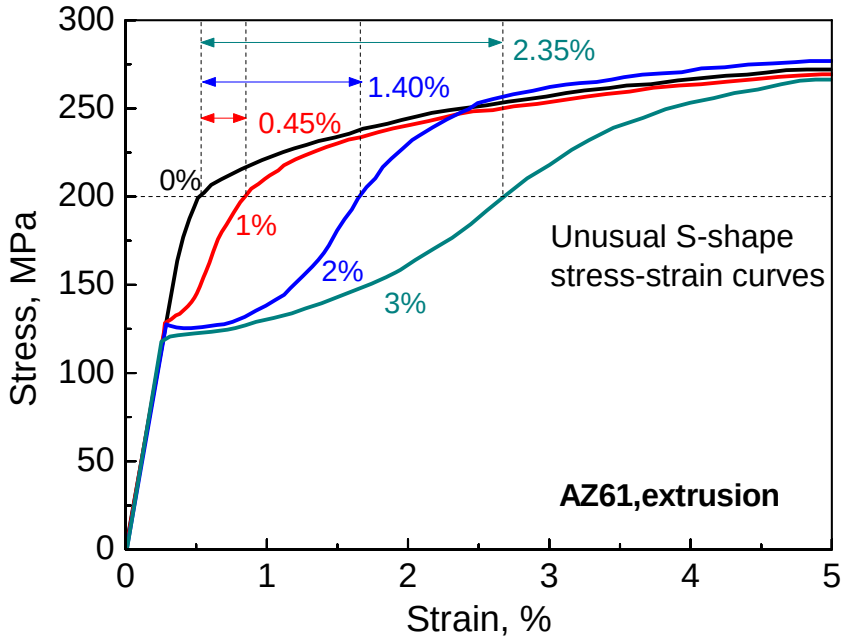

Figure 2.3. The effect of a compressive plastic pre-deformation on the subsequent tensile stress-strain curves loaded along the extrusion direction. The figure shows the unusual S-shape stress-strain curves due to detwinning [26].

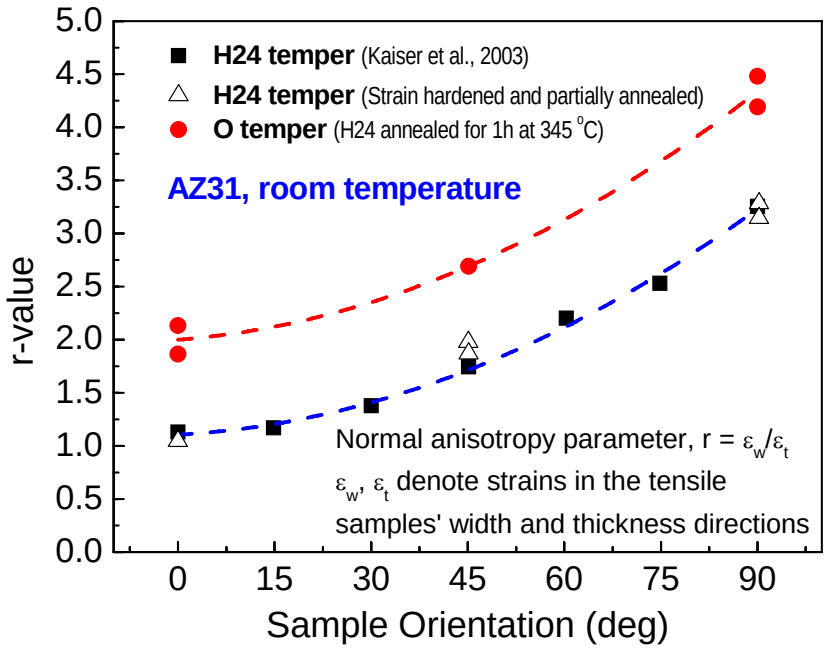

Figure 2.4. Plot of normal anisotropy as a function of sample orientation at room temperature [4].

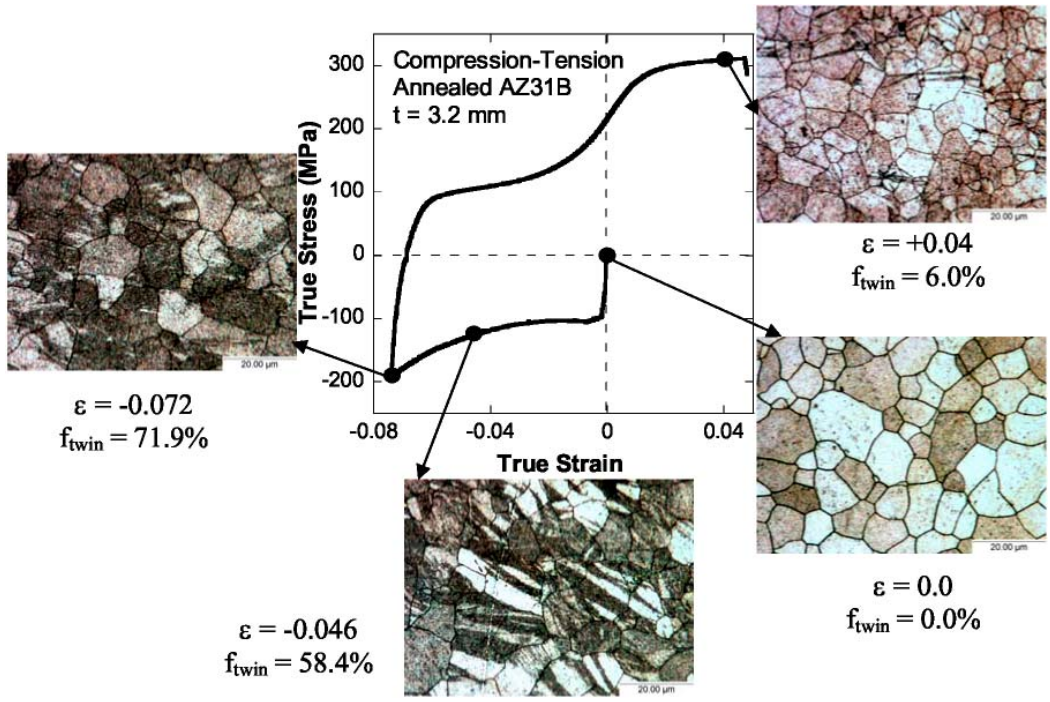

Figure 2.5. Evolution of microstructure under tensile reloading following in-plane compression of an annealed AZ31B sheet [47].

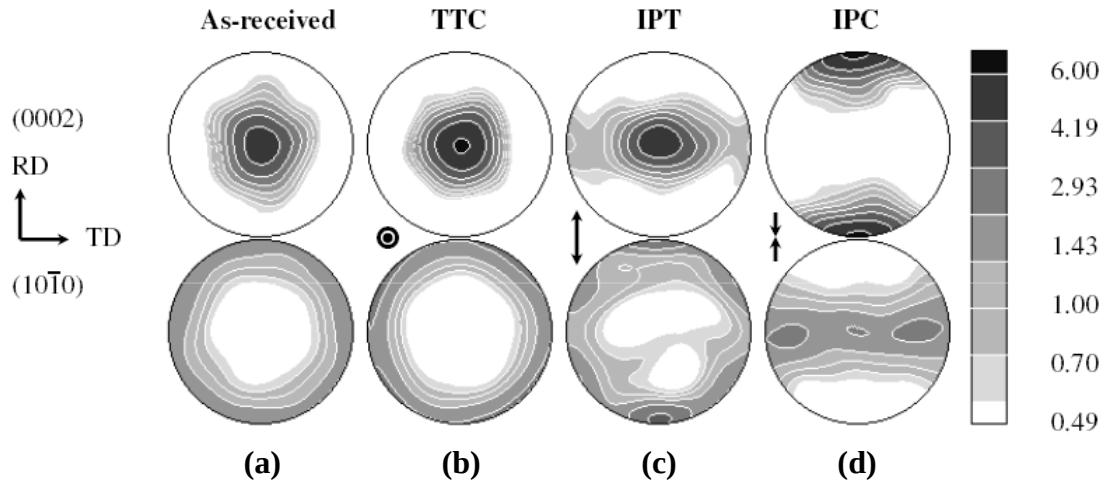

Figure 2.6. Basal and prismatic pole figures from the (a) as-received plate, (b) through-thickness compressed, (c) in-plane tensile tested, and (d) in-plane compressed samples. Arrows in (b), (c), and (d) denote the stress direction in the same coordinate system [36].

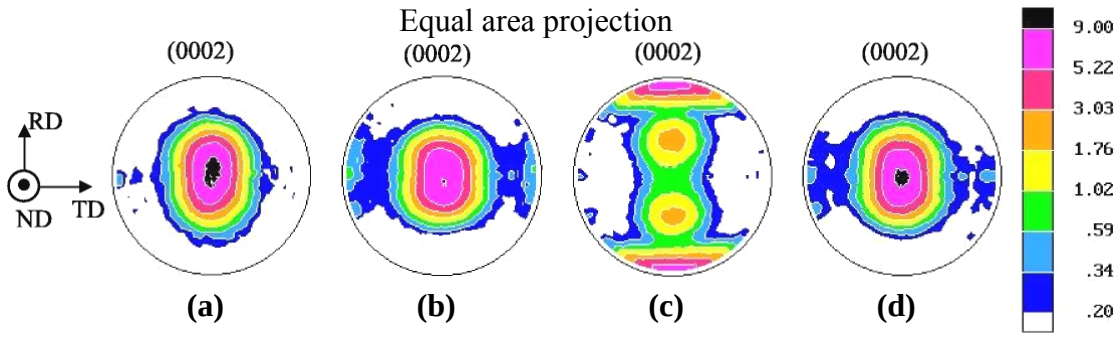

Figure 2.7. Basal (00.2) pole figures in various deformation stages: (a) initial texture, (b) texture after tension along RD (0.1 tensile strain); (c) texture after compression along RD (0.07 compressive strain); and (d) texture after reverse tension along RD (0.1 reverse tensile strain after compression) [47, 54].

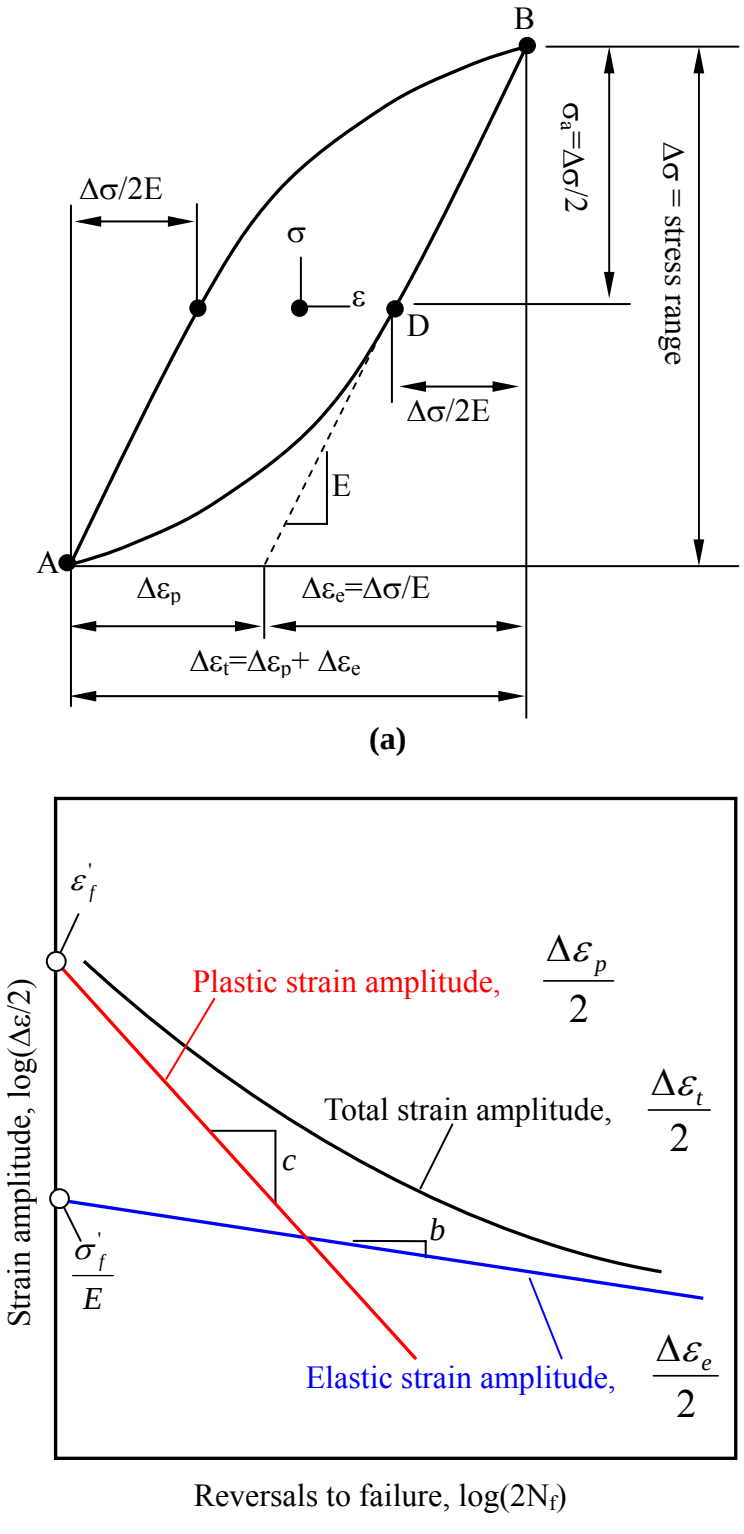

Figure 2.8. Parameters associated with strain-life approach to fatigue [56].

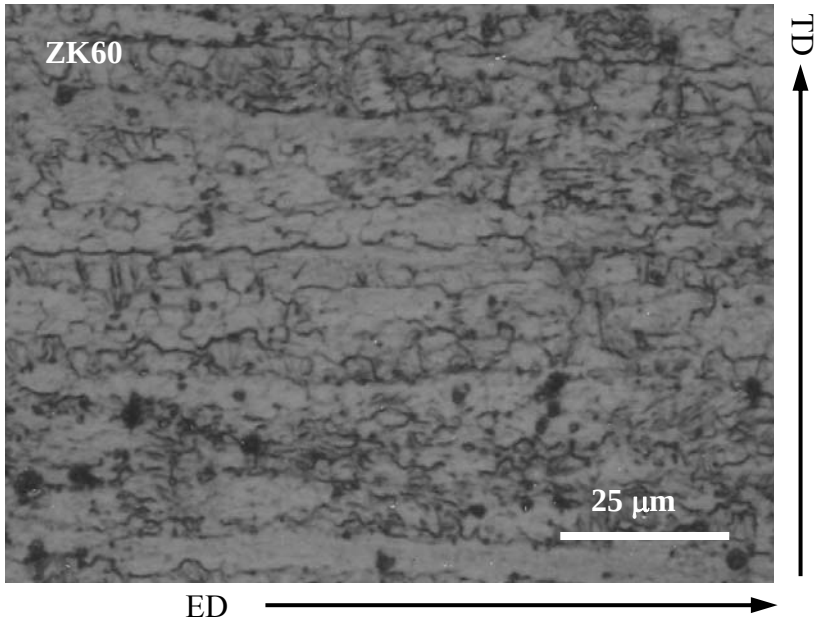

(a) As-extruded magnesium alloy, ZK60A

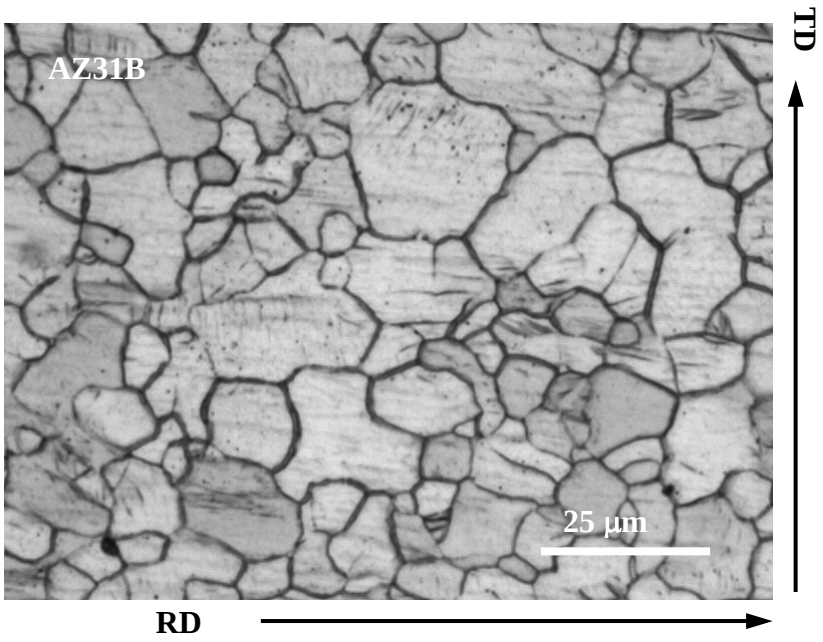

(b) As-rolled magnesium alloy, AZ31B

Figure 3.1. Initial optical microstructures, respectively, for the as-extruded magnesium alloy, ZK60A (a); and the as-rolled magnesium alloy, AZ31B (b).

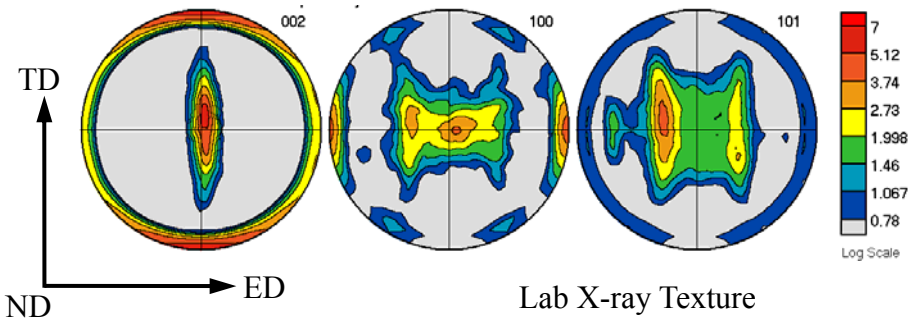

(a) Initial texture for the as-extruded ZK60A

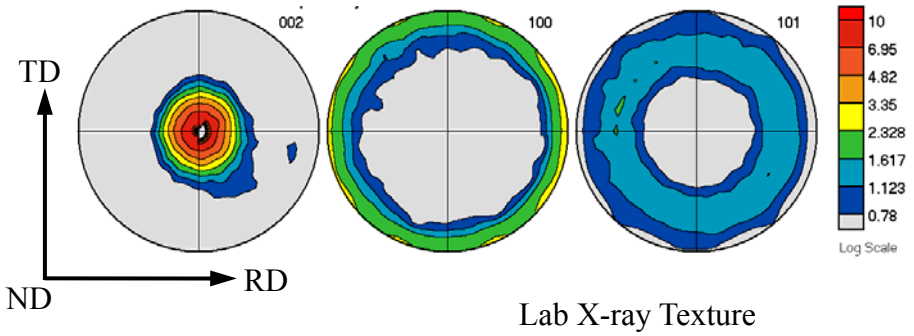

(b) Initial texture for the as-rolled AZ31B

Figure 3.2. Initial crystallographic textures, respectively, for the as-extruded magnesium alloy, ZK60A (a); and the as-rolled magnesium alloy, AZ31B (b). The scales indicate the relative diffraction intensity (1.0 = random).

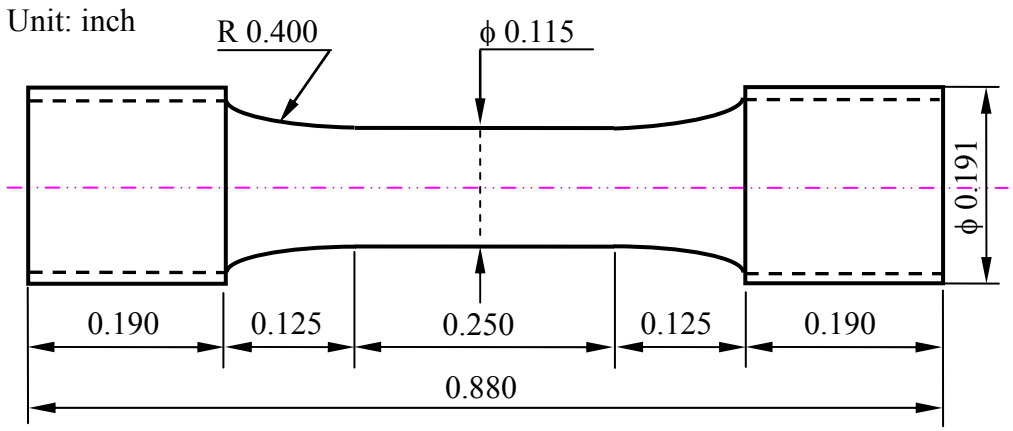

(a) Sample geometry for the mechanical testings and synchrotron measurement at APS

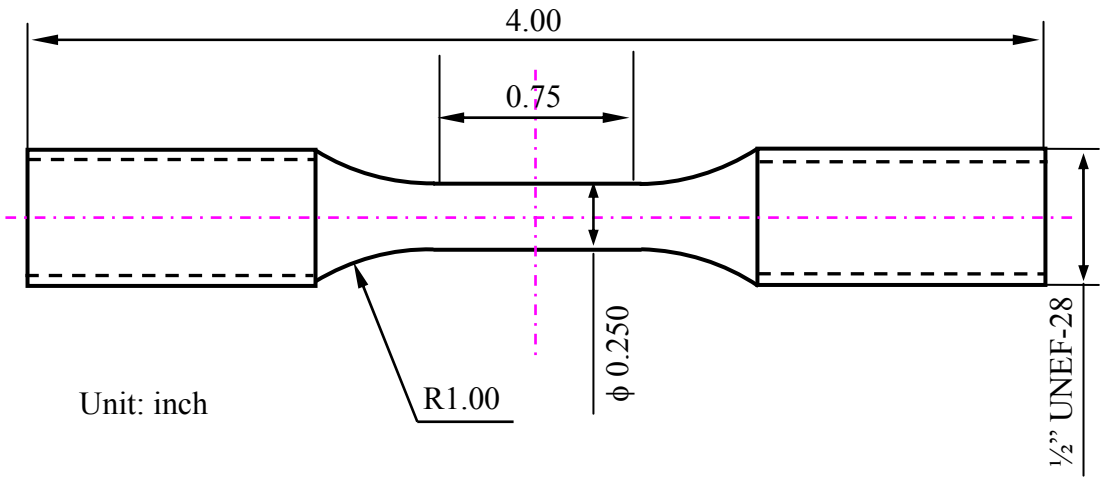

(b) Sample geometry for neutron measurement at SMARTS

Figure 3.3. Sample geometfries for mechanical testings and synchrotron measurements at APS (a); and for neutron measurements at SMARTS (b).

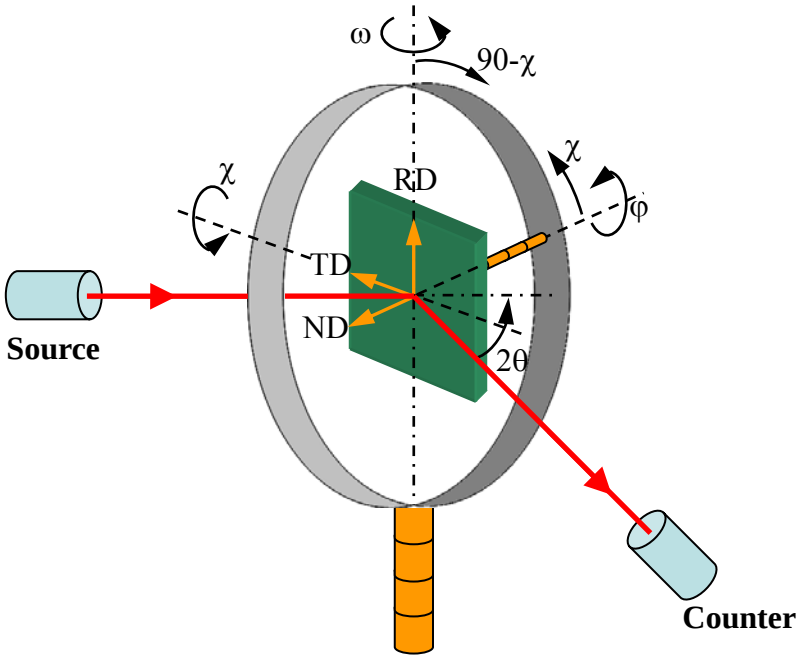

(a) Goniometer texture measurement in reflection geometry

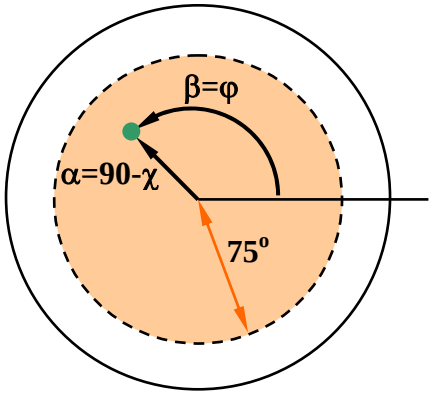

(b) A pole in reflection geometry

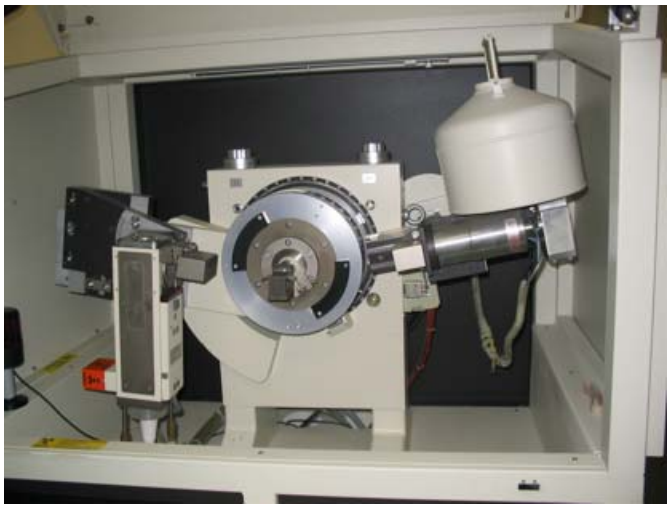

(c) Scintag XDS2000 pole figure diffractometer

Figure 3.4. Diffraction in a four-circle pole figure goniometer and definition of instrument angles: a) Goniometer texture measurement in reflection geometry; b) Definition of a pole in reflection geometry; and (c) Scintag XDS2000 pole figure diffractometer [28, 94].

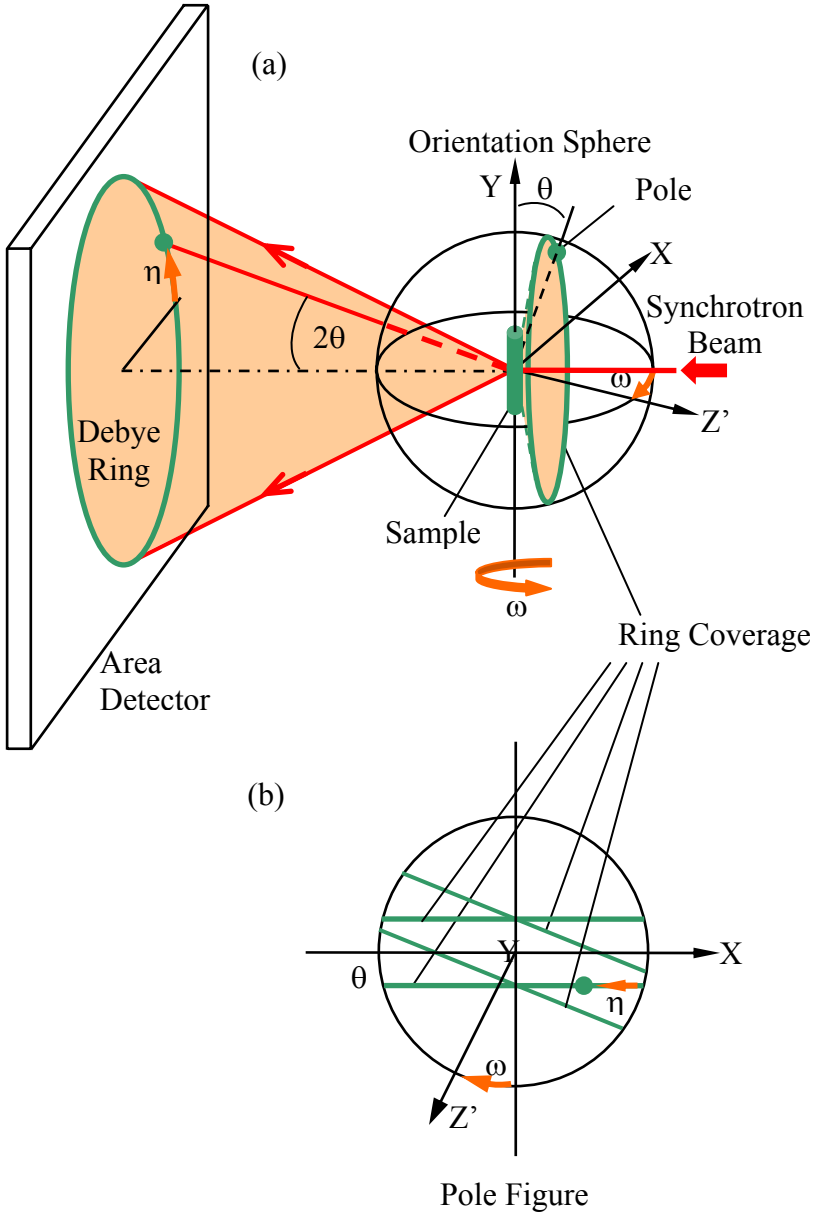

Figure 3.5. (a) Diffraction geometry of a synchrotron texture measurement in transmission; the sample is rotated around the Y axis (ω rotation) for better pole-figure coverage. In the corresponding pole figure (b), the small circle in (a) appears as a pair of parallel straight lines. The indicated 'pole' in (a) corresponds to the scattering vector for a specific Debye ring diffracted at a 2θ angle and at an angle, η, along the ring [86].

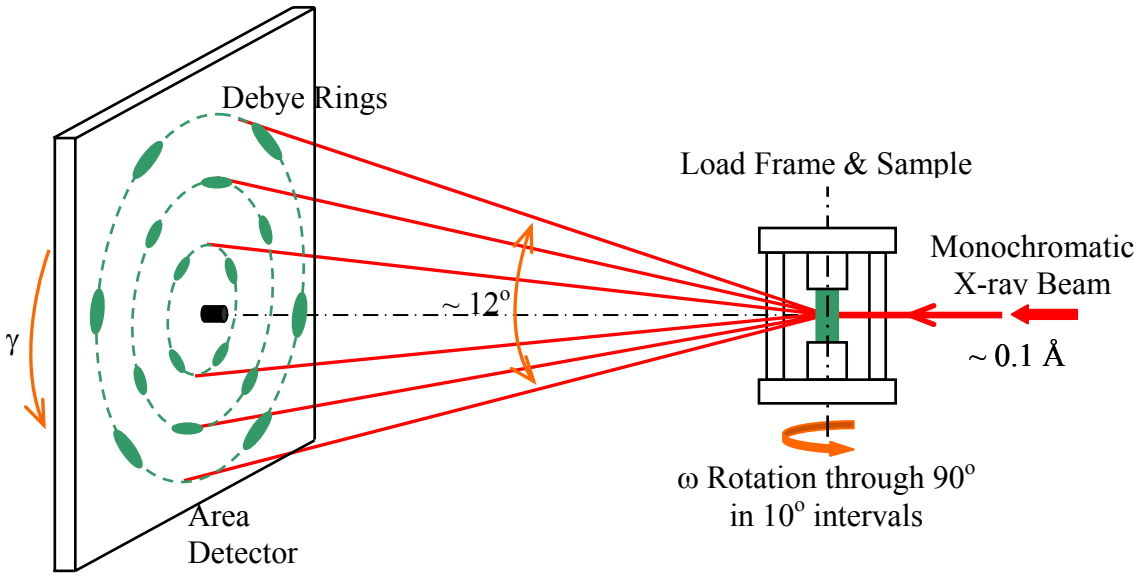

(a) A schematic of texture measurement at APS

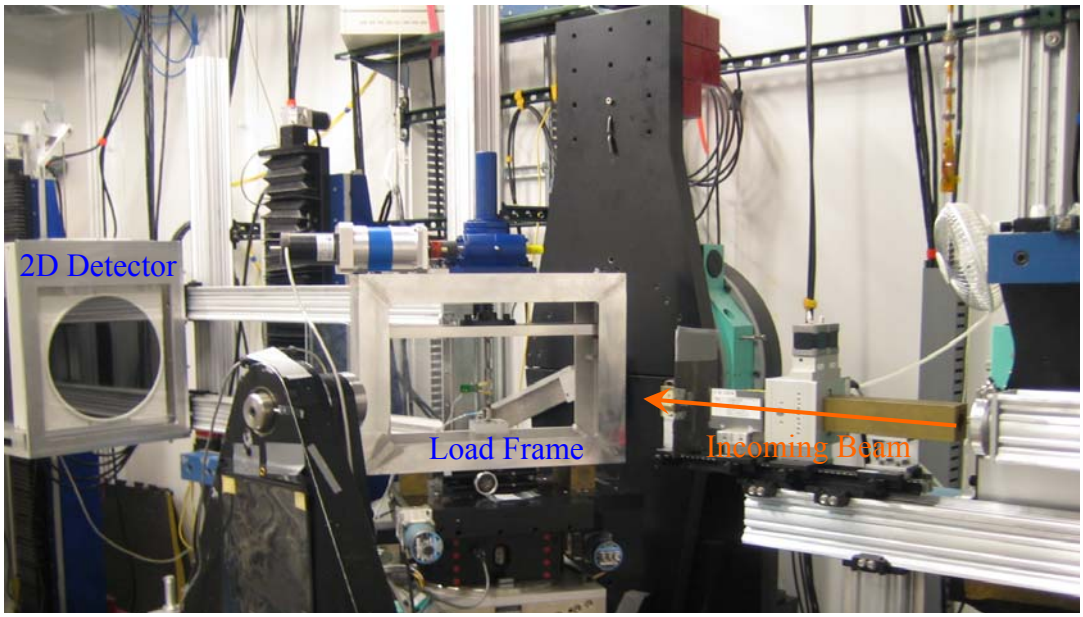

(b) A real view of the beamline 11-ID-C at APS

Figure 3.6. A schematic view of the texture measurement configuration under transmission geometry (a), with the beamline 11-ID-C at APS (b). Diffraction of high-energy synchrotron X-rays in a polycrystalline sample, registered on an area detector.

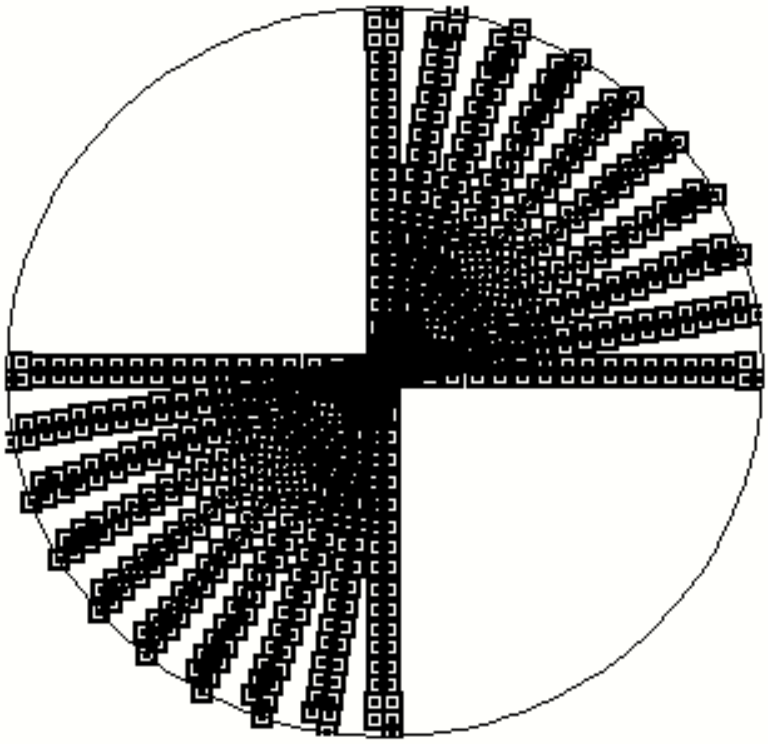

Figure 3.7. Pole figure coverage (Equal area projection) from 10 sample rotations through 90^{o} in 10^{o} interval corresponding to Figure 3.6.

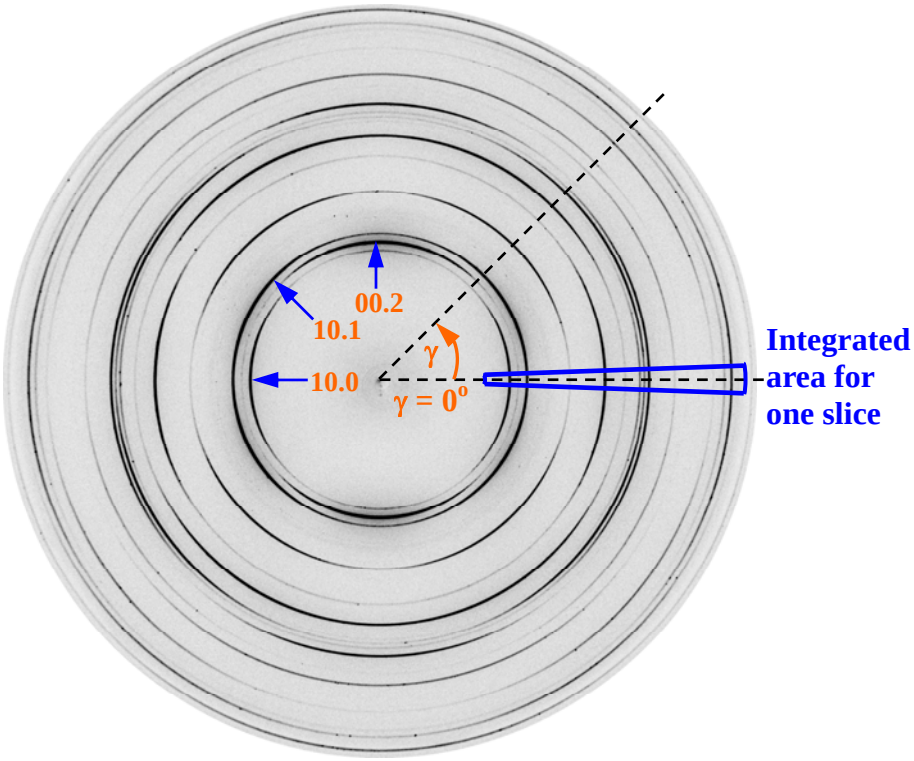

(a) A diffraction image of the as-rolled AZ31 alloy

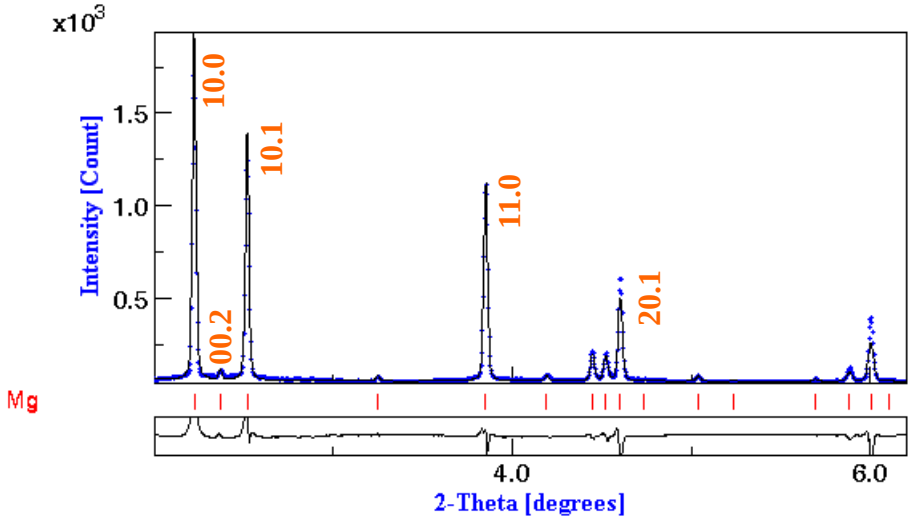

(b) The integrated and fitted profiles corresponding to (a)

Figure 3.8. A typical example of the two-dimensional synchrotron diffraction images used in the Rietveld texture analysis of ZK60A magnesium alloy using MAUD. The Debye rings show strong intensity variations along the azimuth, intuitively indicative of texture.

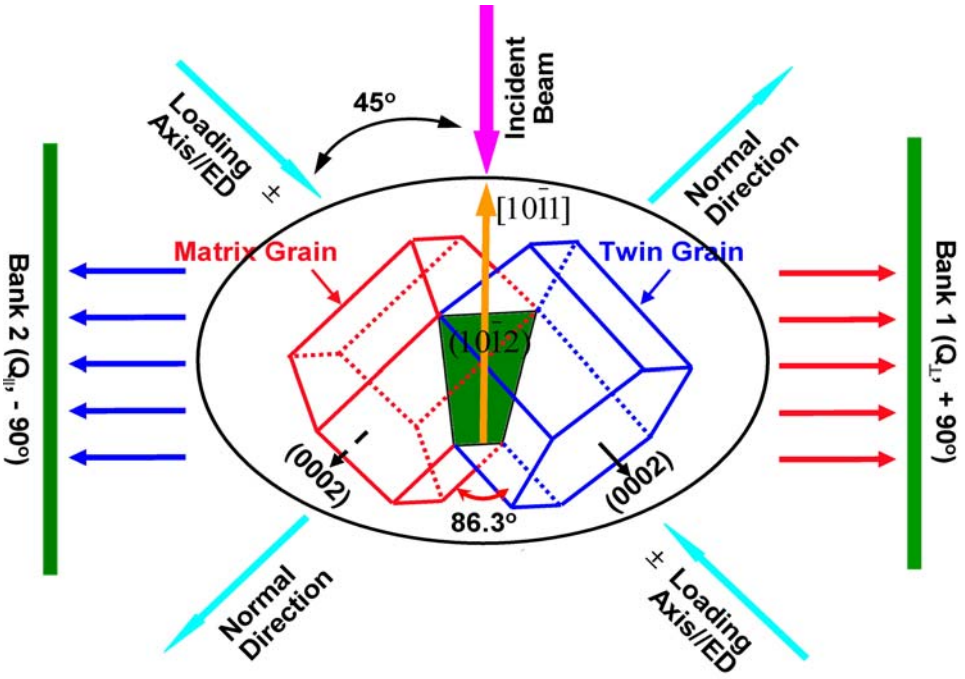

(a) A schematic of the SMARTS at LANSCE

(b) A real view of the SMARTS

Figure 3.9. Experimental setup on the SMARTS at LANSCE, LANL: a) A schematic of the SMARTS; and b) A real view of the SMARTS.

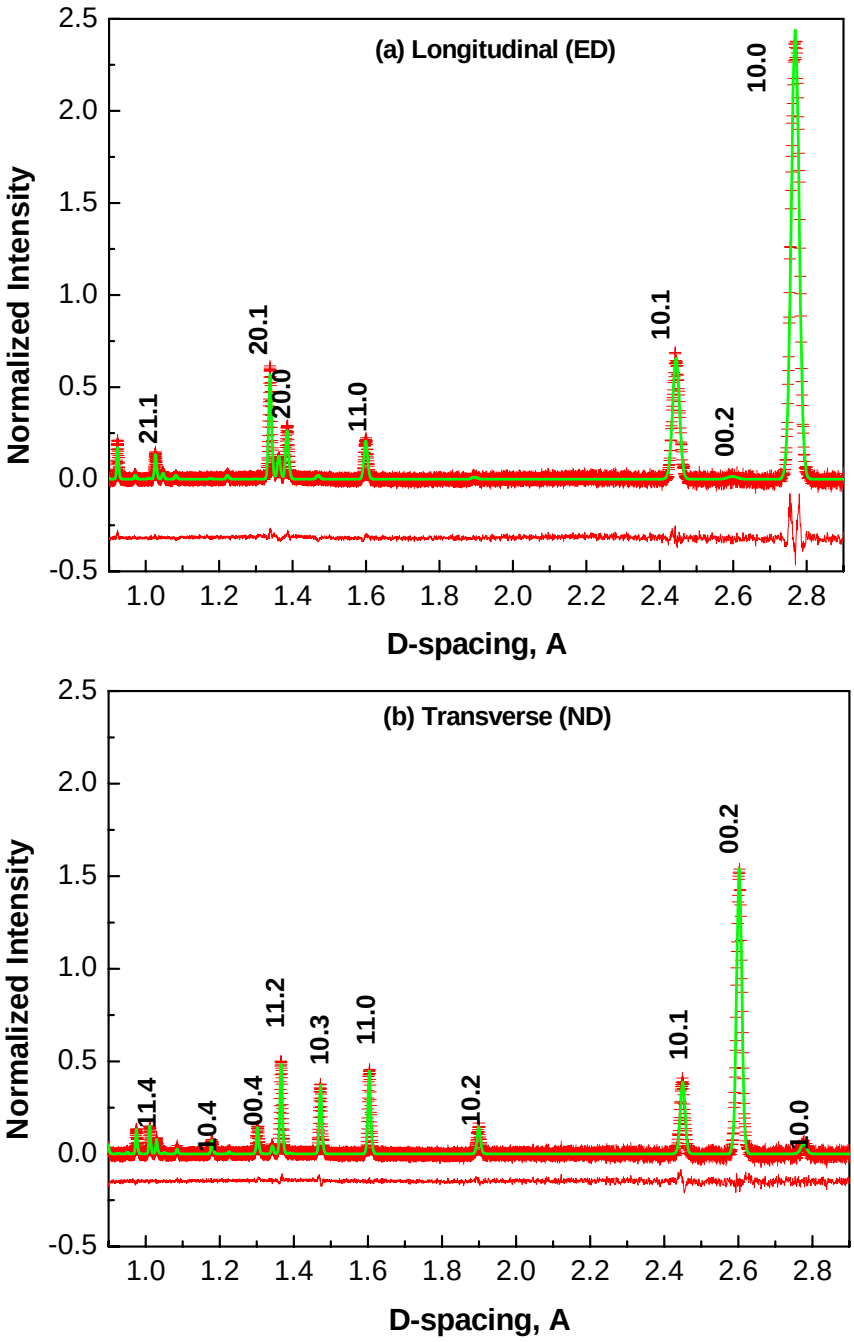

Figure 3.10. Diffraction patterns for the as-extruded ZK60A sample measured on SMARTS: a) Parallel to the loading axis (ED), and b) transverse to the loading axis (ND). The crosses are the measured data, the fitted line is the Rietveld refinement, with a few (*hk.l)* labeled. The lower curve is the difference between the measured data and the calculated curve.

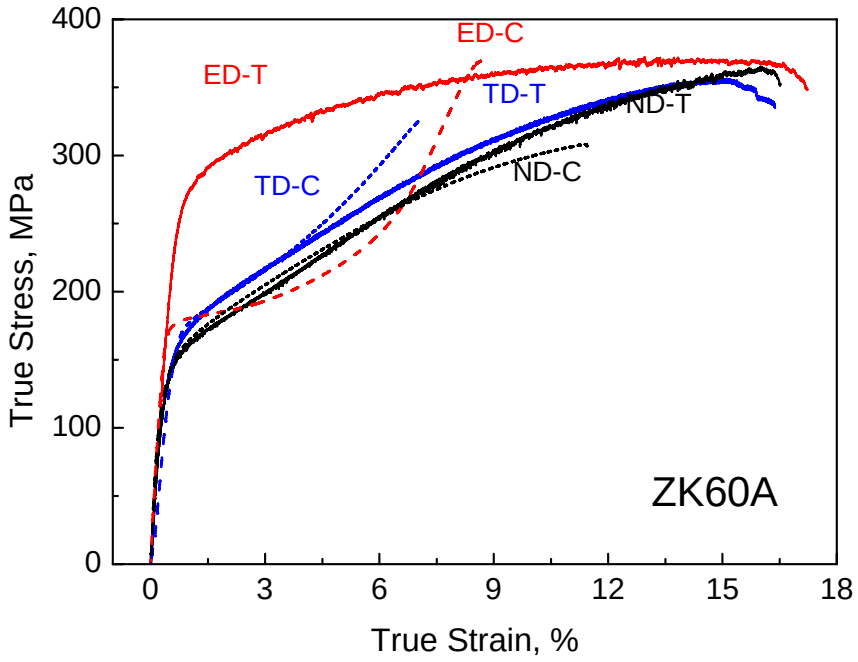

Figure 4.1. The monotonic mechanical responses loaded, respectively, along the RD, TD and ND directions both under compression (C) and tension (T) of the ZK60A alloy. Solid lines for tension, and dashed lines for compression.

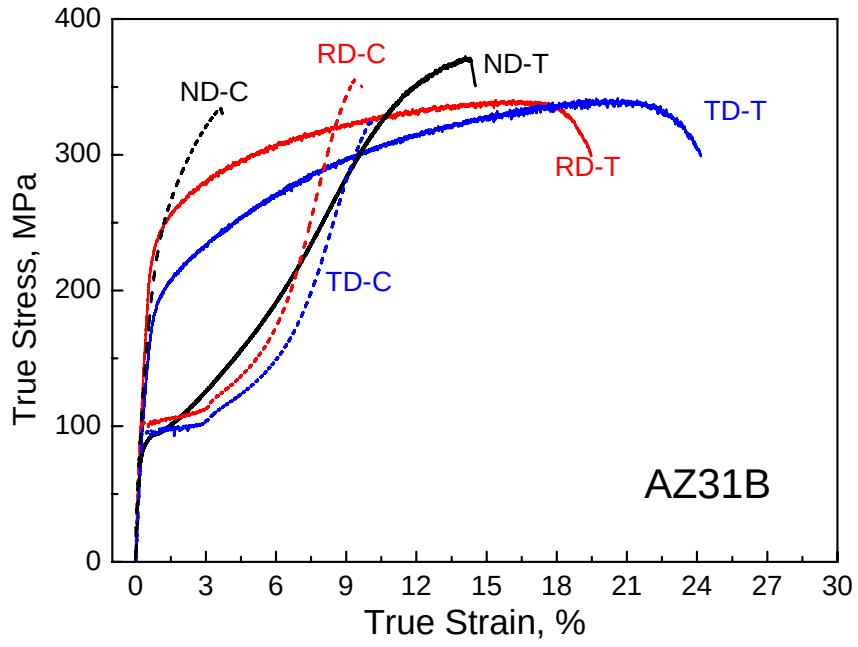

Figure 4.2. The monotonic mechanical responses loaded, respectively, along the RD, TD and ND directions both under compression (C) and tension (T) of the AZ31B alloy. Solid lines for tension, and dashed lines for compression.

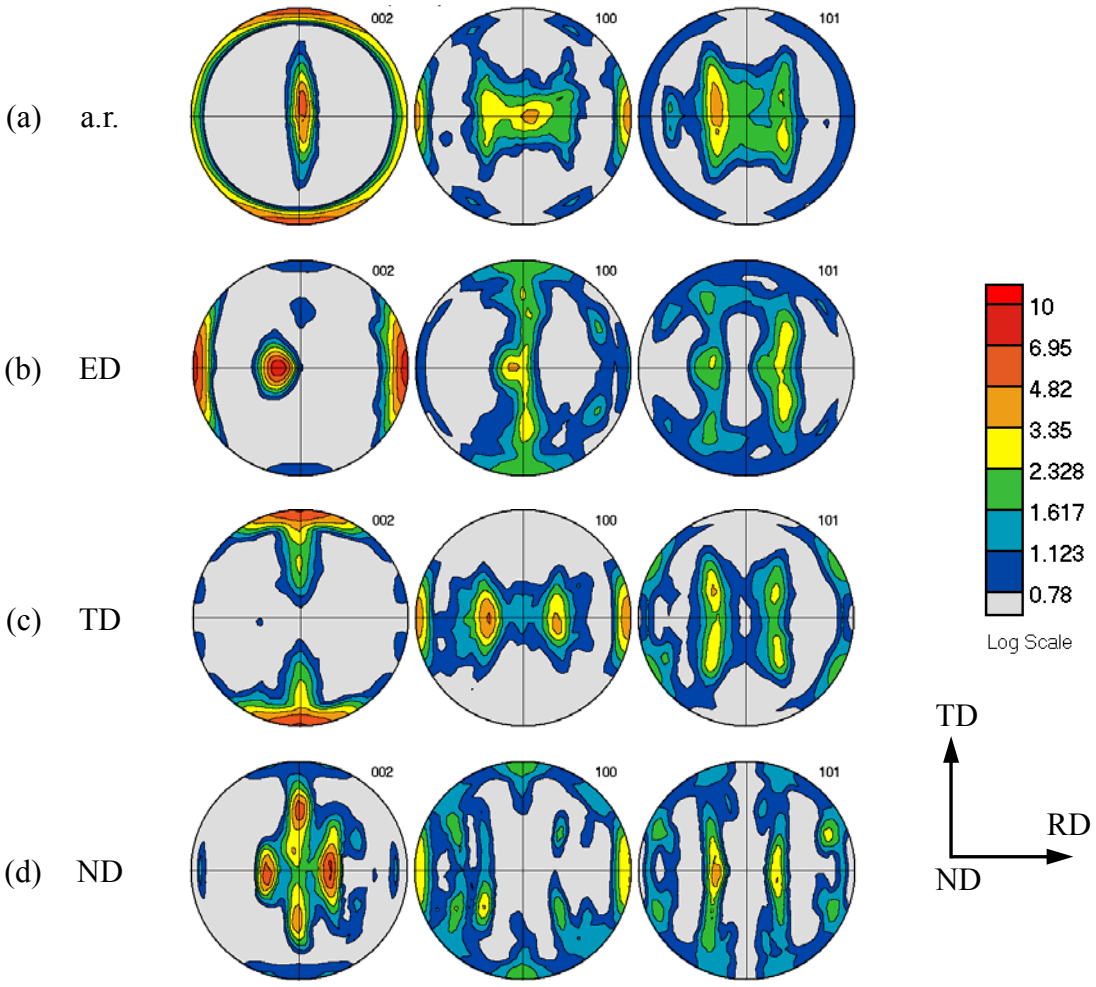

Figure 4.3. Texture evolutions under compression of the ZK60A alloy along the three directions: a) the as-received texture; b) 8% compression along the ED; c) 8% compression along the TD; and d) 8% strain along the ND.

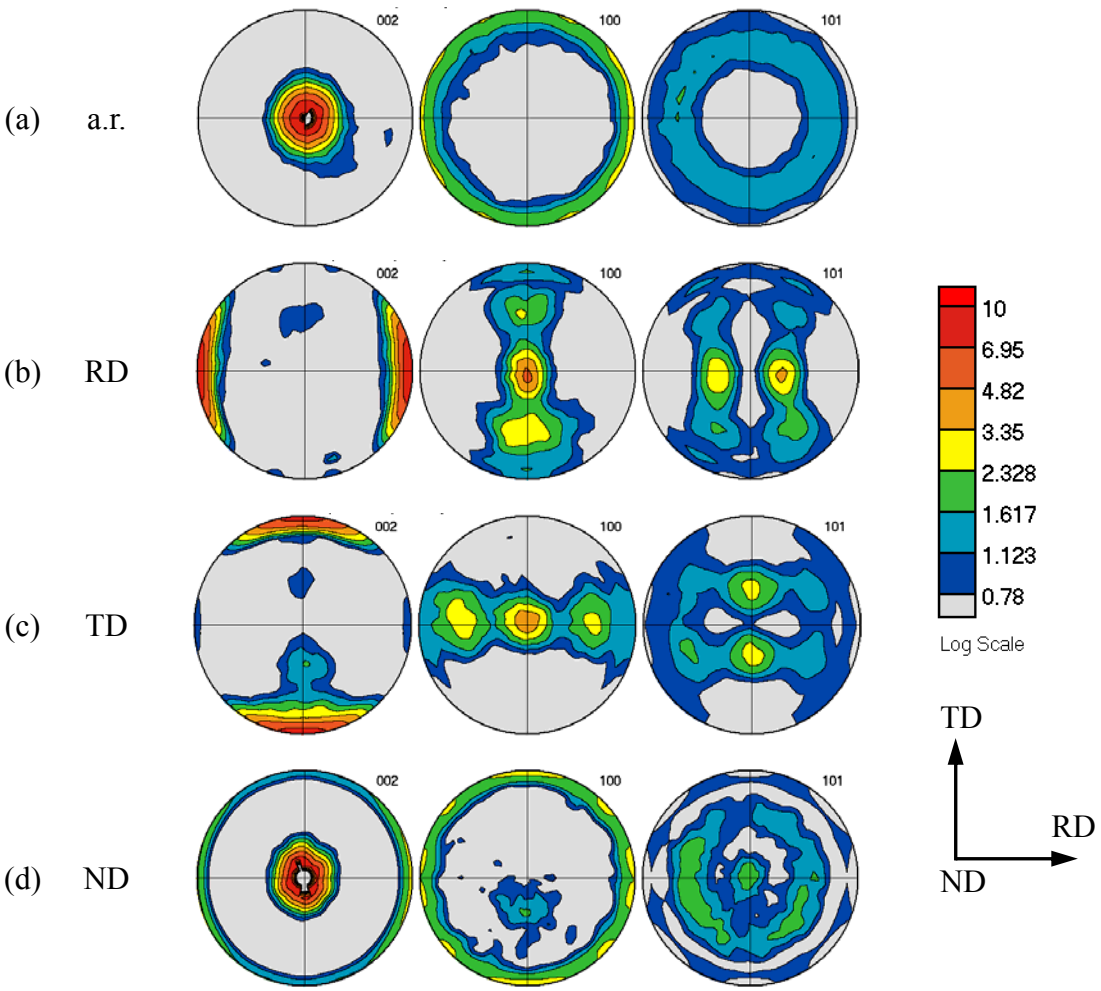

Figure 4.4. Texture evolutions under compression of the AZ31B alloy along the three directions: a) the as-received texture; b) 8% compression along the RD; c) 8% compression along the TD; and d) 8% strain along the ND.

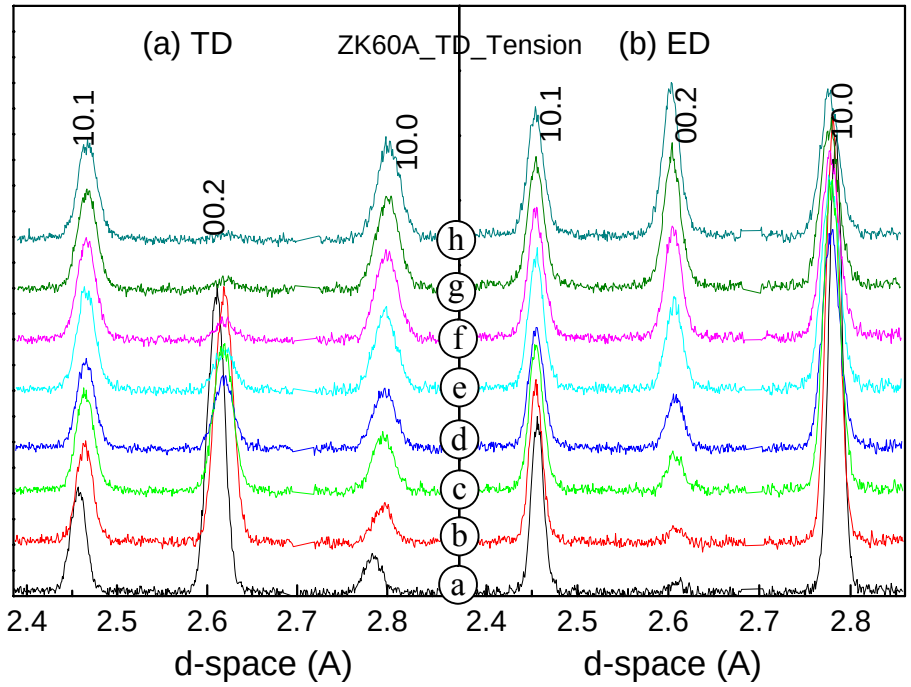

Figure 4.5. Diffraction patterns collected, respectively, from the parallel (TD) and transverse (ED) directions at various strains during the tensile loading of the ZK60A alloy along the TD direction. The patterns have been offset vertically for clarity.

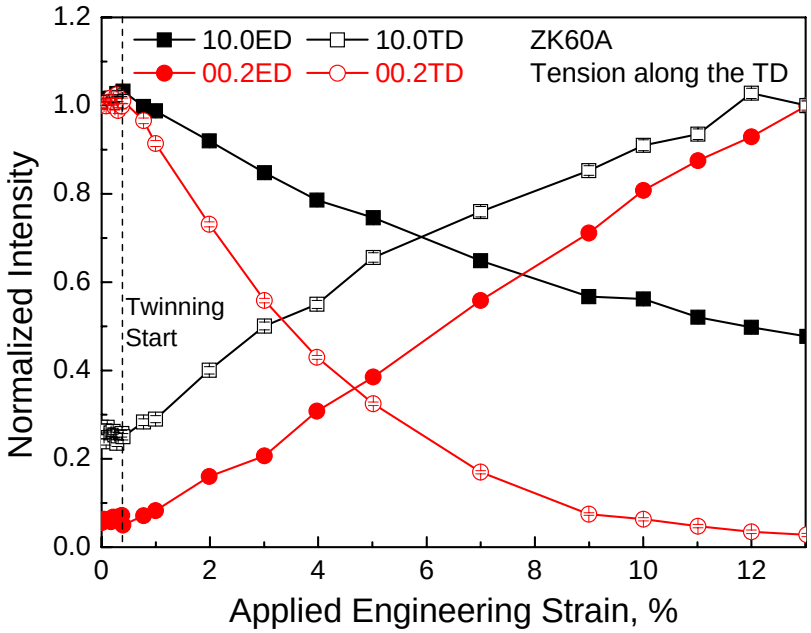

Figure 4.6. The intensity evolutions as a function of the applied engineering strains due to the activation of the extension twinning for ZK60A under tension loaded along the TD direction.

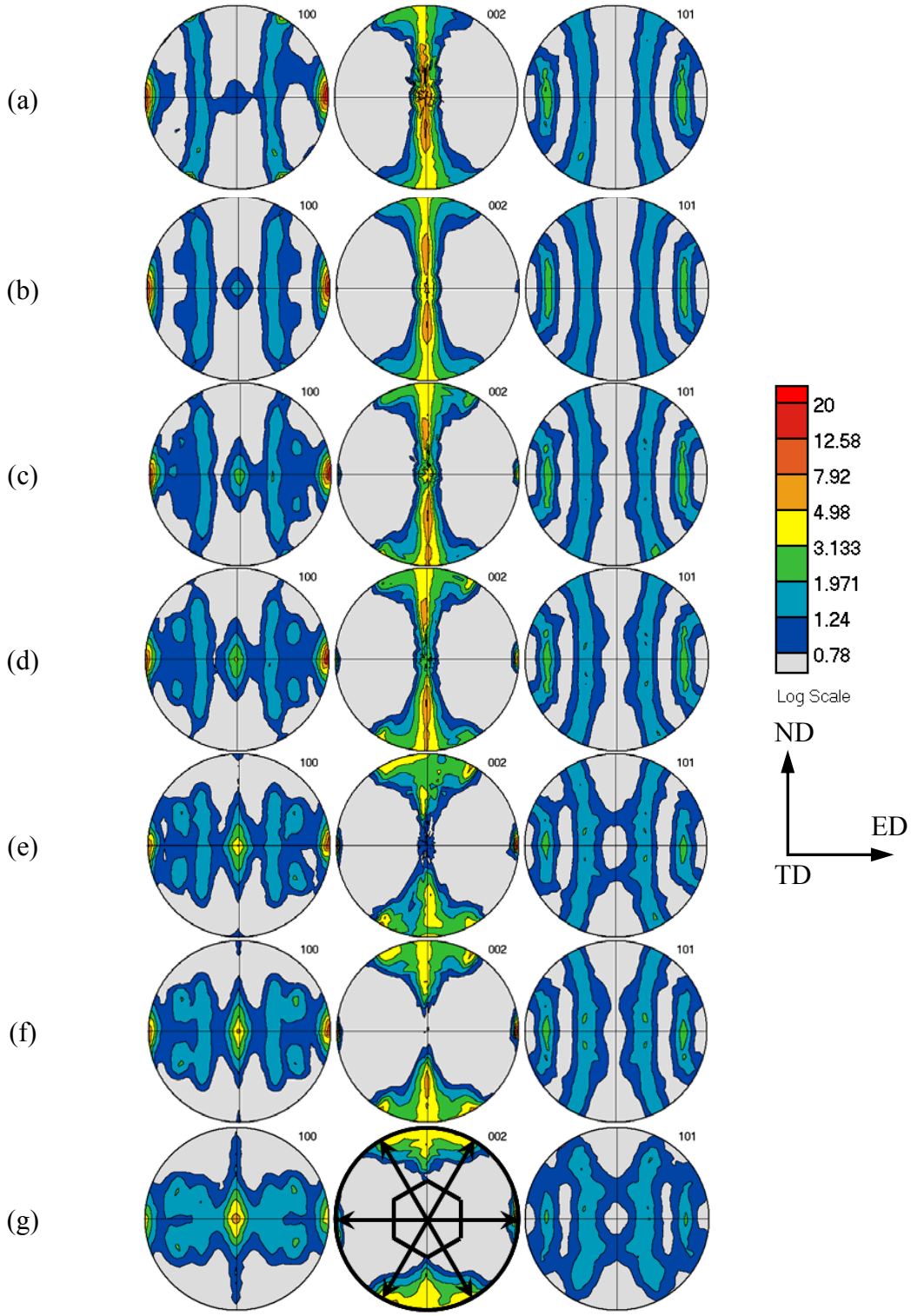

Figure 4.7. Texture evolution for ZK60A measured using synchrotron diffraction under tension along the TD: a) as-received, b) 1.0%, c) 3.0 %, d) 5.0 %, e) 7.0 %, f) 9.0 %, and g) 13.0%. Pole densities are expressed in multiples of a random distribution (mrd).

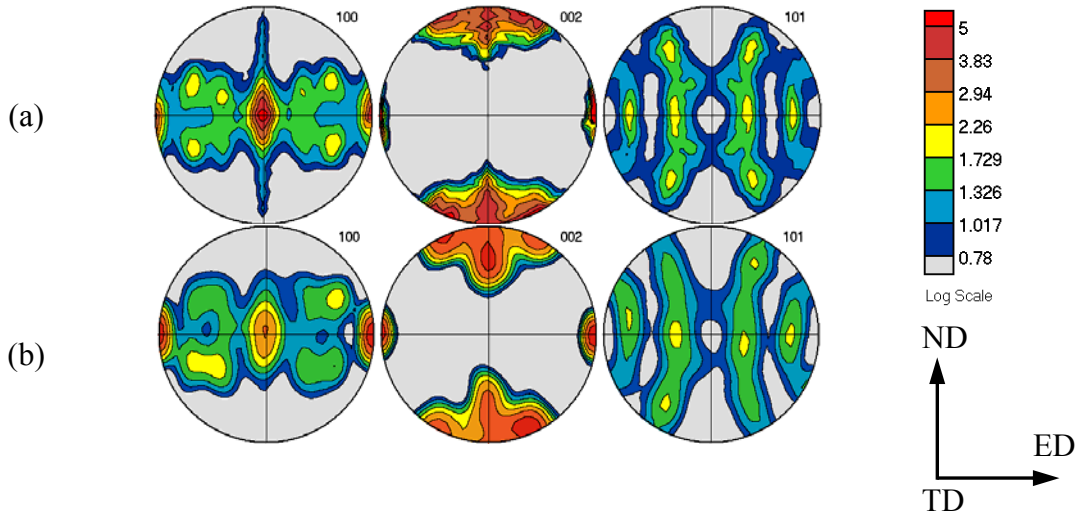

Figure 4.8. Comparison of the final texture at a tensile strain of 13% measured by the synchrotron X-ray diffraction (a) and neutron scattering (b). Pole densities are expressed in multiples of a random distribution (mrd).

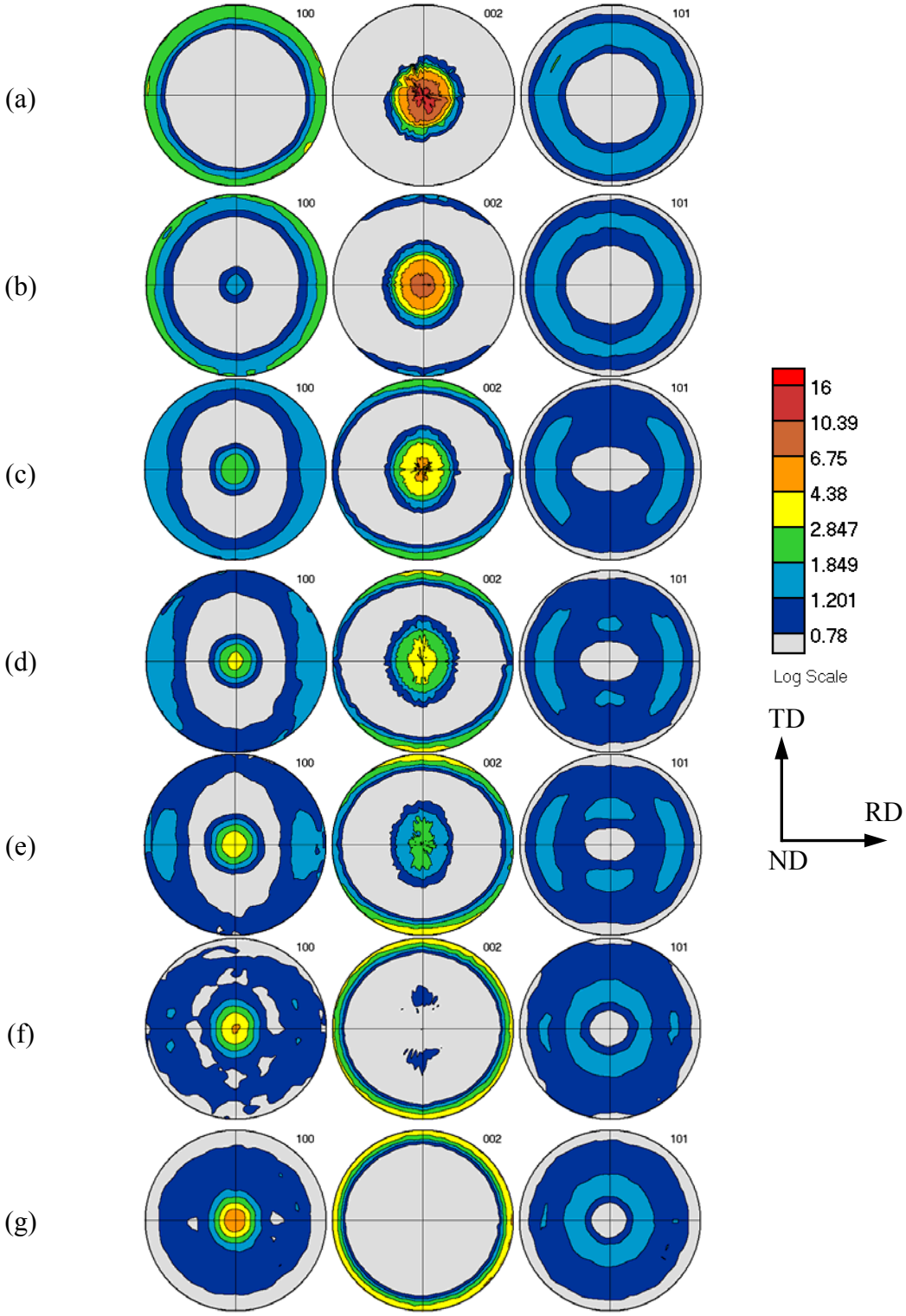

Figure 4.9. Texture evolution for AZ31B measured using synchrotron diffraction under tension along the ND: a) as-received, b) 1.0%, c) 3.0 %, d) 5.0 %, e) 7.0 %, f) 9.0 %, and g) 13.0%. Pole densities are expressed in multiples of a random distribution (mrd).

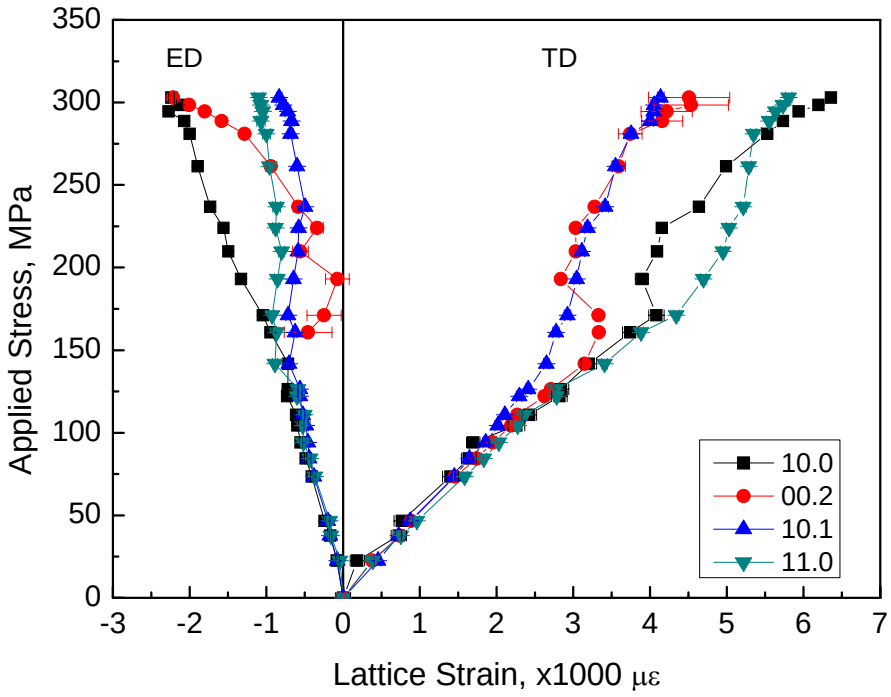

Figure 4.10. Internal-strain evolutions as a function of the applied macroscopic strain for the ZK60A alloy under tension loaded along the TD direction. The internal-strain (stress) evolution in the different grain orientations can be understood in terms of load transfer among those grain orientations.

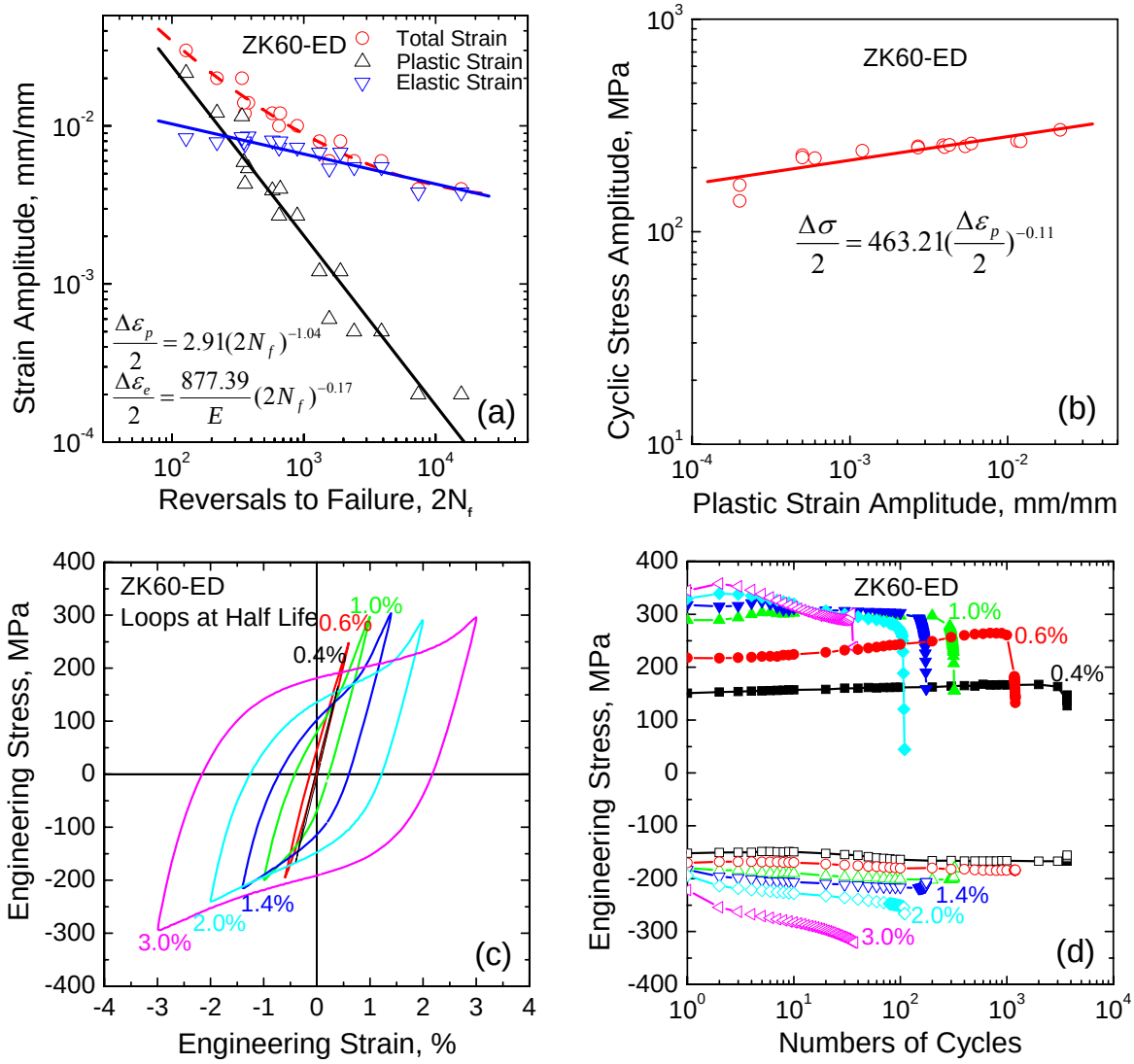

Figure 5.1. The low-cycle fatigue behavior of the as-extruded ZK60A alloy under the ED loading: a) ε–N fatigue life curves; b) cyclic stress and strain curves; c) hysteresis loops at half life for various total strain amplitudes; and d) cyclic tensile and compressive peak stress responses.

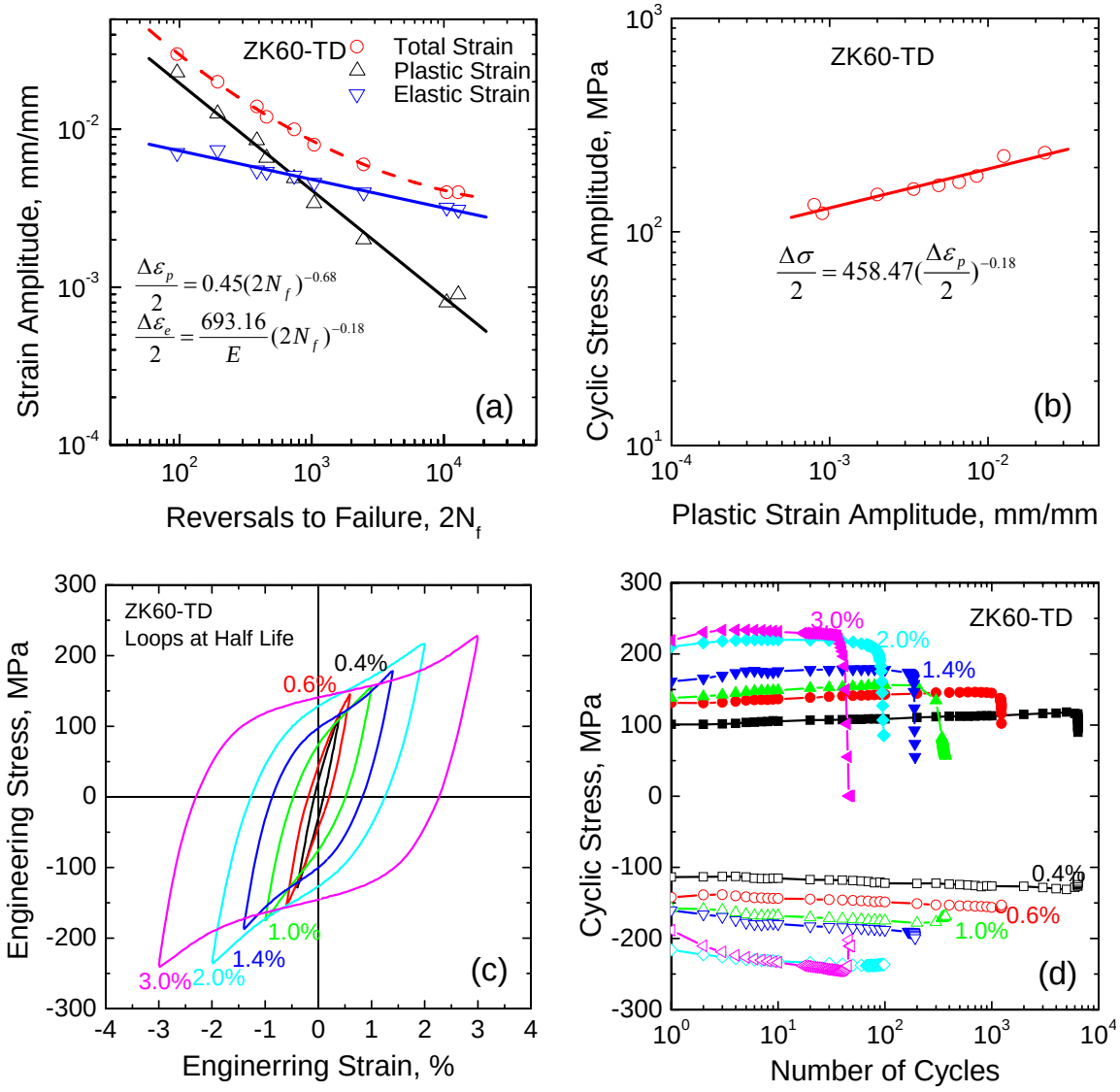

Figure 5.2. The low-cycle fatigue behavior of the as-extruded ZK60A alloy under the TD loading: a) ε–N fatigue life curves; b) cyclic stress and strain curves; c) hysteresis loops at half life for various total strain amplitudes; and d) cyclic tensile and compressive peak stress responses.

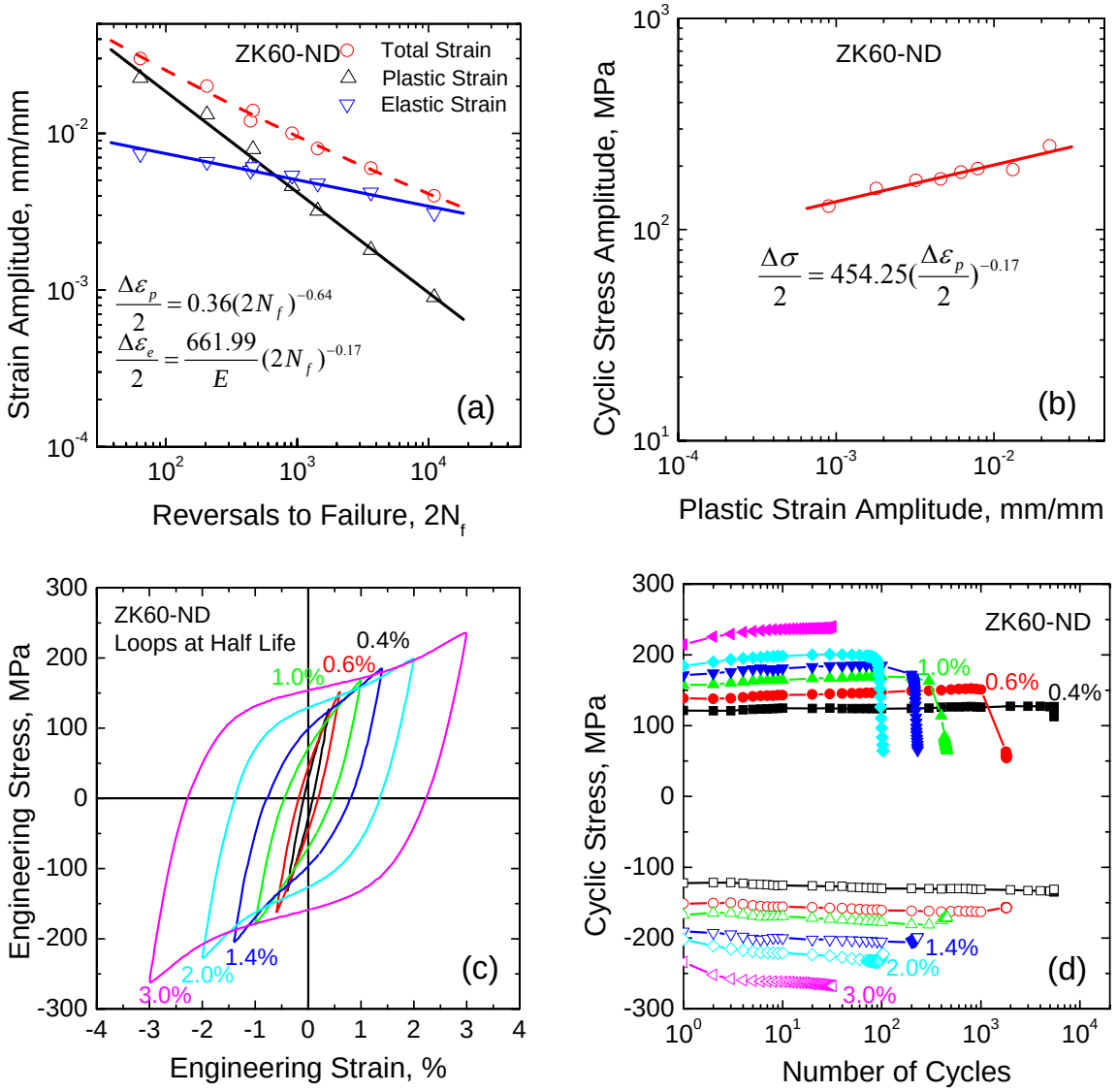

Figure 5.3. The low-cycle fatigue behavior of the as-extruded ZK60A alloy under the ND loading: a) ε–N fatigue life curves; b) cyclic stress and strain curves; c) hysteresis loops at half life for various total strain amplitudes; and d) cyclic tensile and compressive peak stress responses.

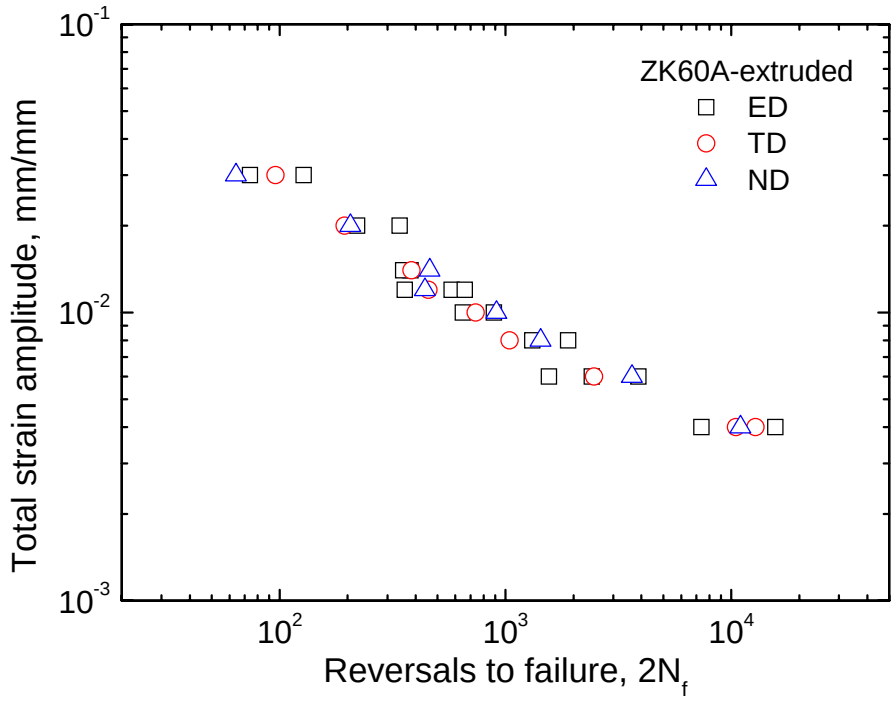

Figure 5.4. Total strain amplitudes as a function of the number of reversals to failure, respectively, loaded along the three directions in the extruded ZK60A alloy.

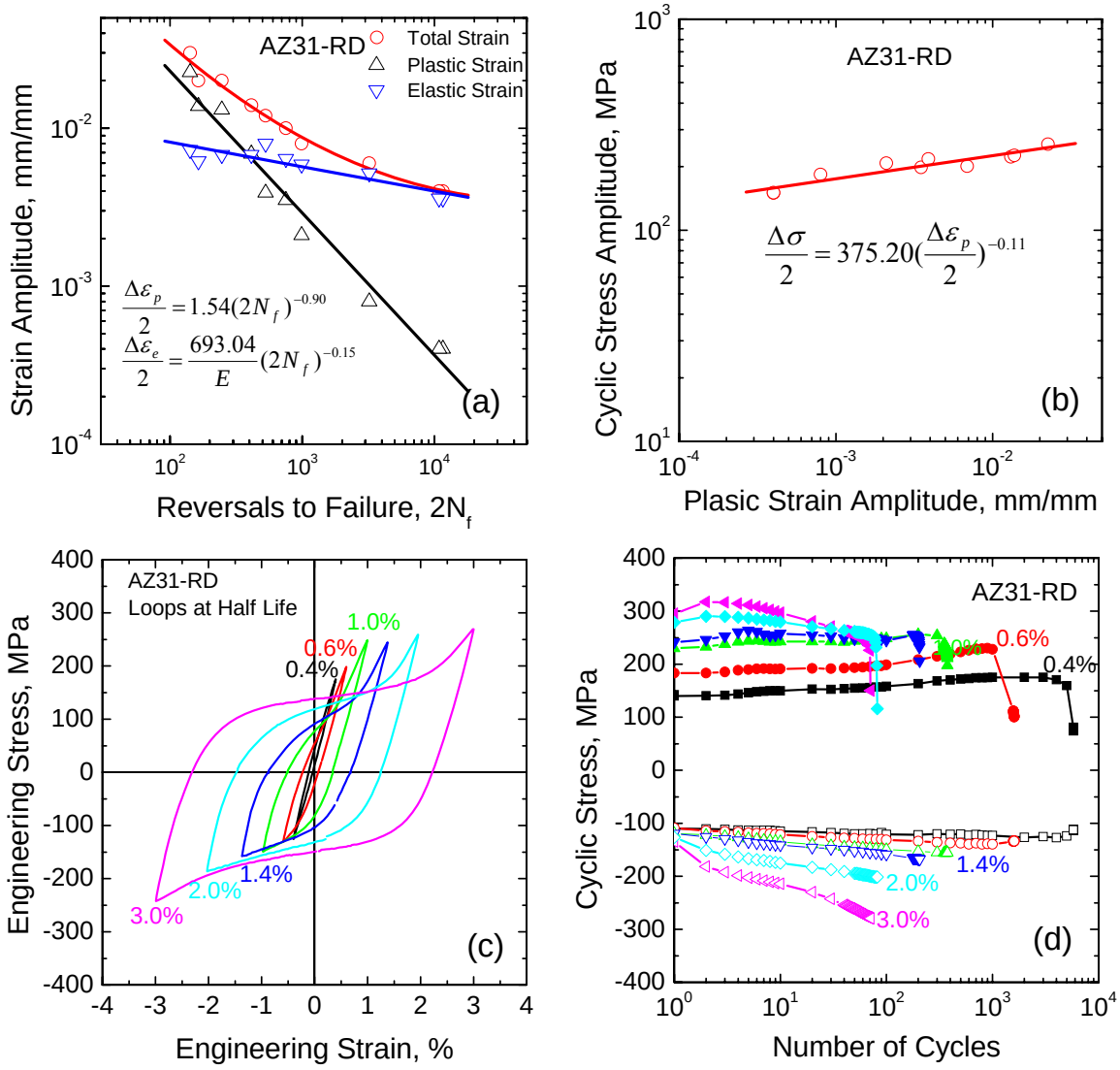

Figure 5.5. The low-cycle fatigue behavior of the as-rolled AZ31B alloy under the RD loading: a) ε–N fatigue life curves; b) cyclic stress and strain curves; c) hysteresis loops at half life for various total strain amplitudes; and d) cyclic tensile and compressive peak stress responses.

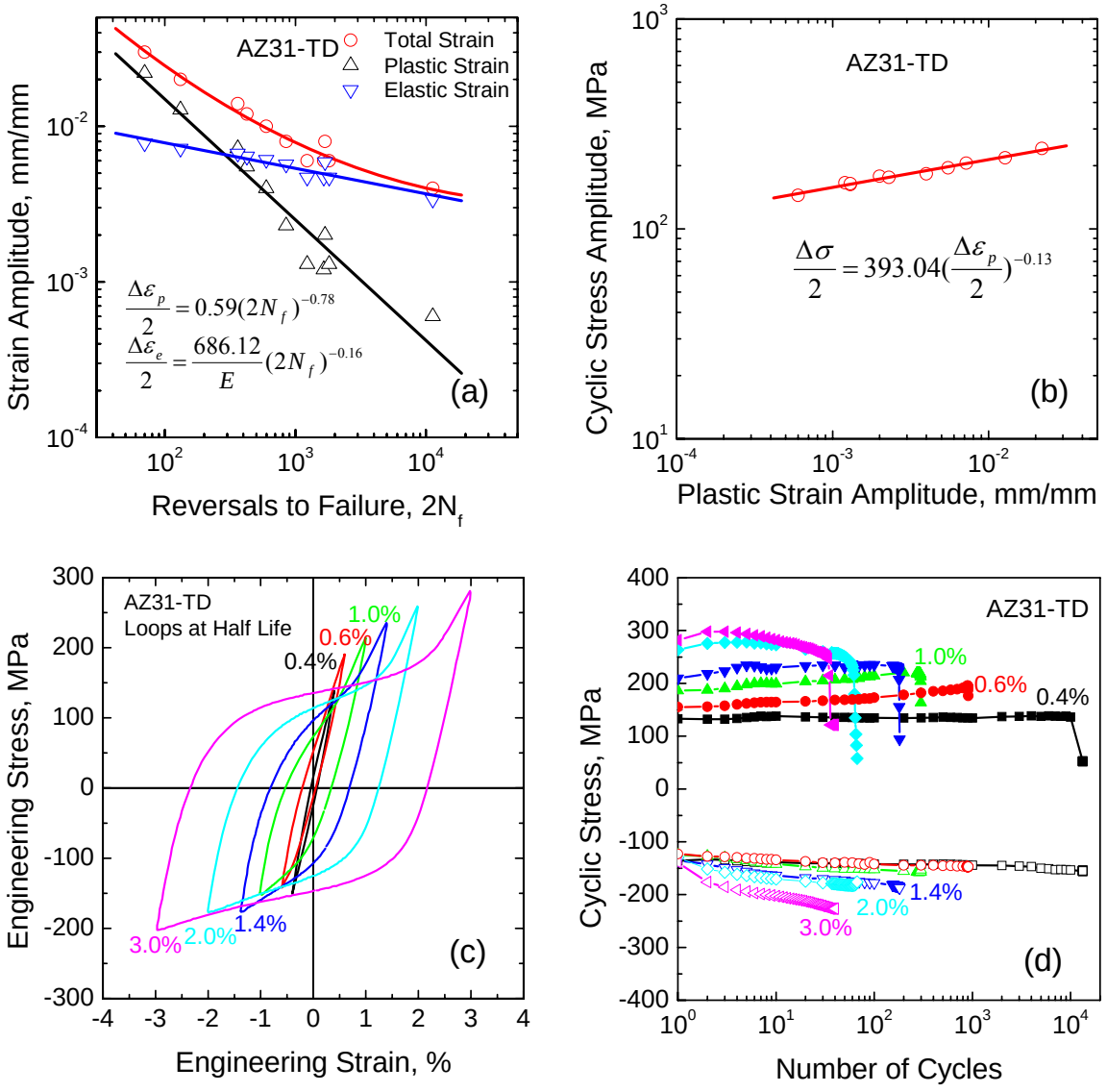

Figure 5.6. The low-cycle fatigue behavior of the as-rolled AZ31B alloy under the TD loading: a) ε–N fatigue life curves; b) cyclic stress and strain curves; c) hysteresis loops at half life for various total strain amplitudes; and d) cyclic tensile and compressive peak stress responses.

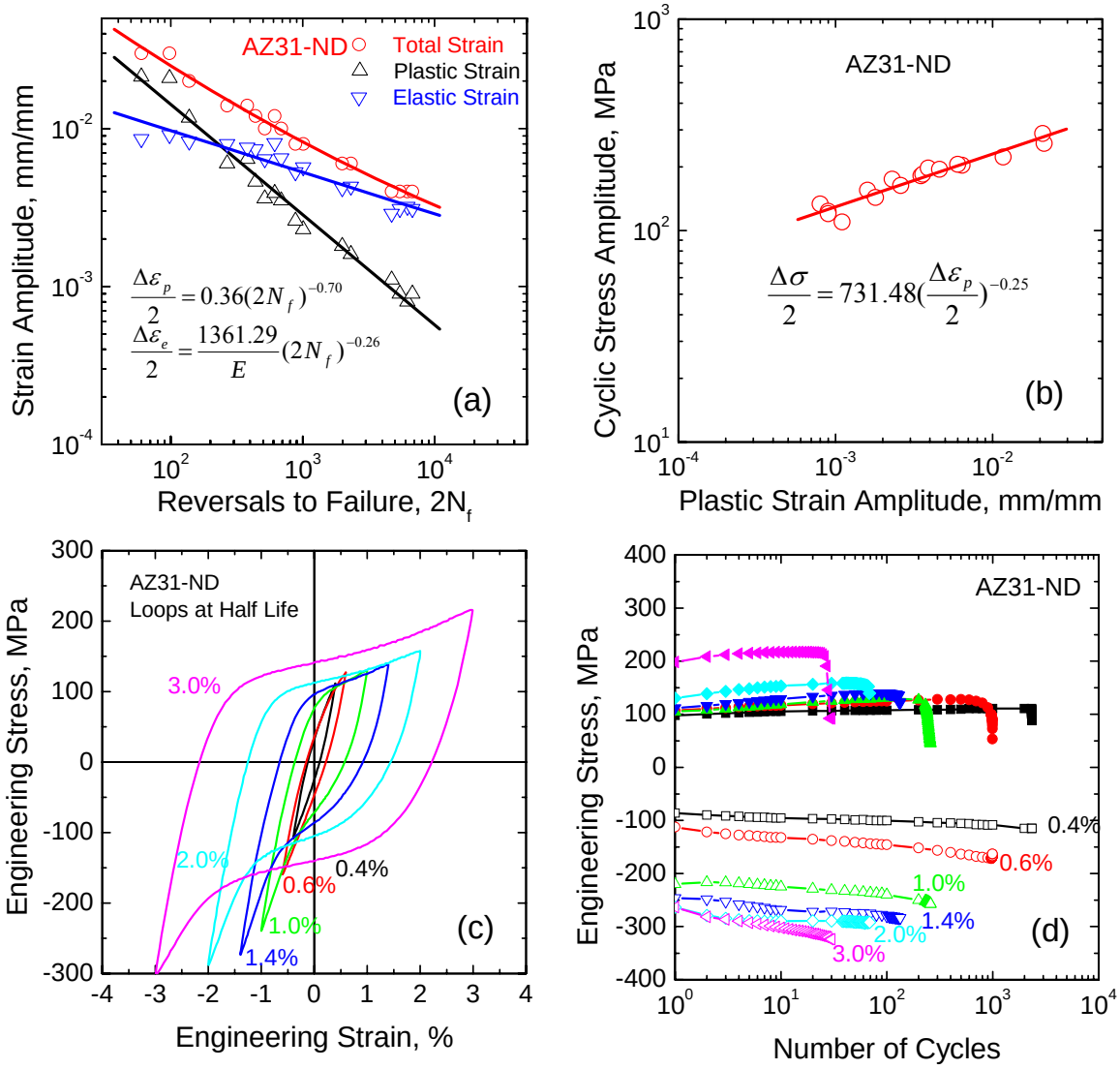

Figure 5.7. The low-cycle fatigue behavior of the as-rolled AZ31B alloy under the ND loading: a) ε–N fatigue life curves; b) cyclic stress and strain curves; c) hysteresis loops at half life for various total strain amplitudes; and d) cyclic tensile and compressive peak stress responses.

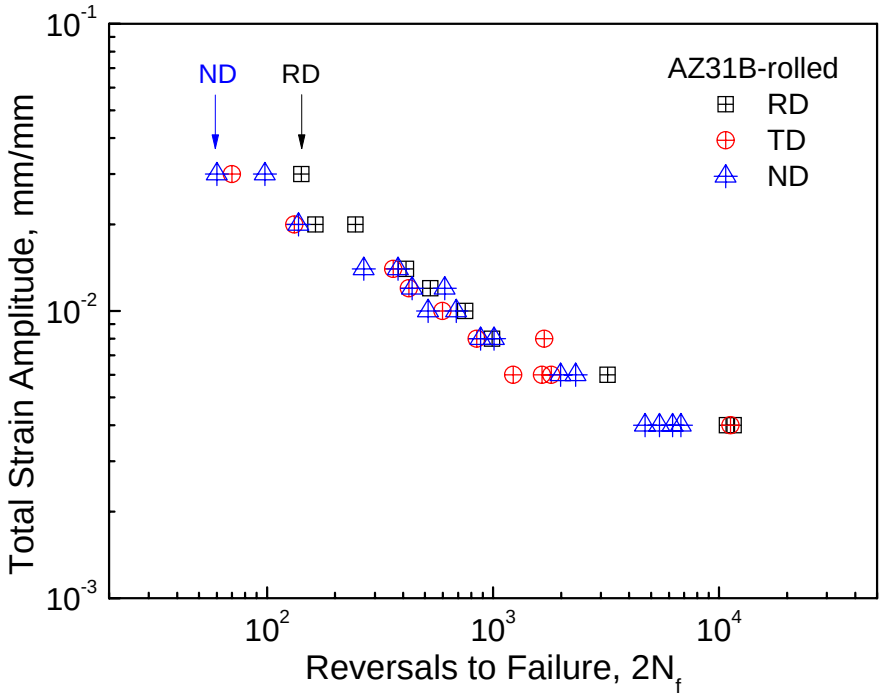

Figure 5.8. Total strain amplitudes as a function of the number of reversals to failure, respectively, loaded along the three directions in the extruded AZ31B alloy.

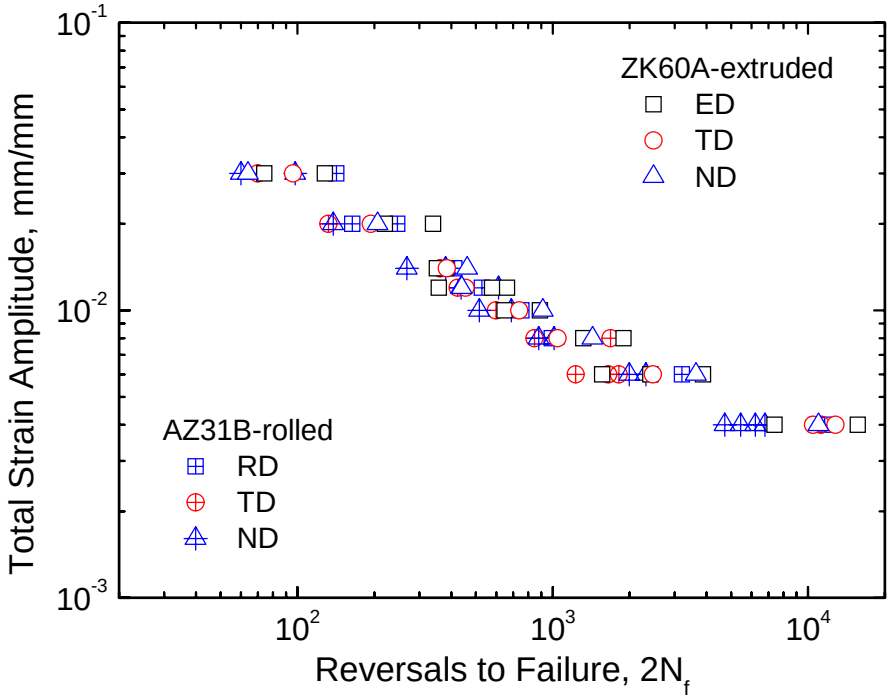

Figure 5.9. Total strain amplitudes as a function of the number of reversals to failure, respectively, loaded along the three directions in the rolled AZ31B alloy, in comparison with the data in the extruded ZK60A alloy.

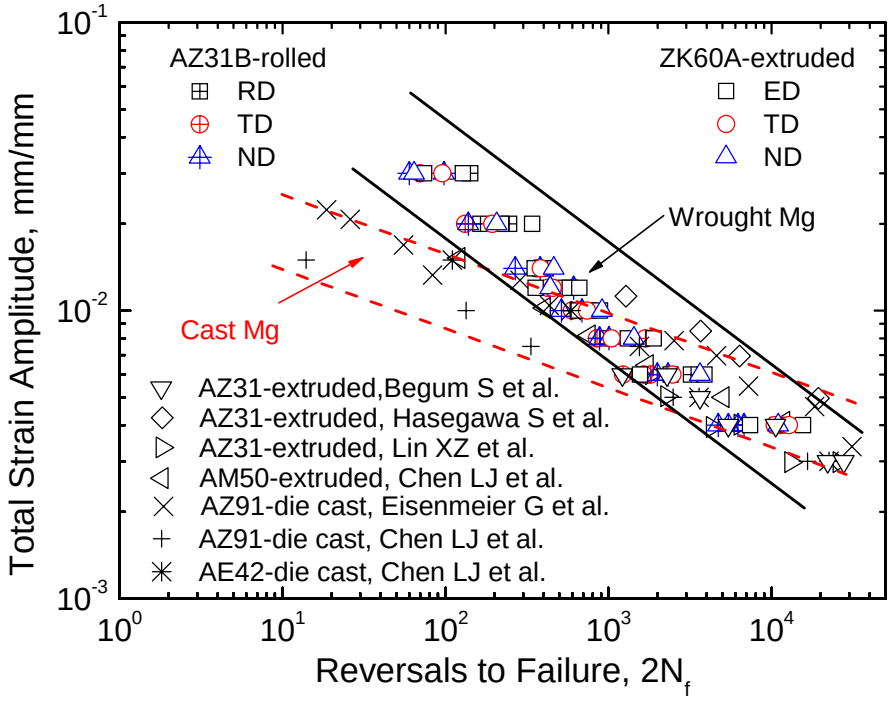

Figure 5.10. Total strain amplitudes as a function of the number of reversals to failure in the rolled AZ31B and extruded ZK60A alloys, in comparison with the data reported in the literature for various wrought or cast magnesium alloys [57, 58, 66, 67, 72, 106].

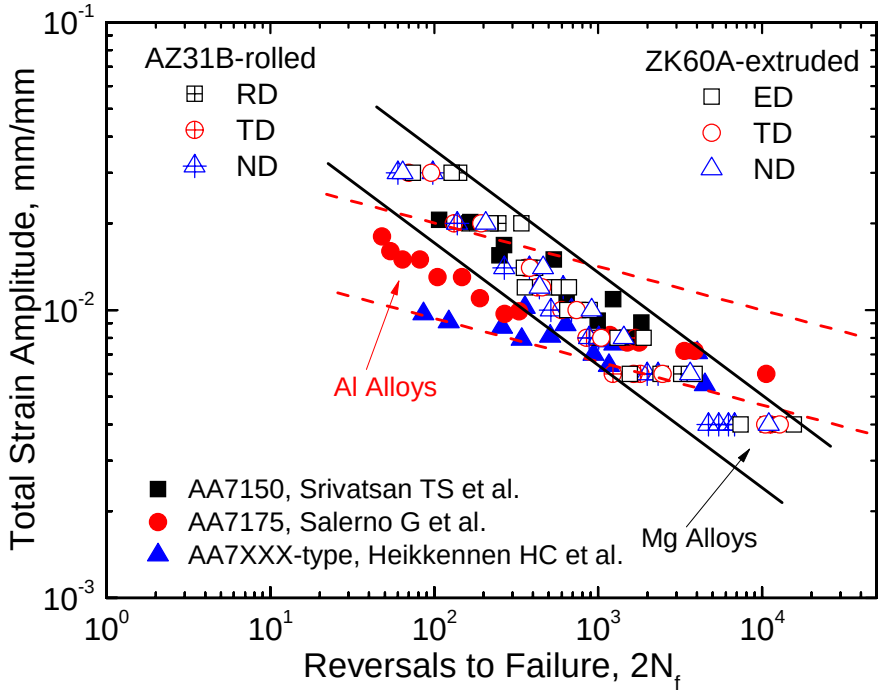

Figure 5.11. Total strain amplitudes as a function of the number of reversals to failure for comparison between the magnesium alloys and the aluminum alloys [107-110].

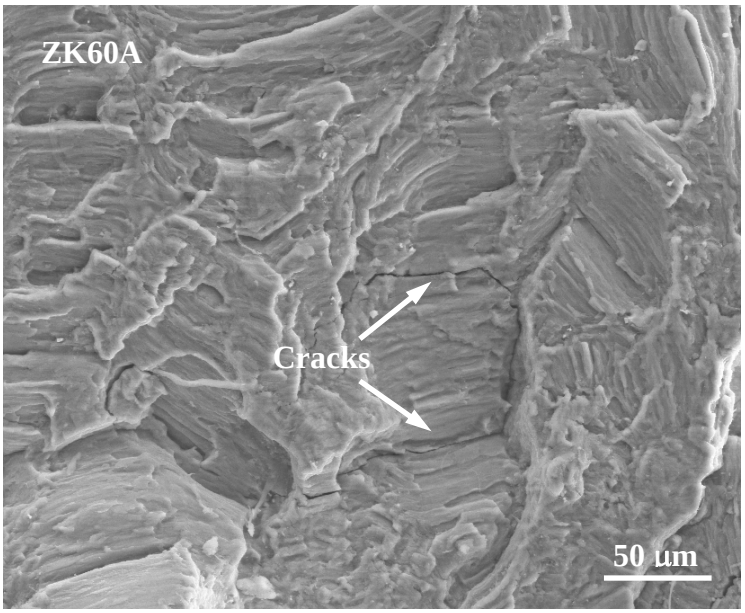

Figure 5.12. Typical fractography of the fatigued sample loaded along the ED direction at the total strain amplitude of 1.2%.

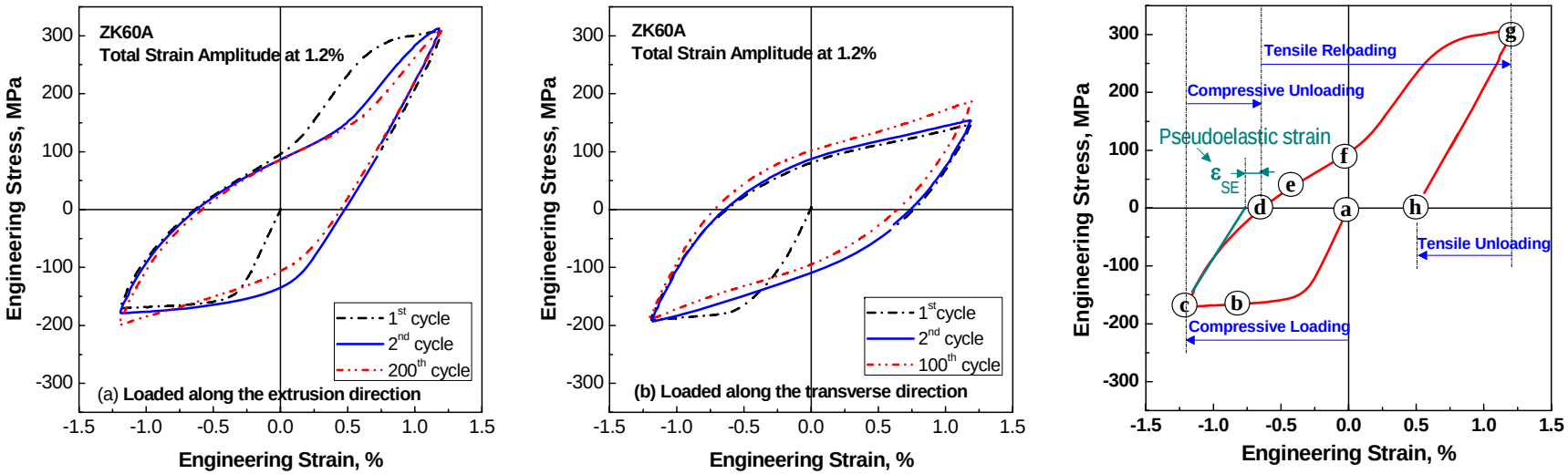

Figure 5.13. Hysteresis loops of the extruded ZK60A alloy at a total strain amplitude of 1.2% loaded along the ED direction (a) and along the TD direction (b). An asymmetric hysteresis loop in the first cycle deformation of the extruded ZK60A alloy loaded along the ED direction at a total strain amplitude of 1.2% (c). The figure indicates the recoverable (or pseudo-elastic) strain, ε_{SE}.

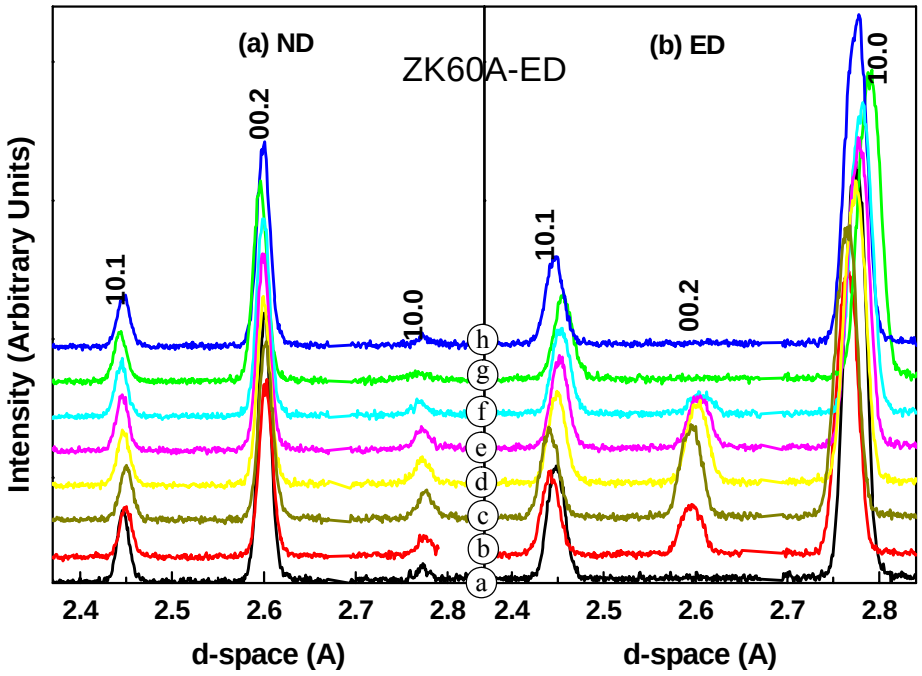

Figure 5.14. Diffraction patterns in the ND and ED directions at various measuring points along the hysteresis loop (indicated in Fig. 5.9c) during the first cycle deformation of the ZK60A alloy. The patterns have been offset vertically for clarity. The diffraction patterns correspond to: a) 0% (initial state); b) – 0.8% strain; c) – 1.2% strain; d) 0 MPa stress; e) – 0.4% strain; f) 0% strain; g) + 1.2% strain; and h) 0 MPa stress.

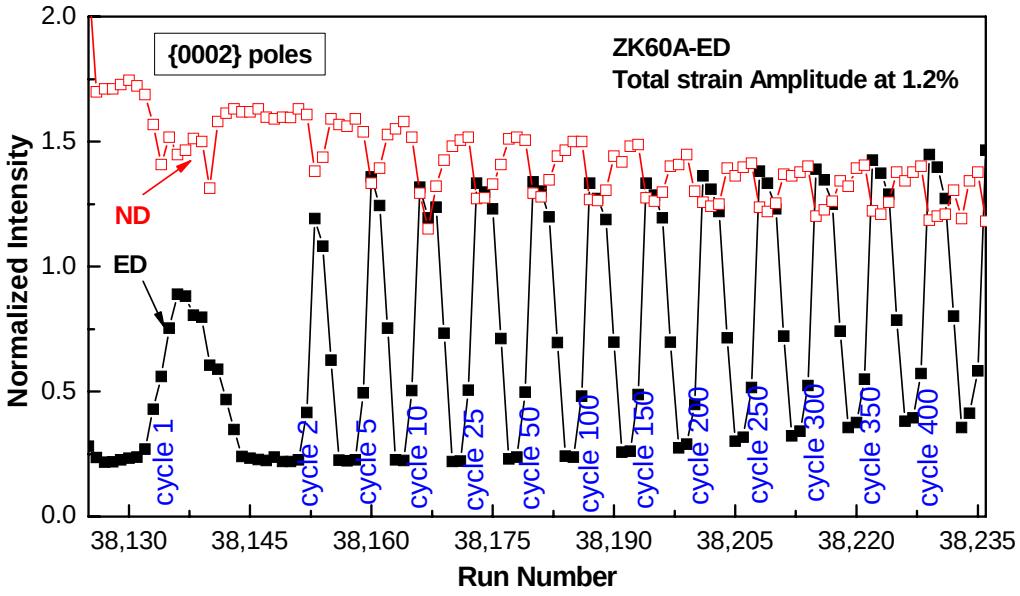

Figure 5.15. Normalized intensity evolutions of the basal (00.2) poles as a function of the rum number, indicating cyclic twinning and detwinning behavior in the extruded ZK60A alloy if loaded along the ED direction.

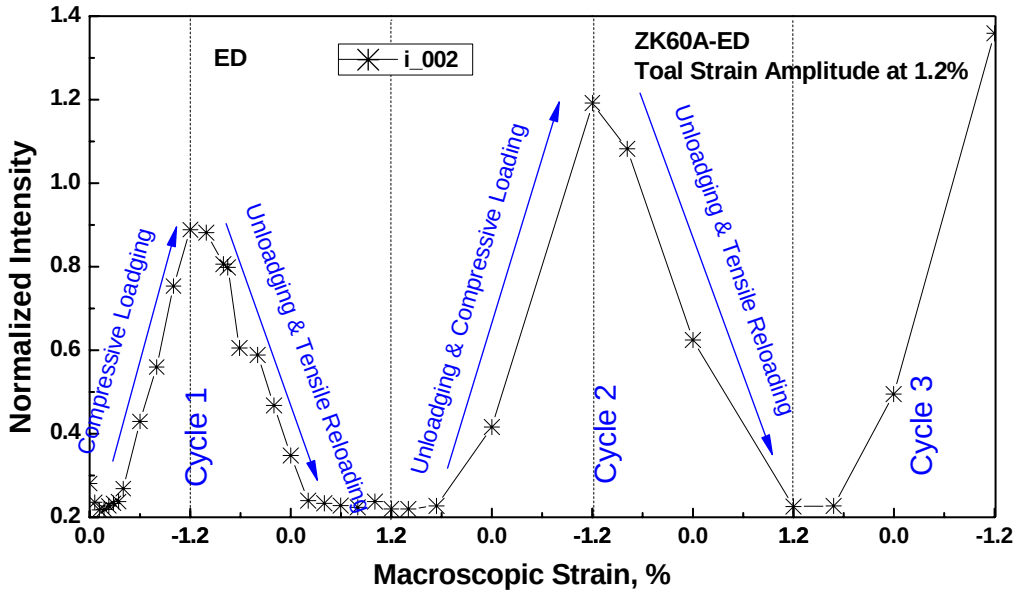

Figure 5.16. Normalized intensity evolutions of the basal (00.2) poles in the ED direction during the first few cycles when the sample of the extruded ZK60A alloy is loaded along the ED direction.

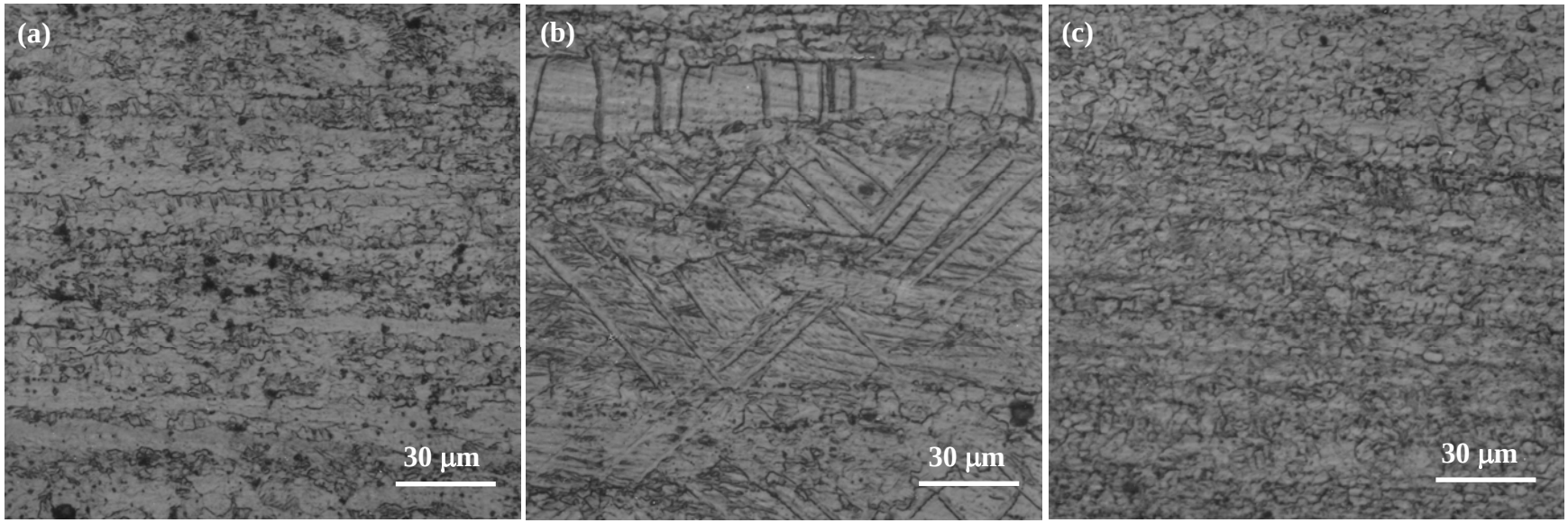

Figure 5.17. Optical microstructures at various strain states for the extruded ZK60A alloy loaded along the ED direction: (a) initial state (0% strain), free of twins; (b) first maximal compression (– 1.2% strain), a lot of twins in some favorably oriented grains; and (c) first maximal tension (+ 1.2% strain), disappearance of twins.

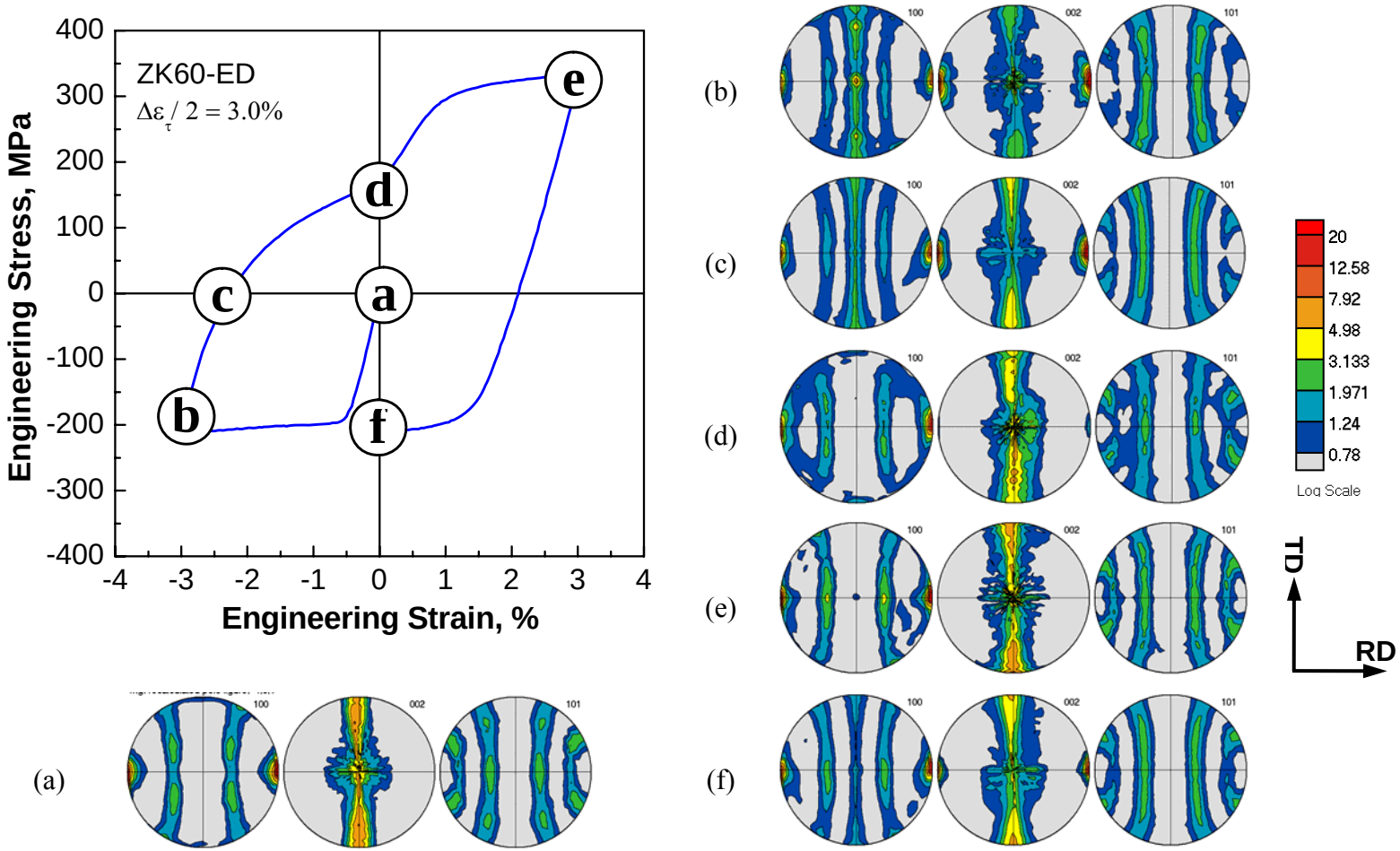

Figure 5.18. Measured crystallographic textures along the hysteresis loop during the first cycle deformation of the extruded ZK60A alloy using *ex situ* synchrotron diffraction: a) strain-free, b) – 3.0 % strain, c) 0 MPa stress, d) 0 % strain, e) + 3.0 % strain, and f) 0 % strain. Pole densities are expressed in multiples of a random distribution (mrd). The loading axis (along ED) is horizontally right.

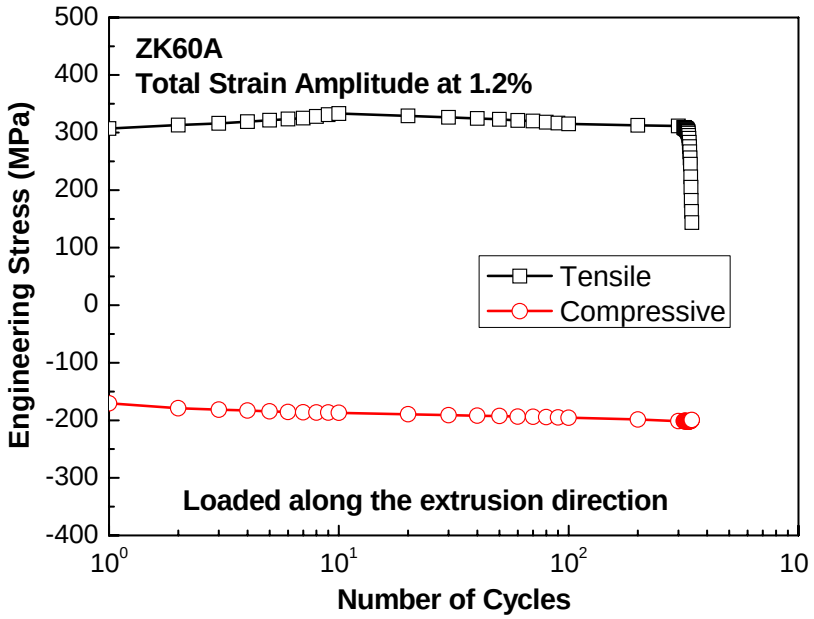

Figure 5.19. Stress-strain curves showing the variation of tensile and compressive streeses with the fatigue cycles in the extruded ZK60 alloy loaded along the ED direction with a total strain amplitude of 1.2%.

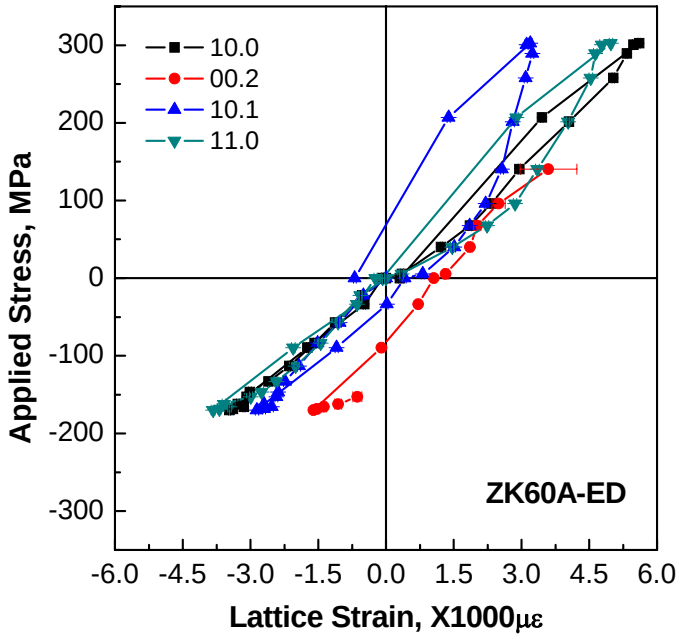

Figure 5.20. Hysteresis loops of applied stress *vs.* lattice strain for the ED direction during the first cycle deformation of the extruded ZK60 alloy along the ED direction with the total strain amplitude of 1.2%. The different Bauschinger-type effect may be explained in terms of grain orientation and Schmid factor for basal slip.

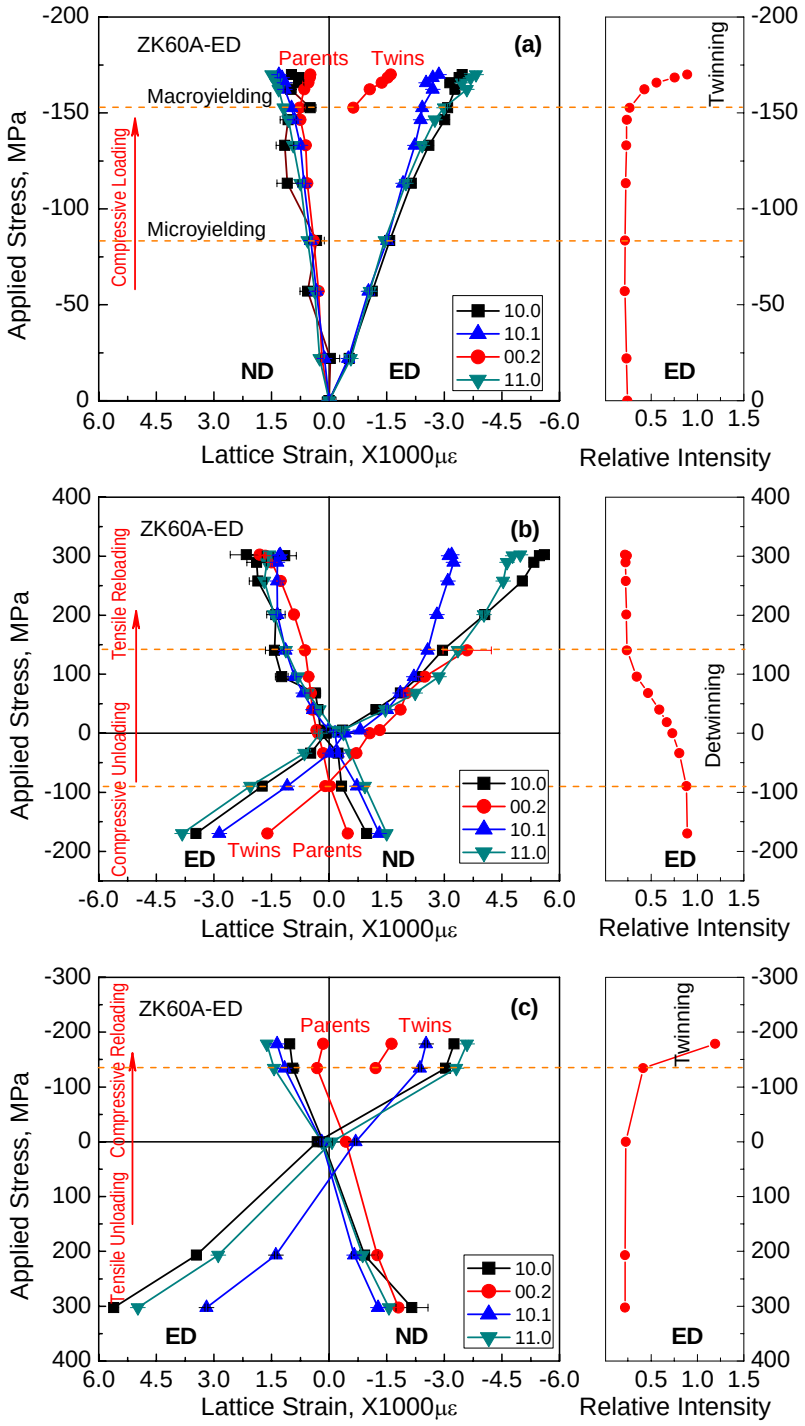

Figure 5.21. Internal-strain evolutions, respectively, for a) initial compressive loading; b) compressive unloading; c) tensile reloading; and d) tensile unloading, during the first cycle deformation of the ZK60 alloy along the ED direction with the total strain amplitude of 1.2%, indicated in Figure 5.9c.

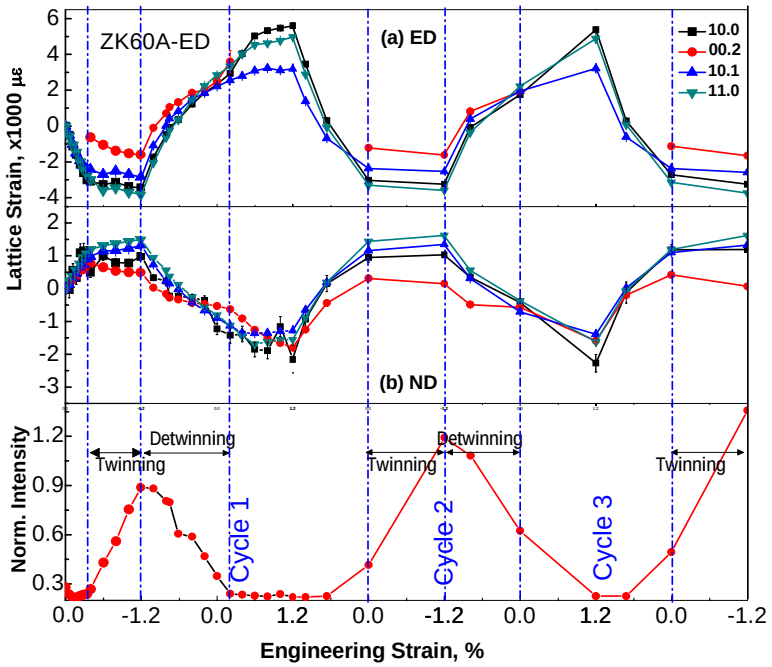

Figure 5.22. Lattice strain evolution as a function of engineering strain for the first few cycles during the cyclic loading of the ZK60A alloy along the ED direction. Also included is a curve of the (00.2) pole intensity evolution in the parallel bank.

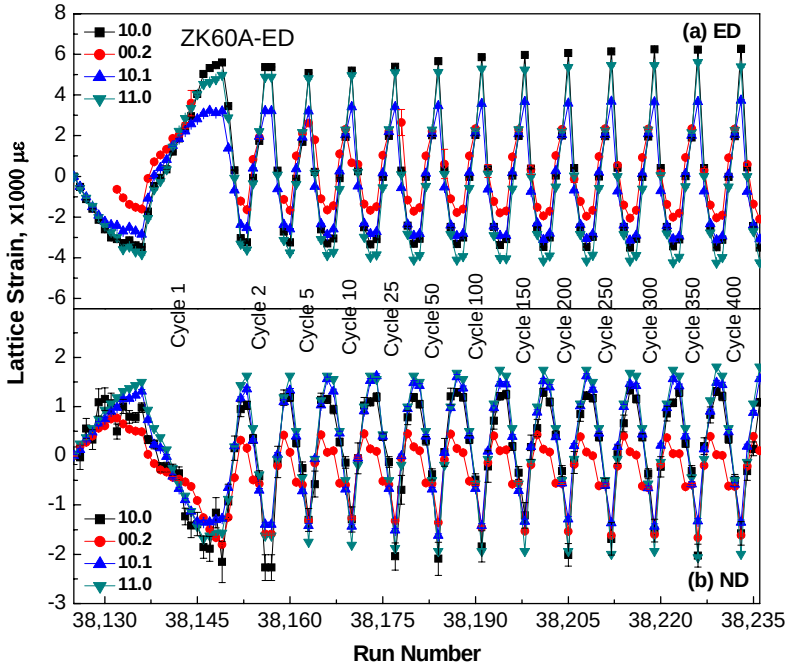

Figure 5.23. Lattice strains as a function of run number during the cyclic loading of the ZK60 alloy along the ED direction, indicating cyclic evolution of lattice strains: a) in the longitudinal direction (ED); b) in the transverse direction (ND).

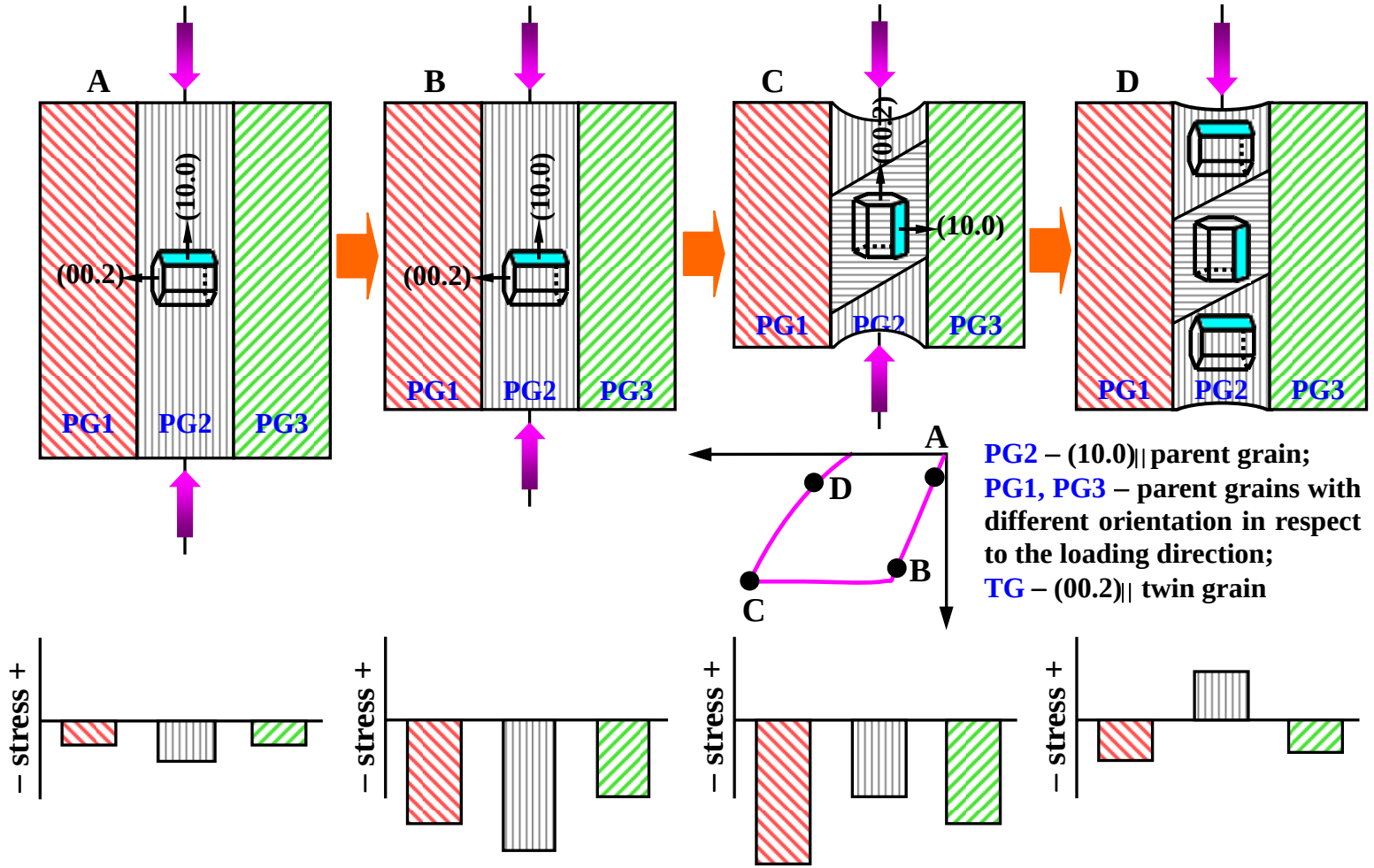

Figure 5.24. A schematic of the evolution of local stresses in three neighboring grains during the loading-unloading cycles. The suggested load partitioning at the bottom corresponds to an approximation of load sharing within the deformed polycrystals [123].

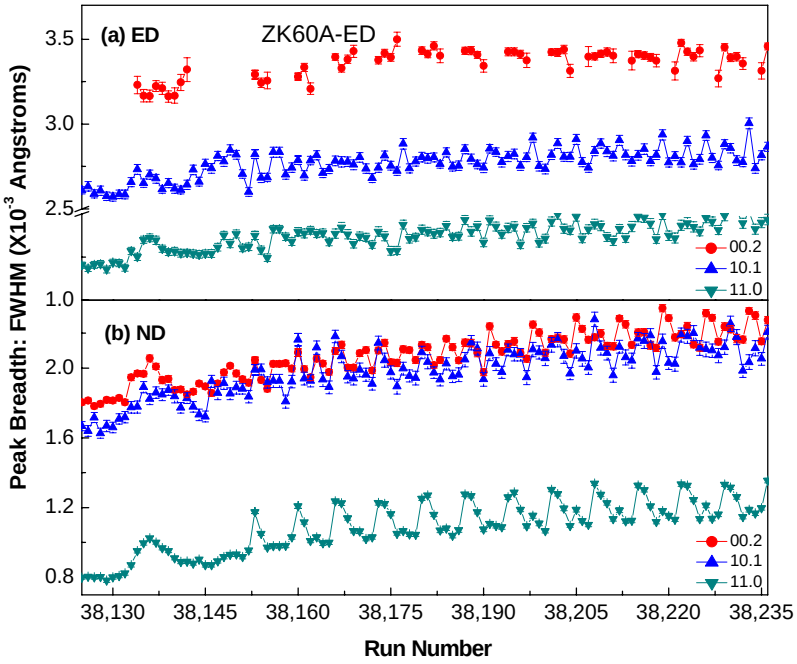

Figure 5.25. Broadening of diffraction peaks as function of run number along the longitudinal direction (ED) (a) and along the transverse direction (ND) (b) during the cyclic deformation of the ZK60 alloy along the ED direction with the total strain amplitude of 1.2%. The peak broadening in the current study is mostly related to the volume of twins and dislocations in the material.

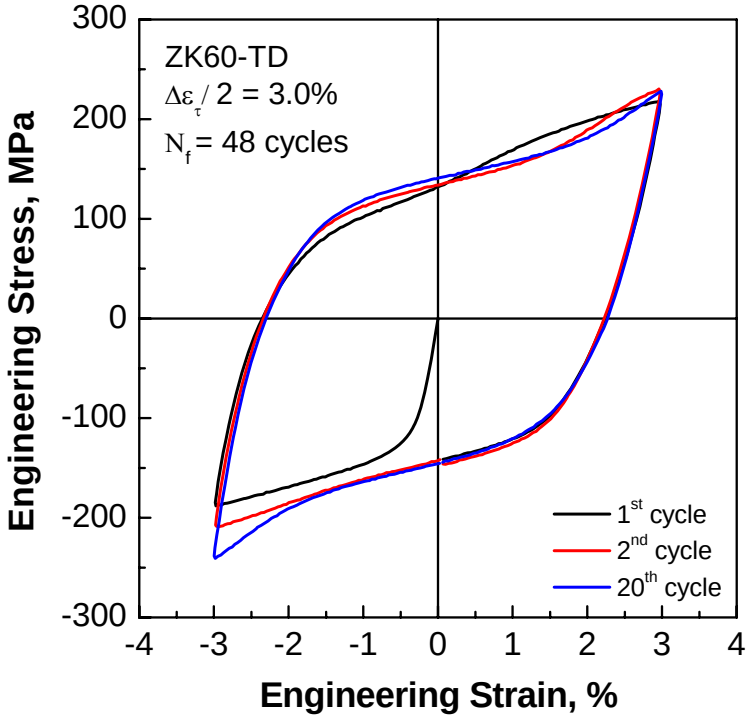

Figure 5.26. Hysteresis loops of the ZK60 alloy loaded along the TD direction at a total strain amplitude of 3.0% with compression as the first deformation stroke.

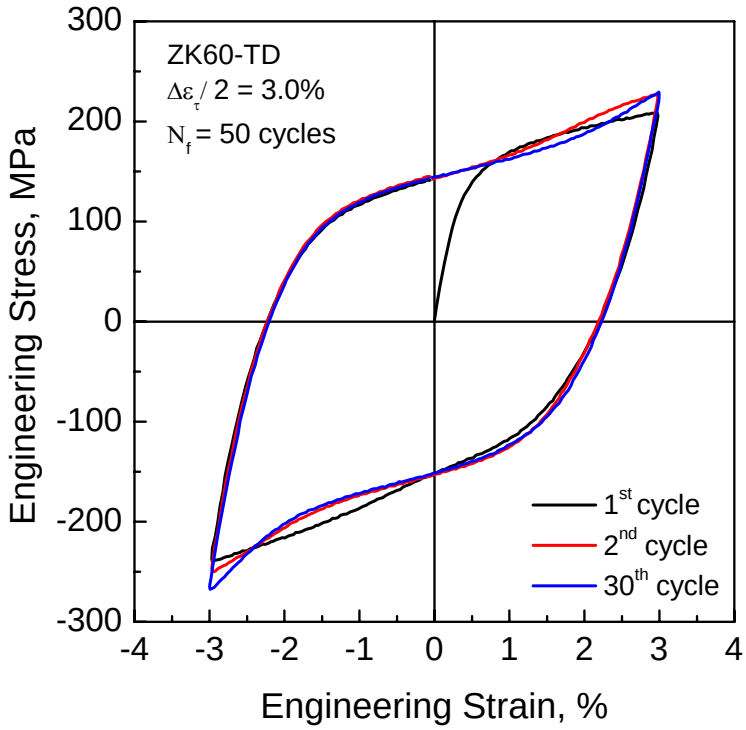

Figure 5.27. Hysteresis loops of the ZK60 alloy loaded along the TD direction at a total strain amplitude of 3.0% with tension as the first deformation stroke.

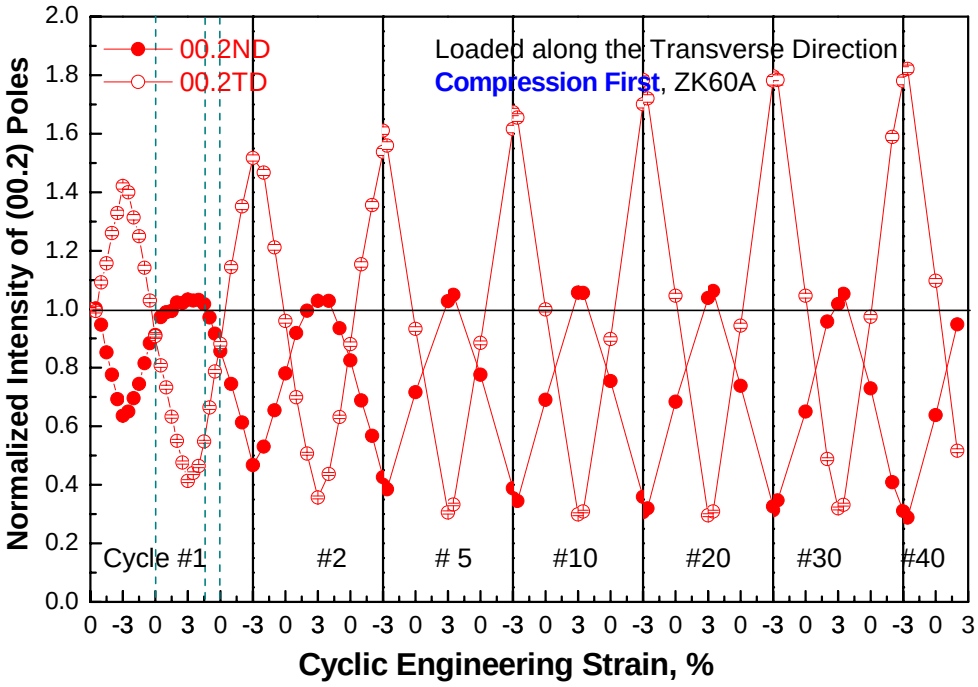

Figure 5.28. Intensity evolutions of the basal poles in the ZK60A alloy loaded along the TD direction at a total strain amplitude of 3.0% with compression as the first deformation stroke.

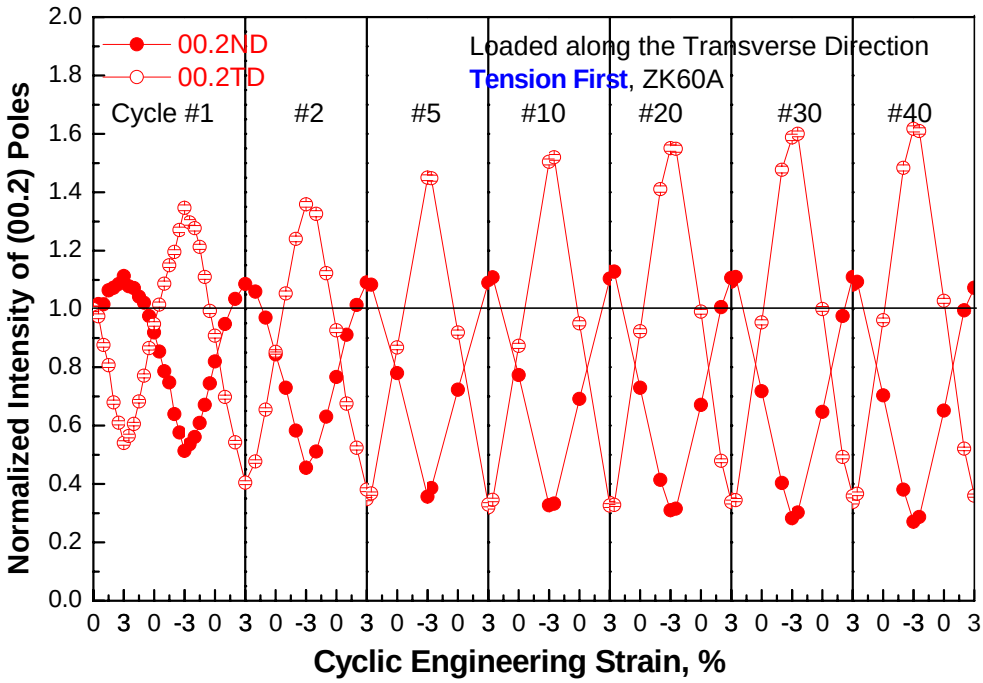

Figure 5.29. Intensity evolutions of the basal poles in the ZK60A alloy loaded along the TD direction at a total strain amplitude of 3.0% with tension as the first stroke.

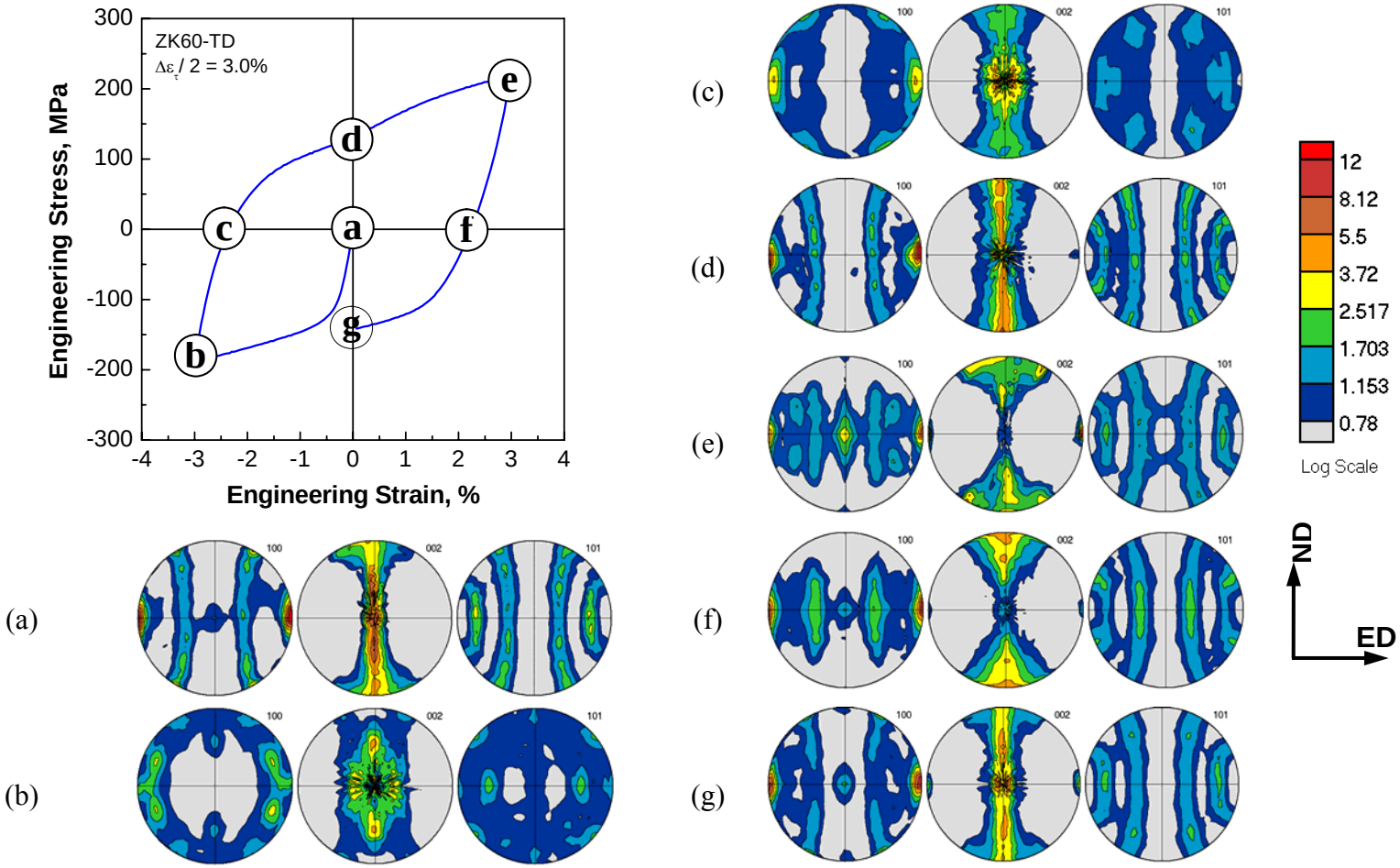

Figure 5.30. Measured textures along the hysteresis loop during the first cycle deformation of the ZK60A alloy along the TD direction with compression as the first deformation stroke using *ex situ* synchrotron diffraction: a) strain-free, b) – 3.0 % strain, c) 0 MPa stress, d) 0 % strain, e) + 3.0 % strain, and f) 0 % strain. Pole densities are expressed in multiples of a random distribution (mrd).

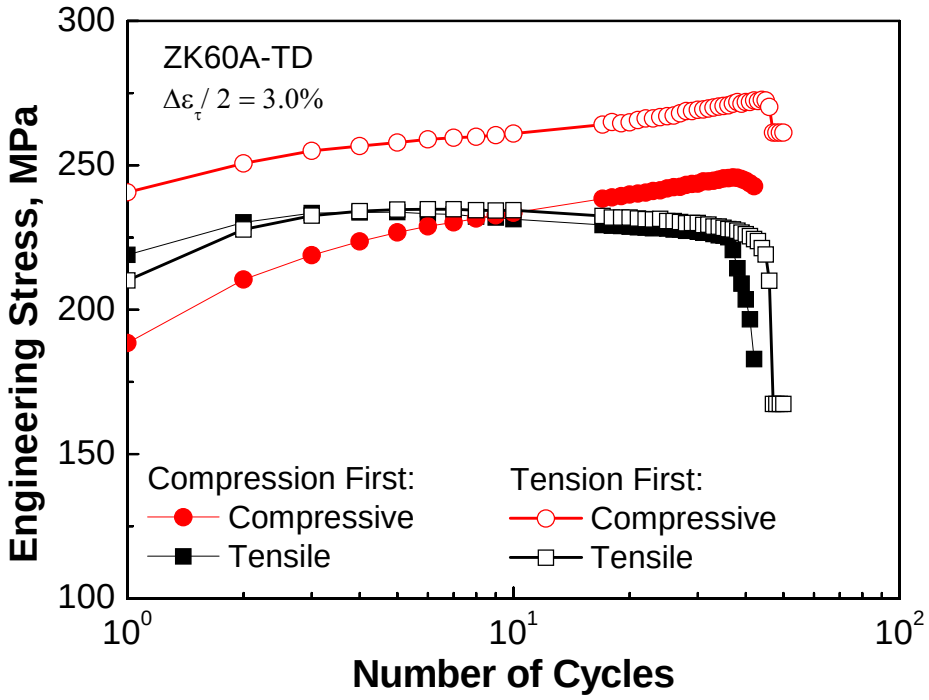

Figure 5.31. Cyclic stress evolutions showing the variations of the maximal tensile and compressive with the fatigue cycles loaded along the TD direction at the total strain amplitude of 3.0%, respectively, with tension and compression as the first deformation stroke.

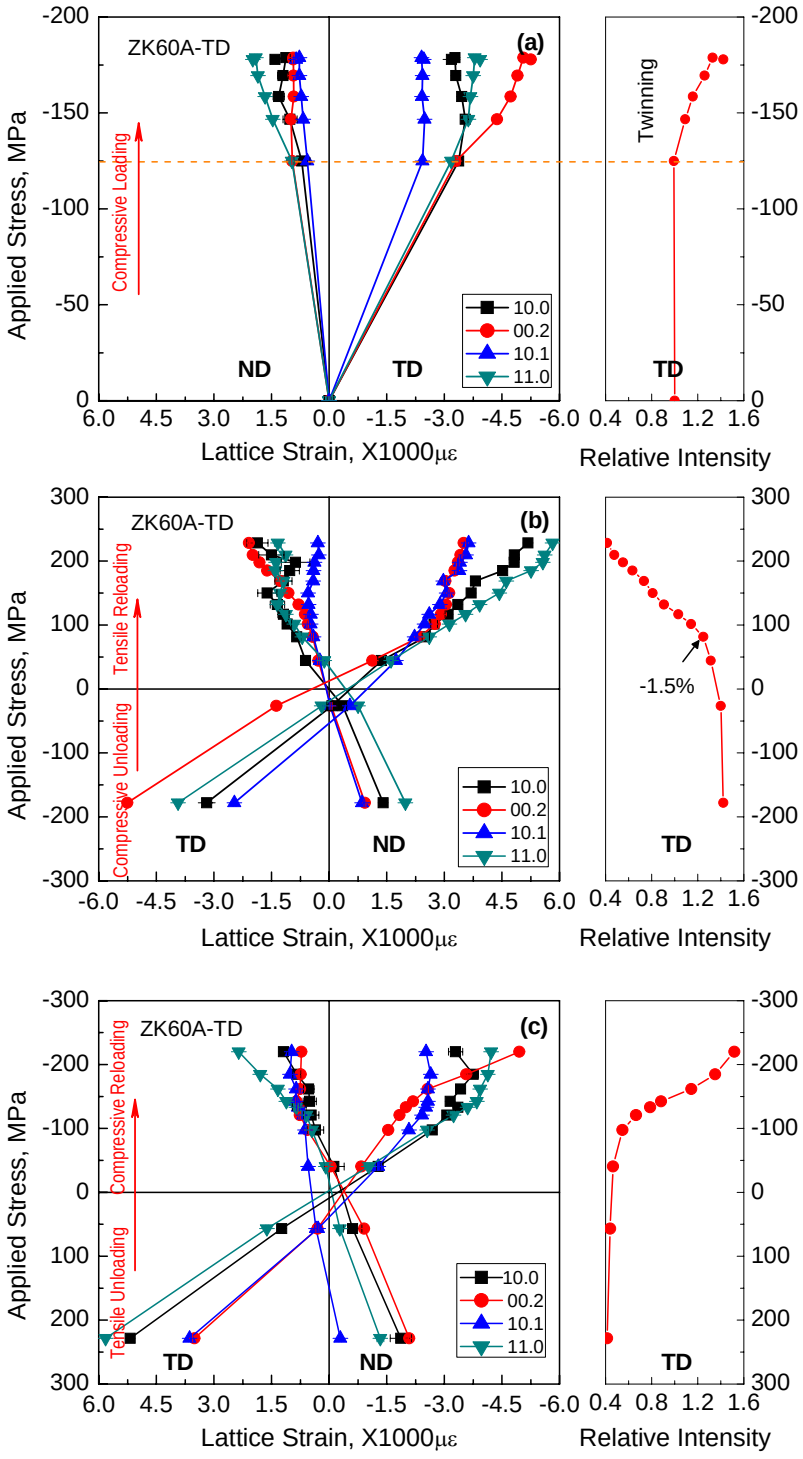

Figure 5.32. Internal-strain evolutions for the ZK60A alloy loaded along the TD direction at a total strain amplitude of 3.0% with compression as the first deformation stroke: a) compressive loading; b) compressive unloading and tensile reloading; and c) tensile unloading and compressive reloading.

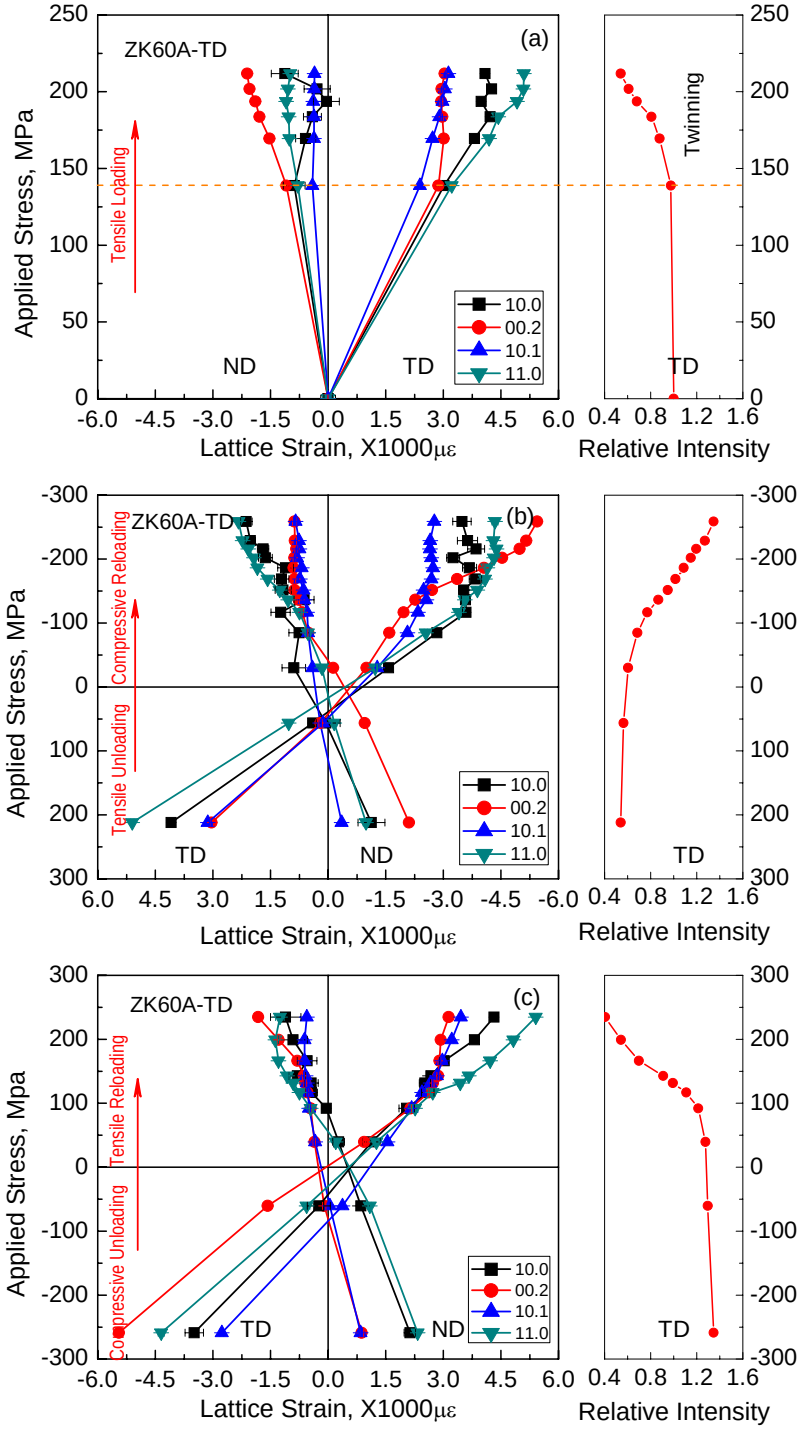

Figure 5.33. Internal-strain evolutions for the ZK60A alloy loaded along the TD direction at a total strain amplitude of 3.0% with tension as the first deformation stroke: a) tensile loading; b) tensile unloading and compressive reloading; and c) compressive unloading and tensile reloading.

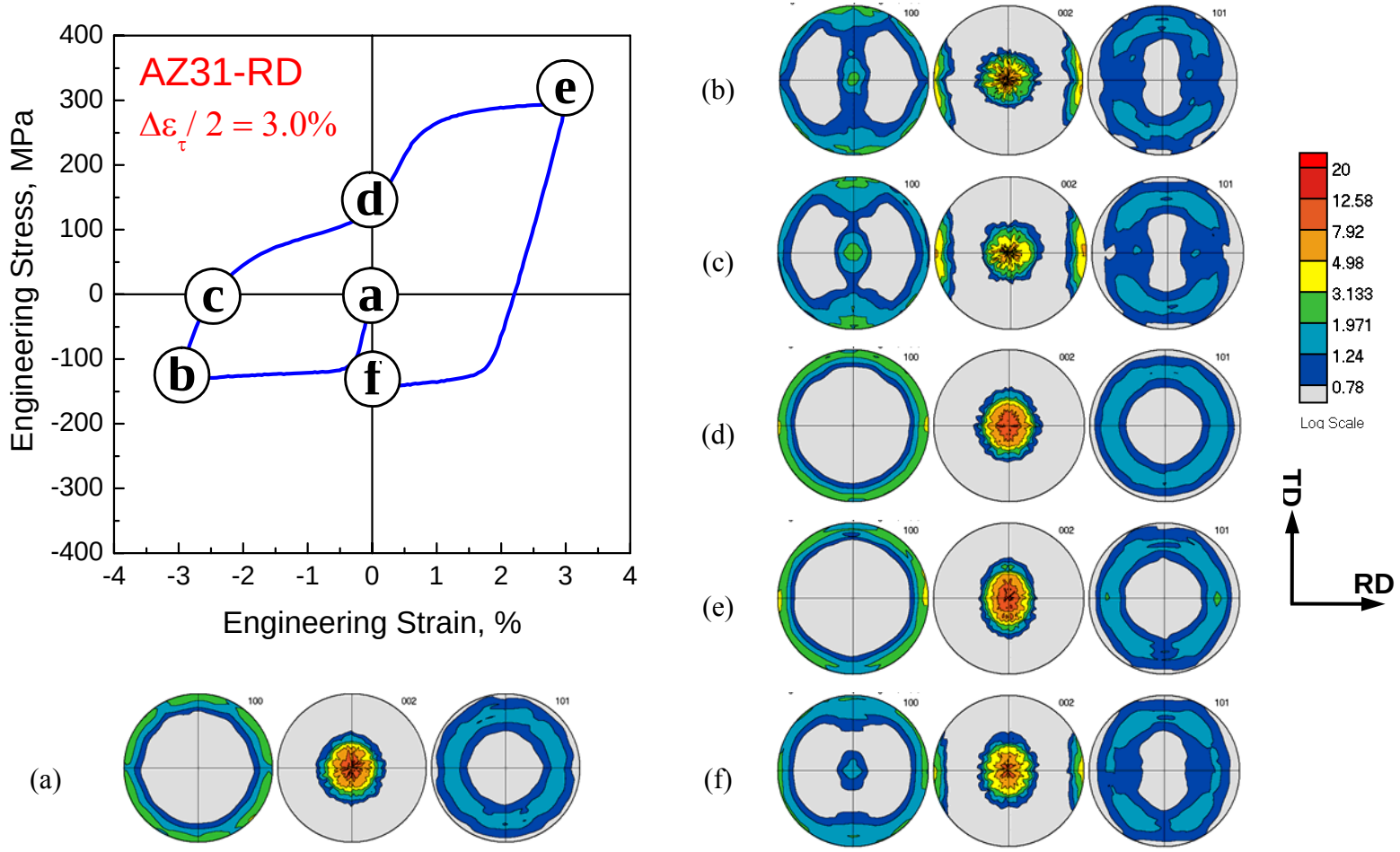

Figure 5.34. Measured crystallographic textures along the hysteresis loop during the first cycle deformation using *ex situ* synchrotron diffraction: a) strain-free, b) – 3.0 % strain, c) 0 MPa stress, d) 0 % strain, e) + 3.0 % strain, and f) 0 % strain. Pole densities are expressed in multiples of a random distribution (mrd). The loading axis (along RD) is horizontally right.

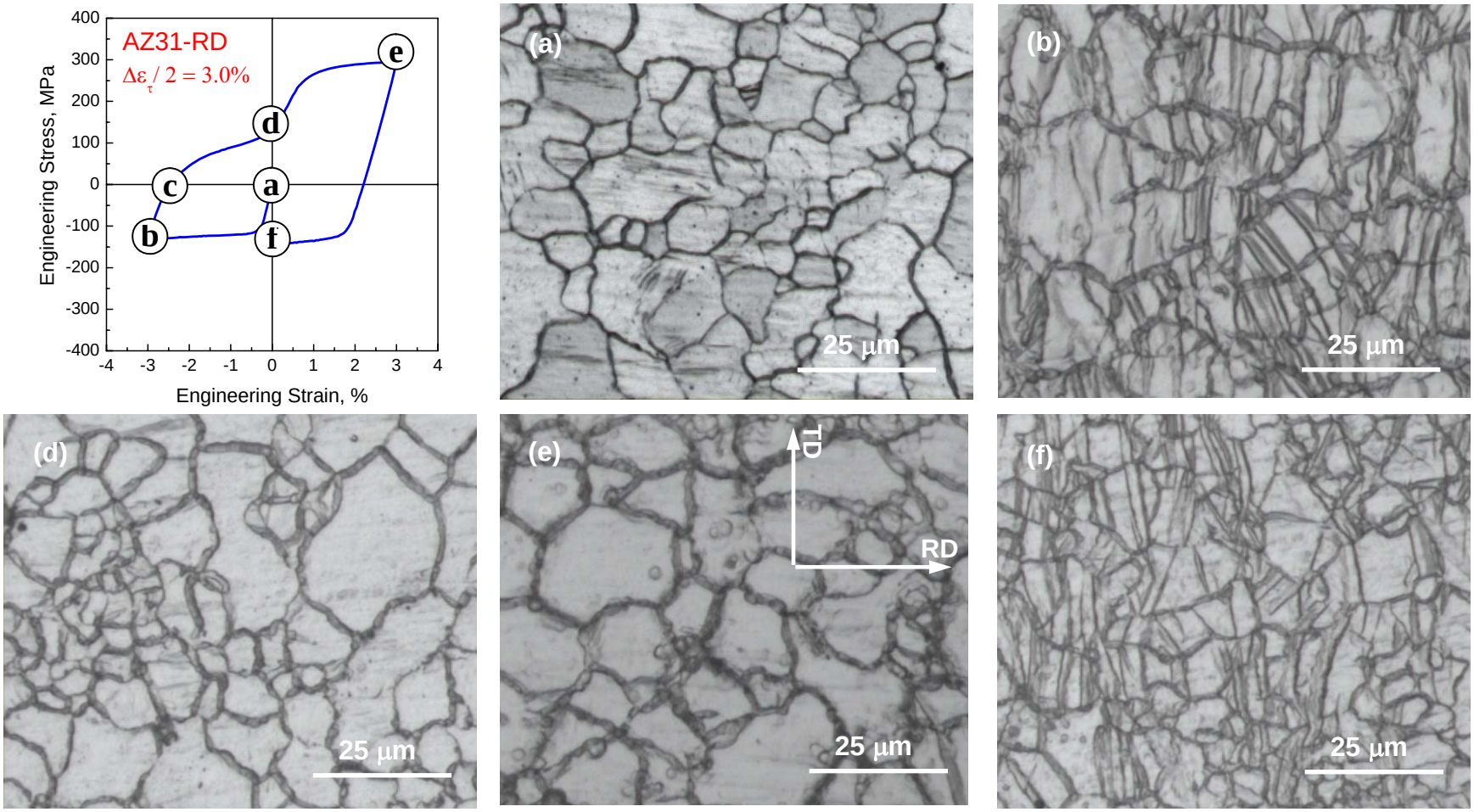

Figure 5.35. Optical microstructure evolution during the first cycle deformation of AZ31B alloy loaded along the RD direction with a total strain amplitude of 3.0%.

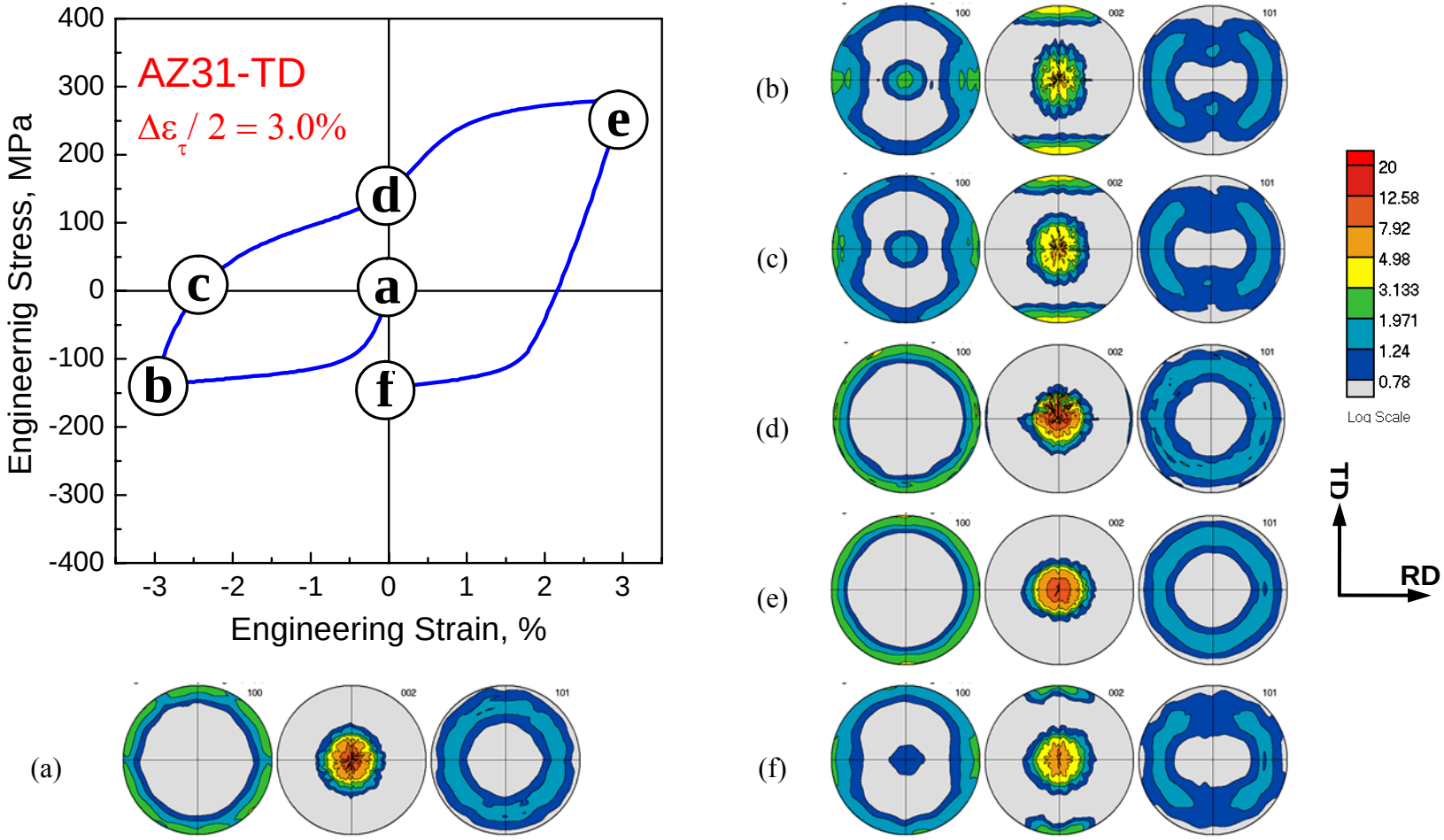

Figure 5.36. Measured crystallographic textures along the hysteresis loop during the first cycle deformation using *ex situ* synchrotron diffraction: a) strain-free, b) – 3.0 % strain, c) 0 MPa stress, d) 0 % strain, e) + 3.0 % strain, and f) 0 % strain. Pole densities are expressed in multiples of a random distribution (mrd). The loading axis (along TD) is vertical.

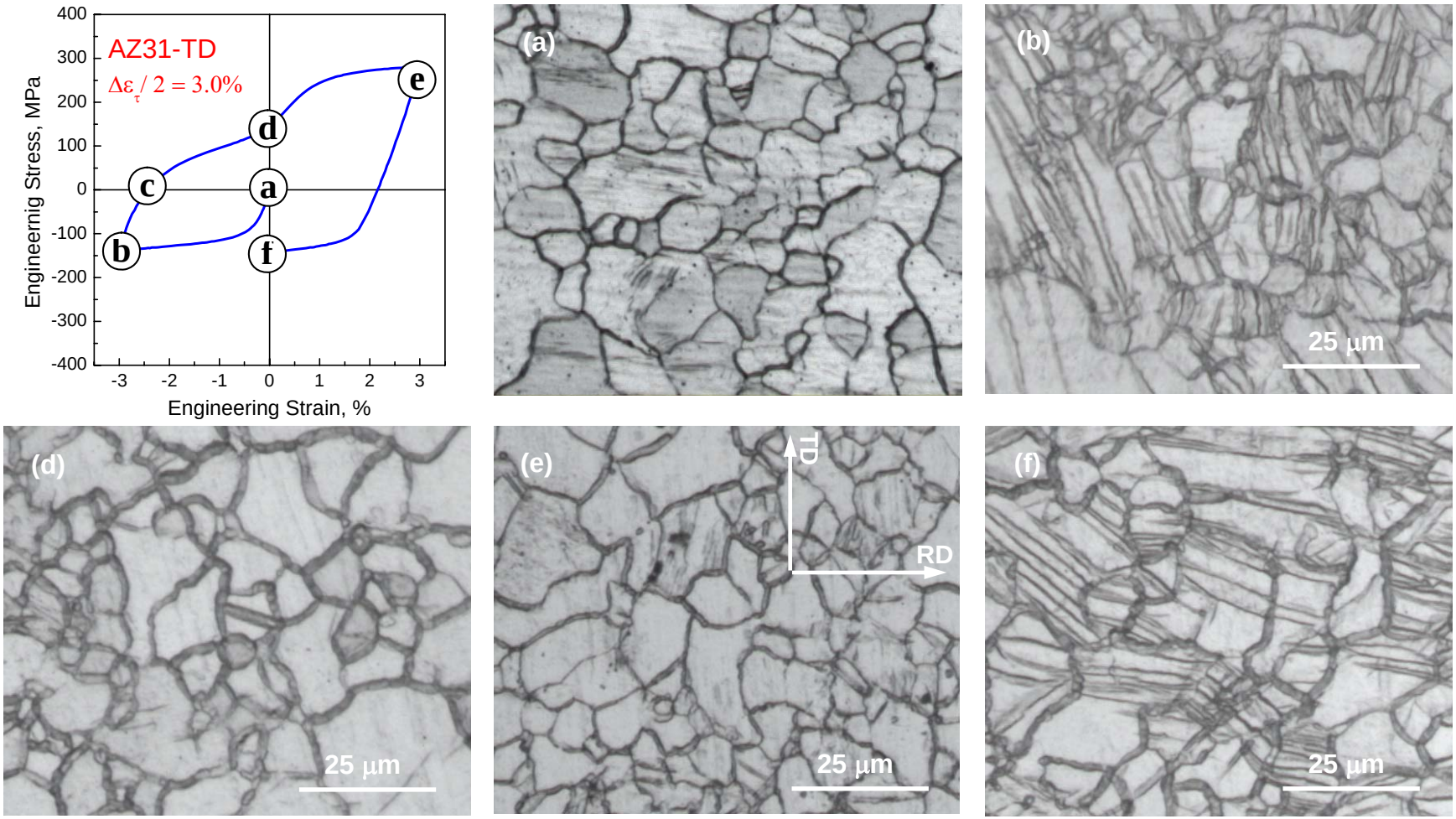

Figure 5.37. Optical microstructure evolution during the first cycle deformation of AZ31B alloy loaded along the TD direction with a total strain amplitude of 3.0%.

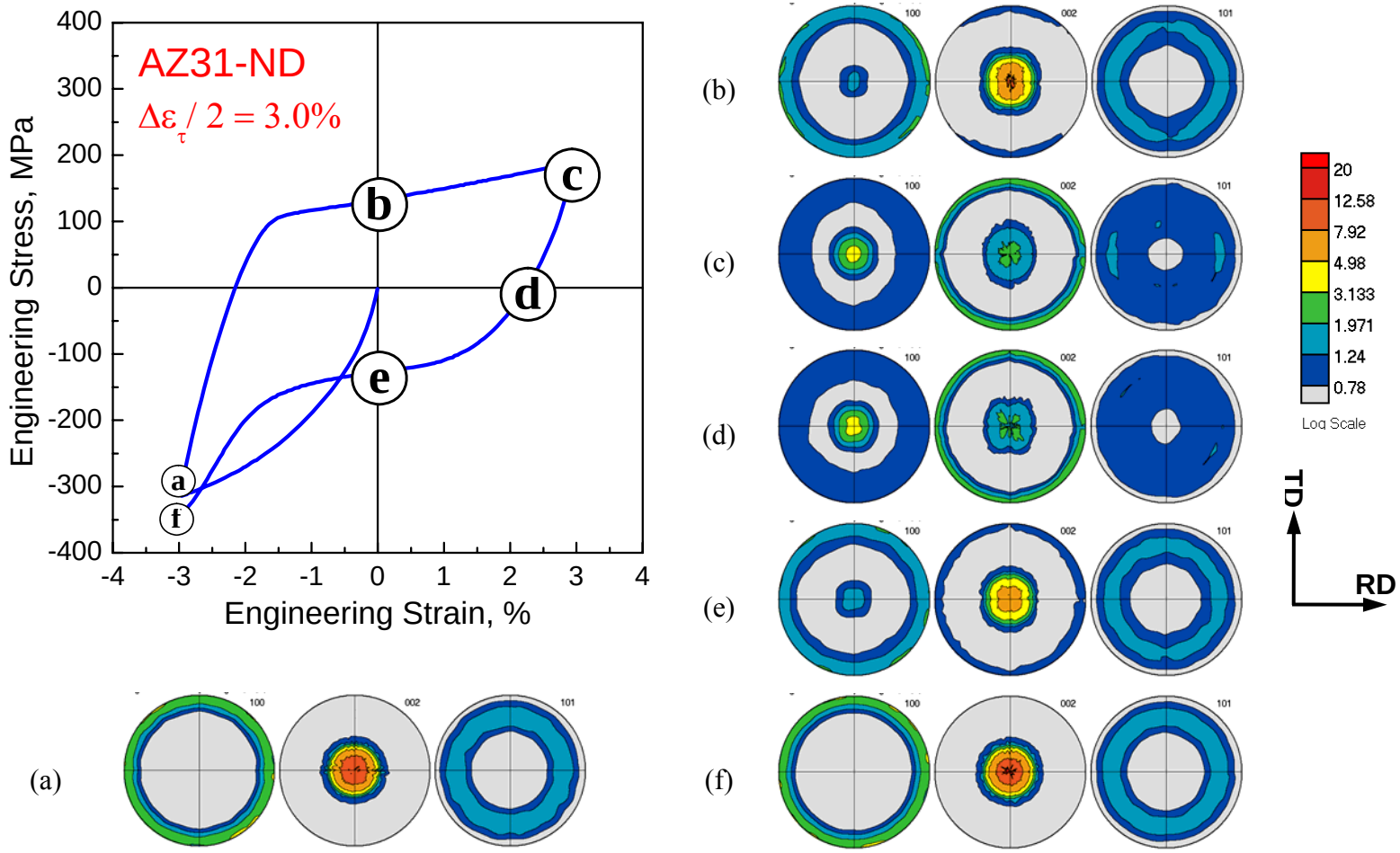

Figure 5.38. Measured crystallographic textures along the hysteresis loop during the first cycle deformation using *ex situ* synchrotron diffraction: a) – 3.0 % strain, b) 0 % strain, c) + 3.0% strain, d) 0 MPa stress, e) 0 % strain, and f) – 3 % strain. Pole densities are expressed in multiples of a random distribution (mrd). The loading axis (along ND) is at the center.

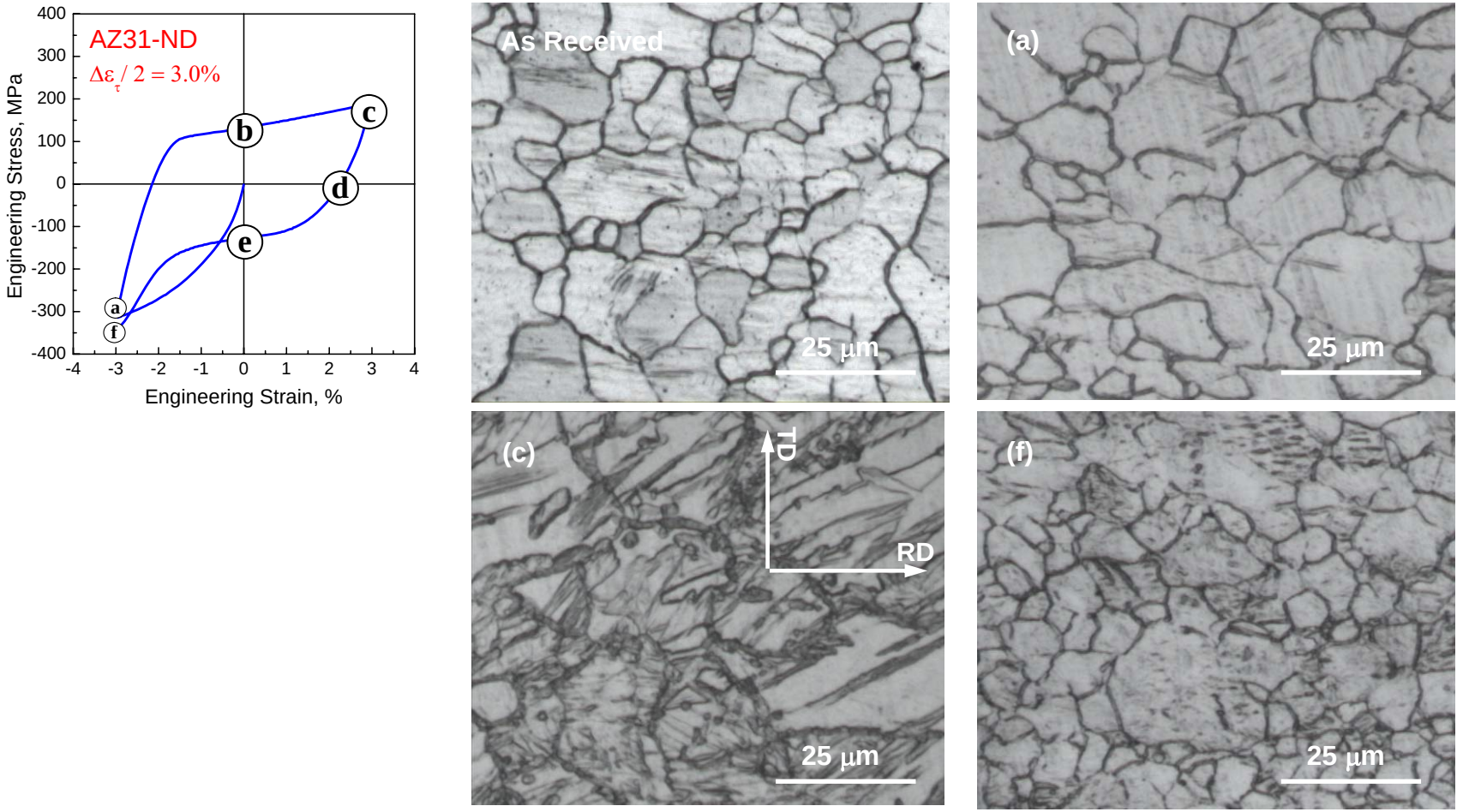

Figure 5.39. Optical microstructure evolution during the first cycle deformation of AZ31B alloy loaded along the ND direction with a total strain amplitude of 3.0%.

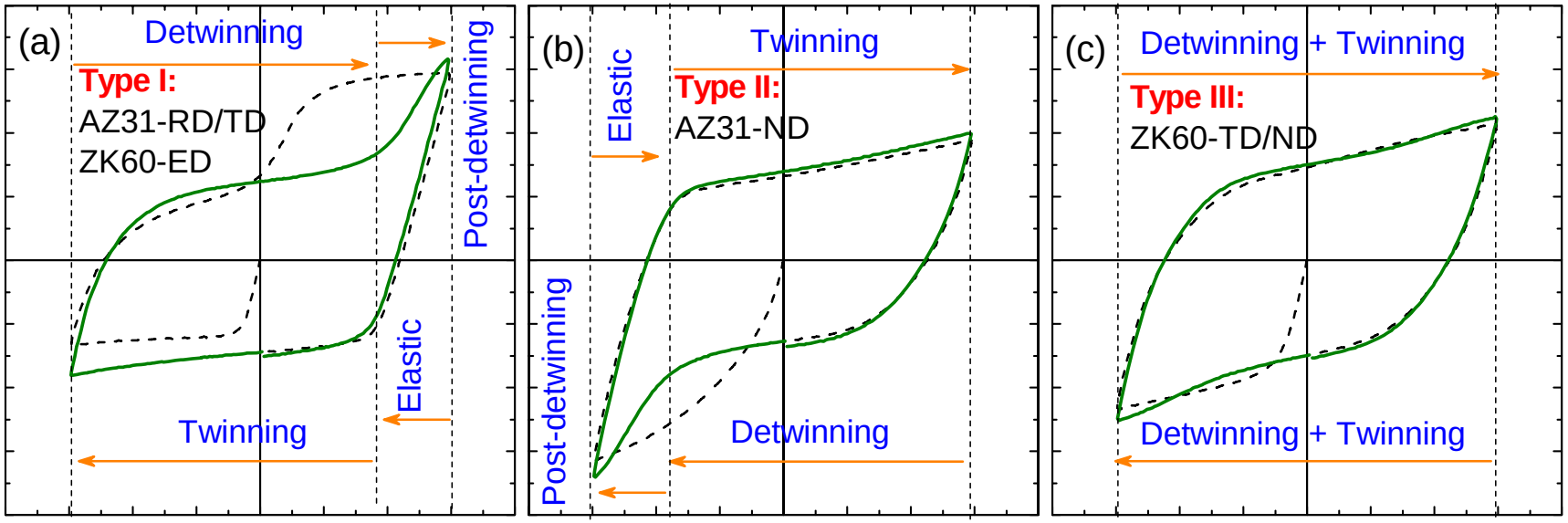

Type I: Asymmetric S-shape

- Twinning in compressive loadings;
- Detwinning in compressive unloadings and tensile reloadings;
- Non-basal <a> dislocation slips in post-detwinning deformation;
- Tensile mean stress;
- Good low-cycle fatigue resistance;
- For example: AZ31B-RD/TD and ZK60A-ED.

Type II: Inverted asymmetric S-shape

- Twinning in tensile loadings;
- Detwinning in tensile unloadings and compressive reloadings;
- No primary deformation modes available in post-detwinning deformation;
- Compressive mean stress;
- Bad low-cycle fatigue.
- For example: AZ31B-ND.

Type III: Nearly symmetric shape:

- Detwinning and twinning in compressive loadings and tensile loadings;
- Twinning in the other texture component for post-detwinning deformation;
- Mean stress close to zero;
- No significant different low-cycle fatigue resistance from the ZK60A-ED.
- For example: ZK60A-TD/ND

Figure 5.40. A summary of the three types of hysteresis loops related to three types of cyclic plastic deformation behaviors, correlating with the low-cycle fatigue properties.

VITA

Liang WU was born and grown up in the city of Jiangyin, Jiangsu Province, China on November 2, 1972. He graduated with a B.S. degree from the Department of Materials Science and Engineering at Yanshan University, China in 1994. Then, he continued his graduate study in the Department of Materials Science and Engineering at Shanghai Jiaotong University, China. Upon graduation with a M.S. degree in 1997, he joined the Specialty Steels Division of BaoSteel Group based in Shanghai as a Materials Engineer. In 1999, he joined Air Products and Chemicals (China) Inc. as an Applications Engineer, and worked there for five years. In August 2004, he started his doctoral study in the Department of Materials Science and Engineering at the University of Tennessee, Knoxville, USA and obtained his Ph.D. degree in December 2009.